# DEVELOPMENT AND MODELING OF A
# POLYMER CONSTRUCT FOR
# PERFUSION IMAGING AND TISSUE ENGINEERING

**by**

**Auresa Thomas**

A dissertation submitted in partial fulfillment
of the requirements for the degree of
Doctor of Philosophy
(Biomedical Engineering)
in The University of Michigan
2014

Doctoral Committee:

> Professor Scott J. Hollister, Co-Chair
> Professor James M. Balter, Co-Chair
> Associate Professor Joseph L. Bull
> Professor Yue Cao

**The Road Not Taken**

Two roads diverged in a yellow wood,
And sorry I could not travel both
And be one traveler, long I stood
And looked down one as far as I could
To where it bent in the undergrowth;

Then took the other, as just as fair,
And having perhaps the better claim
Because it was grassy and wanted wear,
Though as for that the passing there
Had worn them really about the same,

And both that morning equally lay
In leaves no step had trodden black.
Oh, I marked the first for another day!
Yet knowing how way leads on to way
I doubted if I should ever come back.

I shall be telling this with a sigh
Somewhere ages and ages hence:
Two roads diverged in a wood, and I,
I took the one less traveled by,
And that has made all the difference.


*- Robert Frost*




If you can't fly, then *run*.
If you can't run, then *walk*.
If you can't walk, then *crawl*.
But whatever you do, you have to *keep moving forward*.


*- Dr. Martin Luther King, Jr.*

# **DEDICATION**


To my parents for their sacrifices and timely words of support and encouragement
throughout my education.

opportunity to work in the Scaffold Tissue Engineering Group (STEG). Several members of the Radiation Physics group have been a great support: Rojano Kashani, Hesheng Wang, Dr. Kwok Lam, Shu-Hui Hsu and Dr. Peng Wang. Thank you! There are many people (undergraduates and visiting scholars) that I may be forgetting, but am appreciative of all the support I've received throughout my PhD journey.

Thank you to all my 'G-chat friends,' because our daily rantings and venting session were very necessary! Thank you to the friends that randomly texted me to make sure I made it home safely after late nights alone in the lab. Thank you to my writing group for keeping me motivated through what might have otherwise been a lonely process. A special thank you to Dr. Carl S. McGill for sticking around for that PhD! Thank you for supporting me along the way with your optimistic spirit.

Aside from the conferences, research talks and lab meetings, I've had the pleasure of being an active member of the University of Michigan community. SMES-G, AGEP, WISE and the CoE Office have been wonderful supports of any idea I ever wanted to execute. A special thank you to Dr. Debby Mitchell, Mr. Mike Nazareth, Dr. Alex Gallimore (especially for your guidance in the final year of this journey!) and Mrs. Debbie Taylor. Through these organizations and through the many one-on-one interactions, Michigan has broadened my perspective on learning and service. I came to Michigan because I wanted to be on campus that cared about me both as a student and as a citizen of this world. I chose well, 'and that has made all the difference'. There was definitely a Michigan difference, and for that I am grateful.

# TABLE OF CONTENTS

# LIST OF FIGURES

# LIST OF TABLES

# LIST OF APPENDICES

# LIST OF ABBREVIATIONS

| | |
|---|---|
| AIF: | Arterial Input Function |
| AVL: | Arteriovenous Loop |
| BAEC: | Bovine Aortic Endothelial Cell |
| bEC: | Bovine Endothelial Cell |
| BEC: | Human Dermal Blood Endothelial Cell |
| BLI: | Bioluminescent Imaging |
| BMSC: | Bone Marrow Stromal Cell |
| BPMEC: | Bovine Pulmonary Microvascular Endothelial Cell |
| BrdU: | 5'bromo-2'-deoxyuridine |
| CA: | Contrast Agent |
| CAD: | Computer Assisted Design |
| CAM: | Chorioallantoic Membrane |
| CCCD: | Cool Charge-Coupled Device |
| CD 31: | Cluster of Differentiation 31 |
| CFD: | Computational Fluid Dynamics |
| CT: | Computed Tomography |
| DAPI: | 4',6-diamidino-2-phenylindole |
| DCE: | Dynamic Contrast Enhanced |
| EC: | Endothelial Cell |
| ECM: | Extracellular Matrix |
| EDC/Sulfo-NHS: | 1-ethyl-3-(3-dimethylaminopropyl) carbodiimide/N-hydroxysulfosuccinimid |
| EES: | Extravascular Extracellular Space |
| ELISA: | Enzyme-linked Immunosorbent Assay |
| EMP: | Endothelial Microparticle |
| EPC: | Endothelial Progrenitor Cell |

| | |
|---|---|
| Eq.: | Equation |
| Fig.: | Figure |
| FSS: | Fluid Shear Stress |
| Gd: | Gadolinium |
| HA: | Hydroxyapatite |
| HMEC-1: | Human Dermal Microvascular Endothelial Cell |
| HUVEC: | Human Umbilical Vein Endothelial Cell |
| ICAM-1: | Intercellular Adhesion Molecule-1 |
| ICC: | Inverted Colloidal Crystals |
| i.d.: | Inner Diameter |
| LEC: | Lymphatic Endothelial Cell |
| MAD: | Median Absolute Deviation |
| MMPs: | Matrix Metallo-Proteases |
| MPI: | Magnetic Particle Imaging |
| MRE: | Magnetic Resonance Elastography |
| MRI: | Magnetic Resonance Imaging |
| MSC: | Mesenchymal Stem Cell |
| MTT: | 3-(4,5-Dimethylthiazol-2-yl)-2,5-Diphenyltetrazolium Bromide |
| NaOH: | sodium hydroxide |
| NHS: | N- hydroxysuccinimide |
| OFDI: | Optical Frequency Domain Imaging |
| PDGF-B: | Platelet-Derived Growth Factor B chain |
| PDGF-BB: | Platelet-Derived Growth Factor-BB |
| PDMS: | Polydimethylsiloxane |
| PET: | Positron Emission Tomography |
| PET: | Polyethylene Terephtalate |
| PPF: | Poly(propylene fumarate) |
| PCL: | Polycaprolactone |
| PFC: | Perfluorocarbon |
| PLGA: | Poly-lactic-glycolic |
| PMMA: | Polymethylmethacrylate |

| | |
|---|---|
| PS: | Permeability Surface Area Product |
| QA: | Quality Assurance |
| RAEC: | Rat Aortic Endothelial Cell |
| RBC: | Red Blood Cells |
| RGD: | Arg-Gly-Asp Protein |
| ROI: | Region of Interest |
| RP: | Rapid Prototyping |
| RPAEC: | Rat Pulmonary Artery Endothelial Cell |
| SAINT: | Sophia Anatomical Infant Nose-Throat |
| SBF: | Simulated Blood Fluid |
| SC/SL: | Solvent-Casted / Salt-Leached |
| SIMPLE: | Semi-Implicit Method for Pressure Linked Equations |
| SLS: | Selective Laser Sintering |
| SMC: | Smooth Muscle Cells |
| Sulfo-SMCC: | Sulfosuccinimidyl-4-(N-maleimidomethyl)cyclohexane-1-carboxylate |
| SPECT: | Single-Photon Emission Computed Tomography |
| SPIONs: | Superparamagnetic Iron Oxide Nanoparticles |
| SS: | Shear Stress |
| Stdev: | Standard Deviation |
| STL: | Stereolithography File |
| TAC: | Time-Attenuation Curve |
| TCPS: | Tissue Culture Polystyrene |
| TGFβ1: | Transforming Growth Factor-Beta1 |
| UV: | Ultraviolet Lamp |
| VEGF: | Vascular Endothelial Growth Factor |
| vWF: | Von Willebrand Factor |
| WSS: | Wall Shear Stress |

# ABSTRACT

The physical and computational modeling of distributed fluid flow to vascular beds remains a challenging issue. The computational resources required, and the complexity of capillary networks makes modeling infeasible. The resolution limits of manufacturing techniques make physical models difficult to fabricate and manipulate under experimental conditions. As such, an *in vitro* polymer construct was developed with structural properties of small arteries and the bulk flow characteristics of capillary beds. Rapid prototyping and scaffolding techniques were used to fabricate vascular trees amendable to scaffold compartments. Several scaffold architectures were evaluated to achieve target fluid flow characteristics for implementation in a dynamic contrast-enhanced computed tomography (DCE-CT) imaging phantom and endothelial cell bioreactor, respectively. Experimental flow measurements were compared to measurements from computational simulations. In addition, the flow-induced shear stress across the construct was modeled to identify the optimal settings within the bioreactor. In addition, the cytocompatibility of the polymer construct was optimized.

Vascular trees were reliably fabricated to achieve arteriole-like flow. Rapid prototyped polycaprolactone (PCL) scaffolds produced distinct differential flow ranges, marked by a decrease in flow rate across the network. The construct served as a viable dynamic flow phantom capable of generating signals typical of organs imaged with DCE-CT. Furthermore, simulations of the construct as a bioreactor provided guidance on the boundary conditions required for stimulatory shear stress within the scaffolds. Under static conditions, endothelial cells were cultured on PCL scaffolds modified with extra-cellular matrix mimicking biological and chemical agents. All surface modifications exhibited similar cell proliferation and function. However, the Arg-Gly-Asp (RGD) surface-modified constructs exhibited an optimal spatial distribution for future endothelial cell bioreactor investigations.

This work demonstrates a method for modeling and physically simulating a bifurcating vascular tree adjoined to scaffold compartments with tunable flow, for application to perfusion imaging and *in vitro* tissue engineering (tissue and tumors).

# CHAPTER 1

## Introduction

### 1.1  PROBLEM STATEMENT

With over 20 invasive sites, including vital organs such at the lungs, brain, and liver, cancer causes the greatest mortalities worldwide [1-2]. Over the last three decades, there has been increased research focus on prevention, detection, treatment and control of cancer [3-6]. The impact of molecular cancer biology discoveries is evident by the increase in 5-year patient survival rates, rising from by 51.4 to 68.5 percent [7-8]. The greatest increase in survival rates are seen in patients with cancer of the blood (and components), bone marrow, tongue, colorectal, kidney and renal system, tonsil and oropharynx, and Non-Hodgkin lymphoma [7-8]. However, there has been less of a marked increase (in the lungs and brain) and in some cases decreased survival rates (in the liver, pancreas, larynx and uterus) and increased incidents (i.e. childhood cancer, esophagus, kidney and melanoma of the skin) for some disease sites [7-8]. The impact of cancer prevention, detection and treatment can be improved with new and more effective approaches. The next stage of treatment therapies is currently evolving through molecular targeted therapy and applications of biomarkers, nanomedicine and various forms of "personalized" medicine and *in vitro* three-dimensional models [9-14].

Within the perfusion imaging and tissue engineering, the adoption of biomarkers and i*n vitro* three-dimensional models incorporating seeded cells and fluid is under consideration to maximize the effectiveness of existing therapies and research platforms. Despite promising advancements in three-dimensional tissue engineering, the need for *in vitro* culture models remains a prevalent issue limiting the effectiveness of large engineered constructs in the promotion of tissue in-growth. Review papers addressing

topics such as drug discovery, delivery and drug-induced resistance acknowledge the need for culture models more complex than the typical two-dimensional *in vitro* systems [23]. A dynamic endothelial cell bioreactor can provide a platform for studying angiogenesis on clinically relevant scaffold dimensions and future co-cultures with normal cells or cancer cells for the generation of *in vitro* solid tissue or tumors, respectively.

Within radiation therapy treatment assessment, there is significant variability in perfusion imaging protocols used to acquire, post-process and extract perfusion metrics from image datasets [17-19]. The validation of perfusion metrics via a dynamic phantom will allow clinicians to make better generalizations of imaging biomarkers and facilitate longitudinal multicenter clinical trials [20-22]. Thus, the need for *in vitro* fluid bioreactors in tissue engineering and *in vitro* dynamic flow phantoms in radiation oncology, converge on the need to create three-dimensional branching networks supporting distributed fluid flow.

The size scale and vast amount of parallel networking of capillary, however, makes the creation of exact in vitro anatomic flow networks (i.e. artery, arterioles, capillaries, venules and veins), both computationally and physically infeasible, due to the computational complexity and extensive multiscale fabrication that is required [15-6]. The complexity of modeling microcirculation (defined as venule, arteriole, capillary sized vessels, 8-300 μm) has the challenge of appropriately representing anatomical architecture and biofluid-mechanical forces (i.e. flow rate and pressure drops). For noninvasive imaging procedures, a typical 1-mm voxel resolution is two orders of magnitude larger than a capillary. The following thesis addresses the challenges in creating computational and physical models of anatomical and hemodynamic microcirculatory properties by developing an integrated branching network/modular scaffold polymer construct for application to perfusion imaging and tissue engineering.

### 1.1.1 Background

*1.1.1.1 Quality Assurance (QA) of Perfusion Imaging*

Perfusion imaging is currently under investigation as an imaging biomarker indicative of tumor aggressiveness, and tissue response to treatments, such as focal irradiation [24-27]. Dynamic Contrast Enhanced - Computed Tomography (DCE-CT) imaging is one method of perfusion imaging; it involves the acquisition of a time series of single-slice images after the injection of a contrast agent into a patient. The presence of agent allows for the temporal and spatial localization of blood perfusion in the volume of interest (VOI). The acquired images are analyzed to extract perfusion (regional blood supply to tissue) metrics such as blood flow and volume (Fig. 1.1). [27-34].
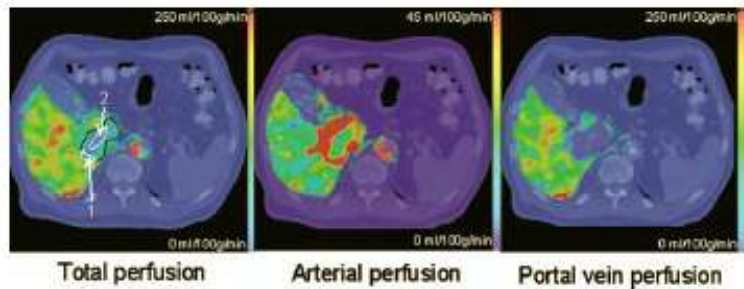


**Figure 1.1 Dynamic Contrast-Enhanced images. Color-coded perfusion maps overlaid on corresponding CT images to denote spatial variation in perfusion. The black contour outlines the tumor region, while the white contours outline regions of interest to be quantified using post-processing techniques [35].**

There is significant variability in the DCE and other imaging protocols used to acquire image datasets and in the post-processing algorithms used to process image data to extract perfusion metrics. The quantification of perfusion from image analysis is a subject of concern, as there is significant variability in DCE acquisition, processing and quantitative metric extraction due to inherent scanner/modality variability, variation in acquisition protocols, spatial and temporal resolution, signal-to-noise ratio, acquisition delays and post-processing methods. Studies have considered (i) the quantification and minimization of measurement variability [29,31], (ii) the discriminatory power of extracted values [34], and (iii) the accuracy of measurements in comparison to "gold

standard" methods (radio-labeled microspheres, O15-water Positron Emission Tomography scans) [27, 32-33], and test-retest and reproducibility cases [32]. Unfortunately, these studies evaluated different DCE metrics, in various tissue locations, in human and animal experiments. This lack of standardization prevents comparisons among studies using the same or different modalities, as the variability in sensitivity of metrics such as blood flow volume has not been quantified. These measures of comparison and reproducibility are useful, but do not provide a repeatable *in vitro* method that is easy to implement across institutions, such as with physical, imaging phantoms. These phantoms provide controllable architectures and fluid environments, across which changes in fluid flow can be assessed under typical, clinical imaging protocols and systems.

*1.1.1.2  Angiogenesis in Engineered Tissue*

Under healthy conditions, angiogenesis is marked by the following stages: endothelial cell (EC) migration and differentiation, tubule formation, and vascular network maturation, remodeling, and regression.   [36-37]. This physical phenomenon, called angiogenesis, is the process by which new capillary blood vessels are grown, either as offshoots or as splits from existing vessels [38] (see Fig. 1.2).  Angiogenesis is critical step to the sustainment of healthy regenerating tissue and newly implanted tissues, in addition to several diseases, such as cancer [37-38]. Tumor angiogenesis is marked by initiation and network formation, but lacks the organization and maturation of vessels characteristic of normal vascular networks [39]. But, for both those interested in tissue regeneration (i.e. bone and cardiovascular) and cancer pathology, re-creating a favorable environment for EC proliferation is key to three-dimensional tissue models. However, overcoming the mass transfer limitations in three-dimensional engineered tissues, greater than 2-mm thick, remains a prevalent and challenging issue [40].
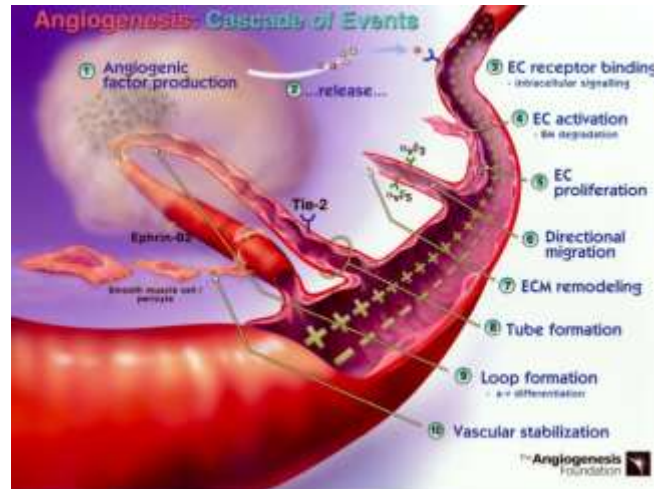
**Figure 1.2 Process of angiogenesis [41].**

Currently, successful tissue replacement therapies are limited to avascular tissues such as the epidermis of skin and nasal septae cartilage [42], or thin tissues (less than 2 mm) such as adipose tissue [43] and smooth muscle [44]. These autologous grafted tissues are supplied oxygen by diffusion. However, oxygen absorption is a limiting factor in cell viability [45], with necrosis normally occurring when oxygen must diffuse over a distance greater than 40-150 μm [42, 46]. Complete oxygen depletion, and resultantly necrosis, occurs within 24 hours of engineered tissue implantation causing donor site morbidity, due to inadequate prevascularization and a slow rate of angiogenesis (upwards of 6 days) [42]. Larger, more complex, engineered tissue requires adequate vascularization to sustain cell viability**Error! Bookmark not defined.**. Successful ascularization of large tissue involves a distributed flow of blood, via capillary networks, to regions of tissue, enabling a high rate of nutrient absorption and waste clearance between the cell and capillary [40].

## 1.2  RESEARCH OBJECTIVES

This research study investigates the physical and computational modeling of distributed flow within an *in vitro* vascular network system, through the adoption of rapid

prototyping (RP) and tissue scaffolding techniques.

### 1.2.1 Aim One

*Hypothesis:* A computer-generated, rapid prototyped bifurcating vascular network can model physiologically realistic flow rates.

*Aim 1:* To design the architecture and evaluate the flow through vascular trees to achieve bulk flow properties (in terms of drop in flow rate and/or velocity) characteristic of *an in vivo* blood supply. To investigate the potential of scaffolds with random and well-organized pore structures to generate distinct differential flow ranges.

#### 1.2.1.1 Aim One Rationale

While not yet translated to complex physical forms, digital models of vascular structures have been developed (Fig. 1.3). Karch et al. proposed an optimization algorithm for generating 3-D coronary vascular trees based on idealized growth principles [47-48]. Similarly, Kretowski et al. presented a more general approach to the modeling of 3-D renal and hepatic arterial trees [49-50]. These algorithms are based on the early works of Murray and Zamir that explored arterial tree morphometry, bifurcation laws (for radii and flow) and work minimization (in terms of blood volume) [51-52]. Computational studies on hemodynamic performance and CT dataset comparisons between real and simulated networks indicate that even with an intrinsic anatomic variability in computer generated trees, these networks behave very similar to *in vivo* vasculature [53-55].



**Figure 1.3 Simulated hepatic vascular network based on optimization algorithm [55]. (Left) Hepatic artery. (Right) Hepatic vein.**

Table A.1 (see Appendix A) summarizes the potential of rapid prototyping to create physical models from digital drawings. Since its advent into the medical arena, in the early 1990s, RP technologies utilizing techniques such as SLS have been used to recreate human anatomy from image (MRI and CT) data [56-57]. Clinicians then use these patient-specific physical models as a visualization tool to more accurately plan treatment, practice and teach surgical procedures and formulate diagnoses [58-63]. As well, researchers have used RP to fabricate patient-specific models to study disease states, anatomical pathologies and the efficacy of medical devices [64-66].

There have been hemodynamic studies of airway passages modeled as hollowed cylindrical tubes; these have been limited to cylindrical tubes with an inner diameter (i.d.) of 1-5 cm [67-69]**Error! Bookmark not defined.**. Janssens et al. modeled the nose-throat (i.d. of .2-3 cm) passageway in infants to better understand and quantify aerosol deposition in the lungs [67]. Clickenbeard et al. used SLS to build tracheobronchial hollow airway models for inhaled aerosol drug studies [69]. Within this model, most airways had an i.d. of 1-2 mm; some airways were slightly smaller than 1 mm. The papers reported clinically relevant results based on their models.

Studies that have attempted to model microcirculation have been unable to fabricate designs on the order of 5-100 microns due to RP resolution limits. As a result, dialysis cartridges with parallel fibers (i.d. of 200 µm) or polydimethylsiloxane (PDMS) derived microchannels (i.d. of 900 µm) have been used to mimic capillary networks [70-72]. Some studies have utilized microfabrication techniques. Wang and Hsu used BioMEMS technology to fabricate bifurcating vessels with an i.d. of 6 µm, to study velocity profiles acting up ECs cultured on the scaffold [73]. Wang et al. studied the use of RP to create scaffolds of hepatocytes that could be plated with bioartificial cells [74], to ultimately grow an artificial liver. Similarly, Lee et al. modeled an artificial liver sinusoidal for hepatocyte culturing using softlithography and replicate molding with PDMS) [75]. Yamada et al. recently reported a new technique for microfabricating structures as fine as 45 µm. However, no such systems are being commercial developed yet [76].

### 1.2.1.2 Aim One Proposed Solution

The proposed work uses porous scaffolds with pore sizes less than 1 mm to produce variable flow resistances that result in differential flow through the scaffold. Civil engineers have taken the approach of modeling the porous media as organized cylindrical structures, whereby the porosity and intrinsic permeability can be directly estimated using Darcy's Law [77]. Subsequently, analytical expressions derived from the Navier-Stokes law are used to define flow properties [78-79]. In the past few years, tissue engineers have adopted this theoretical framework and CFD to evaluate scaffold intrinsic permeability and resulting flow characteristics within bioreactor, drug delivery and tissue regeneration studies [80-81]. Existing models of fluid flow through scaffolds have been limited to stand-alone scaffolds that are not adjoined to feeder networks.

### 1.2.2  Aim Two

*Hypothesis 2*: A physical, dynamic flow phantom with anatomical features and bulk flow characteristic of imaged tissue can provide a framework for the quality assurance of DCE-CT.

*Aim 2:* To prototype a distributed flow phantom that models vessel branching and signals visible with DCE-CT.

### 1.2.2.1  Aim Two Rationale

Generally, physicists perform calibration and QA testing on imaging systems using static phantoms. Phantoms provide a controlled set-up for delineating deviations from a desired output. By simulating an idealized (in terms of branching and symmetry) *in vivo* vascular anatomy, the phantom will model characteristics (vessel bifurcations and diameter size) that affect flow rate [82].. The polymer vascular network and scaffold components are used to achieve i) a CT-compatible phantom with features less than the resolution (approximately less than 1 - 2 mm) of clinical CT, ii) typical contrast-enhancement curves and iii) distinct differential flow ranges through the integration of branching

networks with porous scaffold compartments. The prototype phantom provides a construct for comparing DCE imaging-measured flow rates to experimental and/or computational-based measurements.

Some of the previously implemented flow phantoms have simplified the vascular tree geometry by only using single channel, cylindrical tubes [83], or parallel fibers from commercial dialysis cartridges [71]. On the opposite end, more complex fresh organ-based flow phantoms demonstrated a short lifetime [84], while preserved organs were sensitive to handling and fixation [85]. Recently, Driscoll et al. developed a re-usable dynamic phantom with an internal coiled structure that allowed for variable inputs to reproduce imaging data with time-attenuation curves similar to patient-derived data [86]. The phantom does not evaluate flow within a piping system that is below the resolution of the CT system, as characteristic of *in vivo* imaging of arterioles, venules and capillaries. Instead, the phantom evaluates the bulk flow rates over a VOI encompassing large, arterial-sized tubes.. Fig. 1.4 illustrates the most complex dynamic phantoms presented in the literature.
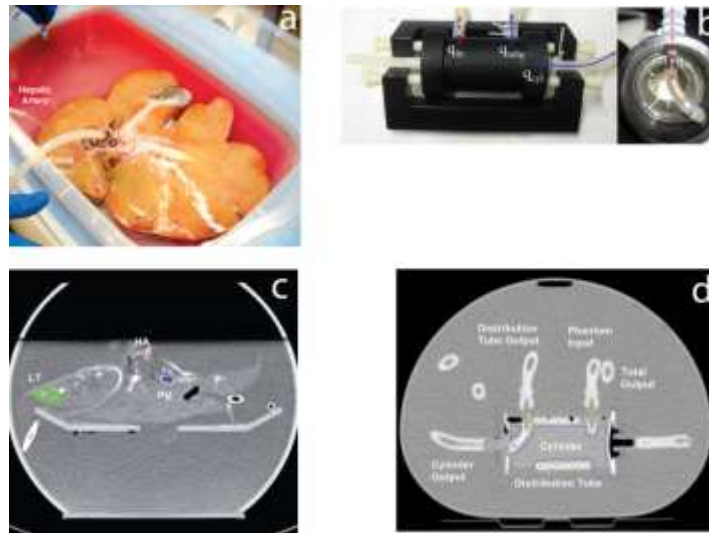


**Figure 1.4 (a) Porcine ex vivo liver phantom [85]. (b) Phantom fabricated using fused deposition model [86]. (c) Single-slice image collected during DCE scan with labeled vasculature [85]. (d) Single axial slice image collected during DCE scan with labeled phantom implanted into a larger phantom structure [86].**

*1.2.2.2 Aim Two Proposed Solution*

The proposed quality assurance phantom seeks to establish a reliable and reproducible method to compare flow measurements acquired via DCE-CT imaging. As well, through the adoption of RP and scaffolding techniques, bulk perfusion characteristics of flow greater than and below the resolution of the typical CT scanner is evaluated for a given input boundary conditions within a physiological flow range.. By altering the porosity and tortuosity of scaffolds within a vascular phantom, we can estimate the flow rates within a closed-system vascular phantom, and fine tune scaffold characteristics to achieve high and low differential flow changes.

## 1.2.3 Aim Three

*Hypothesis 3:* A biocompatible vascular tree adjoined to large porous scaffolds can be optimized to support EC attachment and proliferation.

*Aim 3:* To optimize the attachment and proliferation conditions of endothelial cells seeded on large scaffolds within an *in vitro* endothelial cell bioreactor.

*1.2.3.1 Aim Three Rationale*

Reconstructive surgeries often require the implantation of new tissue into an avascular region, where an adequate nutrient supply cannot be sustained solely by diffusion, but instead requires an alternate source of perfusion. There are several techniques actively studied that seek to expedite the angiogenesis process [87-89] through (1) the implantation of prevascularized engineered or avascular tissue [90-93] that can be pre-seeded with ECs and controlled-release angiogenic factors [94-97] and (2) *in vitro* endothelialized vessels grown on microdevices [98-103], microfluidic devices [104], bioreactors [105-106], or capillary channel fibers or microtubes [1-07-108]. *In vitro* flow perfusion bioreactor studies report that a continuous controlled flow of medium provides mechanical stimulation and increased mass transport to support cell proliferation and differentiation across porous scaffolds for bone regeneration and angiogenesis [109-112].

These successes have been shown for scaffolds 6-8 mm in diameter and 2-3 mm in height. Recently promulgated works by Koch et al. and Arano et al. have demonstrated perfusion for larger (6-12 mm diameter and 10-12 mm height) scaffolds [113-114].

In the area of prevascularized engineered tissue, the arteriovenous loop (AVL) has successfully utilized intrinsic vascularization to support new tissue growth within a loop construct. Mian et al. and Polykandriotis et al. showed that via *angiogenic sprouting*, an arteriovenous loop (AVL) supported new tissue growth within a loop construct: a femoral artery anastomosed to a vein graft and femoral vein [115]. Their AVL studies showed that pre-vascularization of scaffolds resulted in increased vessel in-growth towards the core of the avascular tissue and subsequently an increased wall shear rate within the loop construct. The AVL studies demonstrated that intrinsic prevascularization of scaffolds resulted in an increase in perfusion volume, and subsequently an increase in wall shear rate and angiogenesis with engineered constructs. However, AVLs did not provide distributed flow to a tissue; instead, perfusion is concentrated around the outer boundaries of a tissue region. Using an *in vivo* approach, Laschke et al. implanted a three-dimensional poly-lactic-glycolic (PLGA) scaffold into a host mouse for 20 days to generate microvascular in-growth into the construct [116]. The scaffold was then removed and placed into a recipient mouse. A significant increase in blood perfusion and wall shear stress was observed over the 14 day study, with reperfusion of the implant occurring within 3-6 days. An AVL study by Hofer et al. reported a 23% increase in volume density and the appearance of arterioles within 10 days, along with the appearance of venules after 14-21 days [117].

### 1.2.3.2 Aim Three Proposed Solution

In the aforementioned studies, it has been shown that 1) thick scaffolds can be adequately supplied nutrients/oxygen within a perfusion bioreactor, 2) constructs anastomosed to existing vasculature can successfully shunt flow towards a construct, and 3) pre-vascularized constructs promote angiogenesis faster once implanted into a host. The limitations of these existing methods include: the poor nutrient supply to the core of implantable constructs or the inability to implant successful *in vitro* bioreactor setups.

These studies support aim three's approach to a bioreactor design, which seeks to promote EC growth into tubules, within an implantable vascular network that offers distributed flow across scaffolds, for future *in vitro* or *in vivo* applications. A successful angiogenesis bioreactor system maintains EC viability and proliferation on scaffolds that are embedded within the vascular network construct. As such, the flow conditions, cytocompatibility and distribution of ECs cultured in the bioreactor must be optimized, as the first step in the development of a viable angiogenesis bioreactor.


## 1.3  OVERVIEW OF DISSERTATION

Fig. 1.5 provides a schematic outline of the objectives for Chapters 2 through 6. Chapter 2 provides a review of the anatomical and bulk flow characteristics of human microvascular system that drove the design of the phantom and bioreactor. The computer-generated design for the phantom and bioreactor is described, along with the scaffolding techniques that allowed for control over flow characteristics within the dynamic systems. Chapter 3 reveals the final design of the dynamic imaging phantom system. The reliability and spatial resolution of the fabrication method used to generate the vascular tree and the investigated scaffold (types: solvent casted/salt leached, inverted colloidal crystal and SLS) components are characterized. The intrinsic permeability and differential flow ranges achieved by the different scaffold architectures are compared. Finally, the utility of the phantom was demonstrated through a DCE-imaging study, wherein time-contrast attenuation curves were acquired and examined. Chapter 4 deconstructs the dynamic imaging system in order to perform computational fluid modeling on each component. The mixing of fluids and the uniformity of flow across the system was evaluated. Differential flow measurements from a porous jump and porous geometry model were compared to experimental differential flow measurements in Chapter 3, in order to confirm the flow changes within within the phantom. The scaffolds incorporated into the phantom described in Chapter 3 are widely used as bone scaffolds for tissue engineering. As such, the phantom design was transformed into an *in vitro*, perfusion bioreactor in Chapters 5 and 6. In Chapter 5, the flow-induced shear stress distribution across the scaffold housed within the cell bioreactor design was evaluated for

two scaffold geometries (spherical and orthogonal pores) that have been demonstrated to successfully grow bone (chosen to facilitate future work that may co-culture osteoblasts, then implant in subcutaneous mouse model). The scaffold geometry and the associated inlet velocity that produced the tightest range of shear stress within the physiological range required for EC stimulation was used in the *in vitro* dynamic study. Chapter 6 explores whether a surface modified-SLS PCL scaffold (addition of vascular endothelial growth factor, sodium hydroxide hydrolysis or extracellular matrix adhesion protein) can enhance EC attachment, proliferation and function under static conditions. Based on the identified optimal surface modification, Chapter 6 then presents a preliminary study on the proliferation and cell function of macrovascular ECs under *in vitro* dynamic bioreactor conditions on SLS PCL scaffolds. Based on the limitations of visualizing angiogenesis within the designed bioreactor, Chapter 7 reviewed the existing imaging techniques available for monitoring angiogenesis, and more specifically tubulation, within three-dimensional cell culture constructs (scaffolds, microfluidic devices and bioreactors). Finally, Chapter 8 provides the conclusions from this thesis and describes future studies that may improve the design and/or effectiveness of the phantom and bioreactor.
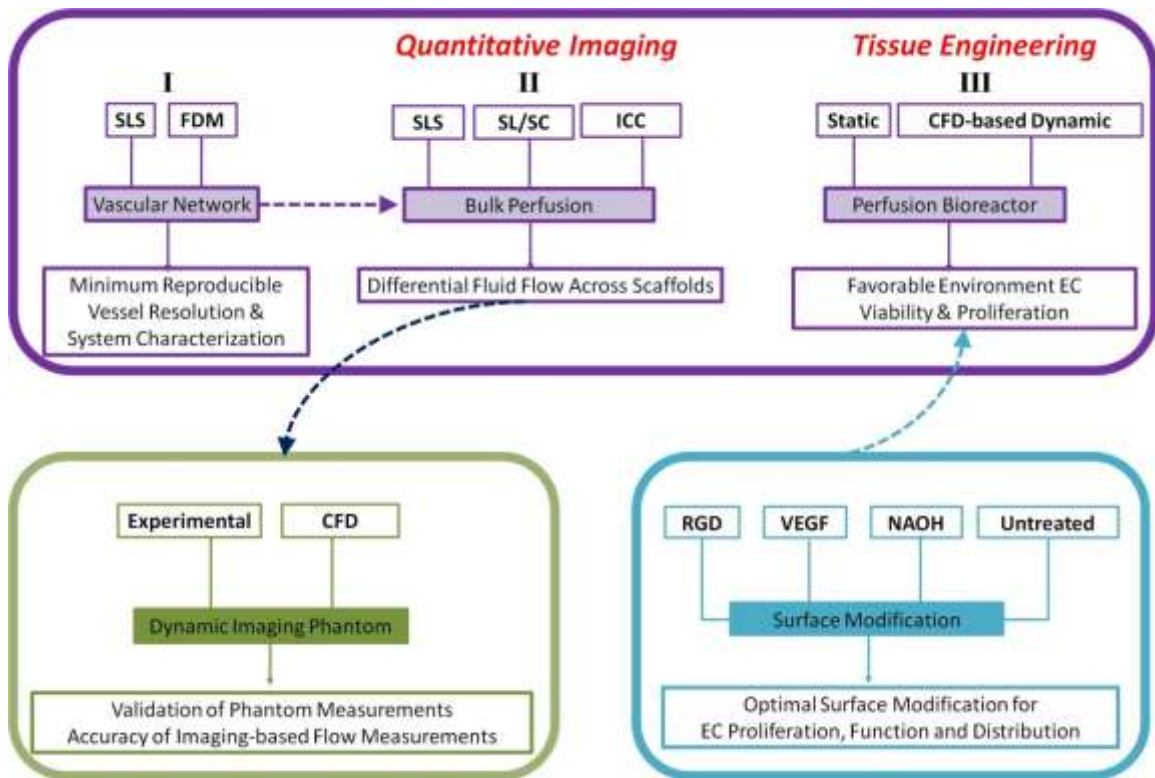
**Figure 1.5 Flow diagram of dissertation goals.**

## 1.4 REFERENCES

[1] Howlader, N., Noone, A.M., Krapcho, M., Neyman, N., Aminou, R., Waldron, W., Altekruse, S.F., Kosary, C.L., Ruhl, J., Tatalovich, Z., Cho, H., Mariotto, A., Eisner, M.P., Lewis, D.R., Chen, H.S., Feuer, E.J., Cronin, K.A., Edwards, B.K. (eds). SEER Cancer Statistics Review, 1975-2008, National Cancer Institute. Bethesda, MD, based on November 2010 SEER data submission, posted to the SEER Web site, 2011 accessed at http://seer.cancer.gov/csr/1975_2008/ on October 14, 2011.

[2] Jemal, A., Bray, F., Center, M.M., Ferlay, J., Ward, E., and Forman, D.. Global cancer statistics. CA: A Cancer Journal for Clinicians. **61**, 69, 2011.

[3] Smith, R.A., Cokkinides, V., von Eschenbach, A.C., Levin, B., Cohen, C., Runowicz, C.D., Sener, S., Saslow, D., and Eyre, H.J.. American Cancer Society Guidelines for the Early Detection of Cancer. CA: A Cancer Journal for Clinicians. **52**, 8, 2002.

[4] Aggarwal, B.B., Shishodia, S.. Molecular Targets of Dietary Agents for Prevention and Therapy of Cancer. Biochemical Pharmacology. **71**, 1397, 2006.

[5] Schilsky, R.L.. Personalized medicine in oncology: the future is now. Nat. Rev. Drug Discov. **9**, 363, 2010.

[6] Weir, H.K., ThunS, M.J., Hankey, B.F., Ries, L.A.G., Howe, H.L., Wingo, P.A., Jemal, A., Ward, E., Anderson, R.N., and Edwards, B.K.. Annual Report to the Nation on the Status of Cancer, 1975–2000, Featuring the Uses of Surveillance Data for Cancer Prevention and Control. Journal of the National Cancer Institute. **95**, 1276, 2003.777

[7] U.S. Cancer Statistics Working Group. *United States Cancer Statistics: 2002 Incidence and Mortality*. Atlanta: U.S. Department of Health and Human Services, Centers for Disease Control and Prevention *and* National Cancer Institute; 2005.

[8] Siegel, R., Ward, E., Brawley, O., and Jemal, A.. Cancer statistics, 2011. CA: A Cancer Journal for Clinicians. **61**, 212, 2011.

[9] Collins, I., and Workman, P.. New Approaches to Molecular Cancer Therapeutics. Nat. Chem. Biol. **2**, 689, 2006.

[10] Gibbs, J.B.. Mechanism-Based Target Identification and Drug Discovery in Cancer Research. Science. **287**, 1969, 2000.

[11] Cao, Y., Tsien, C.I., Sundgren, P.C., Nagesh, V., Normolle, D., Buchtel, H., Junck, L., and Lawrence, T.S.. Dynamic Contrast-Enhanced Magnetic Resonance Imaging As a Biomarker for Prediction of Radiation-Induced Neurocognitive Dysfunction. Clinical Cancer Research. **15**, 1747, 2009.

[12] Murdoch, D., and Sager, J.. Will Targeted Therapy Hold its Promise? An evidence-based review. Current Opinion in Oncology. **20**, 2008.

[13] Kawasaki, E.S., and Player, A.. Nanotechnology, Nanomedicine, and the Development of New, Effective Therapies for Cancer. Nanomedicine: Nanotechnology, Biology and Medicine. **1**, 101, 2005.

[14] Miller, J.C., Pien, H.H., Sahani, D., Sorensen, A.G., Thrall, J.H.. Imaging Angiogenesis: Applications and Potential for Drug Development. Journal of the National Cancer Institute. **97**, 172, 2005.

[15] Grinberg, L., Anor, T., Madsen, J.R., Yakhot, A., Karniadakis, G.E.. Large-scale Simulation of the Human Arterial Tree. Clinical and Experimental Pharmacology and Physiology. **36**(2): 194-205, 2008.

[16] Demongeot, J., Bezy-Wendling, J., Mattes, J., Haigron, P., Glade, N., and Coatrieux, J.L.. Multiscale Modeling and Imaging: the Challenges of biocomplexity. Proceedings of the IEEE. **91**, 1723, 2003.

[17] Padhani, A.. Dynamic Contrast-Enhanced MRI in Clinical Oncology: Current Status and Future Directions. JMRI. **16**: 407-422, 2002.

[18] Sheiman, R. G., Sitek, A.. CT Perfusion Imaging: Know Its Assumption and Limitations. Radiology. **246**(2): 649-650, 2008.

[19] Lopata, R. G., Backes, W. H., van den Bosch, P. P., van Riel, N. A.. On the Identifiability of Pharmacokinetic Parameters in Dynamic Contrast-Enhanced Imaging. Magn. Reson. Med. 58(2):425-9, 2007.

[20] Quantitative Imaging Biomarkers Alliance. 10 July 2009. http://qibawiki.rsna.org

[21] Pandharipande, P., Krinsky, G., Rusinek, H., Lee, V.S.. Perfusion Imaging of the Liver: Current Challenges and Future Goals. RSNA **234**: 661-673, 2005.

[22] Boone, J.. Abstract: AAPM Initiatives in Quantitative Imaging. Medical Physics. **36**(6): 2724, 2009.

[23] Hutmacher, D.W., Horch, R.E., Loessner, D., Rizzi, S., Sieh, S., Reichert, J.C., Clements, J.A., Beier, J.P., Arkudas, A., Bleiziffer, O., and Kneser, U.. Translating Tissue Engineering Technology Platforms into Cancer Research. Journal of Cellular and Molecular Medicine. **13**, 1417, 2009.

[24] Giesel, F.L., Choyke, P.L., Mehndiratta, A., Zechmann, C.M., von Tengg-Kobligk, H., Kayser, K., Bischoff, H., Hintze, C., Delorme, S., Weber, M.A., Essig, M., Kauczor, H., and Knopp, M.V.. Pharmacokinetic Analysis of Malignant Pleural Mesothelioma—Initial Results of Tumor Microcirculation and its Correlation to Microvessel Density (CD-34). Academic Radiology **15**, 563, 2008.

[25] Rosen, M.A., Schnall, M.D.. Dynamic Contrast-Enhanced Magnetic Resonance Imaging for Assessing Tumor Vascularity and Vascular Effects of Targeted Therapies in Renal Cell Carcinoma. Clin Cancer Res. **13**(2): 770s-774s, 2007.

[26] Van Beers, B.E., Leconte, I., Materne, R., Smith, A.M., Jamart, J., Horsmans, Y.. Hepatic Perfusion Parameters in Chronic Liver Disease: Dynamic CT Measurements Correlated with Disease Severity. AJR. 667-673, 2001.

[27] Cenic, A., Nabavi, D..G.. A CT Method to Measure Hemodynamics in Brain Tumors: Validation and Application of Cerebral Blood Flow Maps. Am. Journal Nueroradiol. **21**: 462-470, 2000.

[28] Padhani, A.. Dynamic Contrast-Enhanced MRI Studies in Oncology with an Emphasis on Quantification, Validation and Human Studies. Clinical Radiology. **56**: 607-620, 2001.

[29] Sanelli, P., Nicola, G, Tsiouris, A.J., Ougorets, I., Knight, C., Frommer, B., Veronelli, S., Zimmerman, R.D.. Reproducibility of Postprocessing of Quantitative CT Perfusion Maps. AJR. **188**: 213-218, 2007.

[30] Fiorella, D., Heiserman, J., Prenger, E., Partovi, S.. Assessment of the Reproducibility of Postprocessing Dynamic CT Perfusion Data. Am. J. Neuroradiol. **25**: 97-107, 2004.

[31] Goh V, Halligan S, Taylor SA, Burling D, Bassett P, Bartram CI. Differentiation between diverticulitis and colorectal cancer, quantitative CT perfusion measurements versus morphologic criteria- initial experience. Radiology. 2007;242(2):456-462.

[32] Biederer J, Heller M. Artificial thorax for MR imaging studies in porcine heart-lung preparations. Radiology. **226**:250-255, 2003.

[33] Purdie, T.G., Henderson, E, Lee, T.Y.. Functional CT Imaging of Angiogenesis in Rabbit VX2 Soft-tissue Tumour. Phy Med Biol. **46**: 3161-3175, 2001.

[34] Gillard, J.H., Minhas, P.S., Hayball, M.P., Bearcroft, P.W., Antoun, N.M., Freer, C.E., Mathews, J.C., Miles, K.A., Pickard, J.D.. Assessment of Quantitative Computed Tomographic Cerebral Perfusion Imaging with H2(15)O Positron Emission Tomography. Neurol Res. **22**: 457-464, 2000.

[35] Cao, Y., Alspaugh, J., Shen, Z., Balter, J.M., Lawrence, T.S., Ten Haken, R.K.. A Practical Approach for Quantitative Estimates of Voxel-by-Voxel Liver Perfusion using DCE Imaging and a Compartmental Model. Medical Physics. **33**(8): 3057-3062, 2006.

[36] Nussenbaum, F. and Herman, I.M.. Tumor Angiogenesis: Insights and Innovations. Journal of Oncology. 132641, 2010.

[37] Otrock, Z. K., Mahfouz, R. A. , Makarem, J.A., Shamseddine, A.I.. Understanding the Biology of Angiogenesis: Review of the Most Important Molecular Mechanisms. Blood Cells, Molecules & Diseases. 39(2): 212-220, 2007.

[38] Risau, W. (1997). Mechanisms of Angiogenesis. Nature. **386**: 671-674.

[39] Payne, S.J, Jones, L. Influence of the Tumor Microenvironment on Angiogenesis. Future Oncology. **7**(3): 395-408, 2011.

[40] Novosel, E. C., Kleinhans, C., Kluger, P.J.. Vascularization is the Key Challenge in Tissue Engineering. Advanced Drug Delivery Teviews 63(4-5): 300-311, 2011.

[41] Understanding Angiogenesis. 2011. The Angiogenesis Foundation. 30 October 2011. http://www.angio.org/understanding/process.php

[42] Griffith, C., Miller, C., Miller, C., Sainson, R.C., Calvert, J.W., Jeon, N.L., Hughes, C.C., George, S.C.. Diffusion Limits of an *in Vitro* Thick Prevascularized Tissue. Tissue Engineering. **11**(1/2): 257-266, 2005.

[43] Patrick, C.W., Chauvin, P.B., Hobley, J., Reece, G.P.. Preadipocyte Seeded PLGA Scaffolds for Adipose Tissue Engineering. Tissue Engineering. **5:** 139, 1999.

[44] Kim, B. S., Putnam, A. J., Kulik, T.J., Mooney, D.J.. Optimizing Seeding and Culture Mmethods to Engineer Smooth Muscle Tissue on Biodegradable Polymer Matrices. Biotechnol. Bioeng. **57** : 46, 1998.

[45] Kaully T, Kaufman-Francis, K., Lesman A, Levenberg S.. Vascularization-The Conduit to Viable Engineered Tissues. Tissue Engineering: Part B. **15**(2): 159-169, 2009.

[46] Jain, R.K., Au, P., Tam, J., Duda, D.G., Fukumura, D.. Engineering Vascularized Tissue. Nat. Biotechnol. **23**: 821-823, 2005.

[47] Karch, R., Neumann, F., Neumann, M., Schreiner, W.. A three dimensional model for arterial tree representation, generated by constrained constructive optimization. Computers in Biology and Medicine. **29**: 19-38, 1999.

[48] Schreiner, W., Buxbaum, P. F.. Computer - Optimization of Vascular Trees. IEEE Transactions on Biomedical Engineering. **40**(5): 482-491, 1993

[49] Kretowski, M., Rolland, Y., Bézy-Wendling, J., Coatrieux, J.L.. Fast algorithm for three dimensional vascular tree modeling. Computer Methods and Programs in Biomedicine. **70:**129-136, 2003.

[50] Kretowski, M., Rolland, Y., Bézy-Wendling, J., Coatrieux, J.L.. Physiologically Based Modeling of Three Dimensional Vascular Networks and CT Scan Angiography. IEEE Transactions on Medical Imaging. **22**(2): 248-257, 2003.

[51] Zamir, M.. Optimality principles in arterial branching. J. Theor. Biol. **62**, 227-251, 1976.

[52] Murray, C. D.. The physiological principle of minimum work I. Proc. Nat. Acad. Sci. **12**: 204-214, 1926a.

[53] Schreiner, W.,Neumann, F., Neumann, M., End, A., Roedler, S.M.. Anatomical variability and functional ability of vascular trees modeled by constrained constructive optimization. J. Theor. Biol. **187**, 147-158 ,1997.

[54] Bezy-Wendling, J., Kretowski, M.. Physiological modeling of tumor-affected renal circulation. Computer Methods and Programs in Biomedicine. **91**, 1-12, 2008.

[55] Rolland, Y., Bezy-Wendling, J., Duvauferrier, R. Bruno, A.. Modeling of the parenchymous vascularization and perfusion. Invest. Radiol. **34**, 171-175, 1999.

[56] Binder, T. M., Moertl, D., Mundigler, G., Rehak, G., Franke, M., Delle-Karth, G., Mohl, W., Baumgartner, H., Maurer, G.. Stereolithography Biomodeling to Create Tangible Hard Copies of Cardiac Structures from Echocardriographic Data: In Vitro and In Vivo Validation. Journal of American College of Cardiology. **35**(1): 230-7, 1999.

[57] Markert, M., Weber, S.. A Beating Heart Model 3D Printed from Specific Patient Data. 29th Annual International Conference of the IEE EMBS Cite Internationale. 2007.

[58] Guo, Z., Fenster, A.. Three-Dimensional Power Doppler Imaging: a Phantom Study to Quantify Vessel Stenosis. Ultrasound in Med. & Biol. **22**(8): 1059-1069, 1996.

[59] Alfano, B., Prinster, A., Quarantelli, M.. STEPBRAIN: a Stereolithographed Phantom of the Brain for Nuclear Medicine, Computed Tomography and Magnetic Resonance Imaging. Napoli, Italy, Biostructure & Bioimaging Institute, National Council of Research**:** 1-17, 2002.

[60] Park, M., Zimmerman, R.E., Taberner, A., Kaye, M.W., Moore, S.C.. Design an Fabrication of Phantoms Using Stereolithography for Small-Animal Imaging Systems. Academy of Molecular Imaging. **10**(5):231-6, 2008.

[61] Sun, S.P., Wu, C.J.. Using the Full Scale 3D Solid Anthropometric Model in Radiation Oncology Positioning and Verification. Conf. Proc. IEEE Eng. Med. Biol. Soc. **5**: 3432-5, 2004.

[62] Di Giacomo, G.A., Cury, P.R., de Araujo, N.S., Sendyk, W.R., Sendyk, C.L.. Clinical Application of Stereolithographic Surgical Guides for Implant Placement: Preliminary Results. J. Periodontol. **76**(4): 503-7, 2005.

[63] O'Flynn, P.M., Roche, T.R. , Phandit, A.S.. Generating an Ex Vivo Vascular Model. American Society of Artificial Internal Organs. **51**(4):426-33, 2005.

[64] Faber, J., Berto, P.M., Quaresma, M.. Rapid Prototyping as a Tool for Diagnosis and Treatment Planning for Maxillary Canine Impaction. Am J Orthod Dentofacial Orthop. **129**(4): 583-9, 2006.

[65] Gilon, D., Cape, E. G., Handschumacher, M.D., Song, J.K., Solheim, J., VanAuker, M., King, M.E., Levine, R.A.. Effect of Three-Dimensional Valve Shape on the Hemodynamics of Aortic Stenosis: Three-dimensional Echocardiographic. J. Am. Coll. Cardiol. **40** (8):1479-86, 2002.

[66] Schievano, S., Migliavacca, F.. Percutaneous Pulmonary Valve Implantation Based on Rapid Prototyping of Right Ventricular Outflow Tract and Pulmonary Trunk from MR Data. Radiology. **242**(2): 490-7, 2007.

[67] Janssens, H., de Jongste, J.C., Fokkens, W.J., Robben, S.G., Wouters, K., Tiddens, H.A.. The Sophia: Anatomical Infant Nose-Throat (Saint) Model: A Valuable Tool to Study Aerosol Deposition in Infants. Journal of Aerosol Medicine. **14**(4): 433-441, 2001.

[68] Vial, L., Perchet, D, Fodil, R, Caillibotte, G., Fetita, C., Prêteux, F., Beigelman-Aubry, C., Grenier, P., Thiriet, M., Isabey, D., Sbirlea-Apiou, G.. Airflow Modeling of Steady Inspiration in Two Realistic Proximal Airway Trees Reconstructed from Human Thoracic Tomodensitometric Images. Computer Methods in Biomechanics and Biomedical Engineering. **8**(4): 267-77, 2005.

[69] Clinkenbeard, R.E., Johnson, D.L., Parthasarathy, R., Altan, M.C., Tan, K.H., Park, S.M., Crawford, R.H.. Replication of Human Tracheobronchial Hollow Airway Models Using a Selective Laser Sintering Rapid Prototyping Technique. American Industrial Hygiene Association. **63**: 141-150, 2002.

[70] Veltmann, C., Lohmaier, S., Schlosser, T., Shai, S., Ehlgen, A., Pohl, C., Becher, H., Tiemann, K.. On the Design of a Capillary Flow Phantom for the Evaluation of Ultrasound Contrast Agents at Very Low Flow Velocities. Ultrasound in Med. and Biol. **28**(5): 625-634, 2002.

[71] Hindle, A.J., Perkins, A.C.. A Perfusion Phantom for the Evaluation of Ultrasound Contrast Agents. Ultrasound in Med. & Biol. **20**(3): 309-314,1994.

[72] Raguin, L.G., Honecker, S.L., Georgiadis, J.G.. MRI Velocimetry in Microchannel Networks. Microtechnology in Medicine and Biology, 2005. 3rd IEEE/EMBS Special Topic: 319- 322, 2005.

[73] Wang, G.J., Hsu, Y.. Structure Optimization of Microvascular Scaffolds. Biomed. Microdevices. **10**: 51-58, 2005.

[74] Wang, X., Yongnian, Y., Zhang, R.. Rapid Prototyping as a Tool for Manufacturing Bioartificial Livers. Trends in Biotechnology. **25**(11): 505-513, 2007.

[75] Lee, P. J., Hung, P.J ,M Lee, L. P. (2007). An Artificial Liver Sinusoid with a Microfluidic Endothelial-like Barrier for Primary Hepatocyte Culture. Biotechnology and Bioengineering **97**(5): 1340-1346.

[76] Yamada, A., Niikura, F., Ikuta, K.. A Three-Dimensional Microfabrication System for Biodegradable Polymers with High Resolution and Biocompatibility. J. Micromech. Microeng. **18**: 1-9, 2008.

[77] Muskat, M.. The Flow of Fluids Through Porous Media. Journal of Applied Physics. **8**(4), 274 – 282, 1937.

[78] Cantini, M., Fiore, G. B., Redaelli, A., Soncini, M.. Numerical Fluid-Dynamic Optimization of Microchannel-Provided Porous Scaffolds for the Co-culture of Adherent and Non-Adherent Cells. Tissue Engineering. **15**(3): 615-623,2 009.

[79] Lopez, X. Valvatne, P. H., Blunt, M. J.. Predictive network modeling of single-phase non-Newtonian flow in porous media. Colloid and Interface Science. **264**: 256-65, 2003.

[80] Meuwly, F., Ruffieux, P. A., Kadouri, A. von Stockar, U.. Packed-bed Bioreactors for Mammalian Cell Culture: Bioprocess and Biomedical Applications. Biotechnology Advances**. 25**(1): 45-56, 2007.

[81] Nam, J., Starly, B., Sun, W.. Computer Aided Tissue Engineering for Modeling and Design of Novel Tissue Scaffolds. Computer Aided Design and Application. 633-40, 2004.

[82] Chien, S., Usami, S., Taylor, H.M., Lundberg, J.L., Gregerson, M.I., Effects of Hematocrit and Plasma Proteins on Human Blood Rheology at Low Shear Rates. J. Appl. Physiol. **21**, 81-87, 1965.

[83] Canstein, C., Cachot, P., Faust, A., Stalder, A. F., Bock, J., Frydrychowicz, A., Küffer, J., Hennig, J., Markl, M.. 3D MR Flow Analysis in Realistic Rapid-Prototyping Model Systems of the Thoracic Aorta: Comparison with In Vivo Data and Computational Fluid Dynamics in Identical Vessel Geometries. Magnetic Resonance in Medicine. **59**: 535-546, 2008.

[84] Haberland, U., Cordes, J., Lell, M., Abolmaali, N., Klotz, E.. A Biological Phantom for Contrast-Media-Based Perfusion Studies with CT. Invest. Radiol. **44** (10):676-82, 2009.

[85] Thompson, S.M., Ramirez-Giraldo, J.C., Knudsen, B., Grande, J.P., Christner, J.A., Xu, M., Woodrum, D.A., McCollough, C.H., Callstrom, M.R.. Porcine Ex Vivo Liver Phantom for Dynamic Contrast-Enhanced Computed Tomography: Development and Initial Results. Invest. Radiol. **46**(9):586-93, 2011.

[86] Driscoll, B., Keller, H., Coolens, C.. Development of a Dynamic Flow Imaging Phantom for Dynamic Contrast-Enhanced CT. Medical Physics. **38** (8):4866-4880, 2011.

[87] Griffith, L., Naughton, G.. Tissue Engineering – Current Challenges and Expanding Opportunities. Tissue Engineering. **295**: 1009- 1015, 2002.

[88] Lokmic, Z. M., Mitchell, G. M.. Engineering the Microcirculation. Tissue Engineering: Part B. **14**(1): 87-97, 2008.

[89] Laschke, M., Harder, Y., Amon, M., Martin, I, Farhadi, J., Ring, A., Torio-Padron, N., Schramm, R., Rücker, M., Junker, D., Häufel, J.M., Carvalho, C., Heberer, M., Germann, G., Vollmar, B., Menger, M.D.. Angiogenesis in Tissue Engineering: Breathing Life into Constructed Tissue Substitutes. Tissue Engineering **12**(8): 2093-2104, 2006.

[90] Polykandriotis, E., Arkudas, A., Beier, J.P., Hess, A., Greil, P., Papadopoulos, T., Kopp, J., Bach, A.D., Horch, R.E., Kneser, U.. Instrinsic Axial Vascularization of an Osteoconductive Bone Matrix by means of an Arteriovenous Vascular Bundle. Plastic and Reconstructive Surgery. **120**: 855—868, 2007.

[91] Mian, R., Knight, K. , Penington, A.J., Hurley, J.V., Messina, A., Romeo, R., Morrison, W.A.. Stimulating Effect of an Arteriovenous Shunt on the In Vivo Growth of Isografted Fibroblasts: a Preliminary Report. Tissue Engineering **7**(1): 73-80, 2001.

[92] Erol, O., Spira, M.. New Capillary Bed Formation with a Surgically Constructed Arteriovenous Fistula. Plastic and Reconstructive Surgery. **66**(1): 109-115, 1979.

[93] Beier, J. P., Horch, R.E., Arkudas, A., Polykandriotis, E., Bleiziffer, O., Adamek, E., Hess, A., Kneser, U.. De Novo Generation of Axially Vascularized Tissue in a Large Animal Model. Microsurgery. **29**(1): 42-51, 2008.

[94] Kedem, A., Perets, A., Gamlieli-Bonshtein, I., Dvir-Ginzberg, M., Mizrahi, S., Cohen, S.. Vascular Endothelial Growth Factor-Releasing Scaffolds Enhance Vascularization and Engraftment of Hepatocytes Transplanted on Liver Lobes. Tissue Engineering. **11**(5/6): 715-722, 2005.

[95] Elcin, Y.M., Dixit, V., Gitnick, G.. Extensive In Vivo Angiogenesis Following Controlled Release of Human Vascular Endothelial Cell Growth Factor: Implications for Tissue Engineering and Wound Healing. International Society for Artificial Organs. **25**(7): 558-565, 2001.

[96] Hegen, A., Blois, A., Tiron, C.E., Hellesøy, M., Micklem, D.R., Nör, J.E., Akslen, L.A., Lorens, J.B.. Efficient In Vivo Vascularization of Tissue-Engineering Scaffolds. Journal of tissue engineering and regenerative medicine. **5**(4): e52-62, 2011.

[97] Davies, N., Dobner, S., Bezuidenhout, D., Schmidt, C., Beck, M., Zisch, A.H., Zilla, P.. The Dosage Dependence of VEGF Stimulation on Scaffold Neovascularisation. Biomaterials. **29**, 3531, 2008.

[98] Borenstein, J., Weinberg, E., Orrick, B.K., Sundback, C., Kaazempur-Mofrad, M.R., Vacanti J.P.. Microfabrication of Three-Dimensional Engineered Scaffolds. Tissue Engineering. **13**(8) 1837-1844, 2007.

[99] Shin, M., Matsuda, K., Ishii, O., Terai, H., Kaazempur-Mofrad, M., Borenstein, J., Detmar, M., Vacanti, J.P.. Endotheliazed Networks with a Vascular Geometry in Microfabricated Poly (dimethyl siloxane). Biomedical Microdevices. **6**(4): 269-278, 2004.

[100] Kaihara, S., Borenstein, J., Koka, R., Lalan, S., Ochoa, E.R., Ravens, M., Pien, H., Cunningham, B., Vacanti, J.P.. Silicon Micromachining to Tissue Engineer Branched Vascular Channels for Liver Fabrication. Tissue Engineering. **6**(2): 105-17, 2000.

[101] Fidkowski, C., Kaazempur-Mofrad, M.R.. Endotheliazed Microvasculature Based on Biodegradable Elastomer. Tissue Engineering. **11**(1/2): 302-9, 2005.

[102] Shin, M., Matsuda, K., Ishii, O., Terai, H., Kaazempur-Mofrad, M., Borenstein, J., Detmar, M., Vacanti, J.P.. Endotheliazed Networks with a Vascular Geometry in Microfabricated Poly (dimethyl siloxane). Biomedical Microdevices. **6**(4): 269-278, 2004.

[103] Kaihara, S., Borenstein, J., Koka, R., Lalan, S., Ochoa, E.R., Ravens, M., Pien, H., Cunningham, B., Vacanti, J.P.. Silicon Micromachining to Tissue Engineer Branched Vascular Channels for Liver Fabrication. Tissue Engineering. **6**(2): 105-17, 2000.

[104] Chung, S., R. Sudo, Vickerman, V., Zervantonakis, I.K., Kamm, R.D.. Microfluidic Platforms for Studies of Angiogenesis, Cell Migration, and Cell-Cell Interactions. Sixth International Bio-Fluid Mechanics Symposium and Workshop March 28-30, 2008 Pasadena, California. Annals of Biomedical Engineering. **38**(3): 1164-1177, 2010.

[105] Lee, E. J., Niklason, L.E.. A Novel Flow Bioreactor for In Vitro Microvascularization. Tissue engineering. Part C. **16**(5): 1191-1200, 2010.

[106] Williams, C., Wick, T.M.. Perfusion Bioreactor for Small Diameter Tissue-Engineered Arteries. Tissue engineering. **10**(5/6): 930-941, 2004.

[107] Lu, Q., Sunuibescu, A., Vyavahare, N.. Novel Capillary Channel Fiber Scaffolds for Guided Tissue Engineering. Acta Biomaterialia. **1**(6): 607-14, 2005.

[108] Lovett, M., Cannizzaro, C., Daheron, L., Messmer, B., Vunjak-Novakovic, G., Kaplan, D.L.. Silk Fibroin Microtubes for Blood Vessel Engineering. Biomaterials. **28**: 5271-5279, 2007.

[109] Martin, I., D. Wendt, Heberer, M.. The Role of Bioreactors in Tissue Engineering. Trends in Biotechnology **22**(2): 80-86, 2004.

[110] Barron, V., E. Lyons, Stenson-Cox, C., McHugh, P.E., Pandit, A.. Bioreactors for Cardiovascular Cell and Tissue Growth: a review. Annals of biomedical engineering. **31**(9): 1017-1030, 2003.

[111] Bilodeau, K., Mantovani, D.. Bioreactors for Tissue Engineering: Focus on Mechanical Constraints. A Comparative Review. Tissue Engineering. **12**(8): 2367-2383, 2006.

[112] Konstantinov, S. M., Mindova, M. M., Gospodinov, P.T., Genova, P.I.. Three-Dimensional Bioreactor Cultures: a Useful Dynamic Model for the Study of Cellular Interactions. Annals of the New York Academy of Sciences. **1030**: 103-115, 2004.

[113] Koch, M.A., Vrij, E.J., Engel, E., Planell, J.A., and Lacroix, D.. Perfusion Cell Seeding on Large Porous PLA/Calcium Phosphate Composite Scaffolds in a Perfusion Bioreactor System under Varying Perfusion Parameters. Journal of Biomedical Materials Research: Part A. **95A**, 1011, 2010.

[114] Arano, T., Sato, T., Matsuzaka, K., Ikada, Y., Yoshinari, M.. Osteoblastic Cell Proliferation with Uniform Distribution in a Large Scaffold Using Radial-Flow Bioreactor. Tissue Engineering Part C: Methods. **16**, 1387, 2010.

[115] Mian, R., Knight, K. , Penington, A.J., Hurley, J.V., Messina, A., Romeo, R., Morrison, W.A.. Stimulating Effect of an Arteriovenous Shunt on the In Vivo Growth of Isografted Fibroblasts: a Preliminary Report. Tissue Engineering **7**(1): 73-80, 2001.

[116] Laschke, M.W., Rücker, M., Jensen, G., Carvalho, C., Mülhaupt, R., Gellrich, N.C., Menger, M.D.. Improvement of Vascularization of PLGA Scaffolds by Inosculation of In Situ-preformed Functional Blood Vessels with the Host Microvasculature. Annals of Surgery. **248**(6): 939–948, 2008.

[117] Hofer, S., Knight, K., Cooper-White, J.J., O'Connor, A.J., Perera, J.M., Romeo-Meeuw, R., Penington, A.J., Knight, K.R., Morrison, W.A., Messina, A.. Increasing the Volume of Vascularized Tissue Formation in Engineered Constructs: an Experimental Study in rats. Plast. Reconstr. Surg. **111**: 1186, 2003.

# CHAPTER 2

## Engineering an *In Vitro* Distributed Flow System

### 2.1 INTRODUCTION

This chapter investigates the design and fabrication of a polymer construct that distributes fluid flow across a volume via a vascular tree structure. Bifurcation laws and optimization rules are adopted in the design of computer generated vascular trees. Rapid prototyping techniques available for fabricating small hollow cylinders are assessed. The potential of polymer porous constructs (scaffolds) with random and well-organized pore structures to model disparate changes in flow rates is discussed.

### 2.2  BACKGROUND

#### 2.2.1  Structure and Bio-fluid Mechanics of Blood and Blood Vessels

The human vascular system circulates blood through the body at an average rate of 5 L/min [1]. Blood pumped out of the heart through arteries supplies organs with oxygenated blood and nutrients in exchange for cellular waste. Arteries branch into arterioles, which connect to capillaries, which facilitates active and passive transport of substances between blood and local cells (see Fig. 2.1) [1].
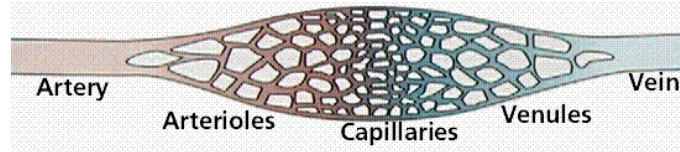
(a)
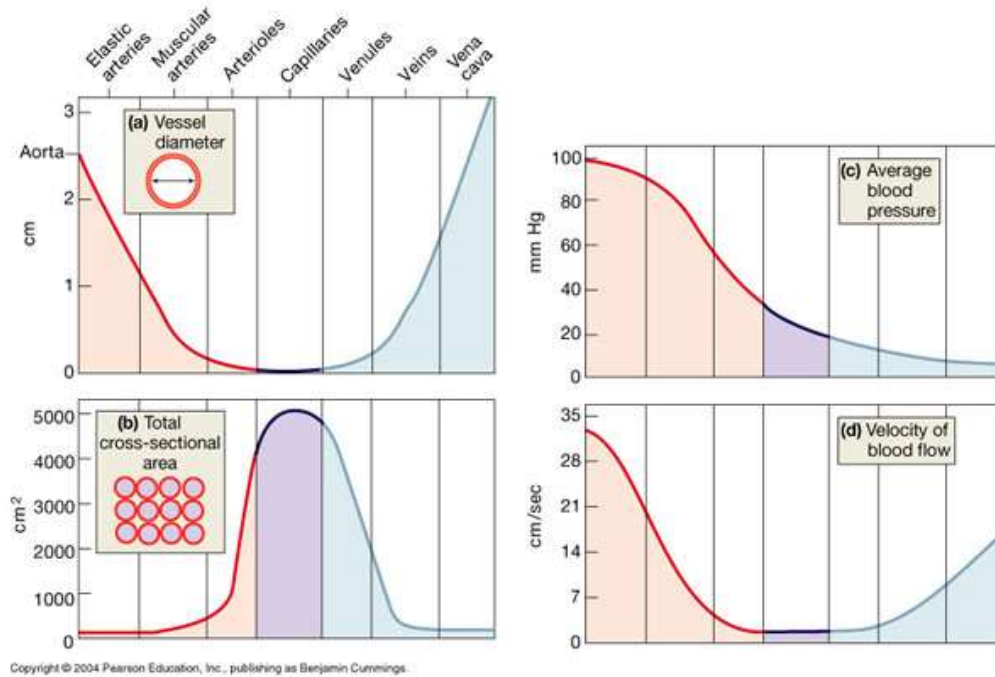


(b)

**Figure 2.1 (a) Schematic illustrates the structural complexity of blood vessel networks from artery/vein down to capillaries [2]. (b) Overview of circulatory physiology, in terms of vessel, diameter, pressure, cross-sectional area and velocity [3]. (Headings shown in the graph on the top left apply to all four plots: elastic arteries, muscular arteries, arterioles, capillaries, venules, veins, vena cava.)**

The anatomical architecture of the circulatory system shunts fluid from a single source through a sequence of serial and parallel vessels whose geometry and composition dictate hemodynamic properties. Each vessel type has a diameter size, wall thickness and composition that uniquely complement its function in the circulatory system [1]. Based on values presented by Boron and Boulpaep [1] and Feher [7], Table 2.1 quantifies a subset of the structural and fluid mechanical properties that characterize blood vessels:

28

wall shear stress (WSS, dyne/cm$^2$), pressure drops ($\Delta$p, mm Hg) and flow velocity (axial and secondary, v, cm/s). Blood flow produces mechanical forces on endothelial cell (ECs) lining the surface of blood vessels. WSS (dyne/cm$^2$) acts tangentially on the surface of ECs. Under physiological conditions, shear stress values within the 1-20 dyne/cm$^2$ range support EC growth and activity [4-6].

**Table 2.1 Summary of average/range *in vivo* values that define blood vessel structures and mechanics, which influence physiological function [1,7].**

| | small artery | arteriole | capillary | venule | small vein |
|---|---|---|---|---|---|
| **inner diameter [mm]** | 2-4 | 0.03 | 0.006 | 0.02 | 5 |
| **wall thickness [mm]** | 1 - 2 | 0.02 | 0.001 | 0.002 | 0.5 - 1.5 |
| **cross sectional area [mm$^2$]** | 0.79 | $7.1 \times 10^{-5}$ | $2.8 \times 10^{-5}$ | $7.1 \times 10^{-5}$ | 0.79 |
| **aggregate flow [ml/s]** | 83 | | | | |
| **single flow [ml/s]** | 0.01 | $4 \times 10^{-6}$ | $8 \times 10^{-9}$ | $2.1 \times 10^{-6}$ | $1 \times 10^{-2}$ |
| **velocity [m/s]** | $1.3 \times 10^{-3}$ | $6 \times 10^{-3}$ | $3 \times 10^{-4}$ | $1 \times 10^{-3}$ | $2.6 \times 10^{-4}$ |
| **pressure [mm Hg]** | 95 | 60 | 15 - 35 | 7-15 | 15 |
| **shear rate [1/s]** | > 100 | < 100 | | | > 100 |

The blood that circulates through these vessels is characterized as a heterogeneous solution composed of plasma, red blood cells (RBC) and white blood cells. It is considered a Newtonian fluid under the following conditions [8-11]:

- shear rates greater than 100/s;

- hematocrit levels greater than 20% (adult normal range lies between 37-50%);

- vessel diameters greater than 800 μm.

Outside of these conditions, blood behaves as a non-Newtonian fluid due to shear-dependent changes in viscosity that occur as RBCs assemble along the center axes of small blood vessels in vessels of decreasing diameter size (known as the Fahraeus-

Lindqvist effect) (see Fig. 2.2) [12]. This phenomenon is especially evident in capillaries, as the inner diameters (i.d.) of these vessels are approximately the same diameter as RBCs. The decreasing viscosity associated with decreased hematocrit levels in small vessels is characterized as a shear thinning, non-Newtonian fluid.
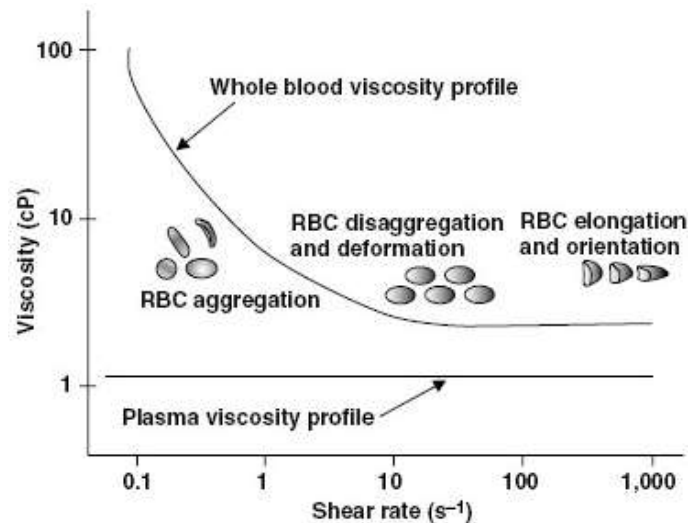


**Figure 2.2 Plot of the dynamic viscosity of blood and plasma across shear rates illustrates the assembly of RBCs. Plasma (devoid of RBC) is Newtonian [13].**

## 2.3 METHODOLOGY

### 2.3.1 Computer Generated Vascular Trees

*In vivo* observations and formulated principles on vascular branching serve as the basis for the implemented three-dimensional vascular network algorithm [14-16]. Two investigating groups pioneered the digital modeling of coronary, renal and/or hepatic arterial trees (i.d. > 1 mm) [14,16]. Karch et al. and Kretowski et al. presented algorithms for generating vascular trees (arterial, renal and hepatic) based on idealized growth principles [14-18]. Both algorithms optimized the structural and hemodynamic properties of vascular trees based on the following:

- Each branch is a rigid, hollow, symmetrical cylinder, with some wall thickness;

- All parent branches give rise to two offspring branches;

30

- Each branch is contained within a pre-defined volume;

- Branching is randomized, with each coordinate within the given volume equally likely to be chosen;

- The bifurcation rule (Murray's Law), where $r$ is the radius of the vessel and $r > 0$ [19]:

$$r^3_{parent} = r^3_{offspring\_left} + r^3_{offspring\_right}$$ Equation 2.1

- If a new branch lies within $n$ millimeters of an existing branch, then the new branch is destroyed; where the value of $n$ is pre-defined— no branches may intersect;

- Blood is considered an incompressible homogenous Newtonian fluid exhibiting laminar flow and governed by Poiseuille's law [20]:

$$\Delta P = Q * \frac{8*\mu*l}{\pi*r^4},$$ Equation 2.2

where $\Delta P$ is the pressure drop across the cylinder, $Q$ is the volumetric flow rate , $l$ is the   length of cylinder and $\mu$ is the fluid's dynamic viscosity;

- The law of matter preservation [16]:

$$Q_{parent} = Q_{offspring\_left} + Q_{offpsring\_right}$$ Equation 2.3

- The pressure drop along a path from root to a terminal branch is the same for all terminals.

In this thesis, these conditions are limited to a single-plane with pre-defined architecture for initial testing and adaptation to the development of an imaging phantom and cell bioreactor. Fig. 2.3 diagrams the implementation of the pre-defined vascular networks in the generated C++ program.
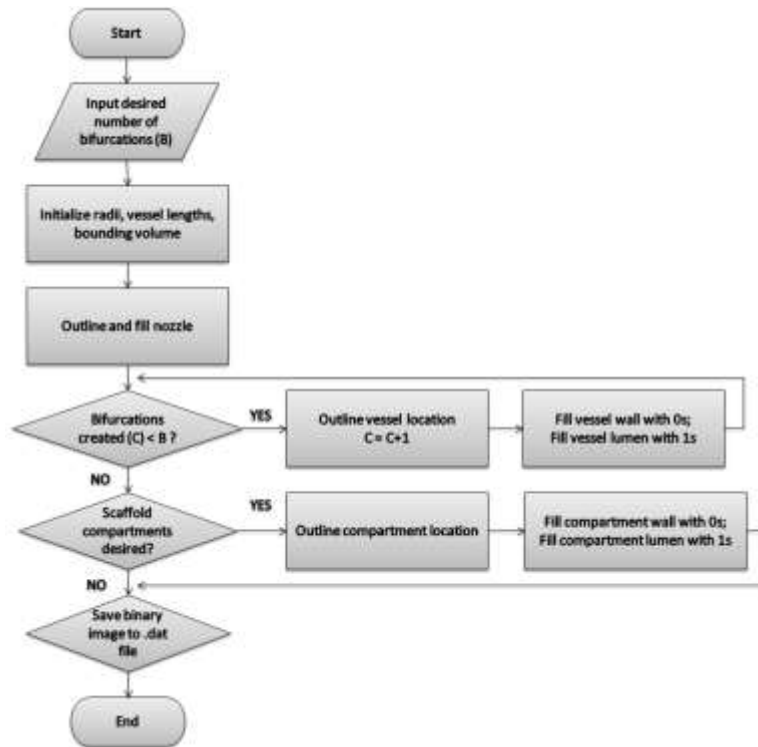
**Figure 2.3 Flow chart of implementation for pre-defined vascular trees with and without scaffold compartments.**

The implemented vascular tree algorithm stored the spatial geometry of the generated networks in a binary image file. The algorithm imposed the following structural conditions: (i) branches were hollow cylinders, with specified wall thickness and i.d., (ii) branches were bounded within a pre-defined volume, (iii) branches birfucated and (iv) branches did not intersect. The cylindrical geometry of each vessel was outlined about its center axis (Fig. 2.4). In Fig. 2.4, the orthonormal vectors, $P_3$ and $P_4$, on the plane orthogonal to line segment ($P_2P_1$) created by the two known points, the start and end positions, define the axis of orientation for the cylinder to be generated.

(a)                                    (b)
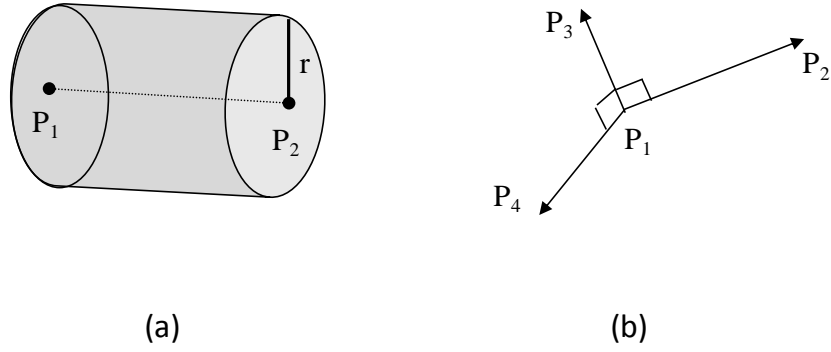
**Figure 2.4 (a) Illustrates cylinder defined by line segment, $P_2P_1$ and radius, r. (b) The cross product of two known points $P_1$ and $P_2$ is the normal vector to $P_3P_1$.**

Assuming X to be a point in the space, not on $P_2P_1$, that satisfies (inner radius) $< XP_1 <$ (outer radius) of the desired vessel, the cylinder was filled based on the following properties and using Equations 2.4. Discrete points, $XP_1$, from the inner radius to outer radius were stepped through along the distance of the line segment $P_2P_1$.

$$XP_1 \times P_2P_1 \rightarrow P_3 \perp P_2P_1$$
$$P_3P_1 \times P_2P_1 \rightarrow P_4 \perp P_2P_1 \perp P_3P_1$$
$$R_x = P_{1x} + rP_{3x}\cos\theta + rP_{4x}\sin\theta$$
$$R_y = P_{1y} + rP_{3y}\cos\theta + rP_{4y}\sin\theta \quad , \text{for} \ \ 0 \leq \theta \leq 2\pi \qquad \text{Equations 2.4}$$
$$R_z = P_{1z} + r\,P_{3z}\cos\theta + rP_{4z}\sin\theta$$

The pre-defined architecture was implemented, whereby vascular networks bifurcated symmetrically along a single axis with each vessel having a programmed inner diameter and length (with left and right offspring congruent, forming a 90° angle). Based on the number of bifurcations desired, the radii size is computed using the bifurcation rule (Equation 2.1).

A three-dimensional binary image represented the geometry of the vascular tree: the lumen and wall with ones and zeros, respectively. Using a data visualization environment

(IDL, ITT Visual Information Solutions, White Plains, New York, USA), a triangulated surface mesh that outlined the geometry of the vascular network was generated from the three-dimensional binary image file. A surface mesh rendering of a vascular branching element is shown in Fig. 2.5. Fig. 2.6a shows CAD representations of the mirrored vascular networks. The initial vessel-generating branching algorithm created surface inconsistencies that produced small holes in the bifurcation region during the STL generation step. The blue areas in Fig. 2.6a delineate regions where holes occurred. These holes were "patched" using rapid prototyping software (Magics, Materialise Belgium) Fig. 2.6b.



**Figure 2.5 CAD of three-dimensional triangulated surface mesh for a first order bifurcating tree.**
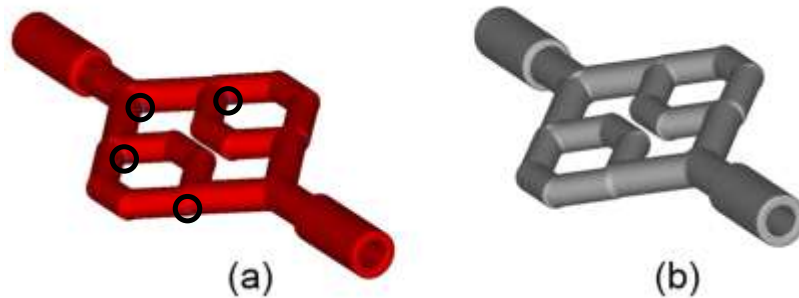


**Figure 2.6 (a) CAD of branching network with holes (blue area; black circles) in the mesh surface at the bifurcation regions. (b) The CAD geometry fixed by the 'patch hole' feature in rapid prototyping software.**

34

*2.3.1.1 Rapid Prototyping Implementation and Considerations*

Physical renderings of the designed vascular tree were achieved using rapid prototyping. Table 2.2 provides a summary of advantages and disadvantages of available rapid prototyping systems. The rapid prototyping techniques involved an automated layer-by-layer process of fusing raw materials (typically metal or polymer) into a CAD-defined three-dimensional shape.

**Table 2.2 Summary of RP methods employed in tissue engineering [21].**

| RP system | Resolution (μm) | Material | Strength | Weakness |
|---|---|---|---|---|
| **Melt-dissolution deposition technique** | | | | |
| Fused deposition modeling | 250 | PCL*, PP-TCP, PCL-HA, PCL-TCP | Good mechanical strength; versatile in lay-down pattern design | High temperature; need to produce filament material; narrow processing window; rigid filament |
| 3D fiber-deposition technique | 250 | PEGT-PBT | Input material in pellet form; preparation time is reduced | High temperature; rigid filament |
| Precision extruding deposition | 250 | PCL | Input material in pellet form | High temperature; rigid filament |
| Precise extrusion manufacturing | 200–500 | PLLA-TCP | Input material in pellet form | High temperature; rigid filament |
| Low-temperature deposition manufacturing | 400 | PLLA-TCP | Can incorporate biomolecule | Solvent is used; requires freeze drying |
| Multi-nozzle deposition manufacturing | 400 | PLLA-TCP | Enhanced range of materials can be used; can incorporate biomolecule | Solvent is used; requires freeze drying |
| Pressure-assisted microsyringe | 10–600 | PCL, PLLA | Enhanced range of materials can be used; can incorporate biomolecule; very fine resolution can be achieved | Small nozzle inhibits incorporation of particle; narrow range of printable viscosities; solvent is used |
| Robocasting | 100–1000 | Organic ink | Enhanced range of materials can be used | Precise control of ink properties is crucial |
| 3D bioplotter | 250 | Hydrogel | Enhanced range of materials can be used; can incorporate biomolecule | Low mechanical strength; smooth surface; low accuracy; slow processing; precise control of properties of material and medium; calibration for new material |
| Rapid prototyping robotic dispensing system | 400–1000 | Chitosanchitosan-HA | Enhanced range of materials can be used; can incorporate biomolecule | Precise control properties of material and medium; requires freeze drying |
| **Particle bonding techniques** | | | | |
| 3-dimensional printing™ | 200 | PLGA, starch-based polymer | Microposity induced in the scaffold; enhanced range of materials can be used; water used as binder; no support structure needed; fast processing | Material must be in powder form; limited mechanical strength; Powdery surface finish; trapped powder issue; might require postprocessing |
| TheriForm™ | 300 | PLLA | Microposity induced in the scaffold; enhanced range of materials can be used; non-organic binder is possible; no support structure is needed; fast processing | Material must be in powder form; powdery surface finish; trapped powder |
| Selective laser sintering | 500 | PEEK-HA, PCL | Microposity induced in the scaffold enhanced range of materials can be used; no support structure needed; fast processing | Material must be in powder form; high temperature; powdery surface finish; trapped powder |
| **Indirect RP fabrication method** | | | | |
| Melt deposition | 250 | Thermoplastic polymer | Enhanced range of materials can be used; control of external and internal morphology | Multisteps involved |
| Droplet deposition | 180 | Wax | Enhanced range of materials can be used; control of external and internal morphology | Multisteps involved |
| Photo-polymerization | 366 | Resin | Enhanced range of materials can be used; control of external and internal morphology | Multisteps involved |

*Abbreviations: HA, hydroxyapatite; PCL, polycaprolactone; PEEK-HA, polyetheretherketone-hydroxyapatite; PEGT-PBT, poly(ethylene glycol)-terephthalate-poly(butylenes terephthalate; PLLA, poly-L-lactide; PP-TCP, polypropylene-tricalcium phosphate.

In this thesis, FDM and SLS were explored. Both systems used biocompatible polymers that offered a direct RP method with a reasonable accuracy (250-500 microns) that did

not require internal supporting structures. The SLS system (EOS FORMIGA P100 SLS, EOS GmbH, Munich, Germany) deposited polymer particles across a layer on the bed of the system, and then selectively fused the particles using a high power laser to produce a three-dimensional object. Each layer was outlined by cross-sections of a three-dimensional image file. Layering was repeated, with each successive layer resting on top of the previous layer (see Fig. 2.7) [22]. The system used a 0.08 mm layer thickness during the build process. The FDM system created three-dimensional objects in a similar layering manner to SLS, however small thermoplastic beads were deposited specifically in locations outlined by CAD cross-sections, instead of being etched onto a powdered bed (see Fig. 2.8) [23]. The FDM system (Dimension Elite Printer, Stratasys Inc., Eden Prairie, Minnesota, USA) used a 0.178 mm layer thickness during the build process. FDM used ABSplus$^{TM}$, while SLS used a powdered thermoplastic mixture of polycaprolactone (PCL) and hydroxyapatite (HA) (CAPA 6501, Solvay Caprolactones, Warrington, Cherise, UK) (HA, Plasma Biotal Ltd., UK).

The final product of rapid prototyping systems was subject to the variances in a given system's humidity level, beam accuracy, bed temperature, laser age and reliability of its mechanical parts [24]. As well, the molecular mass, viscosity and thermal conductivity of the raw material may have introduced variance [25].

Lenses

X-Y scanning mirror

Laser beam

Sintered part

Laser

Leveling roller

Powder feed supply

Powder bed

Powder feed piston

Build chamber

Build piston

Powder feed piston

Powder feed supply

Copyright © 2008 CustomPartNet
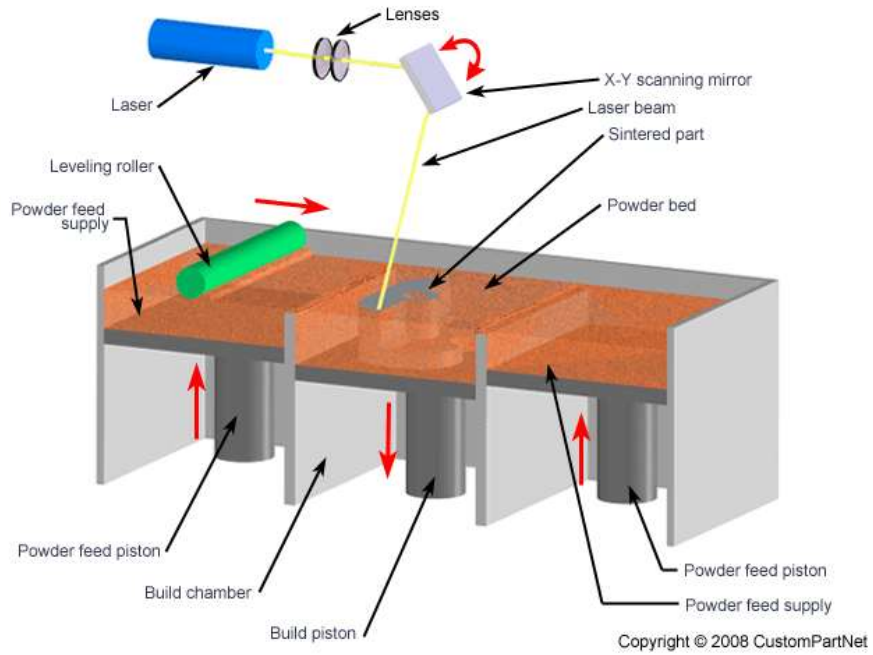
**Figure 2.7 Schematic of SLS system [26].**



Support material filament

Build material filament

Extrusion head

Drive wheels

Liquifiers

Extrusion nozzles

Part

Foam base

Part supports

Build platform

Support material spool

Build material spool

Copyright © 2008 CustomPartNet
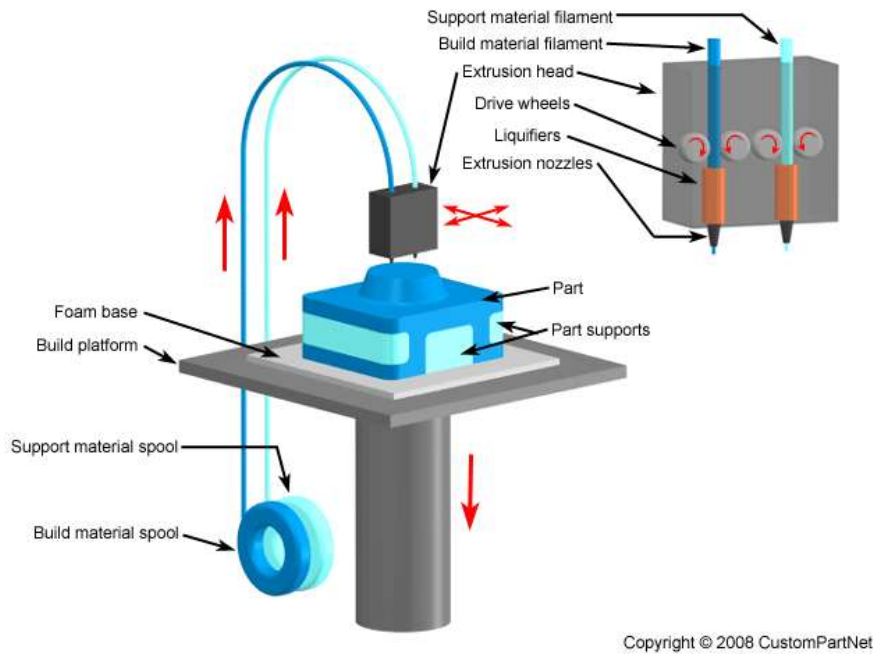
**Figure 2.8 Schematic of FDM system [27].**

### 2.3.2 Controllable Scaffold Architecture

The literature suggests that in the assessment of bulk properties, such as intrinsic permeability and volumetric flow, a simplified porous media model is computationally feasible and may be representative of flow resistance at the capillary level [28-29]. This thesis proposes the use of porous scaffolds with pore sizes less than 2 mm to produce controllable variable flow resistances that result in differential flow through the scaffold. In tissue engineering, a scaffold's pore size, porosity and interconnectivity directly affect its ability to maintain an adequate exchange of oxygen to support cells viability and proliferation [30-31]. As such, there are a multitude of scaffold fabrication techniques offering various methods and materials to control scaffold architecture: electrospinning, particle leaching - solvent casting, inverted colloidal crystal (ICC) formation, RP, etc. Particle leaching - solvent casting offers a less structured [32], random arrangement of pores within a scaffold, while rapid prototyping and ICC provide more structured pore lattices [33]. Each method offers a range of pore sizes and scalable dimension (height and radius).

In practice, *in vivo* capillary networks and/or their pore networks are too complex to individually measure or mathematically represent. Consequently, this thesis offers a simplified representation of these pore networks. SLS and ICC scaffolding techniques consider pores to be equivalent to a collection of vertical and horizontal straight tubes, wherein the radii of those tubes are varied to increase and decrease the level of tortuosity. The orthogonal intersection of these tubes produces a complex network that creates a tortuous flow path for perfusing fluids. The random organization of pores within the SL/SC technique offers greater, but unpredictable tortuosity. Each scaffolding technique employed in this thesis offers a distinct range of porogen diameter sizes that can be used to influence the tortuosity of the final scaffold construct. The increased tortuosity is expected to increase the pressure drop, and as a result decrease the volumetric flow rate across the scaffold [34-36]. A limitation of this model is that the pore sizes across the length of the scaffold do not vary in diameter or length, as capillaries *in vivo*.

*2.3.2.1 Scaffold Design and Fabrication*

To control the flow characteristics of interest in Aim 2 and 3, several PCL scaffold fabrication techniques were explored. Three techniques that produced three distinct geometries were identified: inverted colloidal crystal (ICC) (Fig. 2.9), solvent-casted / salt-leached (Fig. 2.10) and SLS (Fig. 2.11). The SC/SL technique involved the use of salt crystals (less than 1 mm) as porogens to produce sponge-like scaffolds with a random distribution of crystals [39]. The ICC technique offered a highly structured scaffold, in which microspheres (5 - 300 microns) self-assembled into tightly packed hexagonal crystal lattices to form scaffolds [33]. CAD drawings of porous cylindrical scaffolds with three-dimensional spherical, orthogonal and hexagonal periodic porous architectures were designed. The scaffold geometry consisted of a unit cell (1.5 - 2.22 mm) that repeated every 2 mm to fill a desired scaffold height and diameter. The ICC and SLS methods facilitated computational modeling of the scaffold.



(a)                    (b)
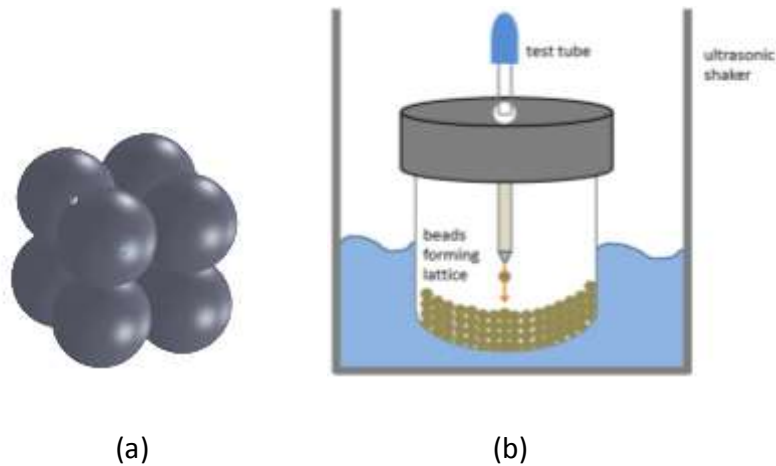
**Figure 2.9 ICC fabrication. (a) Unit cell of spherical lattice representative of ICC scaffold geometry, where the dark grey spheres are representative of glass microspheres. (b) Schematic of the ICC scaffold fabrication process.**
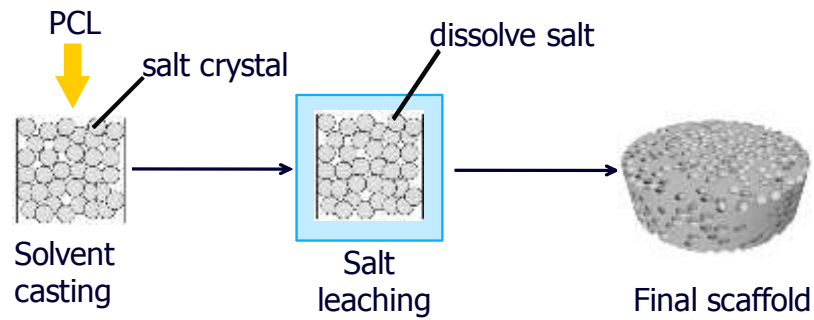
**Figure 2.10 SC/SL fabrication. Example of uneven salt crystals (gray) molded within a cylindrical mold to produce a porous random structure.**



(a)                    (b)
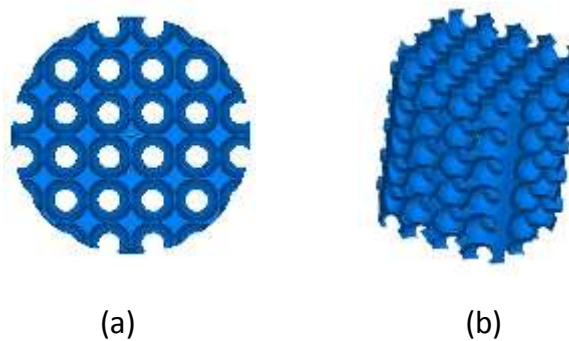
**Figure 2.11 SLS fabrication. (a) Top and (b) isometric view of CAD of SLS scaffold. The spherical pore size is altered to generated scaffolds of exhibiting variable intrinsic permeability.**

### 2.3.3   Fabrication of a Polymer Construct

*2.3.3.1   Vascular Tree Fabrication*

Fig. 2.12a shows the CAD of a second-order prototype network. Fig. 2.12b and Fig. 2.12c show pictures of networks that were fabricated by two rapid prototyping methods, FDM and SLS, respectively. The networks had a wall thickness of 0.6 mm and inner diameters that decreased from 1.4 mm down to 0.9 mm, based on Equation 2.1. Fig. 2.15d-e shows a more complex fourth-order bifurcation structure manufactured using SLS. The network had a wall thickness of 0.6 mm and inner diameter that decreased from 2.2 mm down to 0.9 mm, based on Equation 2.1. These diameters reported for Fig 2.12 are the prescribed diameters set within the C++ algorithm.

41

(a)

(b)

(c)

(d)

(e)
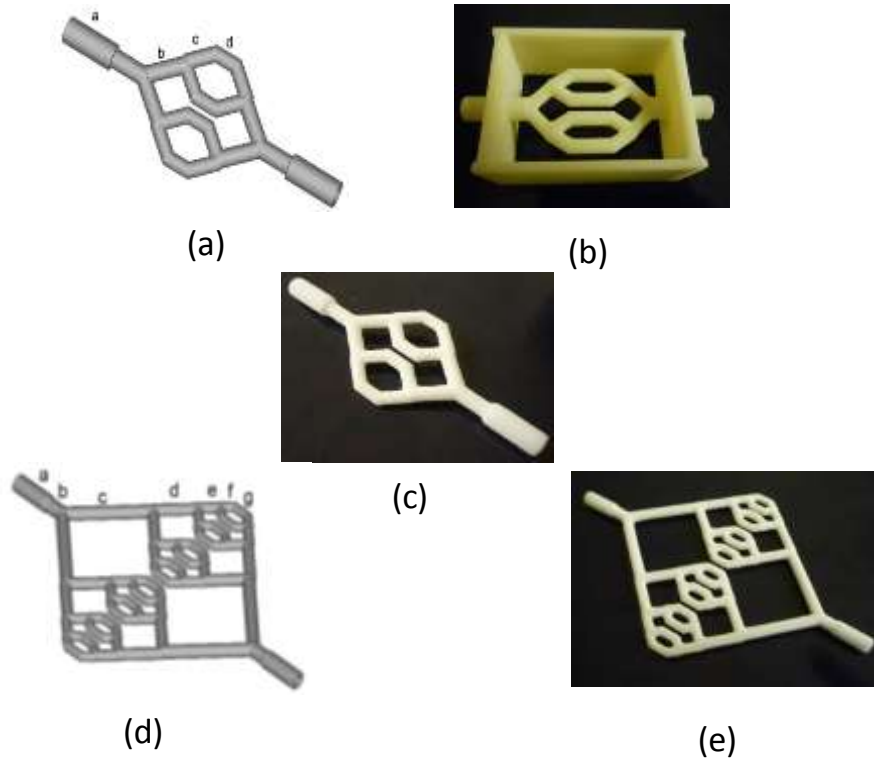
**Figure 2.12 (a) CAD of second-order vascular network. Photograph of second-order vascular network fabricated using (b) FDM and (c) SLS. Inner diameters: a = 1.4. mm, b = 1.2 mm, c = 1.0 mm, d = 0.9 mm (prescribed measurements). Dimensions: 5.5 cm x 2.2 cm x 0.7 cm. The frame seen in in b is external to the vessels and is used for resting the network slightly above table surfaces. (d) CAD of fourth order vascular. (e) Photograph of fabricated fourth order vascular network shown in d. Inner diameters: a = 2.2 mm, b = 2.0 mm, c = 1.58 mm, d = 1.25 mm, e = 1.0 mm, f = 0.79 mm (prescribed measurements). Wall thickness = 0.6 mm Dimensions: 8.5 cm x 4.5 cm x 0.7 cm.**

### 2.3.3.2   Scaffold Compartment

Section 2.3.1 details the design of a vascular tree. FDM and SLS fabrications successfully generated vascular trees with inner diameters between 0.9 - 1.4 mm. Since FDM did not present any apparent advantages in the development of our vascular network, an in-house SLS was used for all future fabrications. The final design was fabricated using SLS to generate a fourth-order vascular tree with an inlet inner diameter of 2.2 mm and an outlet diameter of 0.90 mm (diameter prescribed to algorithm). As discussed in section 2.3.2, the addition of porous scaffold compartments was proposed to control bulk differential

flow across the construct. Therefore, the final vascular network design incorporated a compartment for scaffolds at the midpoint of the mirrored vascular network design (Fig. 2.13). The vascular tree discussed in Section 2.2.1 was modified at the outlet of the network to connect to a cylindrical opening that led to scaffold compartments (Fig. 2.13a-b). The construct consisted of an "arterial" branching network adjoined to modular scaffolds that collect at a "venous" end. A scaffold compartment was centered between the vascular trees. The cylindrical holder shown in Fig. 2.13c was 11 mm in diameter and 10 mm in length (13.7 mm outer diameter). It was designed to contain porous scaffolds and provide a tight, non-leaky fit. Shallow threading and tapering at the ends of the holder allowed for a snap fit into the networks. Through the adoption of rapid prototyping and scaffolding techniques the final assembled distributed flow system was fabricated (Fig. 2.13d) for *in vitro* experimental studies detailed in Chapters 3 and 6.

(a)



(b)



(c)



(d)
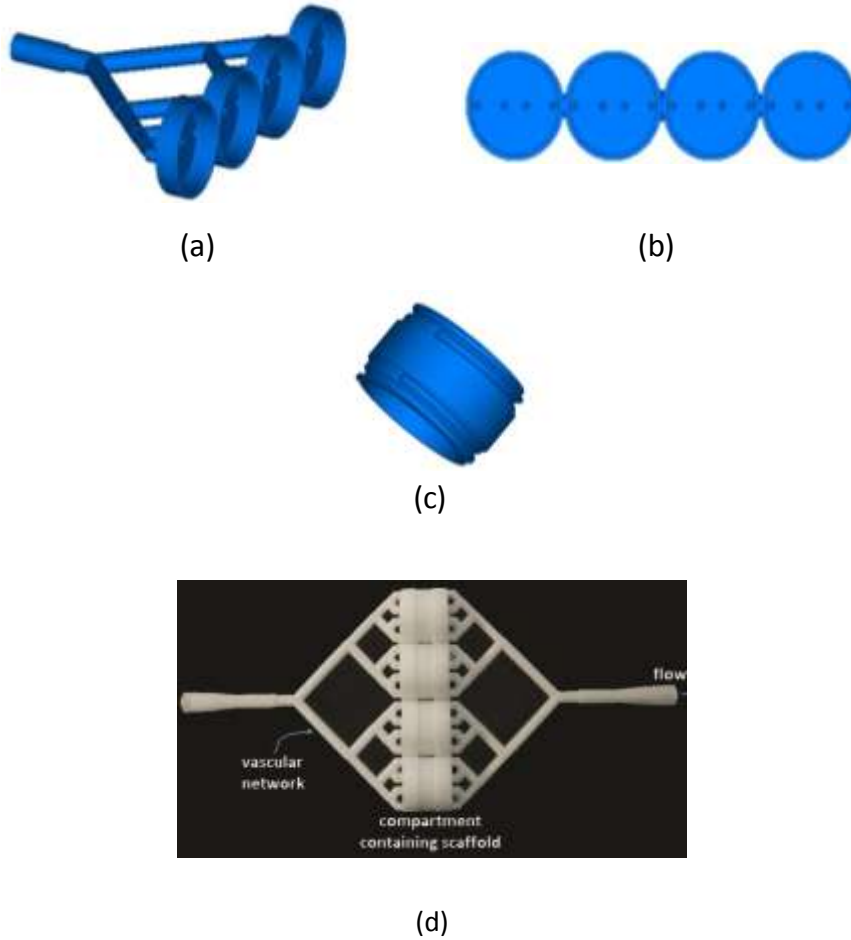
**Figure** 2.13 **(a) Side view and (b) top view of CAD of vascular network with compartments. (c) Isometric view of CAD of scaffold compartment holder, which joined the mirrored ends of vascular network. (d) Top view image of a closed vascular network construct enclosing four porous scaffolds: feeding vascular network, 16 outlets feed four compartments, four porous scaffolds enclosed in compartments by a compartment holder, collecting vascular network.**

## 2.4 REFERENCES

[1] Boron, W.F., and Boulpaep, E.L. Medical Physiology: A Cellular and Molecular Approach. Philadelphia, PA: Saunders/Elsevier, 2009.

[2] Purves, W.K., Orians, G.H., and Heller, H.C. Life, the Science of Biology. Sunderland, Mass. Salt Lake City, Utah: Sinauer Associates ; W.H. Freeman, 1995.

[3] Martini, F.H. Fundamentals of Anatomy & Physiology 6th ed. San Francisco: Pearson Benjamin Cummings, Chapter 21, 2004.

[4] Dewey, C.F., Bussolari, S.R., Gimbrone, M.A., and Davies, P.F. The Dynamic-Response of Vascular Endothelial-Cells to Fluid Shear-Stress. Journal of Biomechanical Engineering-Transactions of the Asme **103**, 177, 1981.

[5] Ando, J., and Yamamoto, K. Effects of shear stress and stretch on endothelial function. Antioxid Redox Signal **15**, 1389, 2011.

[6] Kadohama, T., Nishimura, K., Hoshino, Y., Sasajima, T., and Sumpio, B.E. Effects of different types of fluid shear stress on endothelial cell proliferation and survival. J Cell Physiol **212**, 244, 2007.

[7] Feher, J.J. Quantitative Human Physiology: An Introduction. : Academic Press, 2012.

[8] Rand, P.W., Lacombe, E., Hunt, H.E., Austin, W.H. Viscosity of normal blood under normothermic and hypothermic conditions. J. Appl. Physiol. **19**, 117-122, 1964.

[9] Chien, S., Usami, S., Taylor, H.M., Lundberg, J.L., and Gregersen, M.I. Effects of hematocrit and plasma proteins on human blood rheology at low shear rates. Journal of applied physiology **21**, 81, 1966.

[10] Bugliarello, G., Kapur, C., Hsiao, G. The profile viscosity and other characteristics of blood flow in a non-uniform shear field. Proc IVth Int Cong on Rheol 4, Syrup of Biorheol (Ed. CopleyAL), pp 351-370, Interscience, New York, 1985.

[11] Pedley, T.J. The Fluid Mechanics of Large Blood Vessels. : Cambridge University Press, 2008.

[12] Masako Sugihara-Seki and Bingmei, M.F. Blood flow and permeability in microvessels. Fluid Dynamics Research **37**, 82, 2005.

[13] Rosencranz, R., and Bogen, S.A. Clinical laboratory measurement of serum, plasma, and blood viscosity. Am J Clin Pathol **125 Suppl**, S78, 2006.

[14] Karch, R., Neumann, F., Neumann, M., and Schreiner, W. A three-dimensional model for arterial tree representation, generated by constrained constructive optimization. Comput Biol Med **29**, 19, 1999.

[15] Schreiner, W., and Buxbaum, P.F. Computer-optimization of vascular trees. IEEE Trans Biomed Eng **40**, 482, 1993.

[16] Kretowski, M., Rolland, Y., Bezy-Wendling, J., and Coatrieux, J.L. Fast algorithm for 3-D vascular tree modeling. Comput Methods Programs Biomed **70**, 129, 2003.

[17] Rolland, Y., Bezy-Wendling, J., Duvauferrier, R., and Bruno, A. Modeling of the parenchymous vascularization and perfusion. Invest Radiol **34**, 171, 1999.

[18] Neumann, F., Schreiner, W., and Neumann, M. Computer simulation of coronary arterial trees. Advances in Engineering Software; Computer Simulations in Biomedicine **28**, 353, 1997.

[19] Sherman, T.F. On connecting large vessels to small. The meaning of Murray's law. J Gen Physiol **78**, 431, 1981.

[20] Fung, Y.C. Biomechanics: Circulation. : Springer, 1996.

[21] Yeong, W.Y., Chua, C.K., Leong, K.F., and Chandrasekaran, M. Rapid prototyping in tissue engineering: challenges and potential. Trends Biotechnol **22**, 643, 2004.

[22] Deckard, C.R. Selective Laser Sintering. University of Texas-Austin, Department of Mechanical Engineering, 1988.

[23] Partee, B., Hollister, S.J., and Das, S. Selective Laser Sintering Process Optimization for Layered Manufacturing of CAPA 6501 Polycaprolactone Bone Tissue Engineering Scaffolds. Journal of Manufacturing Science and Engineering **128**, 531, 2006.

[24] Boillat, E., Kolossov, S., Glardon, R., Loher, M., Saladin, D., and Levy, G. Finite element and neural network models for process optimization in selective laser sintering. Proceedings of the Institution of Mechanical Engineers, Part B: Journal of Engineering Manufacture **218**, 607, 2004.

[25] Choi, S.H., and Samavedam, S. Modelling and optimisation of Rapid Prototyping. Computers in Industry **47**, 39, 2002.

[26] CustomPart.Net. CustomPartNet. 2009. August 2012. www.custompartnet.com/wu/selective-laser-sintering

[27] CustomPart.Net. CustomPartNet. 2009. August 2012. ww.custompartnet.com/wu/fused-deposition-modeling

[28] Muskat, M.. The Flow of Fluids Through Porous Media. Journal of Applied Physics. **8**, 4, 274 – 282, 1937.

[29] Song, F., You-sheng, X.U., and Hua-mei, L.I.. Blood flow in capillaries by using porous media model. J. Cent. South. Univ. Technol. s1-0046-04, 2007.

[30] Kannan, R.Y., Salacinski, H.J., Sales, K., Butler, P., Seifalian, A.M. The roles of tissue engineering and vascularization in the development of micro-vascular networks: a review. Biomaterials. **26**, 14, 1857-1875, 2005.

[31] Landman, K.A. and Cai, A.Q. Cell proliferation and oxygen diffusion in a vascularising scaffold. Bulletin of Mathematical Biology **69**, 2405-2428, 2007.

[32] Murphy, W.L., Dennis, R.G., Kileny, J.L., and Mooney, D.J. Salt fusion: an approach to improve pore interconnectivity within tissue engineering scaffolds. Tissue Eng **8**, 43, 2002.

[33] Kotov, N.A., Liu, Y., Wang, S., Cumming, C., Eghtedari, M., Vargas, G., Motamedi, M., Nichols, J., and Cortiella, J. Inverted colloidal crystals as three-dimensional cell scaffolds. Langmuir **20**, 7887, 2004.

[34] Hunt, A.G., and SpringerLink (Online service). Percolation Theory for Flow in Porous Media. Berlin ; New York: Springer, 2005.

[35] Chhabra, R.P., Richardson, J.F., Knovel (Firm), and ScienceDirect (Online service). Non-Newtonian Flow and Applied Rheology Engineering Applications. Amsterdam; Boston: Butterworth-Heinemann/Elsevier, 2008.

[36] Bear, J. Dynamics of Fluids in Porous Media. New York: American Elsevier, 1972.

[37] Tofts, P.S., Brix, G., Buckley, D.L., Evelhoch, J.L., Henderson, E., Knopp, M.V., Larsson, H.B., Lee, T.Y., Mayr, N.A., Parker, G.J., Port, R.E., Taylor, J., and

Weisskoff, R.M. Estimating kinetic parameters from dynamic contrast-enhanced T(1)-weighted MRI of a diffusable tracer: standardized quantities and symbols. J Magn Reson Imaging **10**, 223, 1999.

[38] Maes, F., Claessens, T., Moesen, M., Van Oosterwyck, H., Van Ransbeeck, P., and Verdonck, P. Computational models for wall shear stress estimation in scaffolds: a comparative study of two complete geometries. J Biomech **45**, 1586, 2012.

[39] Kemppainen, J.M. Mechanically stable solid freeform fabricated scaffolds with permeability optimized for cartilage tissue engineering. University of Michigan, Department of Biomedical Engineering, 2008.

# CHAPTER 3

## Development of a Dynamic Flow Phantom for Quantitative Assessment of Flow with Dynamic Contrast Enhanced – Computed Tomography Imaging

**Abstract**

Purpose: To use rapid prototyping (RP) and scaffolding techniques to develop a physical, dynamic flow phantom with controlled vascular-like structural and flow properties, which when imaged by Dynamic Contrast Enhanced-Computed Tomography (DCE-CT) generates time-contrast enhancement curves typical of organs imaged by DCE-CT.

Methods: The dynamic flow phantom consisted of a vascular network adjoined to porous scaffold compartments. This work investigated RP as a method to manufacture high-order computer generate vascular trees that anatomically modeled *in vivo* arterial and venous vasculature. Selective laser sintered (SLS) vascular trees were connected to modular scaffold compartments, which were fabricated using solvent-casted/salt-leached (SL/SC), Inverted Colloidal Crystal (ICC) and SLS approaches. The different methods used variable porous architectures to generate controllable fluid flow characteristics. The realizable range of differential flows possible across the porous compartment was examined. DCE-CT imaging was performed on the phantom to demonstrate the imaging compatibility. From the imaging data, time-contrast enhancement curves were generated and velocities of phantom features were measured to demonstrate the application of the phantom to detailed DCE post-processing.

Results: Computer generated three-dimensional bifurcating cylindrical branches with an inner diameter ranging from 2.2 mm down to 770 microns were reproducibly fabricated with a polymer material to generate an arterial-like bifurcating vascular tree. Significantly different differential flows, from -22% to -90% were achievable using the SLS and

SC/SL manufacturing processes. DCE imaging and analysis of a phantom with SLS scaffolds embedded generated curves characteristic of *in vivo* DCE-CT imaging. Further post-processing calculated flow rates within the vascular tree and differential flows across the scaffold compartment which were similar to the theoretical and experimentally measurements, respectively.

Conclusions: The fabricated vascular trees and porous compartments were patent at sub-voxel sizes and exhibited various flow rates, showing that RP can successfully generate a DCE-compatible phantom with tunable differential flows for DCE imaging and analysis. The results of this chapter will provide a method for developing and using a dynamic phantom that can be further studied to evaluate the sensitivity of the device and to validate DCE-CT measurements in the future.

## 3.1  INTRODUCTION

Various estimates of perfusion are currently under investigation as potential biomarkers to aid in the prognosis, assessment, and individualization of cancer therapy. Perfusion measurements acquired from dynamic contrast-enhanced (DCE) imaging provide a quantitative metric for assessing tumor aggressiveness, tumor response to therapy, and more recently normal tissue damage following treatment such as focal irradiation [1-3]. While quantitative imaging is potentially a very powerful tool to stage and monitor treatment, the actual quantification of perfusion from image analysis is a subject of concern, as there is significant variability in DCE acquisition, processing and quantitative metric extraction [1-2,4-8]. The validation of DCE-derived parameters is limited. Existing methods of providing validation for DCE imaging and analyses are limited to simulated data, which does not account for variances in image acquisition. Similarly, implemented static phantoms neglect the dynamic effects inherent during patient scans and dynamic tools incorporate features that are well above the anatomical resolution of tissue parenchyma.

Organ-based perfusion phantoms employing fresh organs have a short lifetime, while preserved organs may be sensitive to handling and fixation [15-16]. Several previously implemented re-useable three-dimensional flow phantoms have oversimplified the vascular tree geometry by using non-leaky cylindrical tubes [17] or parallel fibers from

50

commercial dialysis cartridges [18]. Recently, Chiribiri et al. [19] and Driscoll et al. [20] and presented re-usable phantom models that aim to produce a gold standard for measuring flow using computed tomography (CT) and magnetic resonance imaging (MRI), respectively (see Fig. 3.1-3.2). Driscoll et al. [20] developed a rapid prototyped phantom comprised of coiled plastic tubing (6.35 mm diameter) wound about a shell (Fig. 3.1) to reproduce target arterial input functions using DCE-CT. The phantom produced time-attenuation curves (TACs) with tunable peaks and shapes based on the preset arterial input function (AIF), which consisted of blood mimicking fluid (2:3 glycerol-water, 2.5 - 5 ml/s) and iodinated contrast agent (0.27 - 1.5 ml/s). Their system was successful in closely matching the shape (in terms of duration and residual enhancement) and peak (in terms of enhancement) of a typical AIF. The phantom and system limitations, which may have introduced error in the final TACS included:

- Heterogeneous mixing of contrast agent and blood mimicking fluid
- Unrealistic physiologically realistic capillary exchange
- Enclosing phantom shells that do not represent physiological situations



(a)                                                                    (b)
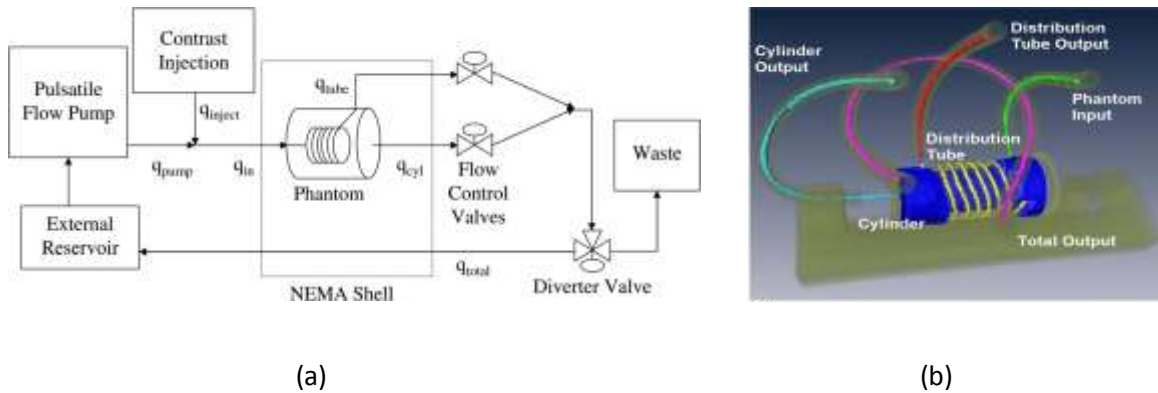
**Figure 3.1 DCE CT flow phantom. $q_{inject}$, contrast agent input flow; qpump, blood mimicking fluid input flow; $q_{in}$, total input flow ; $q_{tube}$, output flow ; $q_{cyl}$ , second output flow ; $q_{total}$, total output flow [20].**

Chiribiri et al. [19] created a physical four chamber heart phantom composed of two 4-cm cylinders containing 124 3-mm pipes (Fig. 3.2)  to simulate dynamic first pass myocardial perfusion (1-10 ml/ml/min) using MRI. The system was perfused with tap water and a gadolinium contrast agent. However, the goal of their reported completed system was not to validate measurements, but instead to provide proof of concept in

51

creating tunable AIFs and to extract those curves using signal deconvolution. The phantom and system limitations, which may have introduced error in the final AIFs included:

- Unrealistic physiologically realistic capillary exchange, unlike animal and human models
- Poor bolus dispersion
- Single compartment of distribution
- Lack of diffusion of contrast agent into interstitial space

Although these two phantoms present more reliable, reusable set-ups for validation studies, both designs based estimations on unrealistic representations of physiological capillary exchange that were above the resolution of the typical CT scanner.



(a)

(b)

(c)
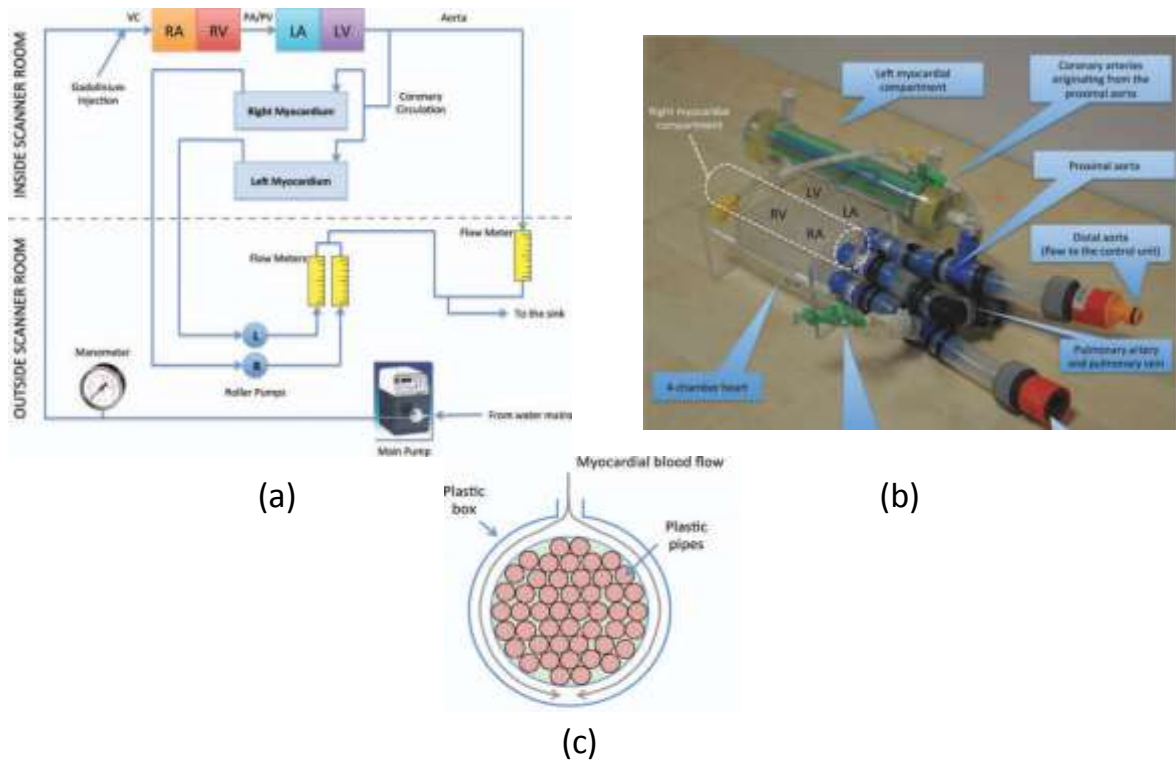
**Figure 3.2 Myocardial MR perfusion phantom. RA, right atrium; RV, right ventricle; LA, left atrium; LV, left ventricle. Simulated heart rate of 60 beats per minute and cardiac output of 4 L/min. [19].**

As such, a flow phantom was designed to increase model complexity over existing flow phantoms through the adoption of porous compartments that offered tunable flow resistance to mimic bulk flow rates (across capillary beds) similar to that discernible in

organs scanned by volumetric imaging systems. The flow phantom consisted of porous scaffold compartments centered between an "arterial" and "venous" vascular tree network (Fig. 3.3). The selective laser sintering (SLS) RP process was used to determine the reliability of manufacturing highly branched vascular trees and porous compartments mimicking differential flow ranges was determined. The advantages of the proposed design are its anatomical "arterial" vascular tree design and the influence of structure on fluid flow across the vascular tree and the porous scaffold compartments.

The design and assembly of the branching network is described in this study. Two scaffold fabrication methods were investigated to produce porous compartments with distinct differential flow ranges, for placement within a dynamic DCE vascular phantom that covers a range of differential flows. An experimental approach to characterize the hydraulic permeability and differential flow across the porous compartments was used. Tests of the prototyped phantom included an evaluation of lumenal occlusion to determine the feature (cylindrical lumens) resolution limit, an assessment of the accuracy of SLS fabrication and precision of inner diameter measurements to evaluate reproducibility.

Experimental analysis of flow through the phantom system, in terms of "arterial" input flow and differential flow across the compartments is performed in this chapter. DCE imaging is performed to demonstrate the practical application of the phantom system in the acquisition of signals, and to confirm compatibility of the phantom to CT. Furthermore, a DCE analysis is performed as an example of the level of detailed analysis that can be performed on the phantom in order to compare imaging-extracted velocity or volumetric flow metrics to experimental and computational (detailed in chapter 4) measurements.

## 3.2 METHODS AND MATERIALS

### 3.2.1 Design of vascular phantom

The phantom (Fig. 3.3) consisted of an "arterial" branching network adjoined to modular scaffold compartments that collect at a "venous" branching network. The design was fabricated with a Luer-lock fitting (International Standards, ISO 594) at the inlet and outlet of the vascular tree. The inlet connected to an inlet inner diameter of 2.2 mm,

which bifurcated over four levels to an outlet diameter of 0.79 mm. The design incorporates multiple porous scaffolds at the midpoint of the mirrored vascular network design (Fig. 3.3a). Each compartment houses an 11 mm x 5.5 mm (height x radius) porous cylindrical scaffold. The compartment encloses 2 mm of space before and after the outlets and inlets of the vascular network, respectively. The two mirrored vascular trees were adjoined by multiple compartment holders, each of which tightly bounds a scaffold, such that fluid passed through the porous scaffolds (Fig. 3.3b). Four scaffolds were enclosed within the system, each housed in a different holder. Shallow threading and tapering at both ends (0.5 mm length) of the holder allowed for a snap fit into the networks. Four outlet vessels from the vascular network serve as fluid entry ports into the hollow compartments, which house the scaffolds (Fig. 3.3c).



(a)



(b)



(c)
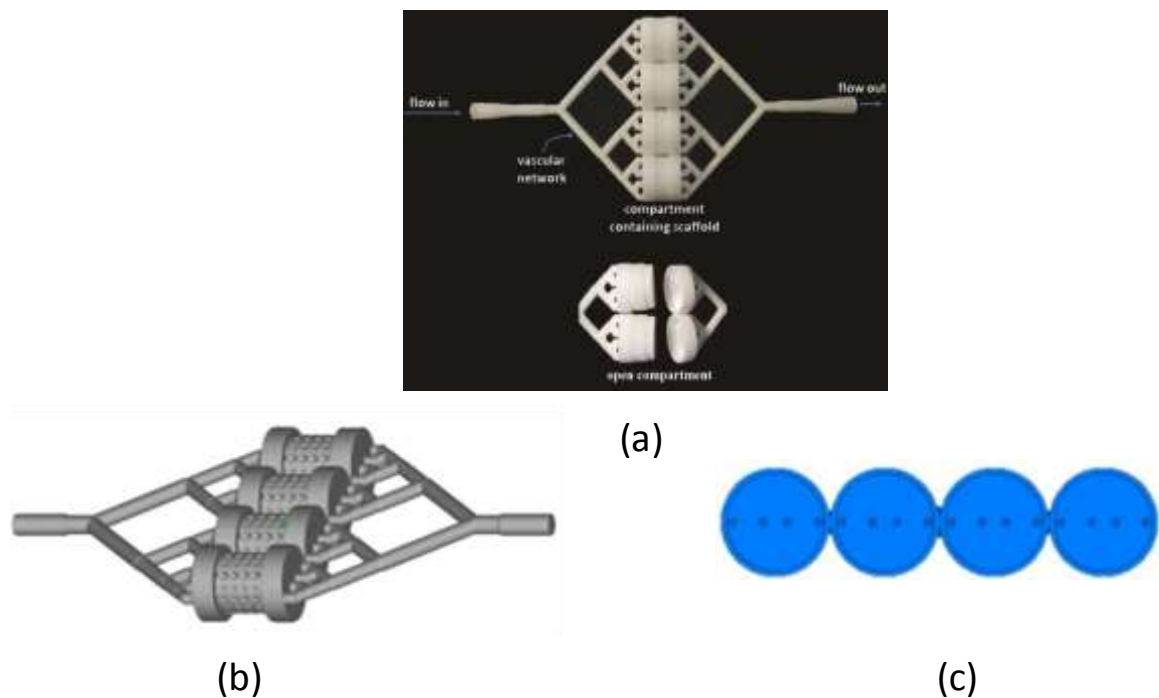
**Figure 3.3 (a) Image of top view of (Top) vascular phantom: "arterial" vascular network has 16 outlets that are connected to four compartments, which are adjoined to a "venous" tree via a compartment holder that housed four porous scaffolds; (Bottom) Image of top of opened compartments that show the modularity of the phantom design (sectioned at first third bifurcation). (b) CAD of fluid domain enclosed within vascular network construct. (c) Front view of the CAD of the vascular network illustrates the four outlets (0.79 mm** inner diameter) which lead to the compartments.

### 3.2.2 Computerized vascular tree design and manufacturing

*In vivo* observations and formulated principles on vascular branching served as the basis for the implemented three-dimensional vascular network algorithm [21-23]. The algorithm generated three-dimensional binary image files which represented the geometry of the vascular networks. Manipulation of these binary files produced triangulated surface meshes that were saved to a stereolithography (STL) file format (3D Systems, Rock Hill, South Carolina, USA), then imported to the SLS system for fabrication. The computer aided design (CAD) of vascular trees scalable to large volumes that corresponded to internal organs offered control over geometric properties (i.e. inner diameter, length, number of branches, bifurcation order) that dictated regional blood flow properties. The implemented vascular tree algorithm generated a binary image file to store the spatial geometry of the generated networks. Generated vascular trees enforce bifurcations and the following structural conditions: (i) branches were modeled as hollow cylinders, with specified wall thickness and inner diameter, (ii) branches were bounded within a pre-defined volume and (iii) branches did not intersect. The cylindrical geometry of each vessel was outlined about its center axis. The starting point for each offspring's center axis initiated from the last point along the center axis of its parent vessel. The geometry was initially represented as a three-dimensional binary image, whereby '1' represents wall and '0' lumenal space. Branches bifurcated at angles between 30-50 degrees and the prescribed inner radius (*r*) dimension of each offspring vessel after a bifurcation decreased based on Murray's branching law (Equation 3.1) [24].

$$r^3_{parent} = r^3_{left, offspring} + r^3_{right, offspring} \quad \text{,}$$

Equation 3.1

In the overlapped areas of the saddle region of the bifurcation, where vessel walls of one offspring protruded into the lumenal space of the second offspring, the algorithm converted the protruded wall into lumenal space ('1'→'0') to create a sharp bifurcation region (Fig. 3.4a).

For this preliminary study, a pre-defined architecture was implemented, whereby vascular networks bifurcated symmetrically along a single axis with each vessel assigned an inner diameter and length (with left and right offspring congruent and perpendicular).
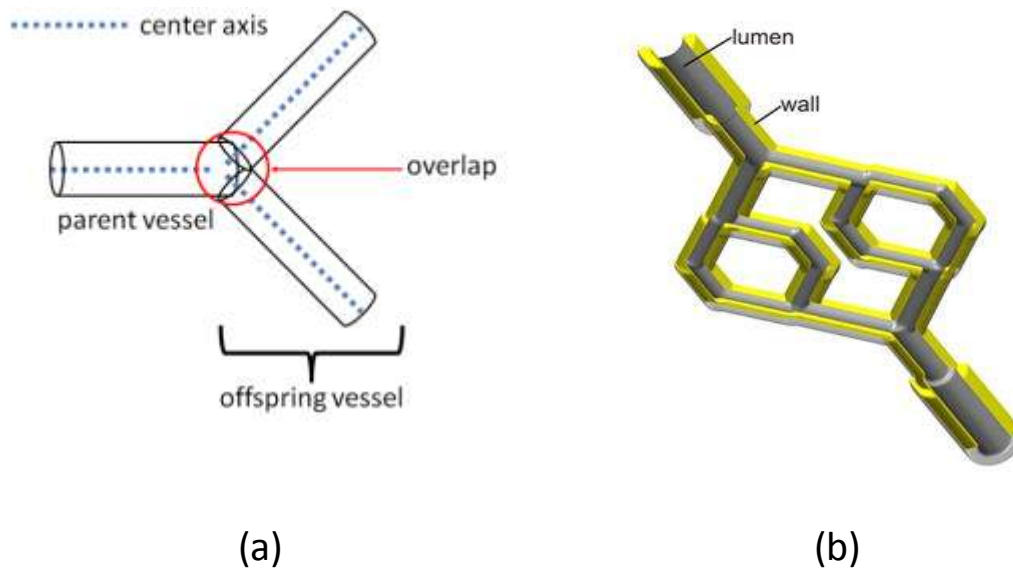
**Figure 3.4 (a) Schematic of vessels' geometry at bifurcation points and (b) coronal view of network with smoothed bifurcation regions. The solid wall is shown in yellow and the lumenal space is highlighted gray.**

The surface renderings of the computer-generated networks served as input to the SLS RP method. An STL generator was developed in a data visualization environment (IDL, ITT Visual Information Solutions, White Plains, New York, USA) to convert the binary image file into a surface mesh (referred to as STL or CAD) that was then manipulated with a commercial software tool (Magics X, Materialise, Belgium) to fix inconsistencies (i.e. inverted normals, intersecting triangles, bad edges, etc.) in the generated mesh. The fixed files were then loaded on to an SLS system (EOS FORMIGA P100, EOS GmbH, Munich, Germany). The vascular network and scaffolds were fabricated using a powdered thermoplastic mixture of polycaprolactone (PCL) and hydroxyapatite (HA). The SLS system deposited plastic particles across a layer on the bed of the system, then selectively fused the particles using a high power laser to produce a three-dimensional object. The system used a 0.08 mm layer thickness during the build process. The SLS fabrication was conducted by preheating the powder to 49.5°C, then scanning the laser (450 mm focused beam diameter) at 4.5W power and 1.257 m/s scan speed. Based on previous in-house testing, a resolution of about 600 microns was achieved on the SLS

system, for the given system parameters: the humidity level, beam accuracy, laser age, properties of the PCL powder and reliability of the mechanical parts for our system.

### 3.2.3 Solvent-Casted/Salt-Leached (SC/SL) PCL scaffolds

Solvent-Casted / Salt-Leached (SC/SL) PCL scaffolds were fabricated based on modifications to a protocol developed by Kemppainen et al. [25]. For the SC/SL technique, sea salt (sodium chloride, Essentials by Catalina, CA, USA) was used as the porogen. Salt crystals were separated by brass sieves (USA standard test *sieve*: *Fisher Scientific* Inc., CA, USA) with a nominal sieve opening of 106, 180, 300, 600, and 700 micron. The salt crystals were sieved to six ranges: <106, 106-180, 180-300, 300-600 and 700-1000 μm, then hydrated with 4% (w/v) deionized water before being casted into Teflon (McMaster-Carr, CA, USA) molds. Salt crystals of various diameters were used to create spongy scaffolds of different levels of porosity to vary the interconnectivity of formed channels, without compromising penetrability caused by ill-formed pore walls. The crystals were packed into cylindrical molds with roughly 11 mm diameter and 13 mm height. 15% (w/v) PCL/chloroform (Polysciences, Inc., PA, USA) (Fisher Scientific Inc., CA, USA) was infused into the salt crystal lattice within the mold. The crystal lattice were saturated with PCL/chloroform, and then placed under vacuum for 4 hours. Thereafter, the scaffolds were dried for 24 hours, for maximum chloroform evaporation. The scaffolds underwent repeated saturation within 70% ethanol alcohol and water to remove the salt porogens and entrapped air. The top and bottom ends of the scaffold were cut to achieve an 11mm scaffold height. Fig 3.5a. illustrates two fabricated SL/SC scaffolds.

### 3.2.4 SLS PCL scaffolds

To prepare SLS-fabricated PCL scaffolds, porous cylindrical scaffolds with three-dimensional orthogonal periodic porous architectures were designed using custom written programs in a data visualization environment (IDL, ITT Visual Information Solutions, White Plains, New York, USA), and then exported as STL files. The scaffold geometry consisted of a cubical unit cell enclosed in a sphere with a 2.15 mm or 2.2 mm diameter (resolution ± 0.5 mm) (Fig. 3.5b). The unit cell was repeated every 2 mm to fill a

cylindrical construct with an 11 mm height and diameter. The generated STL files for the respective scaffolds were loaded onto the SLS system for fabrication as detailed in section II.A.1. Upon completion of SLS fabrication, the parts were flushed with compressed air to remove unsintered PCL powder from the scaffold's interstices. Fig. 3.5b illustrates fabricated SLS scaffolds.



(a)                                    (b)
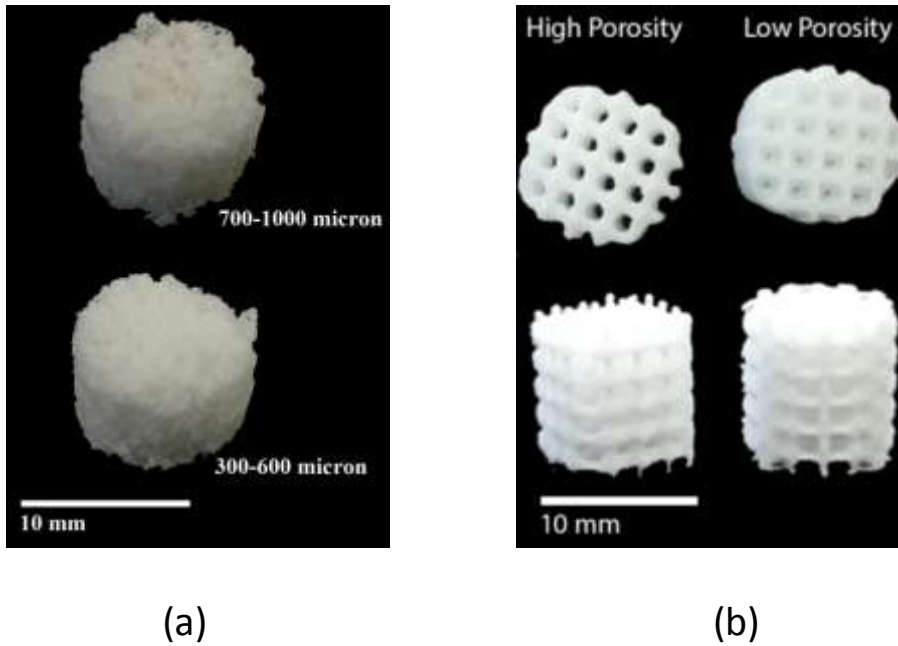
**Figure 3.5 Picture of cylindrical (a) 300-600 and 700-1000 micron SC/SL scaffolds and (b) high (2.2 mm pore size) and low (2.15 mm pore size) permeability SLS scaffolds.**

### 3.2.5 Inverted Colloidal Crystal (ICC) PCL scaffolds

The following method to create ICC PCL scaffolds was a modification of a protocol developed by the Kotov et al., wherein microspheres are allowed to self-assemble into a tightly hexagonally packed crystal lattice (see Fig. 2.11a. Soda lime glass beads (Polysciences, Inc., PA, USA) of 30-50 μm and 105-150 μm diameter were used as the porogen in the ICC technique[26-27]. Pipettes were secured at the perforated centers of the vials' caps. 9g of microspheres (per scaffold) were added to ethylene glycol (Fischer Scientific Inc., CA, USA), then added to a disposable pipette. Each ICC scaffold was cast in a borosilicate shell vial (Fisher Scientific Inc., CA, USA) with a 19 mm diameter. The vial sat within an ethanol alcohol-filled ultrasonic bath. Each vial was filled halfway with

ethylene glycol. Every 20 minutes, five drops of microsphere solution was released from the pipette into the shell vial. The microspheres settled at the bottom of the vial. Drops were continually added until the desired scaffold volume was reached (see Fig. 2.11b). Thereafter, the microspheres were left under sonication for an addition hour. The vials were removed from the sonicator and the contents dried for 24 hours at 80˚C to evaporate the ethylene glycol. The vials were heated to 655˚C to anneal the glass microspheres. The solidified ICC was removed from the vial and placed into Teflon mold (19.5 mm diameter and 13.2 mm height). 15% (w/v) molten PCL/chloroform was infused into the ICC by centrifugation for 60 minutes at 5800 rpm. The PCL saturated scaffolds were then placed under vacuum for 24 hours at room temperature. To dissolve the glass porogens, the scaffolds were dissolved in a 5% hydrofluoric acid (Fisher Scientific Inc., CA, USA), 1.0N hydrochloric acid (Fisher Scientific Inc., CA, USA) and then a phosphate buffered saline (Fisher Scientific Inc., CA, USA) solution. None of the solvents sued underwent further purification.

## 3.3  CHARACTERIZATION OF PHANTOM COMPONENTS

### 3.3.1  Resolution, accuracy and precision of vascular network fabrication

Fabrication of several test blocks (Fig. 3.6a-3.6b) which contained individual cylindrical vessels allowed for the evaluation of the fidelity of inner diameter dimensions and the determination of the SLS resolution limit. The CAD of the first test block contained six vessels with decreasing inner diameter (4.0 mm, 2.0 mm, 1.5 mm, 1.2 mm, 1.0 mm, 0.9 mm) repeated over three rows with a constant wall thickness of 0.6 mm. A second block contained vessels with a 0.6 mm wall thickness and smaller inner diameters (0.90 mm, 0.85 mm, 0.80 mm, 0.70 mm, 0.65 mm, 0.60 mm). To determine the resolution limit of the fabricated prototypes, compressed air and water were flushed through the lumens of the vessels contained in each test block. For vessels that showed patency, manual caliper measurements (accuracy: ± 0.005 mm) were acquired for the inner diameter of fabricated vessels and were compared to CAD inner diameter measurements acquired by a diameter measurement tool (accuracy: ± 0.0005 mm) in commercial visualization software (Solidview, Solid Concepts, Inc., California, USA). Statistical analyses for four independent fabrications of the first block are reported as means ± standard deviation

(stdev) and percent deviation. A two-tail Student's t-test assuming unequal variance was used to compare the measured dimensions to the inner diameter design specifications prescribed in the vascular algorithm, to the CAD and fabricated vessels. Significance was set at P -values< 0.05.



(a)                                 (b)
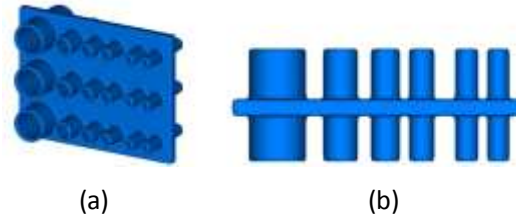
Figure 3.6 CAD of test block. (a) top-front-right view and (b) side view. The frame holds the vesssels together as a block and does not protrude into the vessels.
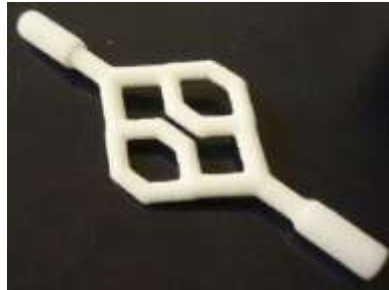


**Figure 3.7 Photograph of SLS-fabricated mirrored vascular network (two-level bifurcation). Inner diameters: inlet = 1.4. mm, first level birfucation = 1.2 mm, second level bifurcation = 1.0 mm, midpoint of vascular network = 0.9 mm (prescribed measurements). Dimensions: 5.5 cm x 2.2 cm x 0.7 cm.**

### 3.3.2  Scaffold characterization: porosity measurement

The reproducibility of the scaffolds fabricated using the respective scaffold techniques were evaluated in terms of the consistency of properties (integrity and porosity) in fabricated architectures. Porosity was defined as the volume of void space over the total scaffold volume within a given PCL scaffold. The density-based approach (Archimedes' principle) represented in Equation 3.2 was used to estimate the porosities of the SC/SL scaffolds:

$$\text{porosity}(\%) = \frac{(m_2 - m_1)d_1}{(m_2 - m_1)d_1 + m_1 d_2} * 100, \qquad\qquad \text{Equation 3.2}$$

whereby $m_1$ = saturated weight of scaffold, $m_2$ = dry weight of scaffold, $d_1$ = density of PCL and $d_2$ = density of absolute ethanol. The scaffold was dried for 24 hours then measured to determine $m_2$. The dried scaffolds were then submerged in absolute ethanol for 24 hours then weighed to determine $m_1$. The salt crystal porogens were assumed to be completely dissolved out of the scaffold. For SLS PCL scaffolds, the porosity was estimated from volume measurements calculated in commercial visualization software (Magics, Materialise, Belgium). The porosity was defined as the volume of scaffold divided by the volume of an 11 mm x 11 mm solid cylinder.

### 3.3.3 Scaffold characterization: experimental measurement of hydraulic permeability and differential flow

For a sample size of six, the height and diameter of each fabricated scaffold was recorded. Before testing, the scaffolds were preconditioned to an aqueous environment for twelve hours. The volumetric flow rate through each scaffold was measured using an in-house flow meter, given a constant hydraulic head [25]. The volumetric input to the system was controlled by a pump that dispensed a simulated blood fluid (SBF) at flow ranges between 18-25 ml/s. The SBF (65% glycerine, 35% water, 0.0075% Xanthan gum) exhibited blood-like shear thinning behavior. The scaffolds were placed inside the flow chamber sealed off at the perimeter by a rubber tube to force fluid through scaffold, and not around it (Fig. 3.8). The mass of SBF that penetrated the scaffold over a given length of time was measured by a scale, which sent the data to a commercial data acquisition tool (LabView, National Instruments, TX, USA). The mass flow was collected over a time period long enough to acquire stable flow. The hydraulic permeability ($\widehat{K}$, m$^4$/N·s) was calculated for each scaffold using equation 3.3, a derivation of the Bernouilli equation and Darcy's law [28]:

$$\widehat{K} = \frac{\Delta x}{A M_s} \cdot \frac{2\pi^2 r^4}{\left(M_0 / M_s\right) - 1}, \qquad\qquad \text{Equation 3.3}$$

where $\Delta x$ = height of scaffold (m), $r$ = radius of the chamber's outlet (m), A=cross-sectional area of medium ($m^2$), $M_s$ = mass flow rate through chamber with the scaffold (kg/s) and $M_0$ = mass flow rate through chamber without the scaffold (kg/s). $M_s$ and $M_0$ capture the bulk (mass) flow rate changes across the compartment with and without a scaffold present.
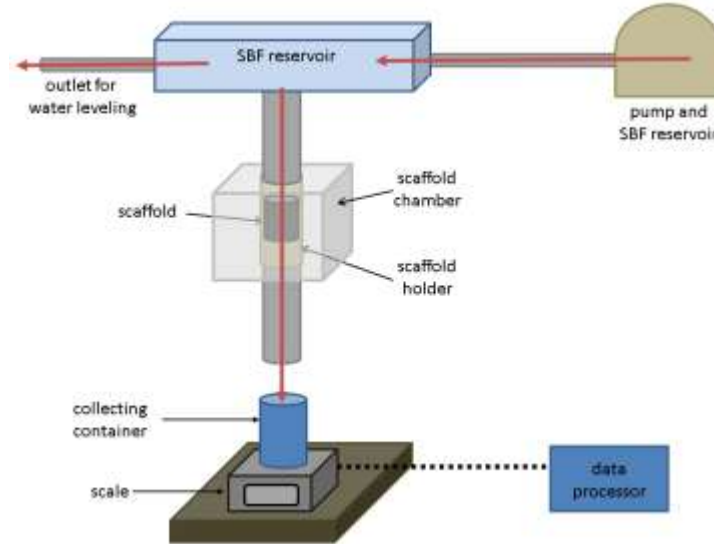


**Figure 3.8 Schematic of experimental set-up used to estimate hydraulic permeability and differential flow. Scaffold was enclosed in a rubber tube fitted to an acrylic chamber.**

The differential flow (%) was calculated as the percent change in bulk flow rate across the compartment with and without the embedded porous scaffold, using equation 3.4.

$$\text{differential flow } (\%) = \frac{M_s - M_0}{M_0} * 100 \qquad \text{Equation 3.4}$$

The statistical significances of differences in hydraulic permeability and differential flow were determined by two-tail Student's t-tests assuming for unequal variance. Significance was set at P -values< 0.05. Based on the results of these metrics, the designs with the two most disparate differential flows were utilized in DCE imaging studies.

## 3.4  DYNAMIC CONTRAST-ENHANCED CT IMAGING

### 3.4.1  Vascular flow phantom system and assembly

Prior to assembly, each scaffold and vascular network was soaked in acetic acid ($\geq$99.7 w/w %, Certified ACS, Fisher Scientific) to reduce contrast agent uptake (see Appendix 2.A). The assembled fourth-order PCL constructs was filled with SBF to reduce the number of air bubbles present in the system. The constructs were left in SBF for one hour. The filled PCL constructs were pulled under a vacuum prior to assembly in the system. The prepared PCL vascular construct was placed into the phantom system (Fig. 3.9). The PCL construct was embedded in a tissue-mimicking equivalent prepared from a 0.85% iodinated contrast agent (Isovue 300, Iopamidol Injection 61%, Bracco Diagnostics, Princeton, NJ, USA) aqueous solution, which was contained in an acrylic bounding box. The bounding box (12 in. x 6 in. x 6 in.) consisted of inlets and outlets attached to Luer Lock connections of tubing to the vascular network and external tubing. The inlet and outlet of the vascular network incorporated Luer Locks for easy connection to the dynamic system. Three-sixteenth-inch clear plastic tubing was used for all connections, except for the injector, which used One-eighth-inch clear plastic tubing. The inlet of the phantom was supplied SBF and contrast agent through a T-shaped stopcock. An inline mixer was positioned downstream of the stopcock. The tubing then connected to the inlet of the bounding box, which was adjoined to the vascular phantom. Fluid that passed through the phantom exited the through the outlet portal of on the bounding box, which released fluid in a reservoir (waste). Once set-up on the CT bed, all tubing that preceded the inlet of the vascular network was filled with SBF, in order to flush air out of the system. SBF from a reservoir circulated through the phantom using a peristaltic pump (MasterFlex® L/S® Easy-Load® II, Cole Palmer, Vernon Hills, IL, USA) (a pulse dampener was used to smooth flow pulsations and maintain a constant flow).
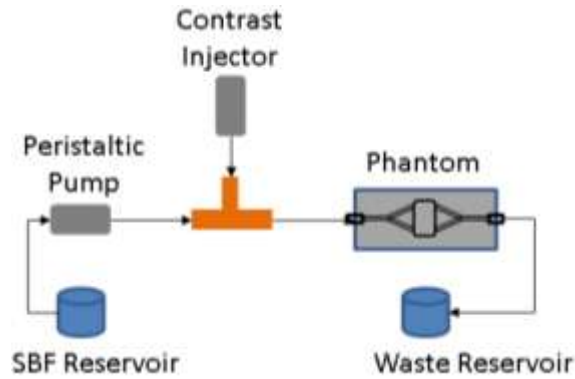
**Figure 3.9 Schematic representation of the single input single-compartment flow phantom within the closed flow system.**

## 3.4.2 DCE-CT image acquisition

Initial flow phantom experiments were performed for two vascular phantoms with SLS scaffolds loaded into their compartments. Fig. 3.10 shows the experimental set up of the vascular phantom, pump and reservoirs on the CT bed. Using a radiotherapy CT scanner (Brilliance, Philips, Cleveland, Ohio, USA), cine CT data for the phantom were collected every second for 50 seconds at a resolution of approximately 1 mm x 1 mm x 1 mm. The DCE-CT scans were taken at 120kV and 200 mA with a gantry rotation time of 0.5 s using 3 mm slice thickness and a cycle time of 1 per second. Starting at t = 0 s, a bolus of iodinated contrast agent (Isovue 300, Iopamidol Injection 61%, Bracco Diagnostics, Princeton, NJ, USA) circulated through the fourth-order prototype phantom housing the lower (hydraulic) permeability SLS scaffolds. Then, SBF was flushed through the system. SBF was allowed to circulate through the system for about one minute before DCE-image data collection began. The SBF continuously circulated at a rate of 0.833 cc/s, while 4 cc of contrast agent entered the system at rate of 2 cc/s for the first bolus. The bolus was flushed with 15 cc of SBF at a rate of 1 cc/s. The experiment was repeated for with the fourth-order prototype phantom housing the higher permeability SLS scaffolds.

CT axial image slices were generated. The Hounsfield unit of the PCL and contrast enhanced-liquid enclosed in the phantom box was evaluated using the CT image data. Time-contrast enhancement curves were generated from the experiment (over 20 seconds of sampling time) using an in-house functional image analysis software package [29].
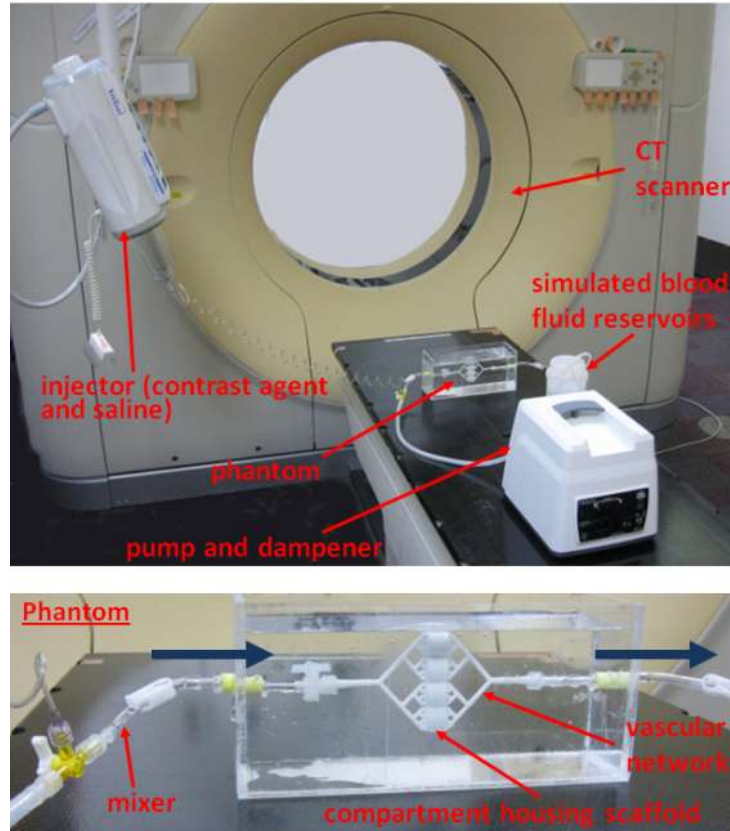
**Figure 3.10 (Top) Picture of vascular flow phantom positioned on CT bed connected to a closed system, which pumps SBF and contrast agent. (Bottom) View of vascular phantom surrounded by an acrylic box filled with an aqueous tissue equivalent solution (in terms of intensity). (Blue arrow indicates the direction of fluid flow).**

### 3.4.3 DCE-CT image analysis

Six tubes filled with iodinated contrast agent (Isovue 300, Iopamidol Injection 61%, Bracco Diagnostics, Princeton, NJ, USA) at the concentrations of 0, 5, 10, 30, 50 and 70 mgI/ml were CT scanned (Brilliance, Philips, Cleveland, Ohio, USA) at 227 mA, 120 kVp and 3 mm slice thickness. The enhancement was averaged over a uniform three-dimensional region of interest manually segmented within each tube. A contrast calibration curve was generated from the collected static image data. Based on this linear relationship, time-contrast enhancement curves extracted from the DCE experiments were scaled to generate time-contrast concentration curves. A single channel pharmacokinetic model [31] represented in Fig. 3.11a was implemented to extract the

velocity from the DCE data. An exponential decay function can be used to describe the flow of contrast agent through the lumen (Eq. 3.5-3.6):

$$C_{vessel}(x) = C_{input}e^{-(xL/v(x))}$$ 
<div align="right">Equation 3.5</div>

$$v(x) = \frac{-xL}{ln(C_{vessel}(x)/C_{input})},$$ 
<div align="right">Equation 3.6</div>

where C(x) = concentration of contrast agent (mgI/ml), x = position of contrast agent in vessel relative to the inlet VOI selected in the first level of bifurcation (m); $0 < x < 1$ , and L = length of tube (m). The volumetric flow rate across each level of bifurcation remains constant (Eq. 2.3). The cross-sectional area increases as the diameter decreases, across the levels of bifurcation. The *in vitro* phantom does not capture vascular constriction or dilation that inherently incurs in small arteries and arterials, *in vivo*. The constant volumetric flow rate coupled with the increasing cross-sectional area results in proportionate changes in velocity, across the levels of bifurcation. The velocity decreases along the increasing level of bifurcation: velocity is a function of x, v(x). At each level of bifurcation, the offspring vessel was considered to be a single large channel (Fig. 3.11a) as shown in Fig. 3.11b. The output concentration, $C_{vessel}$ of a parent vessel serves as the input concentration, $C_{input}$, for the next level of bifurcation.
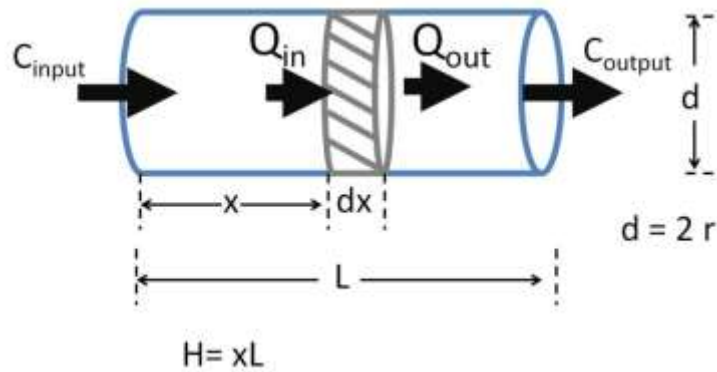
**(a)**
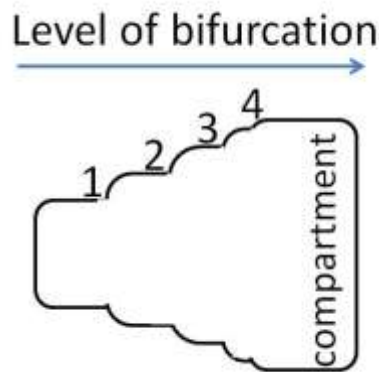
**(b)**

**Figure 3.11 (a) A single channel pharmacokinetic model, wherein a differential element of the model balances the flow going in and out of the element. Exponential decay occurs across the vessel represented by the cylindrical channel. (b) Vascular network modeled by single channel, where the cross-section area increases as x increases. $C_{input}$ = input contrast agent concentration; $C_{output}$ = output contrast agent concentration; r = radius of channel; d = diameter of channel; x = fraction of channel length; L = length of channel / selected volume of interest; $Q_{in}$ = volumetric flow of fluid into the differential element; $Q_{out.}$ = volumetric flow of fluid out of the differential element.**

The Peclet number (Pe) indicates whether convection (Pe >>1) or diffusion (Pe << 1) is the dominant mode of mass transport within a vessel. The unitless number is calculated using Eq. 3.7

$$Pe = \frac{Ql}{\pi r^2 D},$$
<div align="right">Equation 3.7</div>

where Q is the volumetric flow rate, $l$ is the length of the vessel and $D$ is the diffusion coefficient. A diffusion study is required to determine the diffusion coefficient of the iodinated contrast agent within the simulated blood fluid as it travels through the vessel lumen. Given the high speed of the fluid within the lumen of the prototyped phantom, convective flow is assumed, whereby mixing is caused by variations in the convective velocities field. Convection is dominant at the center of the vessel (well mixed), whereas at the vessel walls it approaches zero to produce a parabolic velocity profile (largely unmixed). Therefore Eq. 3.8 can be used to described the relationship between velocity and volumetric flow rate,

$$v_{avg} = \frac{Q_{vessel}}{A},$$
<div align="right">Equation 3.8</div>

where $v_{avg}$ = average fluid velocity and A = cross-sectional area (m$^2$).

Considering Eq. 3.6 and Eq. 3.8,

$$Q = v(x) * A = \frac{-H*A}{ln(^{C_{vessel}(x)}/_{C_{input}})},$$
<div align="right">Equation 3.9</div>

where $H = xL$ = the length of the outlined volume of interest.

For bifurcation level 3 (see Fig. 3.24),

$$Q = \frac{-xL8\pi\,(r_3)^2}{ln(^{C_{vessel}(x)}/_{C_{input}})} = v_4 8\pi (r_3)^2$$

$$v_4 = \frac{H}{8\left(\ln(C_{input})) - ln(C_{vessel}(x_3))\right)}$$
<div align="right">Equation 3.10</div>

For bifurcation level 4 (see Fig. 3.24),

$$Q = \frac{-xL\,16\pi(r_4)^2}{ln(^{C_{vessel}(x)}/_{C_{input}})} = v_4 16\pi(r_4)^2$$

$$v_4 = \frac{H}{16\left(\ln(C_{input})) - ln(C_{vessel}(x_4))\right)}$$
<div align="right">Equation 3.11</div>

The velocities computed in the third and fourth level of bifurcation assume each vessel to be a hollow cylindrical channel through which the fluid flows. In the case below, the fluid travels a tortuous path through the scaffold. As such, the velocity is superficial. The length is the distance of the straight line from the input to output of the compartment. This superficial velocity is a function of the true travel time acquired from acquired DCE-CT image data.

Before or after the scaffold compartment (see Fig. 3.24),

$$Q = \frac{-xL\,\pi r_{scaffold}^2}{ln\left(C_{vessel}(x)\middle/C_{input}\right)} = v_{scaffold}\pi r_{scaffold}^2$$

$$\boldsymbol{v_{scaffold}} = \frac{H}{\ln(C_{input})) - ln\left(C_{vessel}(x_s)\right)} \qquad\qquad \text{Equation 3.12}$$

$Q$ was used to compute the different flow.

Volumes of interest (VOI) were contoured at the inlet of the flow phantom, the outlet of the flow phantom, the third level of bifurcation, the fourth level of bifurcation, the entry of the scaffold compartment and across the entire compartment, in order to generate time-contrast enhancement curves. The average intensity of the first four time steps (baseline) was subtracted from all phases in the respective time-contrast enhancement curve, as described in Eq. 3.13.

$$Signal\ intensity(Phases\ 1-19) \qquad\qquad \text{Equation 3.13}$$

$$= Signal\ intensity(Phases\ 1-19) - Average\ Signal\ intensity(Phases\ 1-4)$$

Partial volume correction was performed using Eq. 3.14

$$HU_{Volume\ of\ interest} = \qquad\qquad \text{Equation 3.14}$$

$$\left(1 - \frac{Estimated\ Vessel\ Volume}{Volume\ of\ VOI}\right) * HU_{PCL\ equivalent\ box} + \frac{Estimated\ Vessel\ Volume}{Volume\ of\ VOI} * HU_{vessel}\ ,$$

where HU = Hounsfield units, and the estimated vessel volume is calculated from the caliper-measured diameter and the length of the selected volume of interest. The volume of the VOI is computed by the in-house functional image analysis software package [29].

The effect of the selected VOI volume on the acquired time-contrast enhancement curve was assessed. Four VOI volumes were considered: 25% of full volume, 50%, of full volume, 75% of full volume and full volume, for an arbitrarily selected initial VOI volume dimension. After baseline removal and partial volume correction, time-contrast enhancement curves were generated. The velocities were computed, along with the differential flow across the high and low permeability compartment. To assess whether there was leakage at the connections that adjoin the compartments to the vascular trees, the area under each time-contrast enhancement curve (AUC) was calculated. In MatLab, a trapezoidal numerical integration (trapz) was implemented to approximate the integral of the scattered data points. The trapz function computed the integral from 0 to 19 seconds, with unit spacing. In addition, two VOIs were selected at the inlet of the vascular tree. Using Eqn. 3.12, where the VOIs represented $C_{vessel}$ and $C_{input}$, the velocity at the inlet of the vascular tree was DCE-measured at the time of peak bolus. The measured value was compared to computationally and experimentally measured values. The level of analysis achievable using the flow phantom, given the vascular-like architecture was demonstrated through analysis of DCE experimental setup enclosing high permeability scaffolds. Similar analysis may be performed on a flow phantom enclosing lower permeability scaffolds.

A two-tail Student's t-test assuming unequal variance was used to compare the experimentally measured differential flow to that calculated from post-processing DCE images. The t-test was also used to compare the computed inlet and outlet AUC for a low permeability and high permeability compartment. Significance was set at P-values $< 0.05$ or P-values $< 0.01$.

### 3.4.4 Measurement of Experimental and Theoretical Boundary Conditions

The "arterial" input velocity to the flow phantom was measured experimentally, independent of the DCE-CT imaging experiment. The contrast agent and SBF were loaded into reservoirs which connected two pumps. Each pump was set to the dispense fluid at the same rate as in the DCE image acquisition. The experimental flow rate was measured using an in-house flow meter system. After an initial 8-9 seconds (delay

incorporated to account for travel time of mixed fluid to travel from T-junction to the outlet of the system), the mass flow rate was measured over 14 seconds. The measurement was repeated three times. The velocity was calculated as the average mass flow rate, divided by the density of the mixed fluid and the cross-sectional area of the outlet.

The theoretical velocity (Eq. 3.17) at the various levels of bifurcation were calculated based on the conservation of mass for identify offspring vessels provided in Eq. 3.16 and Eq. 3.8.

$$Q_{parent} = 2 * Q_{offspring\_left} \hspace{3cm} \text{Equation 3.16}$$

$$Q_{parent} = v_{parent} * A_{parent}$$

$$v_{offspring} = \frac{0.5 * v_{parent} * A_{parent}}{A_{offspring}} \hspace{2.5cm} \text{Equation 3.17}$$

The experimental inlet velocity was compared to a computational fluid dynamics (CFD)-based measurement. The details of CFD are described later on in Chapter 4. The experimental and CFD measurements were compared to image-extracted velocity measurements acquired from the DCE-data.

## 3.5  RESULTS

### 3.5.1 Accuracy and precision of SLS fabrications

The SLS fabrication process builds vessels with an inner diameter accuracy of 130 - 310 microns (Table 3.1). For the larger test block (in which all vessels showed patency) t-tests were performed on the measurements collected (Table 3.1) to compare inner diameter measurements for the CAD and fabricated test blocks against diameters prescribed in the vascular algorithm (pre-STL generation). Results indicate that there was no significant difference (P-values > 0.05) in the inner diameter measurements between the CAD and the fabricated prototypes. However, there was a significant difference (P-values < 0.05) between the prescribed inner diameters of vessels and their fabricated (except for 2.0 and 1.2 mm) and CAD representations. The measured difference between the CAD and prescribed inner diameter increased as the prescribed inner diameter size decreased. Henceforth, the reported inner diameter measurements are corrected values based on the observed diameter-dependent error.

**Table 3.1 Inner diameter data for test block. Statistical summary and analysis of inner diameter measurements collected for vessels with a wall thickness of 0.6 mm.**

| Prescribed [mm] | CAD (n=12) [mm] | | Fabricated (n=12) [mm] | |
|---|---|---|---|---|
| | mean ± stdev | % deviation* | mean ± stdev | % deviation† |
| 0.9 | 0.750 ± 0.013 | -16.6 | 0.77 ± 0.11 | -14.4 |
| 1.0 | 0.862 ± 0.008 | -13.8 | 0.84 ± 0.15 | -15.8 |
| 1.2 | 1.086 ± 0.027 | -9.51 | 1.17 ± 0.06 | -2.64 |
| 1.5 | 1.385 ± 0.041 | -7.66 | 1.44 ± 0.07 | -4.33 |
| 2.0 | 1.930 ± 0.018 | -3.48 | 1.97 ± 0.10 | -1.29 |
| 4.0 | 3.983 ± 0.023 | -0.42 | 3.90 ± 0.12 | -2.40 |

n = sample size

* % deviation = (CAD measurement of inner diameter – prescribed inner diameter) / prescribed inner diameter x 100

† % deviation = (physical measurement of inner diameter – prescribed inner diameter) / prescribed inner diameter x 100

### 3.5.2  Limiting resolution for SLS fabrications

The minimum, reproducible inner diameter dimension was determined through an iterative fabrication process that generated straight hollowed cylindrical vessels. Physical (digital caliper) measurements demonstrate a reproducible construction of vessels with an inner diameter and wall thickness as small as 770 ±110 microns (Table 3.1) and 600 microns, respectively. For the two test blocks generated, all vessels with prescribed diameters greater than or equal to 900 microns (prescribed inner diameter in algorithm) showed patency after an air and water flush; vessels smaller than 900 microns diameter were occluded by fused PCL powder. All subsequent prototype phantoms built on the SLS system consisted of vessels with inner diameters greater than this resolution limit.

### 3.5.3  SC/SL, SLS and ICC scaffold porosity

Fig. 3.11 depicts the variability in porosity for the various porogen ranges used to fabricate SC/SL scaffolds. Three of the six ranges of examined SC/SL scaffolds produced

consistent porosity between 89-93 ± 1-5%. Scaffolds with porogen sizes less than 106 microns, 106 – 180 microns and 180-300 microns experienced larger standard deviations in porosity 79% ± 14%, 84% ± 9%, 81% ± 13% respectively. Since only the 300-600 micron and 700-1000 micron scaffolds were reliably fabricated with consistent porosity, future permeability studies only utilized theses scaffolds. The porosity of the 2.2 mm and 2.15 mm pore design fabricated on the SLS were 68% and 58%, respectively.
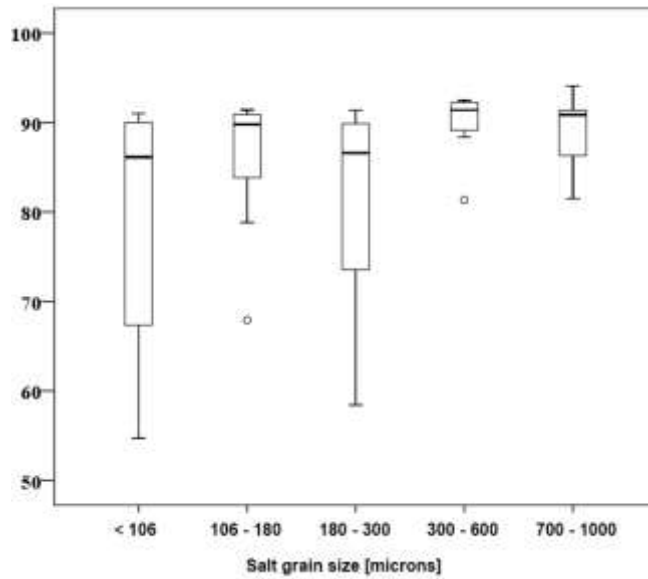


**Figure 3.12 A box plot of the porosity for the fabricated SC/SL PCL scaffolds.**

Manufactured ICC scaffolds were sponge-like, with the core of the scaffold that still enclosed remnant beads, which were not dissolved by the hydrochloric acid. The ICC scaffolds were easily malleable and deformed to the touch. In application, the integrity of the scaffold was compromised upon placement in the scaffold compartment. As such, the architectural and flow characteristics of the scaffold were not evaluated.

### 3.5.4 Scaffold hydraulic permeability and differential flow

Hydraulic permeability and differential flow results are reported as mean ± standard deviation in Fig. 3.12. The experimentally measured hydraulic permeability values for the SLS scaffolds were $7.5 \times 10^{-6} \pm 4.2 \times 10^{-6}$ m$^4$/N·s and $6.3 \times 10^{-7} \pm 4.0 \times 10^{-8}$ m$^4$/N·s for the 2.2 mm and 2.15 mm pore design, respectively. The hydraulic permeability of the SC/SL scaffolds were $4.7 \times 10^{-7} \pm 1.2 \times 10^{-7}$ m$^4$/N·s and $9.1 \times 10^{-9} \pm 5.7 \times 10^{-9}$ m$^4$/N·s for

the 700 - 1000 micron and 300 - 600 micron porogen fabrications, respectively. Fig 3.12a depicts the hydraulic permeability range for both groups. Differences in permeabilities were statistically significant (P-values< 0.05) between all groups, except for the low permeability SLS scaffold and high permeability SC/SL scaffold. Fig. 3.12b illustrates the range of differential flow achievable with the two investigated techniques. SLS scaffolds exhibited a -22 ± 3% and -81 ± 6% differential flow, for high and low permeability scaffolds, respectively. SC/SL scaffolds showed a differential flow of -82 ± 4%, and -90 ± 4% for scaffolds with 700 - 1000 micron and 300 - 600 micron particle size ranges, respectively. Differences in differential flow were statistically significant (P-values< 0.05) between all groups, except the low permeability SLS scaffold and high permeability SC/SL scaffold. The SC/SL scaffolds and the 2.15 mm SLS performed similarly in terms of differential flow, although their estimated hydraulic permeability were statistically different.
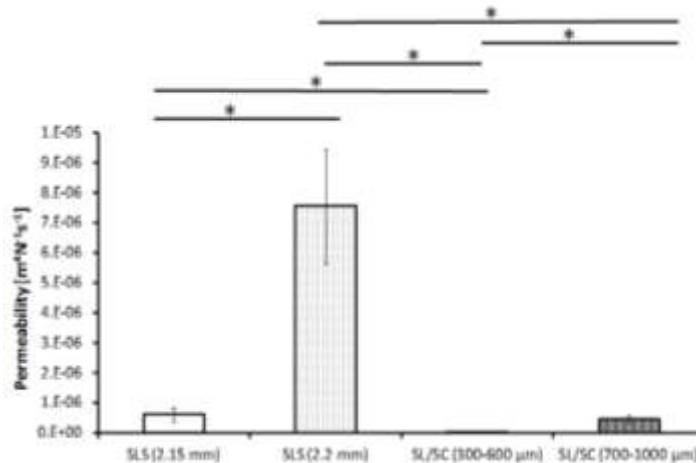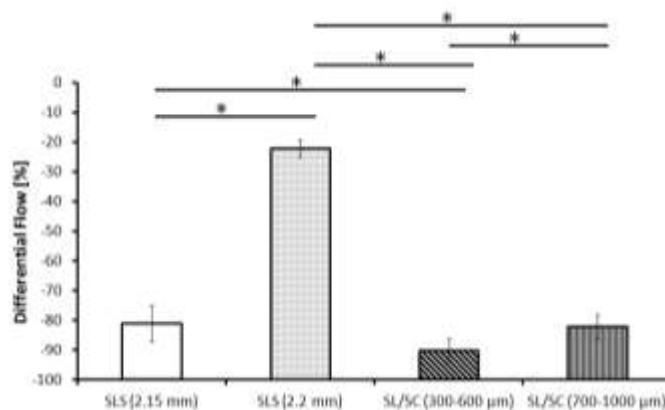
**Figure 3.13 (a) Permeability and (b) differential flow for SLS (2.15 mm and 2.2 mm) and SC/SL (300-600 µm and 700-1000 µm) scaffolds. The differential flow and permeability for all groups was statistically significant, except SLS (2.15 mm compared to SC/SL (700-1000 µm). The significance bar above the respective bars, along with '*' indicate that the two groups are significantly different from one another (p-value < 0.05).**

The preliminary DCE-CT experiments discussed in the remainder of this paper were conducted using SLS scaffolds, since they were easily reproducible and exhibited low variability in their porous architecture.

### 3.5.5 DCE imaging

The CT attenuation values of the PCL/HA plastic mixture and phantom background were at -150 Hounsfield units and 55 Hounsfield units, respectively. Fig. 3.14 shows an axial

slice of the phantom within the tissue-mimicking bounding box over the time course of a DCE experiment. Air pockets were evident within each of the compartments and persisted through the duration of the experiments.
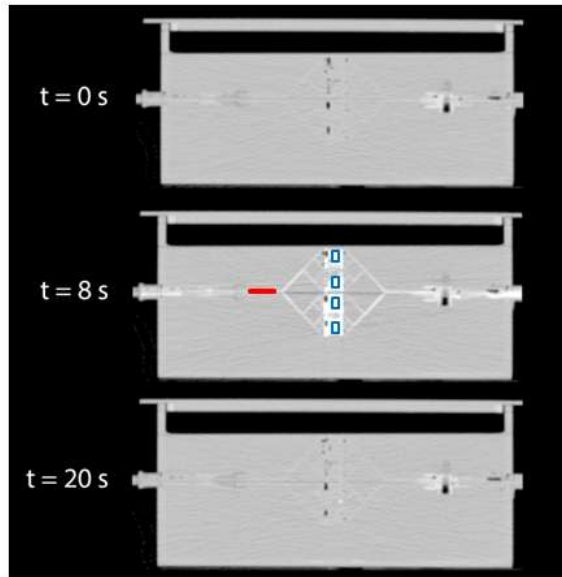


**Figure 3.14 Representative baseline axial image of a single slice of the phantom submerged with tissue-mimicking liquid volume. The highlighted regions of interest outline the location of the inlet (red) and scaffold compartments (blue).**

### 3.5.5.1 Concentration calibration

Assuming uniform mixing between SBF and CA, the signal intensity of the SBF over a VOI was converted to a CA concentration based on a contrast calibration curve that was generated for $0 - 70$ mg of iodinated contrast agent per ml.
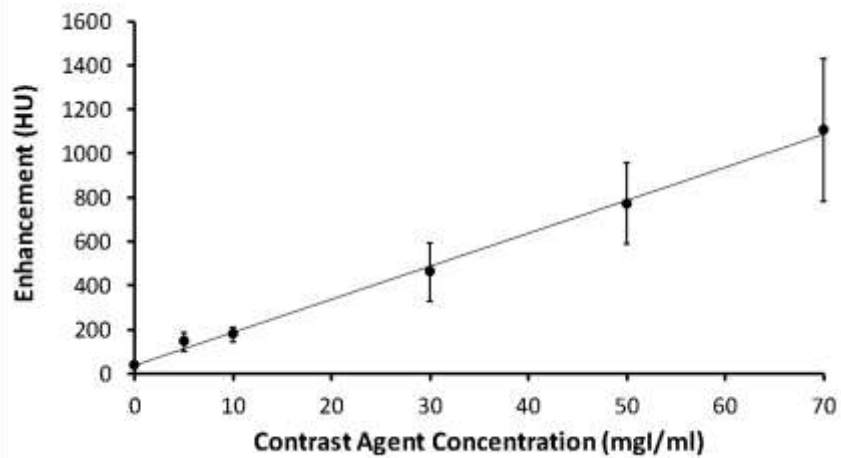
**Figure 3.15 Contrast calibration curve generated from six vessels filled with varied concentrations of iodinated contrast agent. Linear fit between enhancement and contrast agent concentration.**

*3.5.5.2 Volume of Interest Selection*

The mean intensity was measured over the given time course, for a volume of interest at the inlet and outlet of the enclosed within the phantom. These time-enhancement curves were generated from the acquired DCE-CT data for the high and low permeability compartments. The effect of VOI volume on enhancement is shown in Fig. 3.16. Fig. 3.16a illustrates four of the six contours examined at the inlet. In Fig 3.16b and Fig 3.16c, as the volume increases, the enhancement decreases along both the inlet and outlet. Subsequent VOIs use volumes on the order of the 30% sub-volume.



**(a)**

77
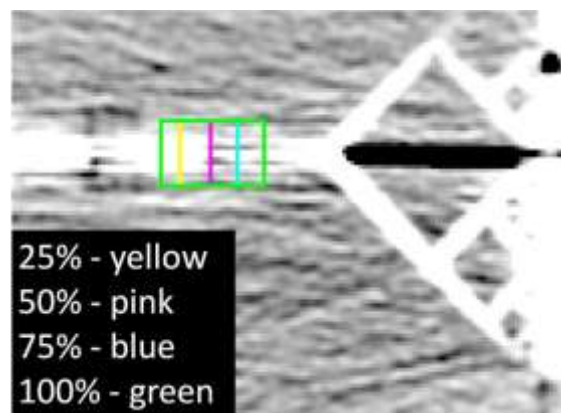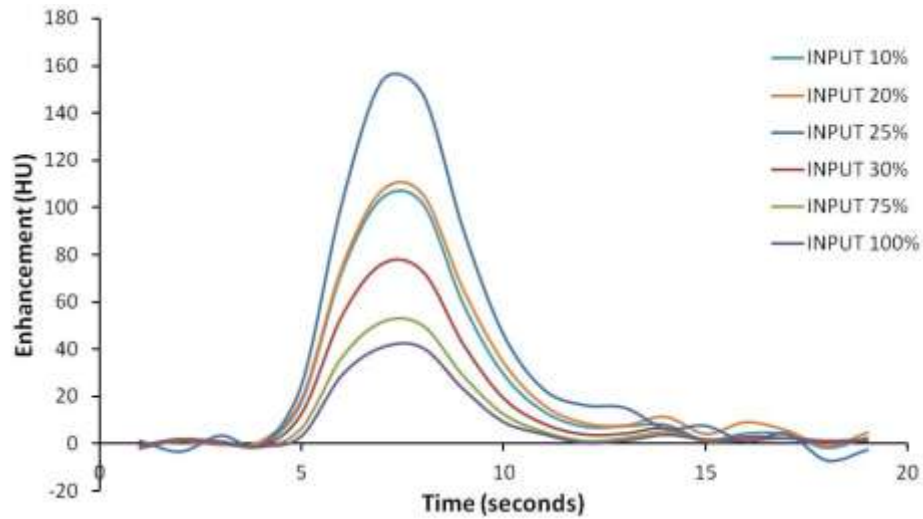
**(b)**
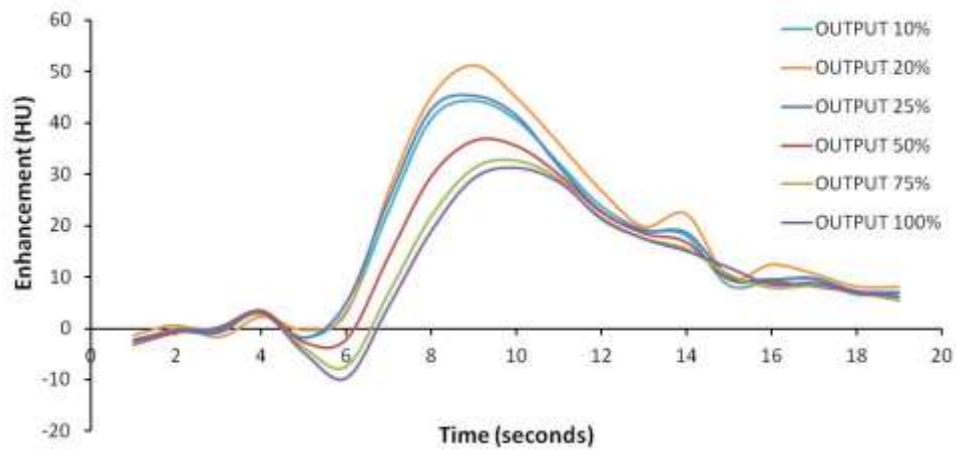


**(c)**

**Figure 3.16 (a) Single axial image of phantom with four volumes of interest (VOIs) selected. Four VOI volumes delineated by the contours over the inlet of the phantom. The 10% and 20% volume are not visible in this image. Representative time-contrast enhancement curves generated from the VOIs shown in (a) and at the outlet of a high permeability compartment: (b) with VOIS at inlet and (b) outlet. Maximum VOI volume = 500 mm$^3$.**

*3.5.5.3  DCE phantom time-contrast enhancement curve analysis*

Fig. 3.17a and 3.18 outline the contours used to generate time-contrast enhancement curves. The three VOI locations selected along the inlet and outlet showed consistent enhancement results for all generated curves (A, B, C), except for at the inlet of the low permeability compartment. Fig. 3.19a and Fig. 3.19b illustrate input functions for the

78

high and low permeability compartments, respectively. Fig. 3.20a and Fig. 3.20b illustrate output functions for the high and low permeability compartments, respectively. Fig. 3.21 shows both "arterial" and output time-contrast enhancement curves on a single plot. In Fig. 3.21a, the output function is flatter and has a lower enhancement than the "arterial" input functions. However, in Fig 3.21b, the "arterial" functions show large variability in enhancement that was not alleviated by partial volume corrections or the alteration of the VOI volume. Fig 3.17b illustrates the artifact present in the DCE data that may have altered the input signals. For both the low and high permeability compartments, the input function arrives first at 4-5 seconds, followed by the output curve at 6-8 seconds.

Across both phantoms (low and high permeability compartment), at $t = 0$ seconds, a bolus of contrast agent was injected into a plastic tubing connected to the vascular network. The curves demonstrate a sharp increase ($t = 5 - 7s$) in signal intensity across the phantom as iodine entered the network and reached the compartments, followed by a more gradual decrease as the bolus cleared and SBF entered the network ($t = 8 - 19s$). The intensity peaked at $t = 8$ seconds.
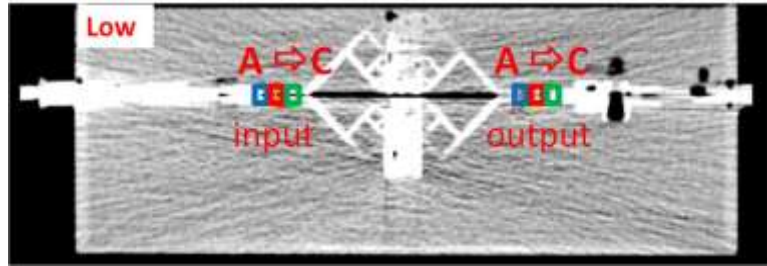
**(a)**
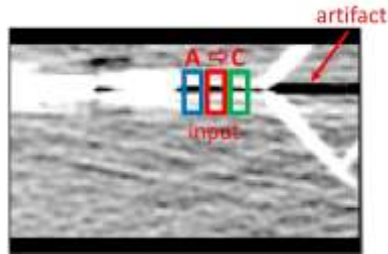


**(b)**

**Figure 3.17 (a) Representative axial slice of DCE-CT scan of low permeability scaffold within phantom. Three volumes of interest selected at the input ("arterial") and output ("venous") of the phantom. t = 8 seconds. (b) Artifact (red arrow) shown in representative axial slice of DCE-CT scan of low permeability scaffold within phantom. Three volumes of interest selected at the input ("arterial") and output ("venous") of the phantom. Blue (A); Red( B); Green (C); from left to right. t = 8 seconds.**
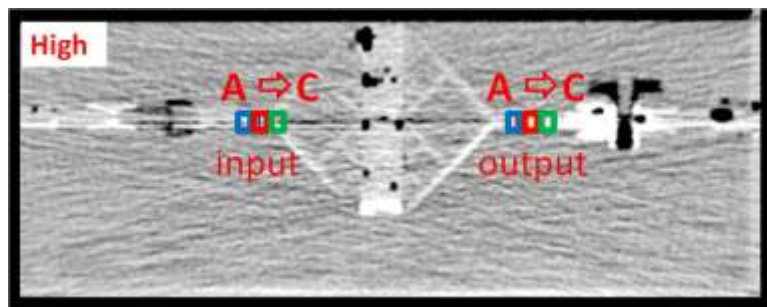


**Figure 3.18 Representative axial slice of DCE-CT scan of high permeability scaffold within phantom. Three volumes of interest selected at the input ("arterial") and output ("venous") of the phantom. Blue (A); Red( B); Green (C); from left to right. t = 6 seconds.**
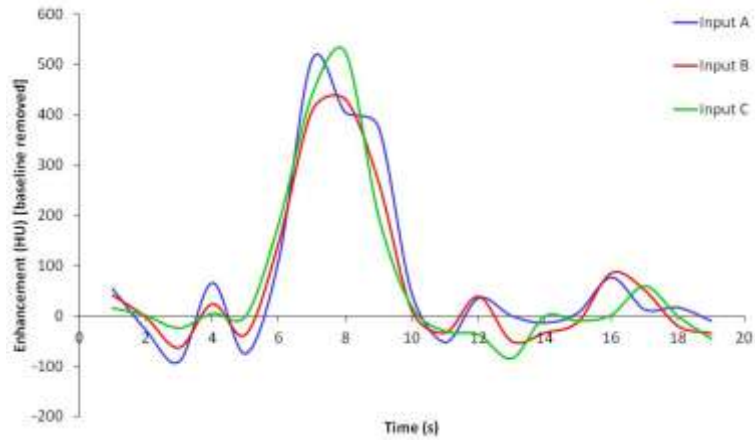
**(a)**
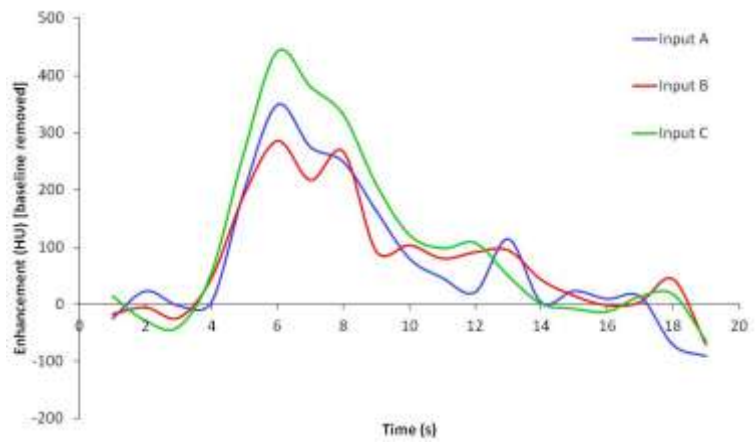


**(b)**

**Figure 3.19 Time contrast attenuation curves. Volumes of interest at inlet of phantom enclosing (a) high permeability scaffold and (b) low permeability. Baseline removal and partial volume correction performed. Representative axial slice view shown. SBF inlet flow = 1.4 g/s; CA inlet flow = 2.8 g/s. Inlet-A (blue); Inlet-B (red); Inlet-C (yellow); Outlet-A (blue); Outlet-B (red); Outlet-C (yellow).**
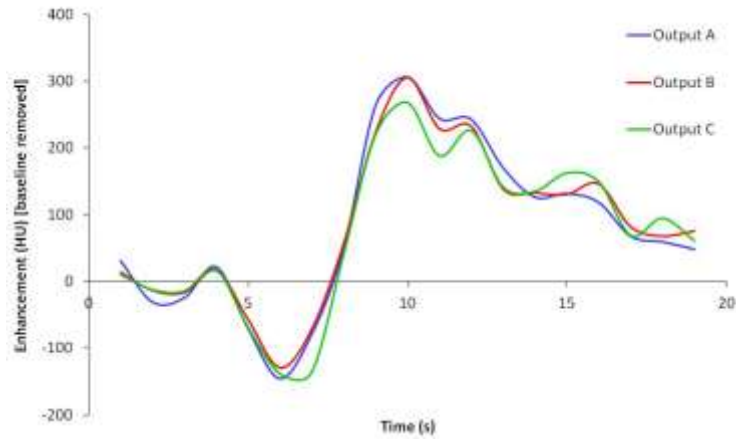
**(a)**
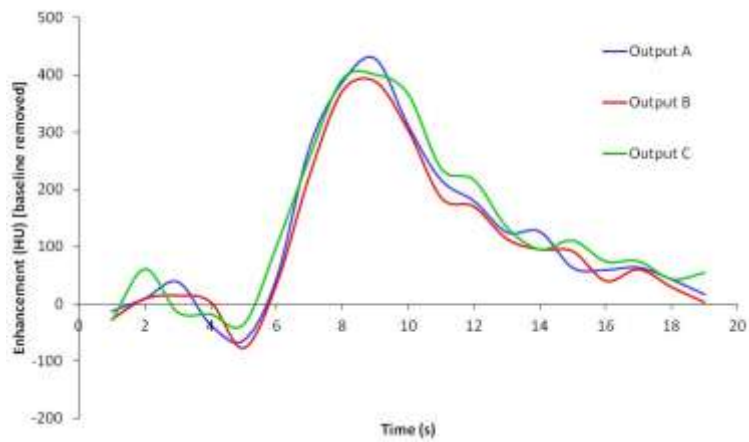


**(b)**

**Figure 3.20 Time contrast attenuation curves. Volumes of interest at outlet of phantom enclosing (a) high permeability scaffold and (b) low permeability. Baseline removal and partial volume correction performed. Representative axial slice view shown. SBF inlet flow = 1.4 g/s; CA inlet flow = 2.8 g/s. Inlet-A (blue); Inlet-B (red); Inlet-C (yellow); Outlet-A (blue); Outlet-B (red); Outlet-C (yellow).**
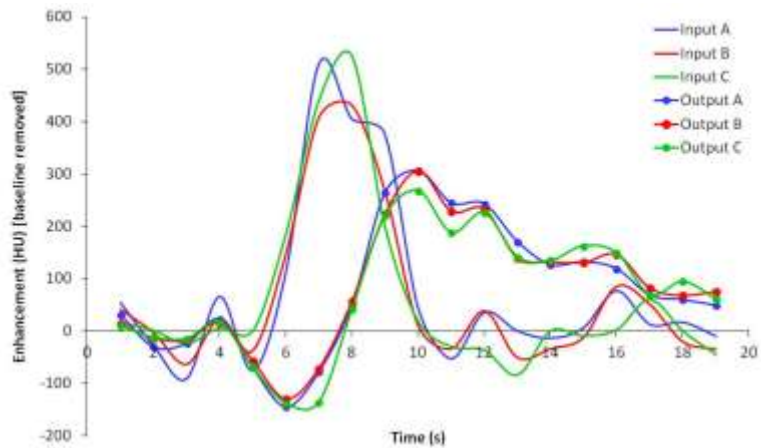
**(a)**
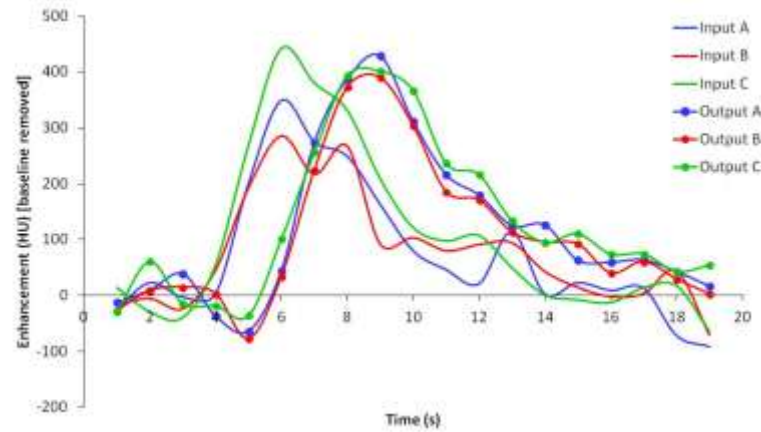


**(b)**

**Figure 3.21 Phantom enclosing (a) high permeability scaffold and (b) low permeability shown in single-slice view of VOIs used to generate time contrast attenuation curves at the vessel input and output. (Combined plots of Figure 3.19 and 3.20.) Baseline removal and partial volume correction performed. SBF inlet flow = 1.4 g/s; CA inlet flow = 2.8 g/s. Color coded volumes of interest correspond to Figures 1 and 2. Inlet-A (blue); Inlet-B (red); Inlet-C (yellow); Outlet-A (blue); Outlet-B (red); Outlet-C (yellow).**

### 3.5.5.4 Evaluation of phantom leakage

Figure 3.22 compares the AUC for the inlet (input function) and outlet (output function) time-contrast enhancement curves. For the high permeability scaffold, the input function AUC was $1.3 \times 10^3 \pm 110$ and the outlet function AUC was $1.5 \times 10^3 \pm 79$. For the low permeability scaffold, the input function AUC was $1.6 \times 10^3 \pm 290$ and the outlet function AUC was $2.3 \times 10^3 \pm 230$. Within each compartment, the AUC of the output function was slightly higher. There was no statistical difference between the AUC for the input and output function time-contrast enhancement curves shown in Fig. 3.21.

83
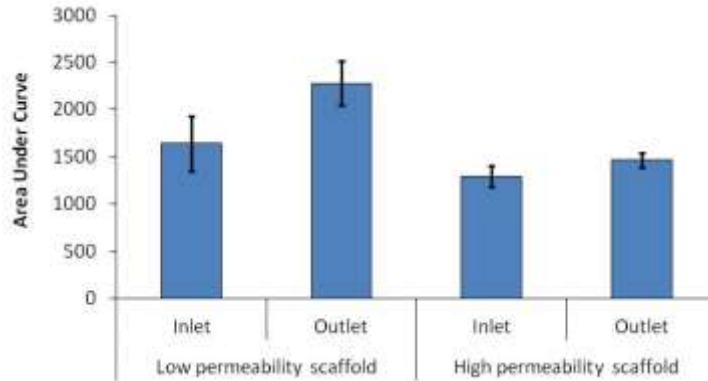
**Figure 3.22 Area under the curve measurements for time-contrast attenuation curves in Fig. 3.21 approximated using trapezoidal integration. Calculation performed after baseline subtraction and partial volume correction. For the high and low permeability scaffold compartment, there was an increase in area of 13% and 39%, respectively. No statistical difference in area under the curve for either scaffold type (Two-tailed student's t-test with significance less than 0.01).**

*3.5.5.5  Measurement of velocity and differential flow*

Fig. 3.23 outlines the VOIs used to calculate the velocities summarized in Table 3.2 and Table 3.3. Table 3.2 summarizes the experimentally, computationally and imaging-derived velocities at the inlet of the phantom. The experimental and computational measurements are similar, while there is a marked decrease in that measured in the image. The DCE-measured velocity was computed using Eq. 3.12 at t = 9 seconds where $C_{input}$ was measured over the blue VOI in Fig 3.17a and $C_{vessel}$ was measured over the red VOI in Fig. 3.17a. $C_{input}$ and $C_{vessel}$ were calculated directly from the contrast calibration curve shown in Fig. 3.15. The final DCE-imaging derived velocity estimated distal to the T-junction and mixer, prior to the inlet of the vascular tree was 0.61 m/s. In Table 3.3, the velocity at the third and fourth level of bifurcation are lower than the theoretical values. Table 3.3 summarizes the theoretical (based on Eq. 3.17) "arterial" values and DCE-imaging extracted measurements for both the "arterial" and "venous" vascular trees. Level 3 and 4 were arbitrarily used to demonstrate post-analysis; the same techniques can be used to compute the velocity at bifurcation level 1 and 2. The 'before scaffold' and 'entire scaffold compartment' values shown in Table 3.2 and Eq. 3.4 (volumetric flow used instead of mass flow rate, before the scaffold and across the whole scaffold compartment) were used to calculate the differential flow across the low and high permeability scaffold. In both cases, compared to the experimental values, the DCE-

imaging derived measurements underestimated the differential flow, by 12% and 32% for the low and high permeability scaffolds, respectively (Fig. 3.24). The high permeability compartment DCE-extracted measurement was -29% and for the low permeability compartment it was -91%.
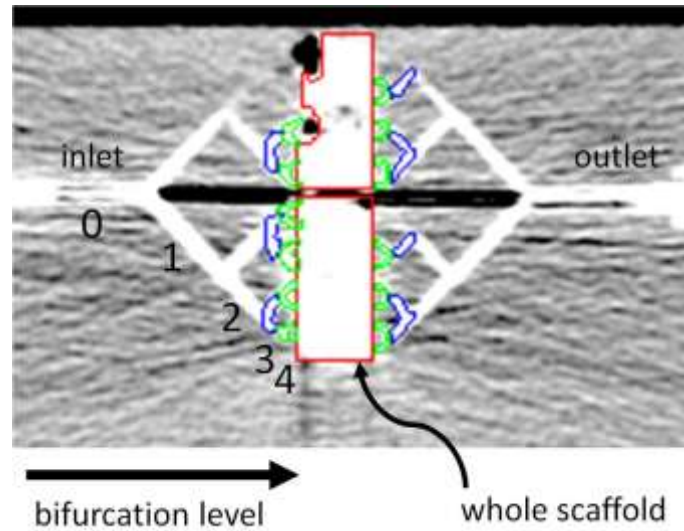


**(a)**
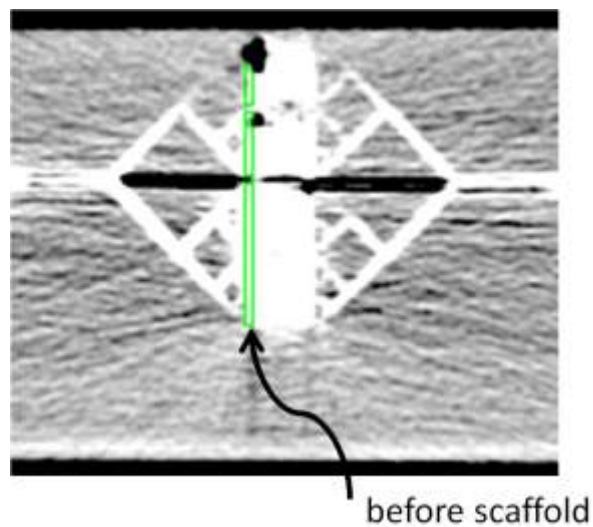


**(b)**

**Figure 3.23 (a) Volumes of interest selected at each level of bifurcation and over the scaffold compartment (11 mm). (b) Volume of interest delineates space before scaffold within the compartment (2 mm). Axial slice from DCE-CT scan of phantom. t = 8 seconds. Bifurcation level 3 – blue ; bifurcation level 4 – green; entire scaffold compartment - red; region before scaffold- yellow.**

85

**Table 3.2. Mass flow measurement acquired distal to T-junction and mixer, prior to the inlet of the vascular tree. SBF inlet flow = 1.4 g/s; CA inlet flow = 2.8 g/s.**

| | SBF (no bolus) [g/s] (Velocity [m/s]) | SBF with bolus [g/s] (Velocity [m/s]) |
|---|---|---|
| **Experimental** | $2.1 \pm 0.2$ ($0.51 \pm 0.02$) | $3.5 \pm 0.1$ ($0.85 \pm 0.01$) |
| **Computational** | 2.4 (0.58) | 3.6 (0.88) |
| **DCE-imaging** | N/A | 0.61 m/s |

Note:
- Conversion from g/s assumes there is negligible density change to the SBF with the addition of contrast agent.
- Phantom inlet diameter = 2.2 mm. Constant viscosity of fluid assumed to be 1080 kg/m$^3$

**Table 3.3 DCE-measured estimated velocities across a high permeability scaffold compartment. DCE-extracted measurements were calculated using Eq. 3.10-3.12 and theoretical values were calculated using Eq. 3.16-3.17.**

| | Velocity (m/s) | |
|---|---|---|
| | **Measured** | **Theoretical** |
| **"Arterial" Bifurcation Level 3** | 0.007 | 0.007 |
| **"Arterial" Bifurcation Level 4** | 0.004 | 0.001 |
| **"Venous" Bifurcation Level 3** | 0.02 | |
| **"Venous" Bifurcation Level 4** | 0.01 | |
| **Before Scaffold** | 0.28 | |
| **Entire scaffold compartment** | 0.20 | |
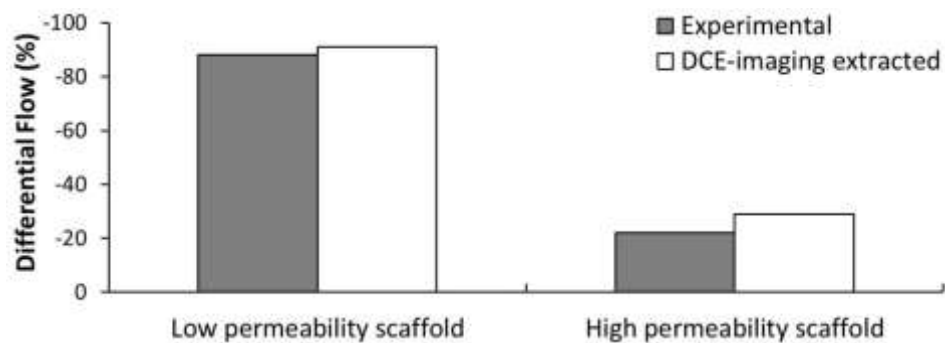


**Figure 3.24 Comparison of differential flow measured by experimental methods and from imaging-extracted metrics.**

## 3.6 DISCUSSION

The predictive value of metrics extracted from quantitative DCE imaging is well-documented in clinical research studies across various organs and modalities. However, the lack of a validation phantom and/or standardization across studies limits the practical, clinical relevance of protocol/system sensitive results, and comparisons of derived metrics such as blood flow rate. Thus, the development of a physical dynamic flow phantom that mimics the behavior of time-contrast enhancement curves seen on *in vivo* imaging is multi-center use of DCE-derived metrics. Image-extracted metrics from the first-pass bolus kinetic curves provide results dependent on the different biological effects in the scanned organ. The hemodynamic changes in blood flow are dependent on vessel bifurcations, vessel compliance, vascular network tortuosity and the volume of available luminal space [33]. In addition, disease-induced pathologies can alter flow and/or the anatomy of vasculature, in cases of occlusion or hyper-vascularization [3]. The tunable architecture of the proposed vascular phantom provides the flexibility to model both normal and pathological conditions present in variable levels of flow. The change or drop in flow rate is measured using the metric, differential flow. A reasonable phantom design representative of "arterial" input will house compartments with scaffolds that exhibit differential flows that cover disparate ranges of flow resistance.

While computer generated vascular trees are based on idealized conditions and theoretical principles, they have been shown to reasonably reproduce *in vivo* hemodynamic conditions [34-35]. The vascular networks are a key component to the flow phantom, as they are representative of the small artery structures that distribute blood to smaller microcirculatory-like compartments (Fig. 3.5). The vessels were fabricated with an inner diameter precision of 220 microns. The computed dimensional accuracy was within reasonable limits since the resolution of clinical CT scanners was 1 mm, roughly 5 times larger than the calculated error (Table 3.1). Results indicate that there was a significant difference (p-values $< 0.05$) in the prescribed inner diameters of vessels and their CAD representations. As the prescribed inner diameter decreased, the fabricated inner diameter decreased. Statistical analysis showed a significant mean difference between prescribed inner diameters and generated CAD inner diameters, indicating a bias between planned and modeled inner diameters using the current

87

algorithms. The shrinkage may be caused by computational rounding and mesh smoothing during tree generation. A calibrated correction based on these measurements was subsequently applied to correct for this diameter-dependent systematic variation in the CAD phase of construction. During the iterative process of building test blocks, it was observed that thicker walls caused the lumens of vessels with inner diameters smaller than 1mm to completely fuse during the build process. The minimum measured (physical) inner diameter size of 620 microns was achievable, however repeated builds showed that only a minimum inner diameter of 770 microns was repeatable. The study demonstrates that a bifurcating vascular network can be reliably fabricated using SLS, but at a minimum resolution greater than that of a capillaries. The apparent limitation of the chosen polymer using the SLS fabrication technique is that it produces rigid walls, when in fact *in vivo* vasculature has some elasticity that causes wall motion in response to the pulsatile nature of arterial blood flow and compliant nature of the venous system. Using SLS or another RP method, an elastomeric material may offer physiological vessel wall motion.

The literature suggests that in the assessment of bulk properties, such as permeability and volumetric flow, a simplified porous media may be representative of perfusion at the capillary level [36]. A multitude of scaffold fabrication techniques offer control over scaffold architecture: pore size, porosity and interconnectivity. SLS and SC/SL scaffolds were successfully fabricated with distinct architectural characteristics. SC/SL created a less structured, random arrangement of pores within a scaffold, while RP provided a more structured pore lattice. The generated SLS scaffolds possess throat sizes that were roughly 60% smaller than the pore diameter. SLS scaffolds had 100% interconnectivity between pores, and a porosity of 68% for larger pore design and 58% for the smaller pore design. SC/SL scaffolds were less interconnected since, during the fabrication process, some salt crystals became completely entrapped in molten PCL and did not dissolve out of the scaffold structure. SC/SL scaffolds with pore diameters between 300 to 1000 microns were highly repeatable and achieved a porosity greater than 89% with less than 5% variability.

The fluid flow properties, in terms of permeability and differential flow of the porous scaffolds were evaluated using a SBF. The permeability of each scaffold described the

88

ease of flow of a fluid through a porous medium under a hydraulic gradient. There was an inverse relationship between permeability and differential flow, as lower permeability scaffolds exhibited a greater differential flow. The differential flow of the both SC/SL scaffolds and the 2.15 mm SLS scaffold exhibited a high differential flow, while the high permeability (2.2 mm pore design) SLS scaffold met the low end of the differential flow range.

Based on experimentally measured hydraulic permeability values in the literature, other scaffold techniques and design parameters can be selected to achieve a hydraulic permeability that can expand the range and/or increase the resolution of the achievable differential flow shown in Fig. 3.12. Computational studies using a homogenization algorithm [37] estimated that a 100-300 micron porogens could achieve intrinsic permeabilities on the order of $10^{-12}$ - $10^{-13}$ $m^2$. The computational estimated hydraulic permeability values suggested that a low permeability scaffold could be achieved, under more structured, reliable (in terms of porogen size and porosity variability) conditions. However, the ICC scaffolds fabricated with porogens between 30 - 150 microns had poor integrity and therefore it was tested. The high differential flow achieved by the SLS (2.15 mm) and SC/SL scaffolds, abrogated the need for a scaffold with lower permeability, at the level of ICC scaffolds

DCE imaging demonstrated that tissue equivalent CT signal values were within a reasonable operating range for simulating tissue attenuation effects. For a fourth order vascular phantom, the DCE-CT data demonstrated a bolus entrance and clearance form with desired behavior (Fig. 3.21). While most DCE analysis will be at a reduced spatial resolution, the phantom successfully generated time-contrasts enhancements curves at the spatial resolution of the acquired images, as shown in Fig. 3.21. The DCE analysis demonstrated the ability of end-users to post-process the phantom data for comparison to theoretical, computational and experimental measurements. The difference in AUCs between the input and outputs curves for the high and low permeability compartments suggest that the phantom was not leaky (Fig. 3.22). DCE-extracted measurements of velocity and differential flow (Table 3.2 and 3.3) corresponded closely with experimental measurements (Fig. 3.25). It is expected that DCE-measured bifurcation values were less than the theoretical measurements, due to frictional forces present. However, within

larger channels, such as at the inlet, measurements closer to the experimental and computational values were expected.

Ongoing studies seek to provide a quality assurance tool to assess the reliability and reproducibility of regional blood flow estimates extracted during DCE imaging analysis. While immediately designed for CT, the phantom may be modified to meet the design requirements and output characteristics of MRI, single-photon emission computed tomography (SPECT) and/or positron emission tomography (PET) for dynamic imaging validation. The sensitivity of image-extracted metrics to parameters such as the volume of the selected volume of interest that are susceptible to partial volume averaging and noise must be examined in future studies in order to provide a robust validation tool. The sensitivity of these metrics may also be examined under a physiological pulsatile fluid flow. Along with these future adjustments, the next generation of the phantom would minimize the occurrence of air pockets in the compartment, so as to reduce the opportunity for signal distortion and the inaccurate calculation of differential flow. The phantom system should be tightly sealed at junctions prior to the inlet of the phantom to ensure that air is not introduced to the system. After the phantom is pulled under a vacuum, it should be transported to the CT scan in a vacuum sealed container, until it is ready for connection to the overall flow system. Future studies should consider lower SBF rates for which the CA speed can be match so as to generate more accurate estimates of velocity. In this study, the velocity was assumed to be the maximum velocity achieved, since there was an increase, followed by a decrease in the speed of the injected bolus. In addition, during post-processing, the contour of the VOIs on which partial volume correction is performed may introduce error into the final calculated velocities. As well, the accuracy of VOI volume measurements made by the in-house software analysis tool should be determined, as they directly affect the partial volume correction factor.

To further mimic peak intensity values seen *in vivo*, the average peak can be adjusted through dilutions of the contrast agent. Future studies should also determine the desired differential flows and/or velocities that would capture the low and high flow rates seen *in vivo*. Previous studies have been cited as evaluating unrealistic capillaries exchanged within their phantoms. Although the developed phantom does not solve this modeling challenge, the tortuous nature of scaffolds with their pore diameters which fall below the

resolution of typical CT, increases the complexity of exchange within the single channel model.

Overall¸ these vascular networks provide a structure from which a more complex system can be design from and coupled with a multitude of scaffold techniques. The stated limitations of RP establish the extents to which this technique can be used in the development of a vascular phantom. Based on the design, future generations of the device can be scaled up to build systems larger volumes (greater than the 4ml shown here) for analysis of larger regions of interest.

## 3.7 CONCLUSION

The proposed SLS, rapid prototyping technique offers a consistent, reliable method to fabricate bifurcating vascular networks to a minimum resolution less than 1 mm. Porous compartments that exhibited a distinct range of differential flow were realized. Time-contrast enhancement curves generated from DCE-CT illustrated the utility of the dynamic flow phantom. The DCE-CT signals exhibited desired behavior for an "arterial" input function and delayed compartment curve. Further improvements to the dynamic flow phantom are necessary for a more comprehensive evaluation of its extractable metrics and its sensitivity to post-processing parameters.

## 3.8 ACKNOWLEDGEMENTS

## 3.9 REFERENCES

[1] Pandharipande PV, Krinsky GA, Rusinek H, Lee VS. Perfusion imaging of the liver, current challenges and future goals. Radiology. 2005; 234(3):661-673.

[2] Lee T. Functional CT: physiological models. Trends Biotechnol. 2002; 20(8):S3-S10.

[3] Cao Y, Platt JF, Francis IR, Balter JM, Pan C, Normolle D, Ben-Josef E, Haken RK, Lawrence TS. The prediction of radiation-induced liver dysfunction using a local dose and regional venous perfusion model. Med Phy. 2007;34(2):604-612.

[4] Padhani AR. Dynamic contrast-enhanced MRI studies in oncology with an emphasis on quantification, validation and human studies. Clin Radiol. 2001;56(8):607-620.

[5] Miles KA. Perfusion CT for the assessment of tumour vascularity, which protocol? Br J Radiol. 2003;76:S36-S42.

[6] Padhani AR. Dynamic contrast-enhanced MRI in clinical oncology, current status and future directions. J Magn Reson Imaging. 2002;16(4):407-422.

[7] Sheiman RG, Sitek A. CT perfusion imaging: know its assumption and limitations. Radiology. 2008;246(2):649-650.

[8] Fiorella D, Heiserman J, Prenger E, Partovi S. Assessment of the reproducibility of postprocessing dynamic CT perfusion data. AJNR Am J Neuroradiol. 2004; 25(1):97-107.

[9] Sanelli PC, Nicola G, Tsiouris AJ, Ougorets I, Knight C, Frommer B, Veronelli S, Zimmerman, RD. Reproducibility of postprocessing of quantitative CT perfusion maps. AJR Am J Roentgenol. 2007;188(1):213-228.

[10] Goh V, Halligan S, Taylor SA, Burling D, Bassett P, Bartram CI. Differentiation between diverticulitis and colorectal cancer, quantitative CT perfusion measurements versus morphologic criteria- initial experience. Radiology. 2007;242(2):456-462.

[11] Gillard JH, Minhas PS, Hayball MP, Bearcroft PW, Antoun NM, Freer CE, Mathews JC, Miles KA, Pickard JD. Assessment of quantitative computed tomographic cerebral perfusion imaging with H2(15)O positron emission tomography. Neurol Res. 2000;22(5):457-464.

[12] Purdie TG, Henderson E, Lee TY. Functional CT imaging of angiogenesis in rabbit VX2 soft-tissue tumour. Phys Med Biol. 2001;46(12):3161-3175.

[13] Cenic A, Nabavi DG, Craen RA, Gelb AW, Lee T. A CT method to measure hemodynamics in brain tumors, validation and application of cerebral blood flow maps. AJNR Am J Neuroradiol. 2000;21(3):462-470.

[14] Biederer J, Heller M. Artificial thorax for MR imaging studies in porcine heart-lung preparations. Radiology. 2003;226(1):250-255.

[15] Haberland U, Cordes J, Lell M, Abolmaali N, Klotz E. A biological phantom for contrast-media-based perfusion studies with CT. Invest. Radiol. 2009;44(10):676-682.

[16] Thompson SM, Ramirez-Giraldo JC, Knudsen B, Grande JP, Christner JA, Xu M, Woodrum DA, McCollough CH, Callstrom MR. Porcine ex vivo liver phantom for dynamic contrast-enhanced computed tomography. development and initial results. Invest Radiol. 2011;46(9):586-593.

[17] O'Flynn PM, Roche ET, Phandit AS. Generating an ex vivo vascular model. ASAIO J. 2005;51(4):426-433.

[18] Veltmann C, Lohmaier S, Schlosser T, Shai S, Ehlgen A, Pohl C, Becher H, Tiemann K. On the design of a capillary flow phantom for the evaluation of ultrasound contrast agents at very low flow velocities. Ultrasound Med Biol. 2002;28(5):625-634.

[19] Chiribiri A, Schuster A, Ishida M, Hautvast G, Zarinabad N, Morton G, Otton J, Plein S, Breeuwer M, Batchelor P, Schaeffter T, Nagel E. Perfusion phantom. An efficient and reproducible method to simulate myocardial first-pass perfusion measurements with cardiovascular magnetic resonance. Magn Reson Med 2012, .

[20] Driscoll B, Keller H, Coolens C. Development of a dynamic flow imaging phantom for dynamic contrast-enhanced CT. Med Phys. 2011;38(8):4866-4880.

[21] Karch R, Neumann F, Neumann M, Schreiner W. A three dimensional model for arterial tree representation, generated by constrained constructive optimization. Comput Biol Med 1999;29(1):19-38.

[22] Zamir M. Optimality principles in arterial branching. J Theor Biol. 1976;62(1):227-251.

[23] Murray CD. The physiological principle of minimum work. I. The vascular system and the cost of blood volume. Proc Nat Acad Sci. 1926a;12(3):204-214.

[24] Sherman TF. On connecting large vessels to small. The meaning of Murray's law. J Gen Physiol. 1981;78(4):431-453.

[25] Kemppainen JM, Hollister SJ. Differential effects of designed scaffold permeability on chondrogenesis by chondrocytes and bone marrow stromal cells. Biomaterials. 2010;31(2):279–287.

[26] Kotov, N, Liu, Y, Wang, S, Cumming, C, Eghtedari, M,Vargas, G, Motamedi, M, Nichols, J, Cortiella, J. Inverted colloidal crystals as three-dimensional cell scaffolds. American Chemical Society 2004;20(19):7887-7892.

[27] Shanbhag, S, Lee, JW, Kotov, N. Diffusion in three-dimensionally ordered scaffolds with inverted colloidal crystal geometry. Biomaterials. 2005;26(27):5581-5585.

[28] Li, J, Mak, AF. Hydraulic permeability of polyglycolic acid scaffolds as a function of biomaterial degradation. J Biomater Appl. 2005;19(3):253-66.

[29] Cao Y. Development of image software tools for radiation therapy assessment [Abstract]. Med Phys. 2005;32(6):2136.

[30] Tofts, PS, Brix, G, Buckley, DL, Evelhoch, JL, Henderson, E, Knopp, MV, Larsson, HB, Lee, TY, Mayr, NA, Parker, GJ, Port, RE, Taylor, J, Weisskoff, RM. Estimating kinetic parameters from dynamic contrast-enhanced T1-weighted MRI of a diffusable tracer. Standardized quantities and symbols. J Magn Reson Imag. 1999;10(3):223–232.

[31] Cao, Y, Alspaugh, J, Shen, Z, Balter, JM, Lawrence, TS, Ten Haken, RK. A practical approach for quantitative estimates of voxel-by-voxel liver perfusion using DCE imaging and a compartmental model. Med Phys. 2006;33(8):3057-62.

[31] Ewing JR, Cao Y, Fenstermacher J. Single-coil arterial spin-tagging for estimating cerebral blood flow as viewed from the capillary: relative contributions of intra- and extravascular signal. Magnetic Resonance in Medicine. 2001 46: 465-475.

[32] Chien S, Usami S, Taylor HM, Lundberg JL, Gregerson MI. Effects of hematocrit and plasma proteins on human blood rheology at low shear rates. J Appl Physiol. 1966;21(1):81-87.

[33] Bezy-Wendling J, Kretowski M. Physiological modeling of tumor-affected renal circulation. Comput Methods Programs Biomed. 2008;91(1):1-12.

[34] Rolland Y., Bezy-Wendling J., Duvauferrier R., Bruno A. Modeling of the parenchymous vascularization and perfusion. Invest Radiol. 1999;34(3):171-175.

[35] Song F., You-sheng XU, Hua-mei LI. Blood flow in capillaries by using porous media model. J Cent South Univ Technol. 2007; 14:46-49.

[36] Sugihara-Seki M, Fu BM. Blood flow and permeability in microvessels. Fluid Dyn Res. 2005;37(1-2):82-132.

[37] Kang HS. Hierarchical design and simulation of tissue engineering scaffold mechanical, mass transport, and degradation properties. Ann Arbor (MI): University of Michigan, Department of Biomedical Engineering; 2010.

# CHAPTER 4

## A Computational Fluid Dynamics (CFD)-Based Approach to Assessing Flow in a Dynamic Flow Phantom for Dynamic Contrast Enhanced (DCE) Imaging

**Abstract**

Purpose:  The complexity of recent dynamic imaging phantoms has increased, such that they grossly model anatomical and/or hemodynamic changes representative of *in vivo* perfusion. This study sought to establish the range of differential flow achievable within a dynamic imaging phantom, as measured by computational fluid dynamics (CFD).

Methods: Transient flow of a simulated blood fluid (SBF) was analyzed within a CFD representation of a physical flow phantom. The mixing of injected contrast agent with SBF was qualitatively and quantitatively evaluated. Using CFD modeling techniques, the differential flow across permeable compartments was evaluated using a porous geometry and porous jump model. A correlation was generated to create a predictive model, which could be used to determine the achievable differential flows across the porous scaffold architecture given a known intrinsic permeability. Quantitative comparisons were made between the experimentally and computationally measured bulk flow changes within the phantom system.

Results: The performed simulations demonstrated the importance of an inline mixer that produced an increase in fluid homogeneity within the phantom system. The CFD simulations closely matched experimental differential flow results and provided a prediction model to determine the intrinsic permeability of porous media needed to increase the resolution of differential flow changes achievable within the system. Simulation results were within the error margins of reported experimental results for high (-73% to -77%) and low (-21% to -25%) differential flows for the low and high permeability scaffold compartment models, respectively..

Conclusions: CFD can be used to assess changes in bulk flow across scaffold compartments with controlled architecture that exhibit disparate differential flow changes within a physical, dynamic imaging phantom.

## 4.1 INTRODUCTION

Dynamic contrast enhanced (DCE) imaging is currently under investigation as an imaging biomarker indicative of tumor aggressiveness, and tissue response to treatments, such as focal irradiation [1-4]. The imaging technique involves the acquisition of a time series of single slice images after the injection of a contrast agent (CA) into a patient. The presence of CA allows for the temporal and spatial localization of blood in the volume of interest (VOI). Each voxel within the VOI of the acquired image series is analyzed to extract bulk properties of tissue perfusion (regional blood supply to tissue). The perfusion estimates provide metrics that can be used to directly track and potentially predict disease progression [5-7]. Across imaging systems and institutions, the implementation of a physical, dynamic phantom capable of validating DCE-extracted measurements can support imaging biomarker-based clinical decisions [8-9]. Unfortunately, DCE imaging validation studies have evaluated various blood flow metrics, in different tissue types, both in human and animal experiments, thus making comparisons difficult [9-16].

Using the analysis of time-contrast concentration curves generated from dynamic flow phantoms, comparisons can be made on the reliability of various post-processing DCE imaging algorithms across systems. Recently, Driscoll et al. [17] presented a re-usable phantom to measure flow using DCE- Computed Tomography (CT). The DCE- Computed Tomography (CT) single compartment phantom developed by Driscoll et al [17] generated time-attenuation curves (TACs) with tunable peaks and shapes based on arterial input functions (AIF) generated from the flow of blood mimicking fluid (2:3 glycerol-water, 2.5 - 5 ml/s) and iodinated CA (0.27 - 1.5 ml/s). The system was successful in closely matching the shape (in terms of duration and residual enhancement) and peak (in terms of enhancement) of a typical AIF. Driscoll et al. cited that the possible non-uniform dispersion of CA and heterogeneous mixing of SBF may have caused variability in experimental results across the phantom, in terms of the CA retention half-life and the peak intensity and shape of generated curves over repeated experiments.

Thomas et al. developed a phantom with anatomically relevant features that achieved bulk flow characteristics below the resolution of a standard clinical CT scanner [18]. The vascular phantom consisted of a vascular tree (diameter of small arteries) that perfused four porous compartments and then mirrored a vascular tree on the venous (diameter of small veins) end of the system. Reported experimental measurements of flow across the porous compartments created differential flow (DF) rates that exhibited variable flow resistances.  The current study applied CFD to investigate the DF range achievable with the branching network phantom we previously developed, as well as to compare these CFD models with experimental DCE imaging data. The uniformity of flow across the system was qualitatively and quantitatively assessed for system with and without a fluid mixer distal to the inlet of the vascular phantom. CFD simulations were performed to determine the degree of mixing between the SBF and injected iodinated CA. The results provide comparative range of DF values that can be used to evaluate the sensitivity of the device to post-processing techniques used in DCE-CT.

## 4.2  METHODOLOGY

Each cylindrical compartment houses an 11 mm high x 11 mm diameter porous scaffold with 0.5 mm of space before and after the inlets and outlets of the attached vascular tree. The two mirrored trees are adjoined by a threaded compartment holder (11 mm inner diameter) which tightly bounds the scaffold, such that water only passes through the permeable scaffold. The fourth-level of bifurcation in the vascular tree that directly perfuse the compartment are 2 mm in length and 0.79 mm in diameter. Four vascular tree outlets and inlets are adjoined to the compartment (shown in Fig. 4.1a). The vascular phantom incorporates a porous scaffold at the midpoint of the mirrored vascular tree design. The vascular phantom is roughly 12.6 cm long and 5.6 cm in width. Fig. 4.1b-c illustrates the setup of the modeled dynamic phantom. SBF circulated through the system at a pump rate of 50 ml/min. 4cc of CA was injected into the system at rate of 2 cc/s by a standard power injector controlled by the CT scanner. The CA inlet tubing was flushed with 15 cc of SBF at 1cc/s before and after the injection of the bolus. Imaging experiments were conducted at room temperature (20-25˚C).
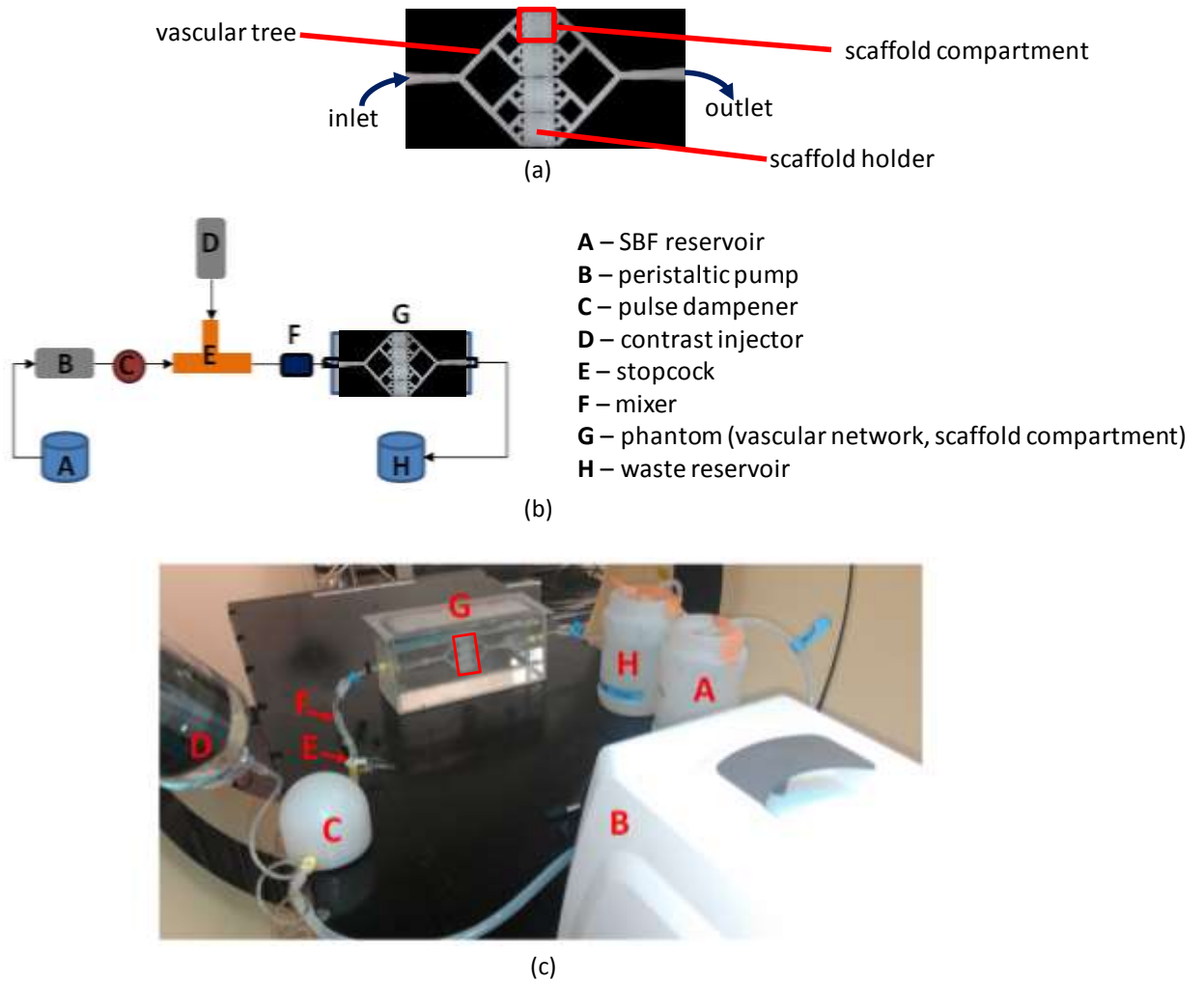
**Figure 4.1 (a) Vascular phantom: "arterial" vascular tree adjoined to four scaffold compartments that connect at their outlet to a "venous" vascular tree. (b) Schematic representation of the assembled single-input single-compartment flow phantom within the closed flow system. (c) Vascular phantom submerged in contrast-enhanced liquid in a bounding acrylic box. Vascular flow phantom adjoined to a closed system via luer lock connectors. Setup is positioned on a CT bed. The red box delineates the scaffold compartment built into the phantom ('G').**

## 4.2.1 Formulation of the CFD Model

The phantom system was evaluated piecewise: vascular tree, scaffold compartment and stopcock (Fig. 4.1). A CFD model was created for the three components. The generated

CFD model used physiologically relevant boundary conditions to simulate experimental and imaging conditions.

### 4.2.1.1  Fluid Junction Model

Iodinated CA (iopamidol, Isovue-300, Bristol-Myers Squibb, Princeton, NJ) and simulated blood fluid (SBF) combined at the three-way stopcock junction in the phantom system. SBF was pumped through three-sixteenth-inch (inner diameter) plastic tubing and CA was injected into the system through one-eighth-inch (inner diameter) plastic tubing. The respective tubes were fixed to a standard T-shaped medical stopcock via luer lock connectors. A 1.45-inch-inline static mixer was positioned downstream (one inch) of the stopcock. The inline mixer was designed in a computer-aided design (CAD) software program (SolidWorks, Waltham, MA) with five to six helical-like elements that created turbulence in order to enhance fluid mixing. Fig 4.2. illustrates the design of the stopcock connected to the mixer.

(a)

(b)
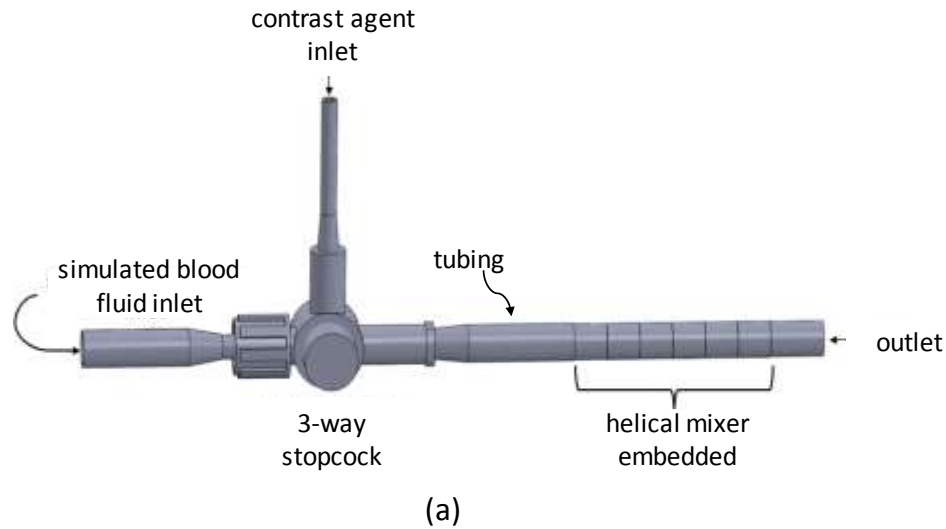
**Figure 4.2 CAD of T-junction that funnels CA and SBF into a single entry pathway towards vascular phantom. CAD of the inverse of the T-junction with inline fluid mixer positioned downstream of the T-junction outlet. (b) Single unit of the helical mixer (complete mixer composed of 6 repeating units).**

### 4.2.1.2 Vascular Tree Model

The vascular tree component of the phantom was composed of rigid, hollow, symmetrical cylinders with a 0.6 mm wall thickness. Each parent branch gave rise to two offspring branches. The vascular tree was designed to adhere to the following principles: (1) Murray's law (bifurcation rule) given in Eq. 4.1, where $r$ is the radius of the vessel and $r > 0$ [19]; (2) the conservation of mass provided in Eq. 4.2, where $Q$ is the volumetric flow rate; and (3) Poiseuille's law in Eq. 4.3 [20], which considers blood to be an incompressible homogenous Newtonian fluid exhibiting laminar flow within small

arteries and veins. In Eq. 4.3, $\Delta P$ is the pressure drop across the cylinder, $l$ is the length of cylinder and $\mu$ is the fluid's dynamic viscosity;

$$r_{parent}^3 = r_{offspring\_left}^3 + r_{offspring\_right}^3 \qquad \text{Equation 4.1}$$

$$Q_{parent} = Q_{offspring\_left} + Q_{offpsring\_right} \qquad \text{Equation 4.2}$$

$$\Delta P = Q * \frac{8*\mu*l}{\pi*r^4}, \qquad \text{Equation 4.3}$$

Selective laser sintering was used to generate the designed vascular tree. The rapid prototyping method accepts stereolithography (STL) files, which store a triangulated surface mesh rendering of the designed part. The STL file was reverse engineered using a meshing software tool (3-matic™, Materialise, Belgium) to generate Initial Graphics Exchange Specification (IGES) files for CFD simulations (Fig. 4.3). The surface mesh of the tree was coarsened to balance the geometry accuracy and the amount of computational resources needed to reverse engineer the component. The surface mesh was modified to rectify bad edges, holes, shells, inverted normal, and intersecting and overlapping triangles.
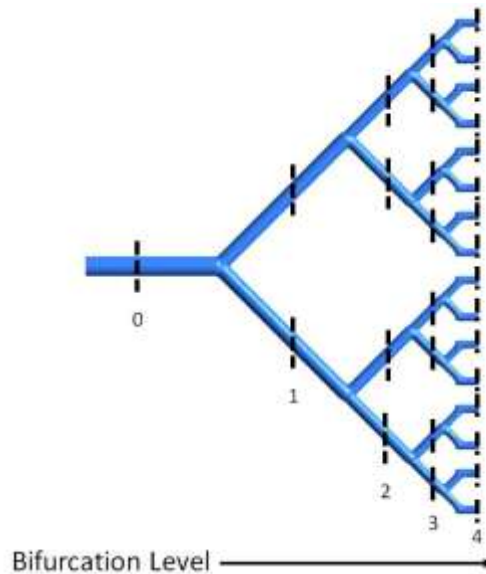


Bifurcation Level ⟶

**Figure 4.3 Side view of CAD of fluid domain enclosed within vascular tree. Tree decreases in diameter over four levels of bifurcation, from one 2.2 mm inlet to sixteen 0.79 mm outlets that perfused 4 cylindrical compartments. Vertical black lines indicate cross-sectional planes where the mass flow was evaluated.**

*4.2.1.3 Modeling of Scaffold Compartment*

A CAD model of a single compartment within the imaging phantom (Fig. 4.4) was designed in SolidWorks (Waltham, MA), then meshed and analyzed in a CFD simulation platform (ANSYS Workbench and Fluent, Canonsburg, PA). Two compartment models were evaluated through CFD simulations. The first model recreated the geometry of a single spherical pore scaffold within the compartment space of a vascular tree (Fig. 4.4) in order to the fluid behavior of the porous scaffolds. The inlet and outlet geometry of the vascular tree, along with that of the scaffold were replicated in Solidworks. Two porous compartments were generated to represent two distinct permeability values that were previously experimentally evaluated with DCE CT imaging. A 2.15 mm and 2.2 mm spherical pore diameter was repeated every 2 mm to fill a cylindrical porous zone within the compartment to generate a low ($6.3 \times 10^{-7}$ m$^2$) and high ($7.5 \times 10^{-6}$ m$^2$) relative intrinsic permeability scaffold, respectively (as discussed in Chapter 2 [18]). The porous zone was 11 mm in height and diameter. The four inlets had a diameter of 0.79 mm and length of 2 mm.



(a)                                    (b)                                    (c)
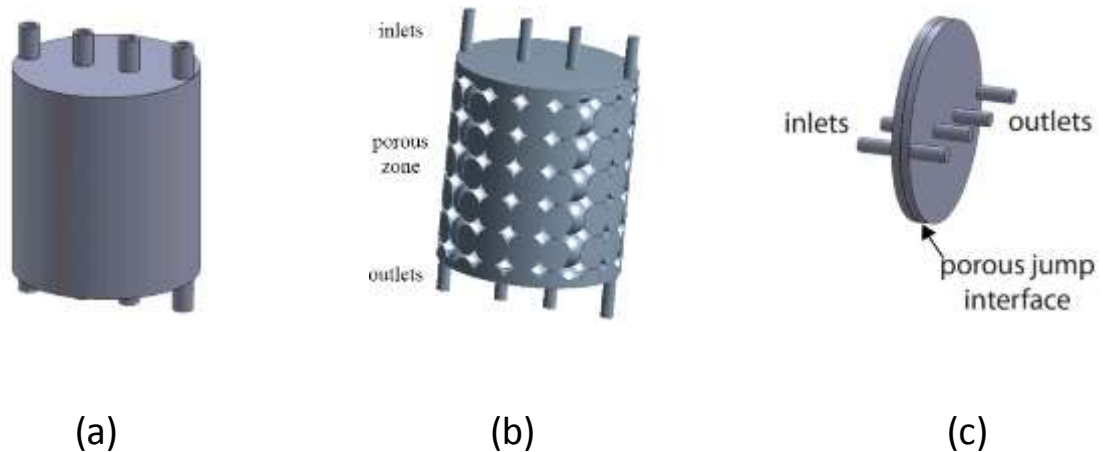
**Figure 4.4 Side view of CAD of (a) a scaffold enclosed in a single compartment in bioreactor and (b) the inverse geometry of (a) representing the fluid volume in Fluent. Representative volume (11 mm height and diameter) shown for spherical pore geometry. (c) Side view of CAD of the porous jump model representing the fluid volume within a single compartment (11 mm diameter) of the imaging phantom.**

In the second model, a porous jump interface provided a two-dimensional simplification of the prior model. The porous jump interface was defined as the face at the center of the compartment, midway between the inlets and outlets (Fig. 4.4c). The four inlets had a diameter of 0.79 mm and length of 2 mm.

This simplified porous model solved the porous jump Eq. 4.4 (Darcy-Forchheimer equation) to determine the resistance to be added to the flow through the volume, based on the boundary conditions set for the face (intrinsic) permeability ($m^2$) ($\alpha$), medium thickness (meters) ($\Delta m$) and pressure jump coefficient ($C_2$).

$$\Delta p = - \left( \frac{\mu}{\alpha} v + C_2 \frac{1}{2} \rho v^2 \right) \Delta m ,$$   Equation 4.4

where $\mu$ is the viscosity, $v$ is the velocity normal to the porous face, $\rho$ is the density and $\Delta p$ is the pressure drop. The pressure jump coefficient was set to zero (negligible) since in the case of laminar flow through a porous media, the pressure drop is proportional to velocity. Based on the dimensions of the scaffold, the medium thickness was set to 0.011 meters. The simplified model evaluated the DF values achievable over a range of intrinsic permeability values. The selected intrinsic permeability values represented the range of low to high permeability values realizable in physical fabrications of the porous compartments. The intrinsic permeability ($k_i$) was calculated as the product of the measured hydraulic permeability and the estimated constant viscosity of the fluid.

### 4.2.1.4 Biofluid Characterization

Simulations were performed using the viscosity of a non-Newtonian mixture of 35% water, 65% glycerin and 0.0075% Xanthan gum (by weight) [21]. The dynamic viscosity of five SBFs was acquired using a rheometer (AR1000 Rheometer, TA Instruments, New Castle, DE) at 25°C for shear rates ranging between 0.02 to 1500 $s^{-1}$. The viscosity

measurements were used to model the non-Newtonian SBF as a Carreau fluid. The shear rate dependence of viscosity was described by the Carreau-Yasuda Eq. 4.5 [22], where a = dimensionless constant, $\mu$ = apparent dynamic viscosity, $\mu_\infty$ = infinite shear rate viscosity, $\mu_0$ = zero shear rate viscosity, $\lambda$ = time constant, $\dot{\gamma}$ = shear rate and n = power index:

$$\mu = \mu_\infty + (\mu_0 - \mu_\infty)[1 + (\lambda\dot{\gamma})^a]^{\frac{n-1}{a}}$$

Equation 4.5

A non-linear least-squares curve fitting was used to fit the experimental SBF viscosity data to the Carreau model, using Microsoft Excel Solver. The solver minimized the sum of the squares of the deviations between the actual viscosity data and the predicted values of viscosity. The model parameters served as input to the CFD model along with the manufacturer reported viscosity and density values for the CA, which were 4.7 cP and 1.369 g/ml at 37ºC, respectively.

### 4.2.1.5 Meshing and Boundary Conditions

Each model was meshed with tetrahedral elements using a patch conforming method. Inflation layers were added to the inlet, fluid volume (porous area and static mixer) and outlet boundaries. For each inlet, a mass flow rate (kg/s) was set along the primary direction of flow, y-direction relative to the orientation of model in the CFD software (Fluent, Waltham, MA). An in-house flow meter system was used to measure the flow rate of SBF at the outlet of the tubing that connected to the stopcock. The mass flow rate at the inlet boundary of the simulation was set to 0.0014 ± 0.0001 kg/s based on the acquired flow meter measurement. The mass flow of the CA was set to 0.0028 kg/s. For SBF flushes through the CA inlet, the mass flow was set to 0.0014 kg/s. Each outlet was set to a pressure outlet (1 atm) boundary condition. The outflow boundary condition assumes a zero normal gradient for all flow variables except pressure. Since, each porous compartment was close to identical and due to the symmetry of the over vascular phantom design, the no pressure variations between outlets was assumed. No-slip on all internal boundaries and solid walls were imposed. For the vascular tree and porous

compartments, mesh independence tests were performed to ensure that the number of meshing elements reduced the sensitivity to less than 5% (Appendix D.1).

The fluid entering the network and compartment were modeled as incompressible, isothermal and laminar (see Table 4.1). Laminar flow at the inlets was confirmed by computation of the Reynolds number, Re, which for values less than 2300 indicate laminar flow. The Reynolds number was calculated using the following Eq. 4.6, where $\rho$ is the SBF density (kg/m$^3$), Q is the volumetric flow rate (m$^3$/s), $D_h$ is the hydraulic diameter (m) and $\mu$ is the dynamic viscosity (Pa·s) of the SBF [23]:

$$Re= \frac{\rho Q D_h}{\mu A}$$

Equation 4.6

**Table 4.1 Flow conditions required to satisfy laminar flow within the phantom, based on a 50 ml/min SBF pump flow rate at the inlet of the system.**

| Component | Inlet Diameter (mm) | Reynolds Number |
|---|---|---|
| Stopcock – SBF inlet | 3.2 | 153 |
| Stopcock – CA inlet | 3.0 | 55 (126*) |
| "Arterial" Vascular Tree | 2.20 | 395 - 576 |
| Compartment | 0.79 | 102 |

\* SBF flush precedes and follows CA injection through the CA inlet.

### 4.2.2 CFD Flow Simulations

Simulations were carried out with a two-phase mixture model (for stopcock and porous compartment) and single-phase model (for vascular tree and porous jump compartment model) in commercial CFD packages (version 14.0, ANSYS Fluent). The vascular tree and porous compartment were assumed to be rigid solid objects, receiving constant, non-pulsatile flow. The governing equations were conservation of momentum and continuity (incompressible flow):

106

$$\rho(\frac{\partial\vec{v}}{\partial t} + \vec{v} \cdot \nabla\vec{v}) = -\nabla p + \mu\nabla^2 v + \rho g \text{ (momentum)} \qquad \text{Equation 4.7}$$

$$\nabla \cdot \vec{v} = 0 \text{ (continuity)}, \qquad \text{Equation 4.8}$$

where $\rho$ is the fluid density (kg/m$^3$), $v$ is the fluid velocity vector, $p$ is the pressure (Pa), $g$ is acceleration due to gravity (m/s$^2$) [24] and $\mu$ is the rate dependent dynamic viscosity defined by the Carreau model (Eq. 4.5). A pressure-based solver, and laminar flow model, under the assumption of shear-dependent viscosity and constant density was used. In Fluent, the velocity-pressure corrections were calculated using the SIMPLEC (Semi-Implicit Method for Pressure Linked Equations - Consistent) algorithm [25]. A least squares cell based gradient algorithm and standard pressure algorithm were used in for spatial discretization. To reduce numerical diffusion, a second order upwind was performed. The tolerance of (spatial) convergence for the continuity, x-velocity and y-velocity were set to 1 x 10$^{-3}$ for the porous jump model and 1 x 10$^{-6}$ for all models. A ±5% sensitivity level was acceptable for the spatial mesh independence (Appendix D.1). In the in commercial CFD code, a two-phase, liquid-liquid, mixture model for miscible fluids was implemented under a transient flow field. The transient model was based on an Euler-Euler approach (Volume of Fluid model), wherein the model assumes the separated heterogeneous flow and solves momentum equations for the mixture. The segregated solver was used to solve the governing equations. The second-order upwind scheme was used as the discretization scheme in the governing equations. The SIMPLE (Semi-Implicit Method for Pressure Linked Equations) algorithm [26] was used to resolve the velocity-pressure coupling used for the transient calculations for the under-relaxation factor of 1 (momentum and pressure combined). A second order upwind method was applied to the transient simulations. A time step was set to 1. The tolerances of (temporal) convergence for the continuity, x-velocity and y-velocity were set to 1 x 10$^{-3}$. Appendix D.1 provides the user defined functions used to set the boundary conditions during the transient analysis.

### 4.2.3 Assessment of Changes in Bulk Flow within the Phantom

A simulation study was performed on the efficiency of passive mixing of CA and SBF downstream of the T-junction. Streamline data was collected for two-phase flow introduced through the two inlets of the system. The distributions of CA and SBF before and after the static mixer were assessed to determine the overall mixer performance. The input mass flow to the vascular tree was set to the value of outlet mass flow rate from the T-junction. The mass flow rate at the outlets, after the fourth-level of bifurcation were measured and used as the inlet mass flow rate in compartment simulations. In addition, the uniformity of flow across the scaffold compartments was evaluated, as these changes affect intensity values analyzed during image post-processing. Flow parallel (profile near center, and right and left offset from center) and perpendicular (top, middle and bottom profile) to the direction of flow across the porous compartment was qualitatively assessed via visual inspection to identify hot spots (velocities more than two standard deviations greater than the average velocity across the 6 planes) and dead zones (velocities more than two standard deviations less than the average velocity across the 6 planes) within the compartment. The mass flow rate across the network was measured to determine the DF across the scaffold (see Fig. 4.2) and to compare flow rates against theoretical flow rates predicted by Eq. 4.2. Two planes were drawn perpendicular to the direction of flow in the porous and scaffold geometry models. For the porous geometry model, the top and bottom planes were slightly offset inward of the boundary edges (perpendicular to the direction of flow) of the porous scaffold within the compartment. For the porous jump model, the top and bottom planes were slightly offset outward of the jump interface (Fig. 4.4c) (perpendicular to the direction of flow). The mass flow rate was calculated across the plane to attain CFD-based DF values. The DF (%) across the scaffold compartment was calculated by the following Eq. 4.9

$$DF = \frac{MF_f - MF_i}{MF_i} \times 100,$$

Equation 4.9

where $MF_i$ is the mass flow rate across plane 1 (g/s) and $MF_f$ was the mass flow rate across plane 2 (g/s).

The CFD-calculated DF values were compared to the experimentally measured values for spherical pore scaffolds previously reported [18]. The DF values calculated from the scaffold geometry models were compared to values from the porous jump model for SBF, to assess the closeness of the models' results. Based on simulations with the mixture of SBF and CA as the fluid, the DF values were calculated and compared to DF values calculated for SBF only, in order to determine the influence of CA.

### 4.2.3.1 Accuracy of Experimental Hydraulic Permeability Measurement

To evaluate the accuracy of the experimentally measured hydraulic permeability values, a benchmark comparison of the permeability output provided by the custom-designed flow meter was performed against another system previously published on by Sanz-Herrera et al. [27]. Sanz-Herrera et al. reported permeability values for Sponceram® carriers (Zellwerk, Oberkraemer, Germany) based on their in-house, Darcy-based permeability chamber (listed in Table 4.3). Their experimental permeability values were confirmed by homogenization theory-based numerical results. Three Sponceram® (30-90)/Hydroxyapatite (HA) discs were acquired from Zellwerk. The discs were porous, zirconium dioxide based ceramic scaffolds. The height and diameter of each disc was measured to estimate the average dimensions of the samples. Micro-CT scans of each scaffold were acquired and processed using MicroView to calculate each specimen's porosity. An average porosity was calculated for each scaffold type. The hydraulic permeability of the each scaffold was measured by water perfusion within the flow meter system [28]. To position the discs in the chamber, plastic tubes were custom-made (Objet Connex 500 using Accura® 60 plastic) to tightly fit the scaffold diameters. Each disc was run five times through the permeability chamber. Statistical values of the intrinsic permeability in terms of the mean value and standard deviation were calculated.

*4.2.3.2 Statistical Analysis*

A two-tail one-sample t-test was performed to determine whether there was a significant difference between the expected and observed DF values. The expected values were those computationally derived. The representative DCE imaging data served as the observed value. Statistical significance was defined as a P-value of less than 0.05.

## 4.3 RESULTS

The SBF rheology exhibited non-Newtonian, shear thinning characteristics. The shear stress increased and viscosity decreases, with increasing shear rate. The fitted data was compared to widely-accepted blood viscosity curves (Fig. 4.5a). The Carreau model coefficients, which provided the best fit were n = 0.23, a = 2, $\mu_0$ = 0.076 kg/m·s, $\mu_\infty$ = 0.004 kg/m·s and $\lambda$ = 22.06 seconds. The SBF viscosity was Newtonian for shear rate values greater than 100 $s^{-1}$ (Fig. 4.5b). For large shear rates values the dynamic viscosity was 3.64 x $10^{-3}$ ± 3.0 x $10^{-3}$ kg/m·s. The fluid density was 1080 ± 10 $kg/m^3$.
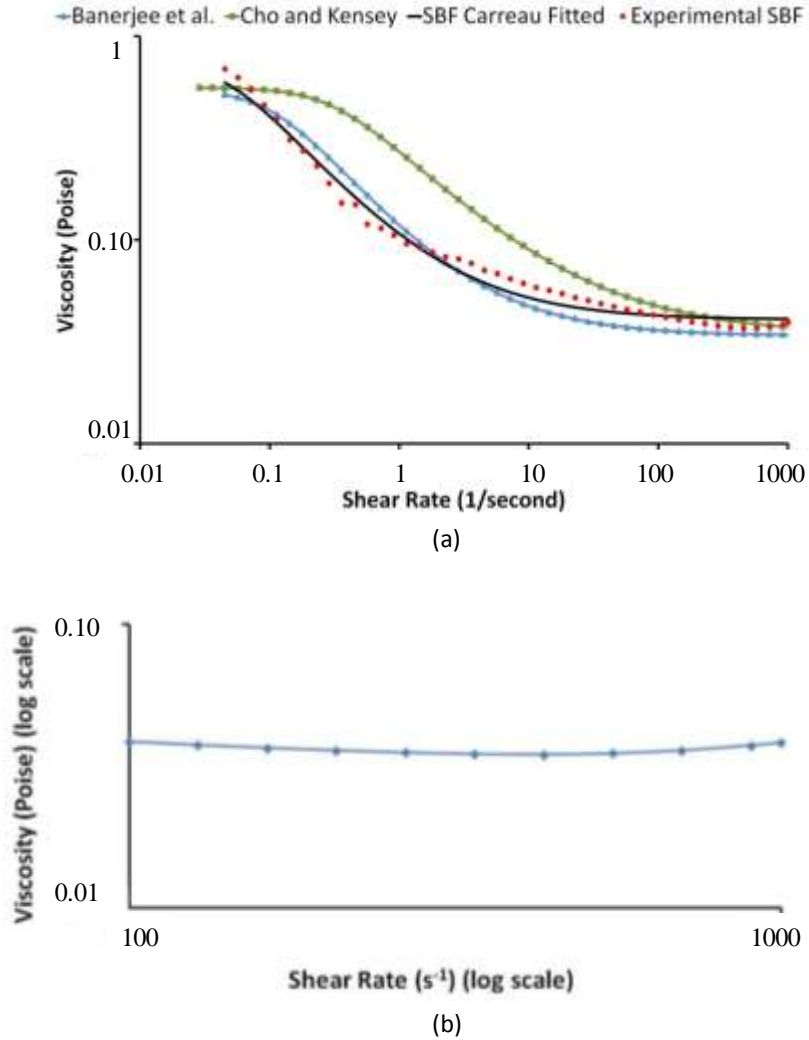
**Figure 4.5 (a) The SBF mixture was fitted by nonlinear least squares to Carreau model and compared to published findings for a similar SBF [29] and human blood fluid [30]. (b) Log-log scale plot of the SBF flow behavior for shear rates greater than 100 s-1 illustrate an approximately constant viscosity.**

Fig. 4.6 illustrates the path of the fluids through the stopcock then mixer 1 second after the bolus enters the system. The yellow and blue streamlines in Fig. 4.6 are intertwined proximal to the outlet. The discharge mass flow rate from the T-junction/mixer increased from 0.00248 kg/s to 0.00362 kg/s, with the addition of the bolus into system. As the fluid entered the "arterial" vascular tree the mass flow rate decreased after each level of bifurcation, closely matching theoretical estimations that were based on the conservation of mass (Eq. 4.2). At all levels of bifurcation the standard deviation for the mass flow rate

across offspring vessels within the same level is approximately ±0.01 g/s. The percent difference in mass flow across all bifurcations is less than 3%.
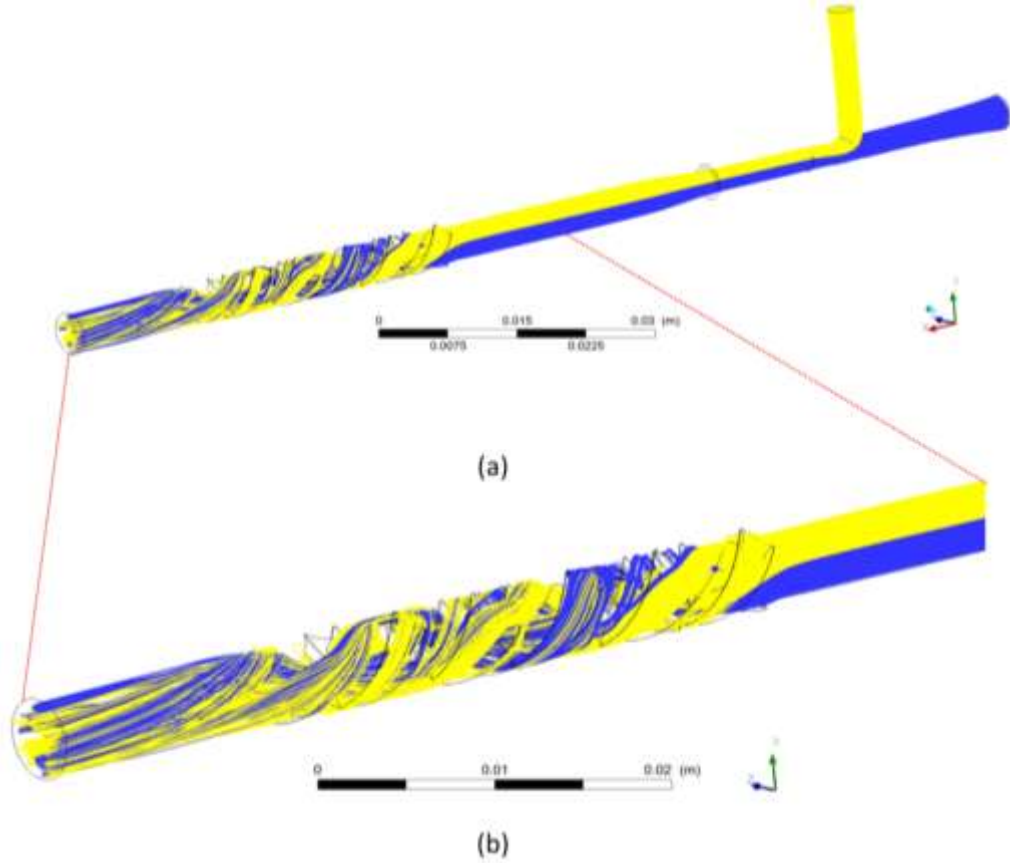


**Figure 4.6 (a) Flow conditions within the T-junction/mixer model, where the mass flow rate from the contrast injector is 0.00273 kg/s for CA and fluid from the peristaltic pump delivers a continuous stream SBF at 0.0014 kg/s. The blue and yellow streamlines show velocity trajectories for the SBF and CA, respectively.  (b) Zoomed in view of the streamlines within the mixer. (Black wireframe outlines geometry.)**

**Table 4.2 Decrease in the average mass flow across the levels of bifurcation. The computational values closely match the expected theoretical values.**

| Bifurcation | Theoretical Mass Flow | CFD-measured Mass | Difference |
|---|---|---|---|

| Level | (g/s) | Flow (g/s) | (%) |
|-------|-------|------------|-----|
| 0 | 3.62 | 3.59 | -0.7 |
| 1 | 1.81 | 1.79 | -0.9 |
| 2 | 0.91 | 0.89 | -2 |
| 3 | 0.45 | 0.44 | -3 |
| 4 | 0.23 | 0.23 | 0.003 |

Using the porous jump model, the DF was estimated for the intrinsic permeability values between $3.3 \times 10^{-7}$ m$^2$ and $1 \times 10^{-9}$ m$^2$. Lower intrinsic permeabilities produced increased resistance that resulted in a larger pressure drop across the compartment. Fig. 4.9 shows the DF measured across the porous jump, dependent on the applied intrinsic permeability.
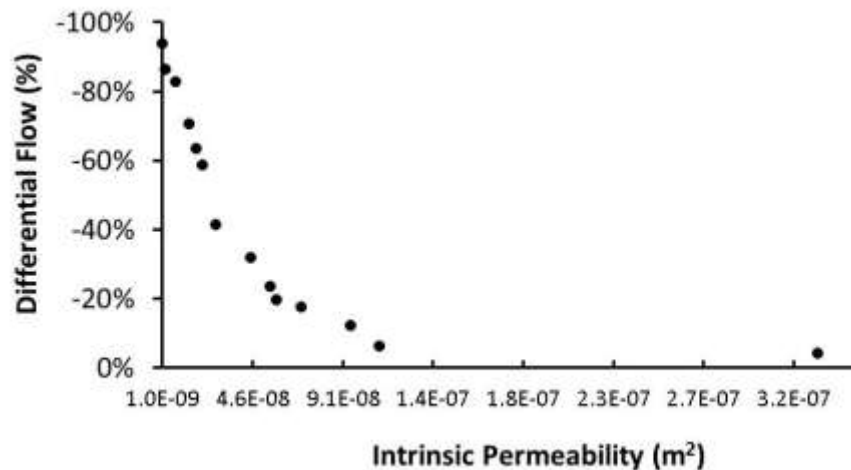


**Figure 4.7 Porous Jump Model. Calculated DF based on the prescribed intrinsic permeability into the porous jump model.**

The measured average porosity, calculated experimental hydraulic permeability and estimated intrinsic permeability of the Sponceram® (30-90)/HA scaffolds are represented in Table 4.3. The measured intrinsic permeability was roughly one order smaller than that

of the published value. Based on these results and those reported Appendix D.2, a correction factor (roughly three times the original value) was applied to the experimental intrinsic permeability. An exponential curve was fitted to the data in Fig. 4.7 (DF = $-0.9e^{-2E+07k}$, where k = intrinsic permeability). The low intrinsic permeability value increased from 2.29 x $10^{-9}$ m$^2$ (hydraulic permeability = 6.3 x $10^{-6}$ N/m·s) to 6.19 x $10^{-9}$ m$^2$ and the high intrinsic permeability value increased from 2.73 x $10^{-8}$ m$^2$ (hydraulic permeability = 7.5 x $10^{-6}$ N/m·s) to 7.37 x $10^{-8}$ m$^2$. The porous jump-derived DFs for the low and high permeability compartments were -89% and -54%, respectively. Based on the porous jump model, the corrected intrinsic permeability generated DFs of -82% and -21%, for the low and high permeability scaffolds, respectively.

**Table 4.3 The benchmark experimentally measured permeability values (mean value ± standard deviation) for Sponceram®(30-90)/HA scaffolds [27] are compared to in-house experimental measurements.**

|  | In-house (n=3) | Published (n=5) |
| --- | --- | --- |
| Porosity (%) | 78.8 ± 1.2 | 79.81 ± 2.18 |
| Experimental Permeability (m$^4$/N·s) | 1.7 x $10^{-6}$ ± 6.0 x $10^{-7}$ | — |
| Intrinsic Permeability (m$^2$) | 1.7 x $10^{-9}$ ± 5.7 x $10^{-10}$ | 1.79 x $10^{-8}$ ± 4.09 x $10^{-9}$ |

The computational estimations of the DF across the low and high permeability compartments from the porous geometry model were -77% and -21%, respectively. Fig. 4.8 compares the experimental results from Chapter 3 to the porous geometry simulation measurements. The porous geometry and porous jump-corrected DF measurements were not significantly different from the experimental measurements ($p > 0.05$). The porous jump-corrected DF was slightly greater than the porous geometry DF for the high permeability scaffold, but fell within the range of experimental measured values.
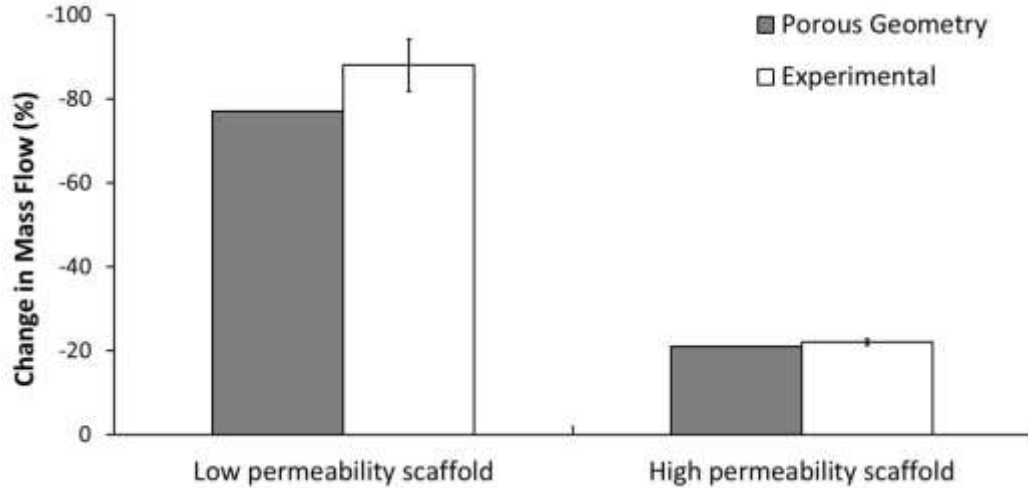
**Figure 4.8 Comparison of measured DF between experimental and computational (porous geometry). There was no statistical difference (p > 0.05) between the simulation and experiment measurements.**

For the high permeability compartment, the average velocity was 0.067 m/s ± 0.033 m/s, with hot zones occurring for velocities greater than 0.098 m/s and dead zones for velocities less than 0.035 m/s. The contour maps in Fig. 4.9a illustrate the range of velocities across the high permeability compartment for the transverse and longitudinal planes. Fig 4.9b shows the velocity contour maps for the low permeability compartment. In the low permeability compartment, the average velocity was 0.015 m/s ± 0.007 m/s, with hot zones occurring for velocities greater than 0.022 m/s and dead zones for velocities less than 0.008 m/s. In Fig. 4.9a-b, the maximum velocity was set to the represent hot zones and the minimum velocity to dead zones. The four-inlet designed fully perfused both compartments. Zero velocities only occurred at the walls of the design. For the high permeability compartment, along the transverse and longitudinal planes the center of the pore (cylindrical core) received the greatest velocities. While for the low permeability compartment, a larger fraction of the pore was perfused at a high velocity along the transverse plane. Along the longitudinal planes, the lowest velocities were experience at the middle of the compartment. For both compartments, non-spherical pores (quarter or half of a pore) at the edges of the cylindrical compartment received the little to no fluid infiltration.
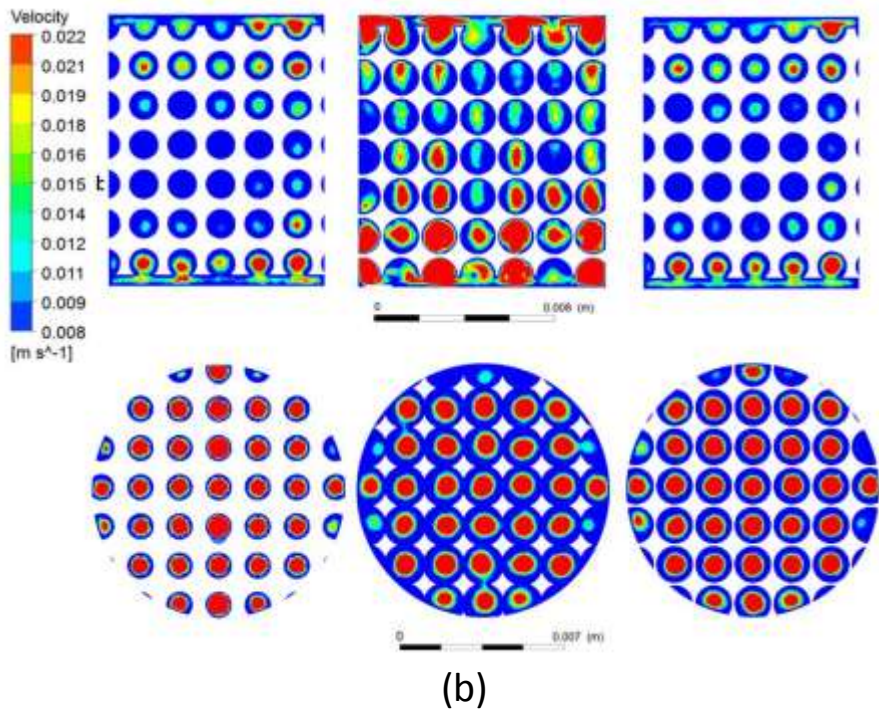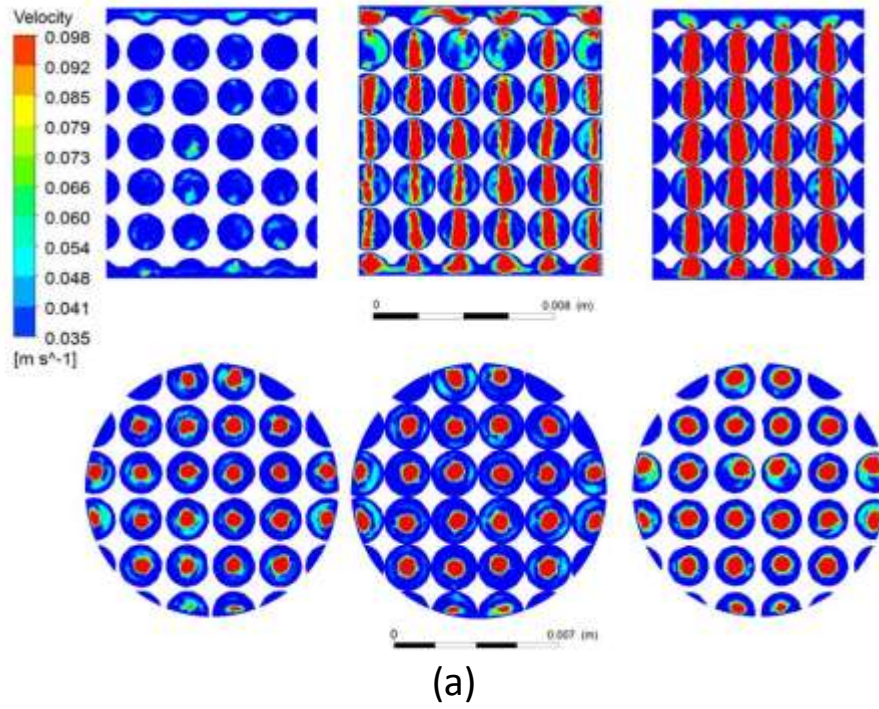
**Figure 4.9 Contour map illustrates velocity profile across** (a) **high permeability and** (b) **low permeability compartment along the longitudinal (***top row, from left to right:*** left offset, near center and right offset) and transverse planes (***bottom row, from left to right:*** top, middle and bottom).**

**4.4 DISCUSSION**

The implementation of the proposed dynamic flow phantom into routine quality assurance of clinical CT systems can provide hemodynamic behavior across bifurcating, arterial-like, vessel structures with differential flow across scaffold compartments. Experimental and computational characterization of the physical system is important to realize the benefits of a physical, dynamic quality assurance tool in the clinic or as a research tool. CFD uses numerical methods to solve fluid mechanics equations and analyze fluid flow through a construct. This paper used the CFD software FLUENT to assess flow conditions of the bifurcating tree and porous media flow within the phantom system illustrated in Fig. 4.1. The system was evaluated piecewise — T-junction/mixer, "arterial" vascular tree and porous compartment — in order to customize the mesh for each complex geometry and to reduce the computational cost of the simulations. The mesh quality was optimized to maintain the contours of the original volume geometry, to have sufficient element quality (specifically, in terms of skewness) and to balance the number and size of elements in order to be computational feasible (balancing accuracy and convergence). Appendix D.1 provides the mesh independence data for each model.

CFD is often used to examine wall shear stress, pressure and velocity profiles within arteries and porous media [31-36]. Computational evaluation of the physical phantom investigated in Chapter 3 [18] can support the previously reported experimental data, as well as address phantom design or setup concerns, such as signal enhancement variations caused by inadequate mixing/dispersion of the bolus. As such, both the fluid and geometry of the phantom were modeled. The aggregation of red blood cells along the center axes of small blood vessels in vessels of decreasing diameter (less than 800 μm) cause blood to exhibit non-Newtonian behavior due to the shear-dependent (less than 100/s) changes in viscosity [37-41]. The SBF composed of 65% glycerine and 0.0075% Xanthan gum at 25˚C achieved the viscous properties of human blood and demonstrated shear-thinning, non-Newtonian behavior that was fit to the Carreau model (Fig. 4.5). The determination of an appropriate SBF at 25˚C eliminated the need for temperature regulation of the phantom device, beyond the controls of the imaging room. The warmed CA that was introduced to the system had a density and viscosity similar to that of human blood. *In vivo*, the iso-osmolality of CA compared to plasma reduces the potential for the

increased disaggregation of red blood cells with increasing concentration of contrast medium [42-43]. Thus, the resultant viscosity of the combined solution is assumed to not be affected by mixing in CA. As such, models downstream of the contrast injection assume the viscosity and density of the SBF.

It was important integrate a mixer into flow phantoms in order to provide adequate mixing, similar to the diffusion that occurs *in vivo*, downstream of the CA injection site. Non-homogenous mixing can lead to variability in the extracted flow rates. Table 4.1 demonstrates that the CA and SBF flow conditions entering the stopcock/mixer (shown in Fig. 4.2) were laminar. Fig. 4.6 illustrates that the CA and SBF fluid layers were stratified prior to entry into the helical mixer. The stream path after the mixer demonstrated increased mixing of the fluids, with a reduced layering effect.

DCE post-processing techniques delineate the high intensity voxels within VOIs located in the input arterial structure (aorta or major artery) and parenchyma of interest, in order to extract signals used to estimate blood flow rates. As such, the flow in the "arterial" vascular tree (Fig. 4.3) and discharge flow within the porous compartments (Fig. 4.4a-b) were qualitatively and quantitatively evaluated. Given the maximum output flow rate from the mixer, simulations of the vascular tree (Fig. 4.3) demonstrated that the flow rate decreased across the bifurcation levels (Table 4.2), as expected, closely matching theoretical predictions (less than 2% difference). A uniform distribution of fluid entered the porous compartments. The velocities exhibited at the inlet ($1.5 \times 10^{-3}$ m/s) and outlet ($3 \times 10^{-4}$ m/s) of the vascular tree fall in the range found *in vivo,* within small human arteries and arterioles, respectively [44].

The flow resistance experienced within the compartment was characterized using the intrinsic permeability of the porous scaffold. A porous jump model (Fig. 4.4c) was used to simulate flow at intrinsic permeability within a reasonable range attainable using scaffolds (i.e. selective laser sintering and solvent casting/salt leaching). Fig. 4.7 shows the exponential relationship between measured DF and prescribed intrinsic permeability. Compared to the published permeability values for Sponceram® scaffolds, the designed in-house permeability measurement system was determined to underestimate the permeability of measured samples (Table 4.3). Based on the observed underestimation of

118

permeability by the in-house permeability setup, additional studies carried out to understand the influence of the Reynolds number and fluid viscosity on the measured hydraulic permeability for different scaffold geometries (see Appendix D.2). A correction factor was applied to the intrinsic permeabilities to estimate the DF.

The results of the computational simulations, demonstrated that flow rate in the porous compartments decreased as the SBF moved across the scaffold compartments. These changes in DF mimicked the decrease in blood flow associated with the pressure drop exhibited *in vivo* as blood flows from arterioles down to capillaries. For the low permeability compartment, the DF was less than that of the high permeability compartment, likely due to the increased tortuosity in the pore architecture. Fig. 4.8 showed that the simulation measurements for the porous geometry and porous jump-geometry closely matched ($\pm$ 5%), for the estimated correction factor (given the viscosity-dependent variability of the experimentally measured hydraulic permeability). The experimental results were not significantly different from the either of CFD models.

By visual inspection, the flow across both compartments' transverse planes was determined to be uniform based on the symmetry of the contour shown in Fig. 4.9a-b. Similarly, the flow across the longitudinal plane of the high permeability compartment was uniform, with the greatest flow rates occurring at the center of the spherical pore. However, for low permeability scaffolds, the longitudinal planes showed non-uniform flows, where the highest flow rates were experienced closer to the edges of the compartment.

An improvement to the physical phantom and simulations would give the SBF a physiological flow waveform. As well, the simulation assumed that the vessel walls were motionless, due to the rigidity of the polymer used to manufacture the physical phantom. However, small arteries are elastic and small veins are highly compliant, with the visco-elastic properties of their walls modulated by oscillatory flow. Future generations of the system and an associated CFD model would incorporate a dynamic motion model. Along with these additions, a coefficient of friction can also be incorporated to account for the fluid's interaction with the polymer construct and tubing. This realistic frictional force model would dampen the fluid behavior and increase the complexity of the CFD model

along with the accuracy of results. The porous jump model provides a prediction tool to identify other scaffolding techniques or spherical pore geometries that can generate porous media within the range of -5% to -95%, in order to represent low and high differential flows within the system.

## 4.5 CONCLUSION

New dynamic imaging phantoms seek to maximize the benefits of rapid prototyping techniques to manufacture a validation tool that closely mimics the anatomical features and hemodynamic properties characteristics of distributed blood flow at the organ-level. This chapter demonstrates the use of CFD and experimental data to confirm flow characteristics (rate or differential flow) within a flow phantom that enclosed either low or high permeability compartments. Velocity flow rates from the artery-level down to arteriole-level were mimicked within the dynamic phantom. These results indicate that CFD can be reliably used to design phantoms to better mimic a range of DFs, for further development and testing of dynamic phantom for quality assurance for DCE imaging.

## 4.6 ACKNOWLEDGEMENTS

## 4.7  REFERENCES

[1] Giesel, F L *et al* 2008 Pharmacokinetic analysis of malignant pleural mesothelioma-initial results of tumor microcirculation and its correlation to microvessel density (CD-34) *Acad Radiol* **15** 5 563-70

[2] Rosen, M A and Schnall, M D 2007 Dynamic contrast-enhanced magnetic resonance imaging for assessing tumor vascularity and vascular effects of targeted therapies in renal cell carcinoma *Clin Cancer Res* **13** 2 Pt 2 770s-6s

[3] Van Beers, B E, Leconte, I, Materne, R, Smith, A M, Jamart, J and Horsmans, Y 2001 Hepatic perfusion parameters in chronic liver disease: dynamic CT measurements correlated with disease severity *AJR Am J Roentgenol* **176** 3 667-73

[4] Jiang, H J, Zhang, Z R, Shen, B Z, Wan, Y, Guo, H and Shu, S J 2008 Functional CT for assessment of early vascular physiology in liver tumors *Hepatobiliary Pancreat Dis Int* **7** 5 497-502

[5] Cao, Y, Platt, J F, Francis, I R, Balter, J M, Pan, C, Normolle, D, Ben-Josef, E, Haken, R K and Lawrence, T S 2007 The prediction of radiation-induced liver dysfunction using a local dose and regional venous perfusion model *Med Phys* **34** 2 604-12

[6] Goh, V, Halligan, S, Wellsted, D M and Bartram, C I 2009 Can perfusion CT assessment of primary colorectal adenocarcinoma blood flow at staging predict for subsequent metastatic disease? A pilot study *Eur Radiol.* **19** 1 79-89

[7] Goh, V, Halligan, S, Taylor, S A, Burling, D, Bassett, P and Bartram, C I 2007 Differentiation between diverticulitis and colorectal cancer: quantitative CT perfusion measurements versus morphologic criteria--initial experience *Radiology* **242** 2 456-62

[8] Sheiman, R G and Sitek, A 2008 CT perfusion imaging: know its assumptions and limitations *Radiology* **246** 2 649; author reply 649-50

[9] Padhani, A R and Husband, J E 2001 Dynamic contrast-enhanced MRI studies in oncology with an emphasis on quantification, validation and human studies *Clin Radiol* **56** 8 607-20

[10] Cenic, A, Nabavi, D G, Craen, R A, Gelb, A W and Lee, T Y 2000 A CT method to measure hemodynamics in brain tumors: validation and application of cerebral blood flow maps *AJNR Am J Neuroradiol* **21** 3 462-70

[11] Sanelli, P C, Nicola, G, Tsiouris, A J, Ougorets, I, Knight, C, Frommer, B, Veronelli, S and Zimmerman, R D 2007 Reproducibility of postprocessing of quantitative CT perfusion maps *AJR Am J Roentgenol* **188** 1 213-8

[12] Fiorella, D, Heiserman, J, Prenger, E and Partovi, S 2004 Assessment of the reproducibility of postprocessing dynamic CT perfusion data *AJNR Am J Neuroradiol* **25** 1 97-107

[13] Miles, K A 2003 Perfusion CT for the assessment of tumour vascularity: which protocol?*Br J Radiol* **76 Spec No 1** S36-42

[14] Stewart, E E, Chen, X, Hadway, J and Lee, T Y 2008 Hepatic perfusion in a tumor model using DCE-CT: an accuracy and precision study *Phys Med Biol* **53** 16 4249-67

[15] Purdie, T G, Henderson, E and Lee, T Y 2001 Functional CT imaging of angiogenesis in rabbit VX2 soft-tissue tumour *Phys Med Biol* **46** 12 3161-75

[16] Gillard, J H, Minhas, P S, Hayball, M P, Bearcroft, P W, Antoun, N M, Freer, C E, Mathews, J C, Miles, K A and Pickard, J D 2000 Assessment of quantitative computed tomographic cerebral perfusion imaging with H2(15)O positron emission tomography *Neurol Res* **22** 5 457-64

[17] Driscoll, B, Keller, H and Coolens, C 2011 Development of a dynamic flow imaging phantom for dynamic contrast-enhanced CT *Med Phys* **38** 8 4866-80

[18] Thomas, A, Thiagaraj, A, Hollister, S J and Balter, J M 2013 Development of a Dynamic Vascular Phantom for Quality Assurance of Differential Flow in Quantitative Perfusion Imaging. *J Appl Clin Med Phy* Submitted

[19] Sherman, T F 1981 On connecting large vessels to small. The meaning of Murray's law *J Gen Physiol* **78** 4 431-53

**[20]** Fung, Y C 1997 *Biomechanics : Circulation* (New York: Springer)

**[21]** Brookshier, K A, Tarbell, J M 1993 Evaluation of a transparent blood analog fluid: aqueous xanthan gum/glycerin *Biorheology* **30** 2 107-16

**[22]** Yasuda, K, Armstrong, R C and Cohen, R E 1981 Shear flow properties of concentrated solutions of linear and star branched polystyrenes *Rheol Acta* **20** 2 163-78

**[23]** Nguyen, N Tand Wereley, S T 2002 *Fundamentals and Applications of Microfluidics* (Artech House)

**[24]** Cebeci, T 2005 *Computational Fluid Dynamics for Engineers : From Panel to Navier-Stokes Methods with Computer Programs* (Long Beach, Calif. Berlin: Horizons Pub. Inc. Springer).

**[25]** Van Doormaal, J.P. and G.D. Raithby, 1984 Enhancements of the SIMPLE method for predicting incompressible fluid flows *Numerical Heat Transfer* **7** 147-163

**[26]** Patankar, S. V., and Spalding, D. B., 1972 A Calculation Procedure for Heat, Mass and Momentum Transfer in Three-Dimensional Parabolic Flows *Int. J. Heat Mass Transfer* **15** 1787–1806

**[27]** Sanz-Herrera, J A, Kasper, C, van Griensven, M, Garcia-Aznar, J M, Ochoa, I and Doblare, M 2008 Mechanical and flow characterization of Sponceram carriers: Evaluation by homogenization theory and experimental validation *J Biomed Mater Res B Appl Biomater* **87** 1 42-8

**[28]** Kemppainen, J M and Hollister, S J 2010 Differential effects of designed scaffold permeability on chondrogenesis by chondrocytes and bone marrow stromal cells *Biomaterials* **31** 2 279-87

**[29]** Banerjee, R K, Ashtekar, K D, Helmy, T A, Effat, M A, Back, L H and Khoury, S F 2008 Hemodynamic diagnostics of epicardial coronary stenoses: in-vitro experimental and computational study *Biomed Eng Online* **7** 24

**[30]** Cho, Y I and Kensey, K R 1991 Effects of the non-Newtonian viscosity of blood on flows in a diseased arterial vessel. Part 1: Steady flows *Biorheology* **28** 3-4 241-62

**[31]** Canstein, C, Cachot, P, Faust, A, Stalder, A F, Bock, J, Frydrychowicz, A, Kuffer, J, Hennig, J and Markl, M 2008 3D MR flow analysis in realistic rapid-prototyping model systems of the thoracic aorta: comparison with in vivo data and computational fluid dynamics in identical vessel geometries *Magn Reson Med* **59** 3 535-46

**[32]** Gemci, T, Ponyavin, V, Chen, Y, Chen, H and Collins, R 2008 Computational model of airflow in upper 17 generations of human respiratory tract *J Biomech* **41** 9 2047-54

**[33]** Goubergrits, L, Kertzscher, U, Schoneberg, B, Wellnhofer, E, Petz, C and Hege, H C 2008 CFD analysis in an anatomically realistic coronary artery model based on non-invasive 3D imaging: comparison of magnetic resonance imaging with computed tomography *Int J Cardiovasc Imaging* **24** 4 411-21

**[34]** Milan, J L, Planell, J A and Lacroix, D 2009 Computational modeling of the mechanical environment of osteogenesis within a polylactic acid-calcium phosphate glass scaffold *Biomaterials* **30** 25 4219-26

**[35]** Maes, F, Van Ransbeeck, P, Van Oosterwyck, H and Verdonck, P 2009 Modeling fluid flow through irregular scaffolds for perfusion bioreactors *Biotechnol Bioeng* **103** 3 621-30

**[36]** Shanglong, X, Pingan, D, Youzhuan, X and Yang, Y 2008 Cell distribution in a scaffold with random architectures under the influence of fluid dynamics *J Biomater Appl* **23** 3 229-45

**[37]** Rand, P W, Lacombe, E, Hunt, H E and Austin, W H 1964 Viscosity of Normal Human Blood under Normothermic and Hypothermic Conditions *J Appl Physiol* **19** 117-22

[38] Merrill, E W, Benis, A M, Gilliland, E R, Sherwood, T K and Salzman, E W 1965 Pressure-flow relations of human blood in hollow fibers at low flow rates *J Appl Physiol* **20** 5 954-67

[39] Pedley, T J 1980 *The Fluid Mechanics of Large Blood Vessels* : Cambridge University Press)

[40] Berger, S A, and Jou, L D 2003 Flows in stenotic vessels. *Annual Review of Fluid Mechanics* **32** 1  347

[41] Masako, S and Bingmei, M F 2005 Blood flow and permeability in microvessels *Fluid Dynamics Research* **37** 1-2 82

[42] Aspelin P, Nilsson PE, Schmid-Schönbein H, Schröder S, and Simon, R 1987 Effect of four non-ionic contrast media on red blood cells in vitro. II. Aggregation. *Acta Radiol Suppl* **370** 85-7

[43] Reinhart, W H, Pleisch, B, Harris, L G and Lutolf, M 2005 Influence of contrast media (iopromide, ioxaglate, gadolinium-DOTA) on blood viscosity, erythrocyte morphology and platelet function *Clin Hemorheol Microcirc* **32** 3 227-39

[44] Boron, W F and Boulpaep, E L 2009 *Medical Physiology : A Cellular and Molecular Approach* (Philadelphia, PA: Saunders/Elsevier)

# CHAPTER 5

## Comparative Computational Fluid Dynamics Study of Flow-Induced Shear Stress on Bone Scaffold Designs for a Perfusion Angiogenesis Bioreactor

**Abstract**

Pore geometries for bone scaffolds are optimized to enhance bone tissue in-growth into the scaffold. In this study, the distribution of flow-induced shear stress across large spherical and orthogonal cylindrical pore scaffolds (67 - 68% porosity) was examined using a computational fluid dynamics model. The scaffolds were embedded within a vascular-like perfusion angiogenesis bioreactor to identify the range of inlet velocities that achieved a stimulatory shear stress range between 1 to 10 dynes/cm$^2$. The results of the simulations demonstrate a tradeoff between shear stresses within the target range and at the extremes (less than1 dynes/cm$^2$ and greater than 10 dynes/cm$^2$), in order to achieve flow within the confines of a laminar flow regime. The spherical geometry exhibit greater uniformity of shear stress across the scaffold and realized more than 50% of the large scaffold surface experiencing shear stresses within the desired range. These findings will aid in the development of thick scaffolds for perfusion angiogenesis bioreactors and the determination of optimal bioreactor operating conditions to be used in future *in vitro* angiogenesis co-culture or pre-vascularization implantation studies.

## 5.1 INTRODUCTION

Angiogenesis is critical for tissue viability [1-2] To date, clinically successful tissue replacement therapies have been limited to avascular tissues (the epidermis of skin and nasal septae cartilage [3]) and thin tissues less than 2 mm thick (adipose tissue [4] and smooth muscle [5]). Oxygen diffusion is a limiting factor to cell viability within tissues

126

greater than 2 mm thick, with necrosis normally occurring when oxygen must diffuse over a distance greater than 100 μm [3,6]. Oxygen depletion can occur within hours of implantation, due to inadequate pre-vascularization of the implant and a slow rate of angiogenesisv [7]. Several pre-vascularization strategies have been investigated to expedite angiogenesis [8-20]. Among them, perfusion angiogenesis bioreactors offer a continuous controllable dynamic *in vitro* environment for supporting endothelial cell proliferation and differentiation across engineered porous scaffolds under optimized growth conditions [17, 21-24]. Table E.1 in Appendix E summarizes recently reported studies of angiogenesis within perfusion bioreactors. The optimization of bioreactor parameters is a critical step in the promotion of physiological phenomena (i.e. osteogenesis [25-28], chondrogenesis [29-30] and angiogenesis) that are influenced by varied levels fluid-imposed shear stress (SS).

Co-culture studies of endothelial cells (or their progenitors) with osteoblasts or mesenchymal stem cells have illustrated the potential of the *in vitro* three-dimensional pre-vascularization strategy, as a tool for accelerating vessel in-growth and enhancing osteogenic differentiation during implantation [31-33]. There have been extensive reviews on the design and viability of bone tissue engineering bioreactors [34-36]. Previous analytical and computational studies have demonstrated that the distribution of shear stress (ss) imposed by the flow rate across engineered constructs is dependent on pore geometry (random versus well-defined), pore diameter, anisotropy, permeability, diffusivity and porosity [37-43]. As such, the goal of the study was to quantitatively evaluate the local ss distribution within two distinct engineered constructs with commonly adopted controlled pore geometries (spherical and orthogonal) in bone tissue engineering [44-47]. Williams et al.[44] and Mitsak et al.[46] demonstrated that bone in-growth representative of trabecular bone was evident within 4 weeks of subcutaneous implantation for the examined orthogonal and spherical pore geometries seeded with bone morphogenetic protein-7 (BMP-7) transduced human gingival fibroblasts, respectively.

Mechanical stress is a modulator of cell physiology and morphology [48-50]. The literature demonstrates the role of mechanical stimulus, specifically fluid-imposed SS,

imposed by variable flow rates on EC proliferation and function during angiogenesis, both in two-dimensional and three-dimensional *in vitro* studies [22, 51]. Both high and low ss have implications on EC viability, elongation and alignment [52]. SS values below 1 dyne/cm$^2$ exhibit negligible shear force, comparable to static environments, while high values ranging from 1 to 15 dyne/cm$^2$ have been reported to stimulate EC realignment along the direction of flow and EC proliferation on biocompatible substrates *in vitro* [53-54]. SS from laminar flow above 20 dynes/cm$^2$ and turbulent flow have been shown to alter cell morphology, as well detach cells from the construct [55]. Table E.2 in Appendix E summarizes the effects of ss on ECs and delineates ss levels that have been shown to promote EC growth and/or function.

Existing angiogenesis perfusion bioreactors have primarily supported EC growth on thin hydrogels (1 - 5 mm; collagen or fibrin) (Appendix Table E.1). Predictive ss studies of natural scaffolds or scaffolds with random architectures are limited by the inherent variability of these constructs. Lesman et al. presented computational results on the flow-induced shear rates on vascular cells seeded on porous sponges with 200-600 micron pore diameters [37]. Their computational fluid dynamic (CFD) model assumed a 500 micron diameter across the sponge scaffold for a given thickness of 1.2 mm. The transition to thick scaffolds for larger defect sites requires the consideration of uniform perfusion in order to avoid necrosis at the core of the scaffold. Koch et al. and Arano et al. have presented bioreactor studies that employed larger scaffolds for thick tissue generation [56-57]. Koch et al. demonstrated osteoblast proliferation on large engineered Poly-95L/5DL-lactic acid (PLA)-calcium composite scaffolds (6 - 12 mm diameter) in a perfusion bioreactor and Arano et al. examined the efficiency of perfusion seeding for osteoblast-like cells onto 10 - 12 mm-thick scaffolds in a radial-flow bioreactor. There have been no similar studies published for ECs cultured on well-organized large scaffolds.

In this study, a CFD model is used to estimate the local ss imposed on the walls of a large cylindrical scaffold embedded in a recently developed implantable vascular-like angiogenesis bioreactor (discussed in Chapter 6 [58]). For each geometry, the input flow rate was varied to determine which architecture and velocity at the inlet produces the

most uniform distribution of the imposed ss across the large scaffold, within a range of 1-10 dynes/cm$^2$ for a physiologically relevant input flow rate.

## 5.2 MATERIALS AND METHODS

### 5.2.1 Design of Perfusion Bioreactor System

The analyzed closed-loop bioreactor system consisted of a pump that circulated EC culture media through a vessel-like network, which perfused adjoined EC-seeded scaffolds. The "venous" end of the vessel-like network shunted media towards a reservoir for re-circulation. Fig. 5.1a illustrates the implantable component of the bioreactor, which housed the scaffolds. The cylindrical scaffolds (11mm x 11 mm) were located at the center of the vascular construct, enclosed in a cylindrical holder 11 mm in diameter and 10 mm in length. Within the compartment, a 500 micron guidance inlet was positioned before and after the scaffold. A holder tightly secured the scaffolds, in order to ensure perfusion through the scaffolds. Each compartment enclosed a single scaffold perfused with media by four 0.79 mm outlets from the preceding vascular tree. The outlets were aligned in parallel at the center of the compartment. Fig. 5.1b depicts the bioreactor set-up. Flow from a peristaltic pump is dampened to produce constant flow prior to passing through a flowmeter, which monitored the dispensed flow rate entering the vascular construct (see Fig. 5.1b). The inlet and outlet diameter of the vascular construct had a 2.2 mm diameter attached to Luer Lock connections.
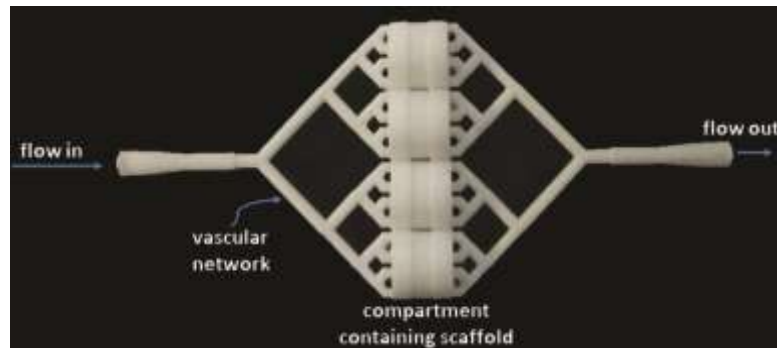
(a)
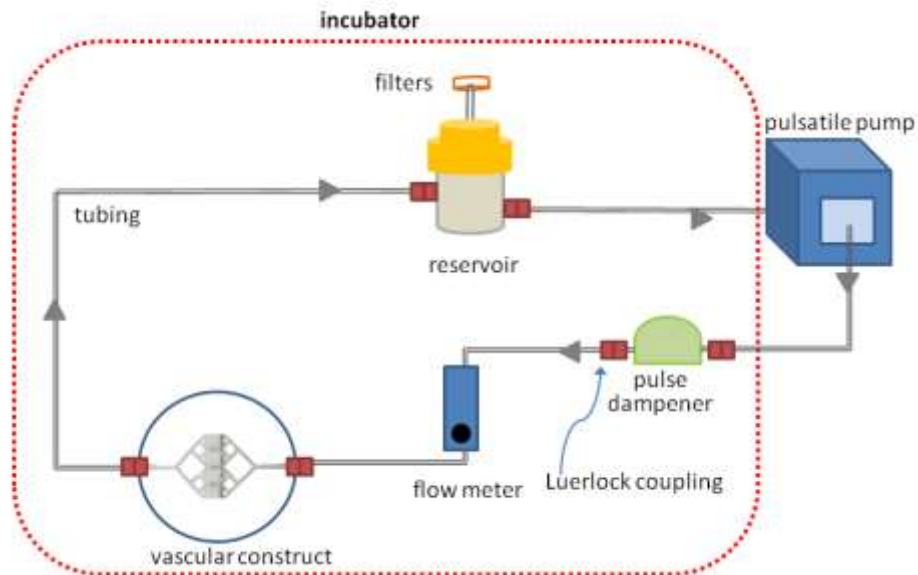


(b)

**Figure 5.1 (a) Vascular PCL construct which fed four porous scaffolds (12.0 cm length x 5.6 cm width). (b) Schematic diagram of bioreactor containing vascular network construct seeded with endothelial cells.**

## 5.2.2 PCL Scaffolds: Architecture and Fabrication

Three-dimensional cylindrical scaffolds with periodic porous architectures were designed using Computer Assisted Design (CAD) design software (Solidworks, Waltham, MA, USA). The scaffold geometries included (i) a spherical unit cell enclosing a sphere with a 2.22 mm pore diameter and (ii) an orthogonal lattice with a 1.5 mm pore diameter. Fig.

5.2. illustrates the CADs for the spherical and orthogonal scaffold geometries. For the spherical scaffold designs, the unit cell was repeated every 2 mm to fill a cylindrical construct with an 11 mm height and 11 mm diameter. The 0.9 mm cylinders that formed the orthogonal lattice were repeated every 1.5 mm to fill a cylindrical construct with an 11 mm height and 11 mm diameter.

Triangulated surface renderings of the scaffolds were generated in the CAD software. The renderings were used to fabricate the scaffolds on an SLS system (EOS FORMIGA P100, EOS GmbH, Munich, Germany) using a mixture of polycaprolactone (PCL) with a small percentage of hydroxyapatite (HA). The SLS system was set to 49.5°C, with a 450 mm focused laser beam diameter at 4.5W power and 1.257 m/s scan speed. The system used a 0.08 mm layer thickness. Three fabrications for each pore geometry were MicroCT scanned with an isotropic resolution of 15 μm (μCT 100, Scanco Medical AG, Bassersdorf, Switzerland). Diameter and porosity measurements for each MicroCT dataset were collected in a three-dimensional image analysis tool (MicroView, General Electric Healthcare, Waukesha, Wisconsin, USA). Measurements of the pore diameter and porosity for the designed scaffolds were collected in (Magics, Materialise, Leuven, Belgium) (Fig. 5.2c). Based on a comparison of the designed and fabricated scaffold pore and throat diameters, a correction factor was applied to the modeled CAD design parameters to realize the actual fabricated (physical) pore and strut diameters.
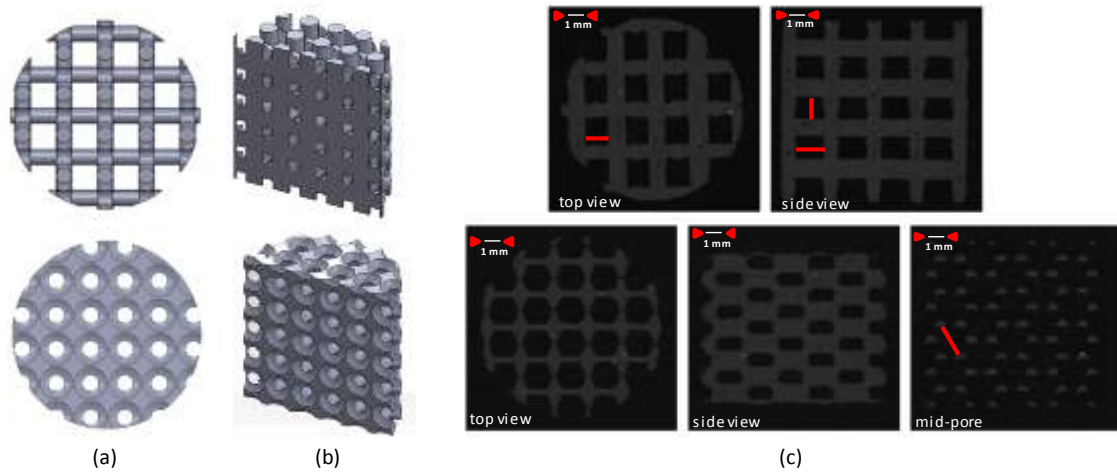
**Figure 5.2 (a) Top view of CAD and (b) trimetric cross-sectional view of CAD of bone scaffolds. (c) Axial (leftmost) and coronal slices (right) of three-dimensional renderings of spherical and orthogonal scaffold from Micro-CT scans. For the spherical geometry, a cross-section of the middle of a pore is shown. Red lines indicate measured pore. Scale bar = 1 mm.**

### 5.2.3  Bio-Fluid Characterization

The endothelial cell culture media was modeled as a homogenous, incompressible fluid. The dynamic viscosity of the EC media was acquired using a rheometer (AR1000 Rheometer, TA Instruments, New Castle, DE) at 37°C for shear rates ranging between 90 to 1000 $s^{-1}$. The fluid behavior of the EC media was characterized. The average of the collected viscosities was calculated. The density was calculated as an average of three repeated weighings of a known volume of the EC media on an analytical balance (37°C). The estimated viscosity and density served as input to the CFD simulation.

### 5.2.4  Formulation of CFD Model and Simulation Conditions

For each geometry, flow through the scaffold compartment was evaluated for a single representative scaffold compartment, since Chapter 4 demonstrated uniform flow through the vascular network, which perfuses the four compartments in the system [59]. The vessels at the last level of bifurcation in the vascular tree were 2 mm long. Thus, a single scaffold compartment connected to four 2-mm-long inlets and outlets was designed in

132

CAD design software (Solidworks, Waltham, MA, USA) to represent the bioreactor. The generated fluid volume (Fig. 5.3a) was meshed with tetrahedral elements (ANSYS Meshing, Lebanon, NH, USA). Mesh independence tests were conducted to improve the accuracy of the solution. Mesh refinement was performed until the number of meshing elements reduced the sensitivity in the average shear stress to less than 5% (see Appendix E.2). Based on the evaluation of the spatial resolution, approximately 3 million elements (32 - 650 micron, adaptive proximity and curvature sizing) were used to mesh both scaffolds.
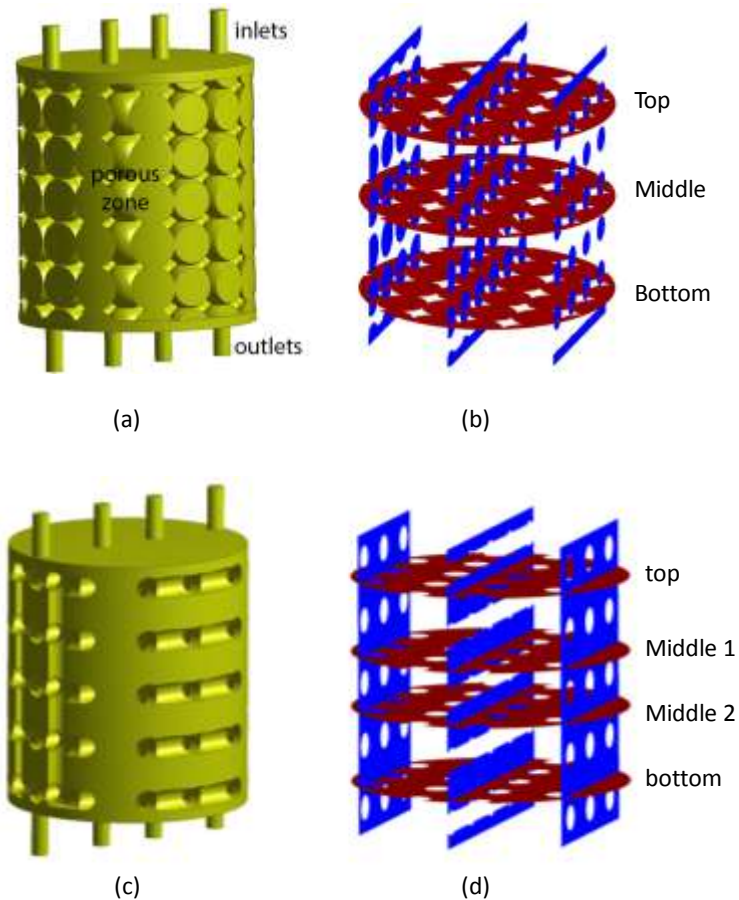


**Figure 5.3 CAD of the inverse geometry of compartment illustrates the fluid volume modeled in CFD, with vascular network outlets shunting EC media into the (a) spherical and (c) orthogonal scaffold compartment. The transverse planes (red) and longitudinal planes (blue) along which the ss was evaluated in the (b) spherical and (d) orthogonal scaffold compartment.**

CFD simulations were carried out using the commercial CFD package, Fluent (ANSYS Fluent, Lebanon, NH, USA). Each CFD simulation assumed the scaffold to be a rigid solid object, receiving constant, non-pulsatile flow. Simulations were solved using a steady-state Navier-Stokes equation, pressure-based solver, and laminar flow model, under the assumption of constant viscosity, constant density and continuity (incompressible flow). The solved Navier-Stokes equations for momentum 5.1 and continuity 5.2 were

$$\rho \frac{Dv}{Dt} = -\nabla p + \mu \nabla^2 v + \rho g \qquad\qquad \text{Equation 5.1}$$

$$\nabla u = 0, \qquad\qquad \text{Equation 5.2}$$

where $\rho$ was the fluid density (kg/m$^3$), $\mu$ was the dynamic viscosity (kg/m·s), $v$ was the fluid velocity, $p$ was the pressure (Pa) and $g$ was acceleration due to gravity (m/s$^2$) [60]. The velocity-pressure coupling was solved using the SIMPLEC (Semi-Implicit Method for Pressure Linked Equations - Consistent) algorithm [61] (momentum and pressure under-relaxation factors summed to 1). Spatial discretization was achieved with the least squares cell based gradient algorithm, standard pressure algorithm and second order upwind algorithm for momentum. To reduce numerical diffusion, a second order upwind was performed. A no-slip boundary condition was imposed on solid walls. Convergence was set to 1 x 10$^{-6}$ and 1 x 10$^{-4}$ for continuity and residuals, respectively.

Each volume was meshed with tetrahedral elements. The mass flow rate (kg/s) at the inlets was set along the primary direction of flow, y-direction relative to the orientation of model. The outlets were defined as outflow boundaries, which assumed a zero normal gradient for all flow variables except pressure. Due to the symmetry of the vascular phantom design, there were no pressure variations assumed among the outlets. Inflation layers were added to the four inlets and outlets. The fluid entering the network and compartment were modeled as isothermal and laminar. Laminar flow at the inlets was confirmed by computation of a Reynolds number that was less than 2300 for relevant mass flow rates, based on the following equation 5.3

$$Re = \frac{\rho Q D_h}{\mu A}, \qquad\qquad \text{Equation 5.3}$$

where ρ was the density of given fluid (kg/m$^3$), Q was the volumetric flow rate (m$^3$/s), $D_h$ was the hydraulic diameter (m) and $\mu$ was the dynamic viscosity (Pa·s) [62]. For the vascular tree and compartment, $D_h$ was based on the inlet diameters, while for the orthogonal geometry, $D_h$ was set to the pore diameter. For the spherical geometry, the throat diameter (smallest pore within geometry), which connected two adjacent spherical units, was used to estimate the maximum *Re*.

## 5.2.5 Shear Stress Analysis

The ss across the scaffold was determined along 6-7 planes (3-4 transverse and 3 longitudinal) located at the middle and peripheral (1.4 mm below/above and left/right of edges) of the structures (Fig. 5.3b). The orthogonal scaffold has two transversal middle planes located 1.1 mm from the middle of the scaffold. Histograms were generated to evaluate the frequency of ss values along each plane. The maximum and average wall ss were computed. The median absolute deviation (MAD) was calculated using equation 5.4 to evaluate the dispersion of induced SS.

$$MAD = median\left(\left|Y_i - \tilde{Y}\right|\right),$$
                                                                                      Equation 5.4

where $Y_i$ is an indexed ss value and $Y$ is the median of the ss values within the given plane. Hotspots and dead zones were quantified by the relative frequency of ss values greater than 10 dynes/cm$^2$ and less than 1 dynes/cm$^2$, respectively.

## 5.3 RESULTS

Table 5.1 summarizes the scaffold properties for the spherical and orthogonal scaffolds. The void space within both designs is roughly the same, at 67 - 68%. Based on the pore diameter measurements collected from the μCT (Fig. 5.2c), the CAD designs were changed to the actual fabrication diameters. The spherical scaffold CAD designed pore

diameter was reduced to 2.13 mm and the orthogonal pore diameter was decreased from 1.50 mm to 1.46 mm. Table 5.2 provides the measured designed, CAD and fabricated pore diameters for both pore geometries.

**Table 5.1 Summary of the pore diameter measurements for the designed and fabricated scaffolds: spherical and orthogonal geometries.**

| Pore Design | Designed Pore Diameter [mm] | Surface Area [mm$^2$] | Porosity [%] |
|---|---|---|---|
| Spherical | 2.22 | 1583 | 67 |
| Orthogonal | 1.5 | 1255 | 68 |

**Table 5.2  Pore diameter measurements for the designed and then fabricated scaffolds.**

| | Pore Diameter [mm] | | |
|---|---|---|---|
| Pore Design | Designed | CAD (n = 15) | Fabricated (n = 24) |
| Spherical | 2.22 | 2.20 ± 0.004 | 2.13 ± 0.07 |
| Orthogonal | 1.50 | 1.50 ± 0.001 | 1.46 ± 0.14 |

Using the modified scaffolds, the EC media flow conditions within the bioreactor compartment were analyzed. The relationship between the ss and shear rate of the EC media at 37°C was indicative of a Newtonian fluid. The media viscosity was $1.16 \times 10^{-3} \pm 1.25 \times 10^{-4}$ Pascal-seconds and the density was $957 \pm 2$ kg/m$^3$. Table 5.3 summarizes the inlet velocities needed to generate laminar flow within the system. Based on these theoretical measurements, compartment inlet velocities less than 0.61 m/s generate laminar flow, while higher velocities produce turbulent flow within the system.

**Table 5.3  Upper limit of the flow conditions required to satisfy laminar flow within the bioreactor, for the vascular tree and bone scaffold geometry within each compartment.**

| Component | Maximum Reynolds Number | Inlet Velocity (m/s) |
|---|---|---|
| Vascular Tree | 2300 | 1.27 |
| Compartment | 400 | 0.61 |
| Orthogonal Scaffold | 867 | 0.72 |
| Spherical Scaffold* | 594 – 1,726 | 0.34 – 2.85 |

* Reynolds number and velocity through the pore and throat (connection between two pores) within the scaffold provided.

Simulations were performed for compartment inlet velocities of 0.11 - 0.86 m/s and 0.32 - 1.2 m/s for the spherical and orthogonal geometry, respectively. The inlet velocities achieved an average ss between 1.9 - 15 dynes/cm$^2$ and 0.79 - 18 dynes/cm$^2$ for the spherical (Fig 5.4a) and orthogonal (Fig 5.4b) geometry, respectively. The minimum ss imposed on the scaffolds was negligible at $10^{-4}$ - $10^{-6}$ dynes/cm$^2$. The ss peaked at 74 - 1900 dynes/cm$^2$ and 310 - 2300 dynes/cm$^2$ for the spherical and orthogonal geometry, respectively. The plot in Fig. 5.4 illustrates the increased ss imposed on the scaffold for higher inlet velocities. For the overlapping inlet velocity range between 0.32 - 0.86 m/s, the average ss imposed on the spherical scaffold were higher in comparison to the orthogonal scaffold. The MAD of the ss for the spherical and orthogonal scaffold ranged from 0.5 - 3.5 dynes/cm$^2$ and 0 - 1 dynes/cm$^2$, respectively, for the overlapping inlet velocities. Overall, for both geometries, the MAD steadily increased for higher inlet velocities.

(a)



(b)
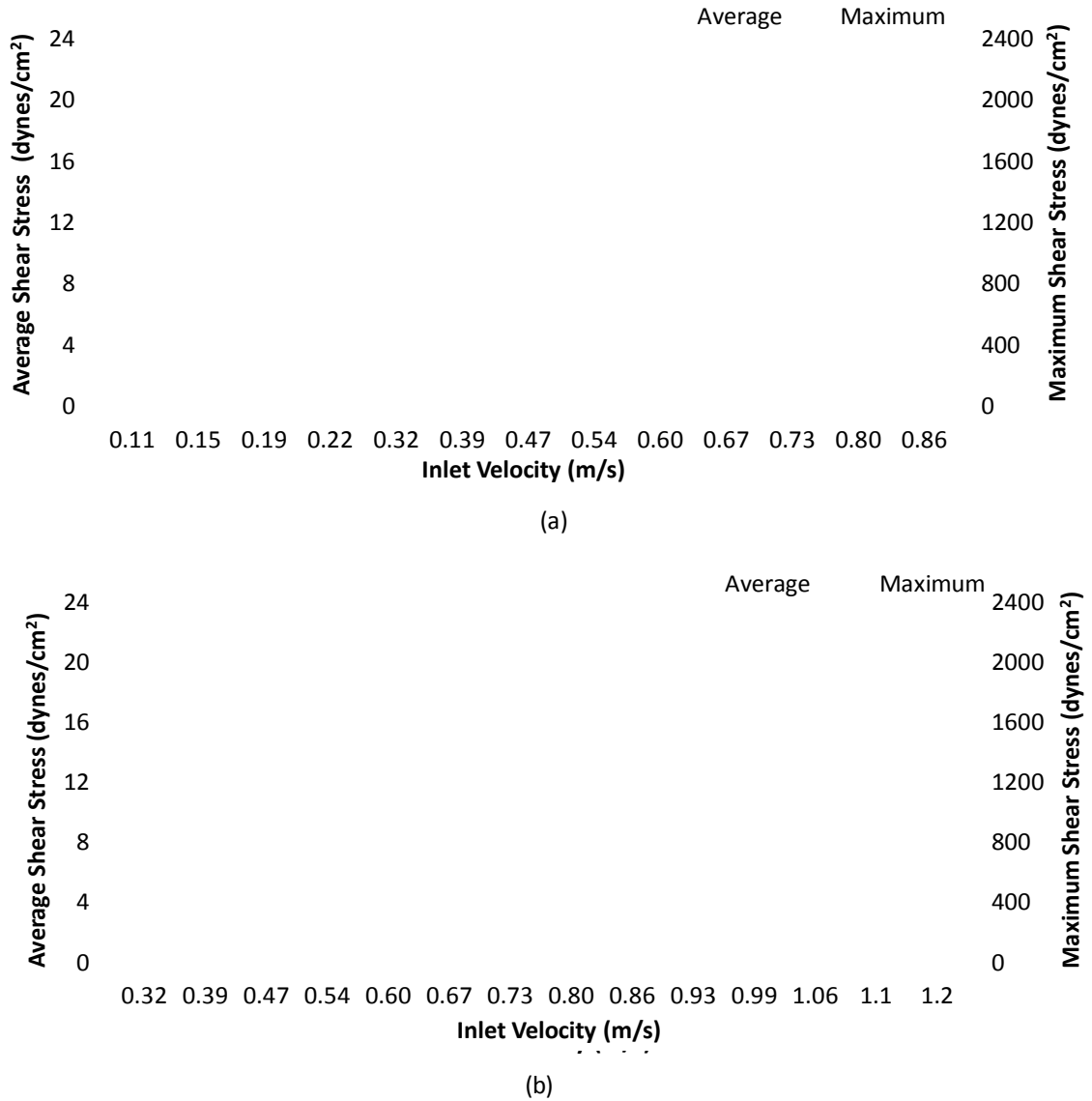
**Figure 5.4 Linear relationship between the average and maximum ss and the inlet velocity within the (a) spherical and (b) orthogonal scaffold compartments.**

Fig. 5.5 illustrates the dependence of the distribution of the imposed ss on the inlet velocity. Across all inlet velocities, the low (less than 1 dynes/cm$^2$) and very high (more than 20 dynes/cm$^2$) ss imposed on the scaffolds geometries was at least 21% and at most 15% of their surface areas (SA), respectively. Fig. 5.5a and 5.5c show the ss distribution across the spherical and orthogonal scaffold, respectively, for the different flow rates. Fig. 5.5b and 5.5d categorizes the imposed ss into low (less than 1 dynes/cm$^2$), target (1 -

10 dynes/cm$^2$) and high (more than 10 dynes/cm$^2$) for the spherical and orthogonal geometry, respectively. For the spherical scaffold, the percentage of SA that experienced the low, target and high ss ranges was 21-91%, 9-64% and 1-15%, respectively. While for the orthogonal scaffold, the percentage of SA was 43-84%, 14-45% and 2-12% for the low, target and high ss ranges. Particularly, within the overlapping inlet velocity range, the percentage of SA that achieved the target ss for the spherical geometry was 35 - 64%, which was higher compared to the 14 - 40% that was imposed on the orthogonal geometry.

Fig. 5.6 illustrates the average ss along the transverse and longitudinal planes for both geometries. The top planes experienced 4-5 and 2-3 times higher average ss than the middle and bottom planes for the spherical (Fig. 5.6a) and orthogonal (Fig. 5.6c) geometries, respectively. The average ss imposed on the lower half of the spherical scaffold was uniform along the transverse direction (Fig. 5.6a), but for the orthogonal geometry (Fig. 5.6c) the middle planes experienced twice as much average SS, in comparison to the bottom planes. For overlapping velocities, along the top plane, the spherical geometry experienced an average ss 5 times higher than along middle or bottom plane, whereas the orthogonal was 2-3 times higher. For both geometries, the average imposed ss along left and right planes were approximately equal. As the inlet velocity increased, the difference between the average ss along the middle plane and the left and right planes decreased for both geometries. For the spherical geometry, the average ss along the middle plane was 57 times higher than along the left and right planes at the lowest velocity and 4 times higher at the highest velocity (Fig. 5.6b).  For the orthogonal geometry, at the lowest and highest inlet velocity, the average ss imposed along the middle plane was 28 and 3 times higher than along the left and right planes, respectively (Fig. 5.6d). For overlapping velocities, the spherical geometry exhibited a lower difference in average ss in the longitudinal direction than the orthogonal geometry. Overall, for both geometries, the average ss imposed in the direction of the longitudinal planes and transverse direction was uniform, for all inlet velocities.

For both geometries, across all planes, the imposed ss and its respective MAD increased as the inlet velocity increased. For inlet velocities greater than or equal to 0.47 m/s, the

139

spherical geometry achieved a ss between 1 - 10 dynes/cm$^2$ along all planes. The orthogonal geometry achieved a ss between 1 - 9 dynes/cm$^2$ along all planes for velocities greater than or equal to 0.67 m/s. Fig. 5.7 shows that distribution of low, target and high ss for each inlet velocity across the spherical and orthogonal scaffold. For the spherical scaffold, only the top and middle planes experienced high ss (Fig. 5.7a). In the orthogonal geometry, the left, right, longitudinal middle 2 and transversal middle planes experience high SS. For the orthogonal scaffold, the dominant ss range was low, with a slight decrease for inlet velocities greater than or equal to 0.92 m/s (Fig 5.7c-d). However, for the spherical geometry, the percentage of SA that experienced 1-10 dynes/cm$^2$ was only greater than 1 dynes/cm$^2$ across the scaffold for the maximum inlet velocity of 0.67 m/s (Fig 5.7a-b). Otherwise, the low ss was dominant. Fig. 5.8 illustrates that for both geometries, as the inlet velocity increased, the difference in ss across the transverse and longitudinal planes decreased. For the spherical geometry, the percentage of SA that experienced 1-10 dynes/cm$^2$ along the transverse planes was greater than 50% for a 0.86 m /s inlet velocity and greater than or equal to 0.73 m/s along the longitudinal planes (Fig 5.8a-b). Collectively, across the whole scaffold, Fig 5.5b shows that 1 - 10 dynes/cm$^2$ of ss was imposed on more than 50% of the SA for inlet velocities greater than or equal to 0.54 m/s. However, the orthogonal geometry did not achieve 1 - 10 dynes/cm$^2$ over 50% of its SA along any of the planes (Fig 5.8c-d). Similarly, the target ss was not achieved for 50% or more of the whole orthogonal scaffold (Fig 5.5d). Table 5.4 summarizes the benefits and drawbacks between the computational ss results for the spherical and orthogonal geometries. Fig. 5.9 illustrates the ss and the velocity distributions across the spherical compartment, for an inlet velocity of 0.54 m/s along the transverse and longitudinal planes. In Fig. 5.9a and Fig. 5.9d, the highest wall shear stress and corresponding fluid velocity were experienced in the middle of the scaffold along the direction of flow. Fig. 5.9b and Fig. 5.9d shows that for the edge (top and bottom) regions of the scaffold where there were higher fluid velocities, the ss stress imposed on the scaffold surface was also high. The ss was moderately uniform across the scaffold, with peaks occurring at the throats regions that connect the two adjoined pores.
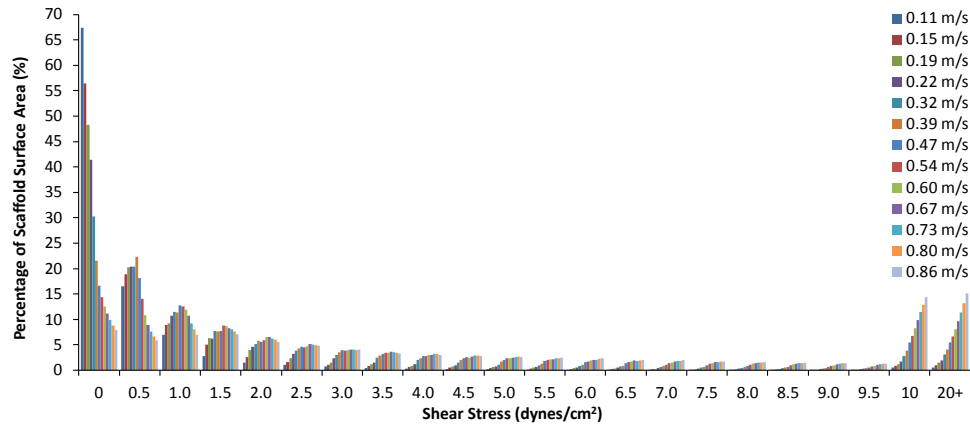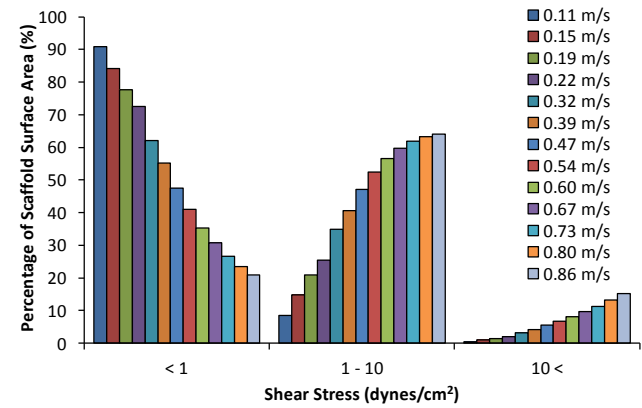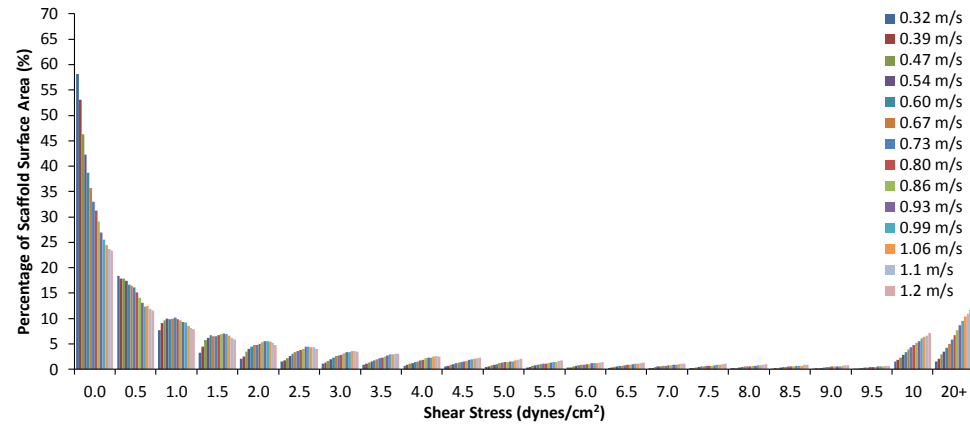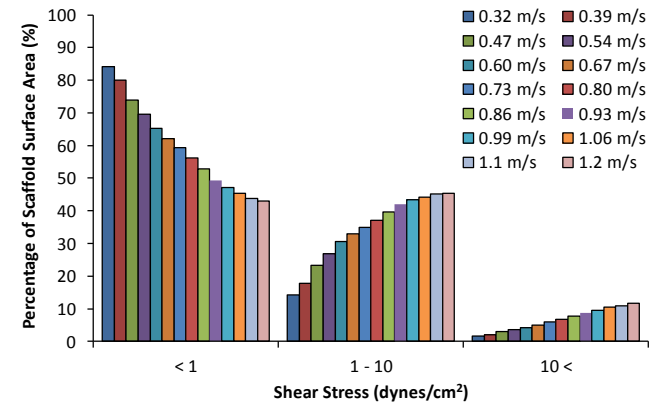
**Figure 5.5 Distribution of imposed ss on the (a) spherical and (c) orthogonal scaffold compartment for the given inlet velocities. Summary of the imposed ss on the (b) spherical and (d) orthogonal scaffold for low (< 1 dynes/cm$^2$), target (1-10 dynes/cm$^2$) and high < (10 dynes/cm$^2$) SS.**
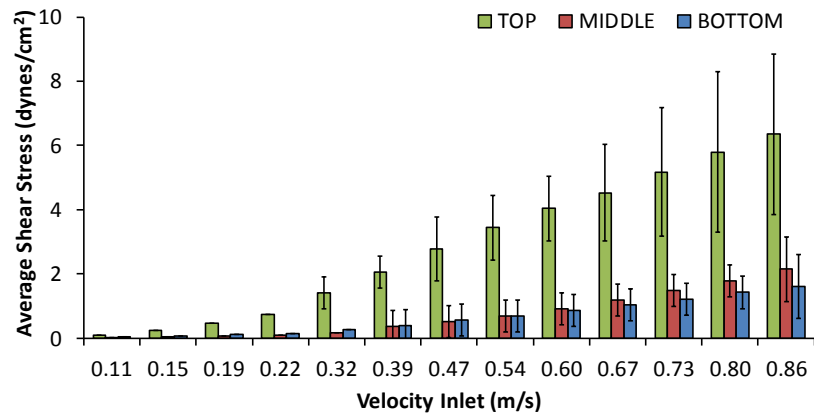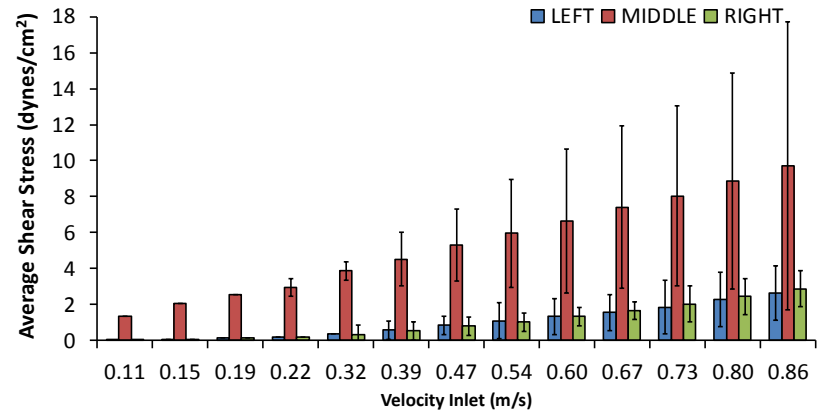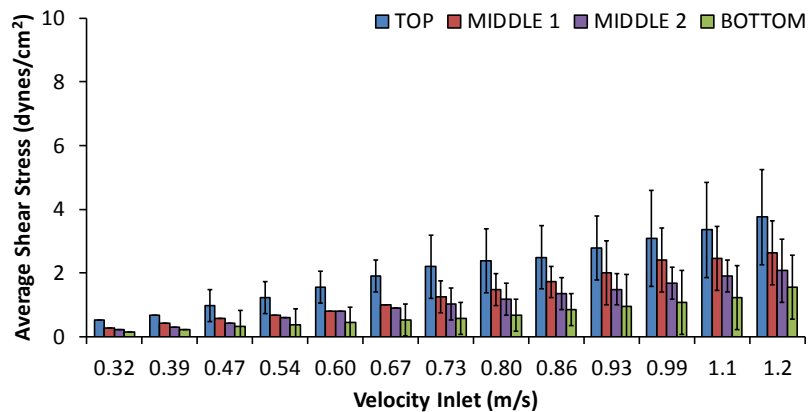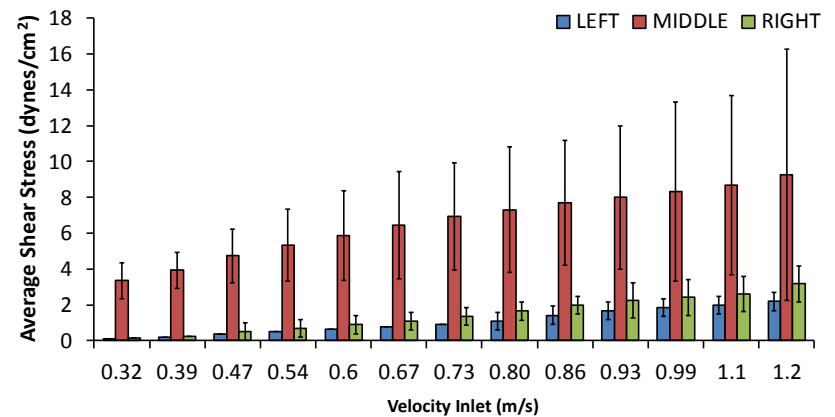
**Figure 5.6** Average ss along the (first column) transverse and (second column) longitudinal cross-sectional planes of the (a and b) spherical and (c and d) orthogonal scaffold, for the given inlet velocities.
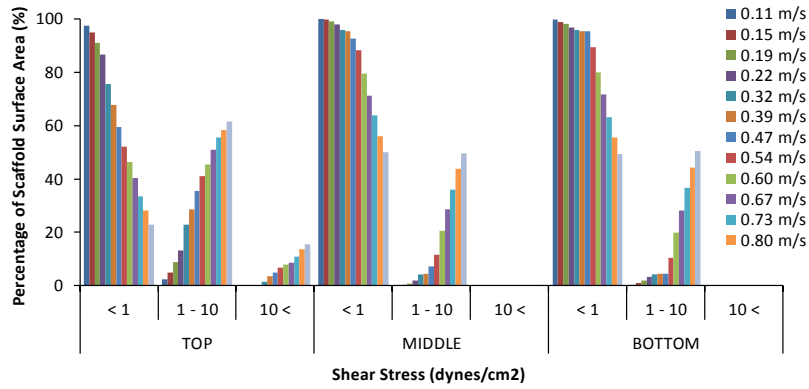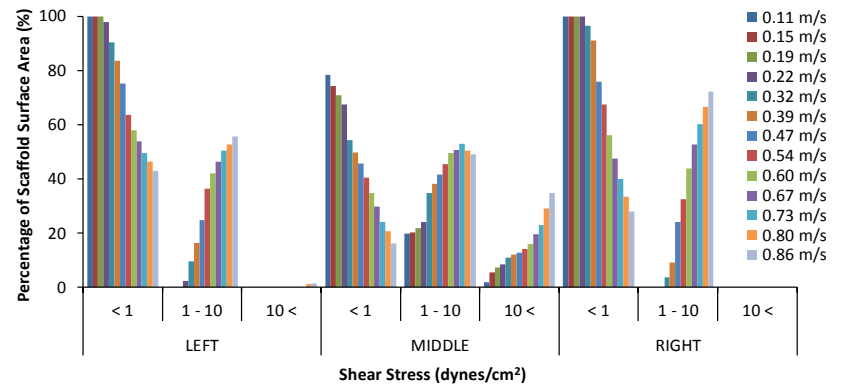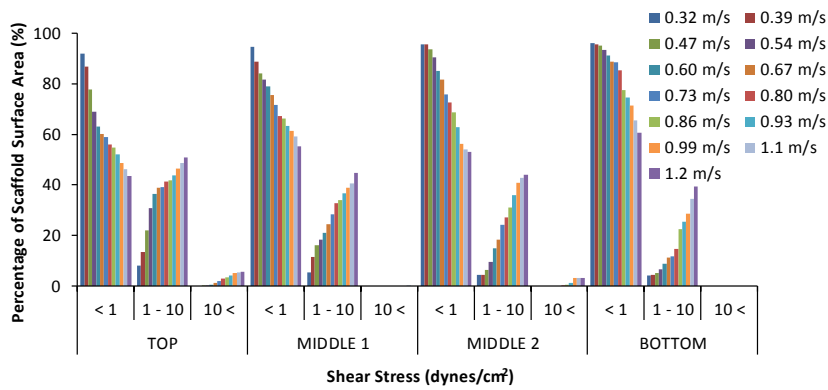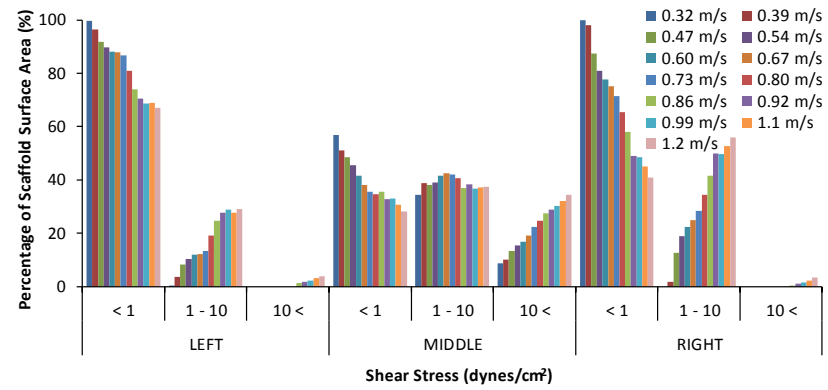
**Figure 5.7** Distribution of ss along the (first column) transverse and (second column) longitudinal planes of the (a-b) spherical and (c-d) orthogonal scaffold compartment, for the given inlet velocities.
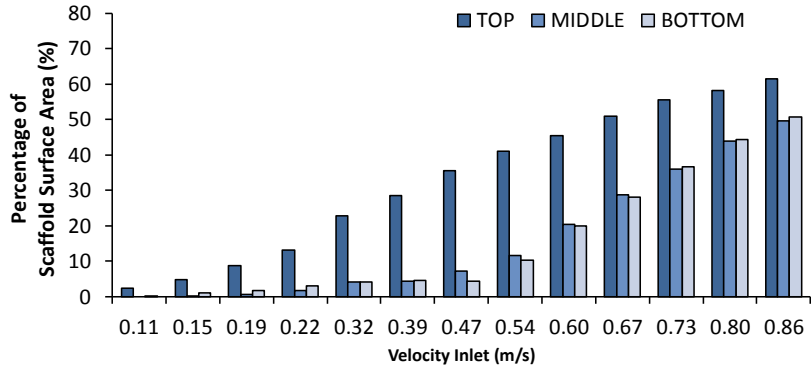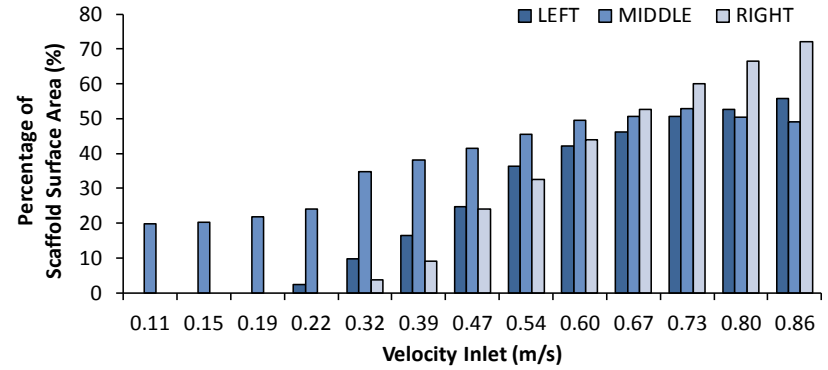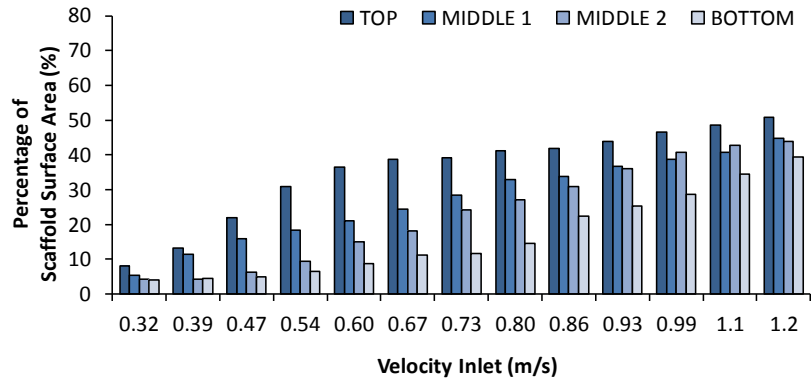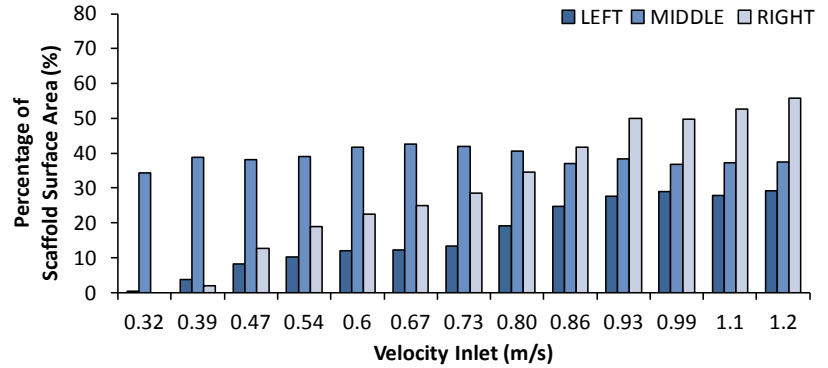
**Figure 5.8** Percentage of (a-b) spherical and (c-d) orthogonal scaffold SA that experienced 1-10 dynes/cm$^2$ along the (a,c) transverse and (b,d) longitudinal planes, for the given inlet velocities.

144

**Table 5.4 Upper limit of the flow conditions required to satisfy laminar flow within the bioreactor, for the vascular tree and bone scaffold geometry within each compartment.**

| Geometry | Benefits | Drawbacks |
|---|---|---|
| Spherical | • Lower maximum ss<br><br>• Higher average ss<br><br>• Target ss imposed over larger % of SA<br><br>• More than 50% of SA experienced target ss for inlet velocities ≥ 0.54 m/s<br><br>• Inlet velocity of 0.47 - 0.86 m/s required to achieve target ss (laminar flow regime realizable)<br><br>• Greater ss uniformity in longitudinal direction<br><br>• Average ss below top plane largely uniform | • Higher variation in average ss |
| Orthogonal | • Smaller variation in average ss along transversal direction | • Inlet velocity of 0.67 - 1.2 m/s required to achieve target ss (non-laminar flow)<br><br>• Low ss dominant across scaffold<br><br>• Larger % of SA experienced high ss (greatest potential for EC detachment) |
| Conclusion: For inlet velocities between 0.54 – 0.61 m/s, the spherical geometry provides the best balance of the tradeoffs between EC detachment and stimulation. | | |

**Figure 5.9 Contour maps of ss along (a) longitudinal and (b) transversal cross-sections of the spherical scaffold. The velocity distribution along the (c) longitudinal and (d) transversal planes are shown. Left to right, the left, middle and right plane cuts are shown for the longitudinal cuts. Left to right, the top, middle and bottom plane cuts are shown for the transversal cuts. Flow was from top to bottom, for a compartment inlet velocity of 0.54 m/s.**

## 5.4 DISCUSSION

To solve the thick tissue challenge, which hinders the translation of bench top tissue engineering successes to practical clinical therapy, bioreactors have been employed as a pre-vascularization strategy and technique to study *in vitro* angiogenesis. Dynamic bioreactors provide a three-dimensional platform that offers efficient mass transfer and a tunable stimulant mechanical environment. The controlled growth of capillary-like structures from endothelial cells on a matrix under dynamic *in vitro* bioreactor conditions provides a platform for studying angiogenesis and can also serve as a precursor step to efficiently generate pre-vascularized large constructs (greater than 2 - 4 mm) for implantation. The presented vascular-like bioreactor allows for an *in vitro* setup to be transferred to an *in vivo* environment to support bone tissue growth, with or without scaling to meet the constraints of the defect site. Existing bioreactors assume that a defect site can provide a large inflow of nutrients directly into the scaffold. This vascular-like bioreactor provides a structure for the anastomosis of an artery and vein to the structure in order to shunt blood towards the thick scaffold upon subcutaneous implantation. Tanaka et al. and Asano et al. demonstrated that a vein graft anastomosed to a femoral artery and femoral vein supported new vessel in-growth towards the core of the avascular tissue [63-64]. Asano et al. suggested that the increased shear stress within the loop construct stimulated a pro-angiogenic cell response (expression of growth factors and stimulatory proteins) [64]. Using an *in vivo* approach, Laschke et al. implanted a three-dimensional poly-lactic-glycolic (PLGA) scaffold into a host mouse for 20 days, then removed it and it placed into a recipient mouse [65]. A significant increase in blood perfusion and wall ss was observed over the 14 day study, with reperfusion of the implant occurring within 3-6 days.

Optimized pore architectures for bone scaffolds enhance bone tissue in-growth into the scaffold, possess mechanical properties characteristic of trabecular bone (i.e. compressive strength) and allow for the adequate exchange of cell signaling molecules, nutrients and waste (i.e. high interconnectivity and pore diameters greater than 100 microns [66-67]) [68-69]. The co-culture of osteogenic and angiogenic lineages can enhance bone formation [70]. The scaffold architectures employed in this investigation have already

147

been demonstrated to support *in vivo* bone growth based on their optimized designs (in terms of porosity, permeability or pore size) for smaller dimensions between 3 – 4.5 mm in thickness and 5 – 6.4 mm in diameter [44,46]. The spherical and orthogonal scaffolds can be reliably fabricated by selective laser sintering (SLS) of the polyester, polycaprolactone (PCL), which is a biodegradable polymer commonly used for *in vivo* EC studies [71-73]. The rapid prototyping technique allows for the repetition of pore shape and size. The scaffold dimensions were corrected to account for the fabrication inconsistencies that typically narrow the pore diameter.

Based on the performed simulations, spherical scaffolds were determined to achieve more uniform ss within the desired EC stimulation range of 1-10 dynes/cm$^2$ for inlet velocities between 0.47 - 0.86 m/s. Although the ss across the spherical and orthogonal scaffolds was evaluated for the inlet velocity range 0.11 - 0.86 m/s and 0.32 - 1.2 m/s in order to characterize the system, velocities greater than 0.60 m/s generated turbulent flow regimes within the system. Based on the literature, EC viability, morphology, attachment and directionality are maintained for ss ranges within 1-10 dynes/cm$^2$ under laminar flow conditions. The spherical scaffold demonstrated that 52 - 57% of scaffold surface experienced a ss between 1 - 10 dynes/cm$^2$ for the inlet velocities between 0.54 - 0.60 m/s, compared to the orthogonal scaffold that only achieved a distribution between 14 - 31% for inlet velocities between 0.32 - 0.6 m/s (Fig. 5.8). Both low and high ss ranges were dominant across the orthogonal scaffold (Fig. 5.7). As such, the spherical scaffold was determined to be a better design choice for future in vitro angiogenesis studies, as it realized the optimal ss range with moderate uniformity (Fig 5.5). The optimal inlet velocity was determined to be the lower limit of the range, 0.54 m/s, to reduce the likelihood of falling within the transitional flow region. For this given inlet velocity the spherical geometry achieved an average ss of 8.6 ± 1.5 dynes/cm$^2$ across the scaffold, with a maximum shear stress of 900 dynes/cm$^2$ occurring over 7% of the scaffold (Fig. 5.4 and Fig. 5.5). For both scaffolds, EC detachment was likely for surfaces that experienced ss greater than 20-25 dynes/cm$^2$, as seen for extracellular matrix and glass substrates [74-75]. There is a clear tradeoff between the stimulation of attached scaffolds and the detachment of cells, particularly at the top and middle planes (transversal and longitudinal). These distribution inconsistencies within the scaffolds can lead to cell wash

outs in hot spots (high fluid velocities), cell apoptosis in dead zones (low fluid velocities) or non-uniform growth across the scaffold. *In vitro* cell studies will be required to determine the impact of the high ss along these planes. The ss imposed over the transverse middle/bottom and left/right planes were approximately the same, with the greatest spike in ss occurring along the middle and top planes (Fig 5.6). However, Fig. 5.9 illustrates that these high ss ranges are primarily at the top and bottom edges along the fluid direction.

The performed study did not account for the surface roughness (underestimation of surface area) of the PCL scaffold, as CFD implemented a no-slip boundary condition on the model. As such, the acquired results may be an overestimation of the imposed fluid velocities and ss on the surface of the scaffold. Nonetheless, the identified inlet velocity serves as a useful initial condition for beginning an *in vitro* bioreactor study. Further studies are required to understand the changes in ss distribution as the EC monolayer extends with the formation of tubules. These changes will decrease the size of the void space within the scaffold.

Given the constraints of the proposed vascular-like perfusion bioreactor and the limits of computational models, the identified boundary conditions for the spherical scaffold are predicted to support and stimulated EC proliferation. After the formation of a vascular monolayer on the surface of scaffold, the vascular-like bioreactor may be implanted into a pig (2.1 - 2.9 mm; 99.4 ± 5.0 ml/min) [76] and anastomosed to a peripheral artery for the continuation of a pre-vascularization *in vivo* study. The inlet flow into the bioreactor would impose an average ss of 2.1 ± 0.5 dynes/cm$^2$ and 73-78% of the scaffold surface would receive less than 1 dyne/cm$^2$. Flow-induced ss levels between 0.001 - 0.1 dynes/cm$^2$ have been used in three-dimensional osteogenic studies, while higher levels between 0.1 - 10$^+$ dynes/cm$^2$ have been utilized in two-dimensional studies [35].

## 5.5  CONCLUSION

Orthogonal and spherical scaffold geometries are commonly adopted in tissue engineering to promote bone in-growth. The results of this study demonstrated that

scaffolds with a well-organized spherical pore (2.22 mm diameter) lattice imposed ss within the desired ss range to stimulate EC proliferation. Compared to an orthogonal design (1.46 mm), the spherical pore achieved better ss uniformity across the scaffold under a laminar flow regime. These results provide guidance on the appropriate inlet velocity for an *in vitro* vascular-like perfusion bioreactor construct. Furthermore, this study demonstrates the utility of computational models in understanding the distribution of flow for larger scaffolds and within angiogenesis bioreactors, at the start of a culture. The presented study can readily be extended to other pore geometries (i.e. hexagonal and cubical) in order to assess shear stress across the scaffold and to identify an optimal bone scaffold design for future EC co-culture studies.

## 5.6 ACKNOWLEDGEMENTS

## 5.7 REFERENCES

[1] Otrock ZK, Mahfouz RA, Makarem JA, Shamseddine AI. Understanding the biology of angiogenesis: review of the most important molecular mechanisms. Blood Cells, Molecules & Diseases 2007;39:212-20.

[2] Risau W. Mechanisms of angiogenesis. Nature 1997;386:671-4.

[3] Griffith CK, Miller C, Sainson RC, Calvert JW, Jeon NL, Hughes CC, George SC. Diffusion limits of an in vitro thick prevascularized tissue. Tissue Engineering 2005;11:257-66.

[4] Patrick CW, Chauvin PB, Hobley J, Reece GP. Preadipocyte seeded PLGA scaffolds for adipose tissue engineering. Tissue Engineering 1999;5:139-51.

[5] Kim BS, Putnam AJ, Kulik TJ, Mooney DJ. Optimizing seeding and culture methods to engineer smooth muscle tissue on biodegradable polymer matrices. Biotechnol Bioeng 1998;57:46-54.

[6] Kaully T, Kaufman-Francis K, Lesman A, Levenberg S. Vascularization--the conduit to viable engineered tissues. Tissue Engineering: Part B 2009;15:159-69.

[7] Muschler GF, Nakamoto C, Griffith LG. Engineering principles of clinical cell-based tissue engineering. J Bone Joint Surg Am 2004;86-A:1541-1558.

[8] Lokmic Z, Mitchell GM. Engineering the microcirculation. Tissue Engineering: Part B 2008;14:87-103.

[9] Polykandriotis E, Arkudas A, Beier JP, Hess A, Greil P, Papadopoulos T, Kopp J, et al. Intrinsic axial vascularization of an osteoconductive bone matrix by means of an arteriovenous vascular bundle. Plastic and Reconstructive Surgery 2007;120:855-68.

[10] Kedem A, Perets A, Gamlieli-Bonshtein I, Dvir-Ginzberg M, Mizrahi S, Cohen S. Vascular endothelial growth factor-releasing scaffolds enhance vascularization and engraftment of hepatocytes transplanted on liver lobes. Tissue Engineering 2005;11:715-22.

[11] Elcin YM, Dixit V, Gitnick G. Extensive in vivo angiogenesis following controlled release of human vascular endothelial cell growth factor: implications for tissue engineering and wound healing. International Society for Artificial Organs 2001;25:558-65.

[12] Hegen A, Blois A, Tiron CE, Hellesoy M, Micklem DR, Nor JE, Akslen LA, et al. Efficient in vivo vascularization of tissue-engineering scaffolds. Journal of Tissue Engineering and Regenerative Medicine 2011;5:e52-62.

[13] Davies N, Dobner S, Bezuidenhout D, Schmidt C, Beck M, Zisch AH, Zilla P. The dosage dependence of VEGF stimulation on scaffold neovascularisation. Biomaterials 2008;29:3531-8.

[14] Borenstein JT, Weinberg EJ, Orrick BK, Sundback C, Kaazempur-Mofrad MR, Vacanti JP. Microfabrication of three-dimensional engineered scaffolds. Tissue Engineering 2007;13:1837-44.

[15] Fidkowski C, Kaazempur-Mofrad MR, Borenstein J, Vacanti JP, Langer R, Wang Y. Endothelialized microvasculature based on a biodegradable elastomer. Tissue Engineering 2005;11:302-9.

[16] Chung S, Sudo R, Vickerman V, Zervantonakis IK, Kamm RD. Microfluidic platforms for studies of angiogenesis, cell migration, and cell-cell interactions. Sixth International Bio-Fluid Mechanics Symposium and Workshop March 28-30, 2008 Pasadena, California. 2010;38:1164-77.

[17] Lee EJ, Niklason LE. A novel flow bioreactor for in vitro microvascularization. Tissue Engineering: Part C 2010;16:1191-200.

[18] Williams C, Wick TM. Perfusion bioreactor for small diameter tissue-engineered arteries. Tissue Engineering 2004;10:930-41.

[19] Lu Q, Simionescu A, Vyavahare N. Novel capillary channel fiber scaffolds for guided tissue engineering. Acta Biomaterialia 2005;1:607-14.

[20] Lovett M, Cannizzaro C, Daheron L, Messmer B, Vunjak-Novakovic G, Kaplan DL. Silk fibroin microtubes for blood vessel engineering. Biomaterials 2007;28:5271-9.

[21] Bilodeau K, Couet F, Boccafoschi F, Mantovani D. Design of a perfusion bioreactor specific to the regeneration of vascular tissues under mechanical stresses. Artif Organs 2005;29:906-12.

[22] Ueda A, Koga M, Ikeda M, Kudo S, Tanishita K. Effect of shear stress on microvessel network formation of endothelial cells with in vitro three-dimensional model. Am J Physiol Heart Circ Physiol 2004;287:H994-1002.

[23] Dvir T, Benishti N, Shachar M, Cohen S. A novel perfusion bioreactor providing a homogenous milieu for tissue regeneration. Tissue Engineering 2006;12:2843-52.

[24] Tan Q, Steiner R, Yang L, Welti M, Neuenschwander P, Hillinger S, Weder W. Accelerated angiogenesis by continuous medium flow with vascular endothelial

growth factor inside tissue-engineered trachea. Eur J Cardiothorac Surg 2007;31:806-11.

[25] Carpentier B, Layrolle P, Legallais C. Bioreactors for bone tissue engineering. Int J Artif Organs 2011;34:259-70.

[26] Rauh J, Milan F, Gunther KP, Stiehler M. Bioreactor systems for bone tissue engineering. Tissue Engineering: Part B 2011;17:263-80.

[27] El Haj AJ, Cartmell SH. Bioreactors for bone tissue engineering. Proceedings of the Institution of Mechanical Engineers, Part H: Journal of Engineering in Medicine 2010;224:1523-1532.

[28] Jungreuthmayer C, Donahue SW, Jaasma MJ, Al-Munajjed AA, Zanghellini J, Kelly DJ, O'Brien FJ. A comparative study of shear stresses in collagen-glycosaminoglycan and calcium phosphate scaffolds in bone tissue-engineering bioreactors. Tissue Engineering: Parta A 2009;15:1141-9.

[29] Raimondi MT, Moretti M, Cioffi M, Giordano C, Boschetti F, Lagana K, Pietrabissa R. The effect of hydrodynamic shear on 3D engineered chondrocyte systems subject to direct perfusion. Biorheology 2006;43:215-22.

[30] Raimondi MT, Boschetti F, Falcone L, Migliavacca F, Remuzzi A, Dubini G. The effect of media perfusion on three-dimensional cultures of human chondrocytes: integration of experimental and computational approaches. Biorheology 2004;41:401-410.

[31] Rouwkema J, de Boer J, Van Blitterswijk CA. Endothelial cells assemble into a 3-dimensional prevascular network in a bone tissue engineering construct. Tissue Engineering 2006;12:2685-93.

[32] Santos MI, Unger RE, Sousa RA, Reis RL, Kirkpatrick CJ. Crosstalk between osteoblasts and endothelial cells co-cultured on a polycaprolactone-starch scaffold and the in vitro development of vascularization. Biomaterials 2009;30:4407-15.

[33] Grellier M, Bordenave L, Amedee J. Cell-to-cell communication between osteogenic and endothelial lineages: implications for tissue engineering. Trends Biotechnol 2009;27:562-71.

[34] Yeatts AB, Fisher JP. Bone tissue engineering bioreactors: dynamic culture and the influence of shear stress. Bone 2011;48:171-81.

[35] McCoy RJ, O'Brien FJ. Influence of shear stress in perfusion bioreactor cultures for the development of three-dimensional bone tissue constructs: a review. Tissue Engineering: Part B 2010;16:587-601

[36] Gaspar DA, Gomide V, Monteiro FJ. The role of perfusion bioreactors in bone tissue engineering. Biomatter 2012;2:167-175.

[37] Lesman A, Blinder Y, Levenberg S. Modeling of flow-induced shear stress applied on 3D cellular scaffolds: Implications for vascular tissue engineering. Biotechnol Bioeng 2010;105:645-54.

[38] McCoy RJ, Jungreuthmayer C, O'Brien FJ. Influence of flow rate and scaffold pore size on cell behavior during mechanical stimulation in a flow perfusion bioreactor. Biotechnol Bioeng 2012;109:1583-1594.

[39] Cioffi M, Boschetti F, Raimondi MT, Dubini G. Modeling evaluation of the fluid-dynamic microenvironment in tissue-engineered constructs: a micro-CT based model. Biotechnol Bioeng 2006;93:500-10.

[40] Porter B, Zauel R, Stockman H, Guldberg R, Fyhrie D. 3-D computational modeling of media flow through scaffolds in a perfusion bioreactor. J Biomech 2005;38:543-9.

[41] Maes F, Van Ransbeeck P, Van Oosterwyck H, Verdonck P. Modeling fluid flow through irregular scaffolds for perfusion bioreactors. Biotechnol Bioeng 2009;103:621-30.

[42] Olivares AL, Marsal E, Planell JA, Lacroix D. Finite element study of scaffold architecture design and culture conditions for tissue engineering. Biomaterials 2009;30:6142-9.

[43] Kang H, Lin CY, Hollister SJ. Topology optimization of three dimensional tissue engineering scaffold architectures for prescribed bulk modulus and diffusivity. Structural and Multidisciplinary Optimization 2010;42:633-644.

[44] Williams JM, Adewunmi A, Schek RM, Flanagan CL, Krebsbach PH, Feinberg SE, Hollister SJ, et al. Bone tissue engineering using polycaprolactone scaffolds fabricated via selective laser sintering. Biomaterials 2005;26:4817-27.

[45] Cuddihy MJ, Kotov NA. Poly(lactic-co-glycolic acid) bone scaffolds with inverted colloidal crystal geometry. Tissue Engineering: Part A 2008;14:1639-49.

[46] Mitsak AG, Kemppainen JM, Harris MT, Hollister SJ. Effect of polycaprolactone scaffold permeability on bone regeneration in vivo. Tissue Engineering: Part A 2011;17:1831-9.

[47] Kim K, Yeatts A, Dean D, Fisher JP. Stereolithographic bone scaffold design parameters: osteogenic differentiation and signal expression. Tissue Eng Part B Rev 2010;16:523-539.

[48] Chien S, Li S, Shyy YJ. Effects of mechanical forces on signal transduction and gene expression in endothelial cells. Hypertension 1998;31:162-9.

[49] Li YS, Haga JH, Chien S. Molecular basis of the effects of shear stress on vascular endothelial cells. J Biomech 2005;38:1949-71.

[50] Dewey CF, Bussolari SR, A. GM,Jr, Davies PF. The dynamic response of vascular endothelial cells to fluid shear stress. J Biomech Eng 1981;103:177-85.

[51] Galbusera M, Zoja C, Donadelli R, Paris S, Morigi M, Benigni A, Figliuzzi M, et al. Fluid shear stress modulates von Willebrand factor release from human vascular endothelium. Blood 1997;90:1558-64.

[52] Teichmann J, Morgenstern A, Seebach J, Schnittler HJ, Werner C, Pompe T. The control of endothelial cell adhesion and migration by shear stress and matrix-substrate anchorage. Biomaterials 2012;33:1959-1969.

[53] Ando J, Yamamoto K. Effects of shear stress and stretch on endothelial function. Antioxid Redox Signal 2011;15:1389-403.

[54] Kadohama T, Nishimura K, Hoshino Y, Sasajima T, Sumpio BE. Effects of different types of fluid shear stress on endothelial cell proliferation and survival. J Cell Physiol 2007;212:244-51.

[55] Davies PF, Remuzzi A, Gordon EJ, F. DC,Jr, A. GM,Jr. Turbulent fluid shear stress induces vascular endothelial cell turnover in vitro. Proc Natl Acad Sci USA 1986;83:2114-7.

[56] Koch MA, Vrij EJ, Engel E, Planell JA, Lacroix D. Perfusion cell seeding on large porous PLA/calcium phosphate composite scaffolds in a perfusion bioreactor system under varying perfusion parameters. J Biomed Mater Res A 2010;95:1011-8.

[57] Arano T, Sato T, Matsuzaka K, Ikada Y, Yoshinari M. Osteoblastic cell proliferation with uniform distribution in a large scaffold using radial-flow bioreactor. Tissue Eng Part C Methods 2010;16:1387-98.

[58] Thomas, A, Genesteir, L, Thiagaraj, A, Hollister, SJ and Balter, JM. The effect of surface-modified PCL constructs on human umbilical vein endothelial cells (HUVECS) cultured *in vitro*: a static and dynamic study. J Biomed Mater Res A 2013; *Submitted*.

[59] Thomas, A, Hollister, SJ and Balter, JM. A Computational Fluid Dynamics (CFD)-Based Approach to Validating Flow in a Dynamic Perfusion Phantom for Dynamic Contrast Enhanced (DCE) Imaging. Physics of Medicine in Biology 2013; *Submitted*.

[60] Cebeci T, Shao JP, Kafyeke F, Laurendeau E. Computational Fluid Dynamics for Engineers: From Panel to Navier-Stokes Methods with Computer Programs. : Springer-Verlag GmbH., 2005.

[61] van Doormaal JP and Raithby, GD. Enhancements of the SIMPLE method for predicting incompressible fluid flows. Numerical Heat Transfer 1984; 7:147-163.

[62] Nguyen NT, Wereley ST. Fundamentals and Applications of Microfluidics. : Artech House, 2002.

[63] Tanaka Y, Tsutsumi A, Crowe DM, Tajima S, Morrison WA. Generation of an autologous tissue (matrix) flap by combining an arteriovenous shunt loop with artificial skin in rats: preliminary report. Br J Plast Surg 2000;53:51-57.

[64] Asano Y, Ichioka S, Shibata M, Ando J, Nakatsuka T. Sprouting from arteriovenous shunt vessels with increased blood flow. Med Biol Eng Comput 2005;43:126-130.

[65] Laschke MW, Rucker M, Jensen G, Carvalho C, Mulhaupt R, Gellrich NC, Menger MD. Improvement of vascularization of PLGA scaffolds by inosculation of in situ-preformed functional blood vessels with the host microvasculature. Ann Surg 2008;248:939-48.

[66] Klenke FM, Liu Y, Yuan H, Hunziker EB, Siebenrock KA, Hofstetter W. Impact of pore size on the vascularization and osseointegration of ceramic bone substitutes in vivo. J Biomed Mater Res A 2008;85:777-86.

[67] Holtorf HL, Datta N, Jansen JA, Mikos AG. Scaffold mesh size affects the osteoblastic differentiation of seeded marrow stromal cells cultured in a flow perfusion bioreactor. J Biomed Mater Res A 2005;74:171-80.

[68] Hollister SJ, Maddox RD, Taboas JM. Optimal design and fabrication of scaffolds to mimic tissue properties and satisfy biological constraints. Biomaterials 2002;23:4095-103.

[69] Lovett M, Lee K, Edwards A, Kaplan DL. Vascularization strategies for tissue engineering. Tissue Eng Part B Rev 2009;15:353-70.

[70] Kanczler J, Oreffo R. Osteogenesis and angiogenesis: the potential for engineering bone. Eur Cell Mater 2008;15:100-114.

[71] Choong CS, Hutmacher DW, Triffitt JT. Co-culture of bone marrow fibroblasts and endothelial cells on modified polycaprolactone substrates for enhanced potentials in bone tissue engineering. Tissue Engineering 2006;12:2521-31.

[72] Yu H, VandeVord PJ, Mao L, Matthew HW, Wooley PH, Yang SY. Improved tissue-engineered bone regeneration by endothelial cell mediated vascularization. Biomaterials 2009;30:508-17.

[73] Yu H, Vandevord PJ, Gong W, Wu B, Song Z, Matthew HW, Wooley PH, et al. Promotion of osteogenesis in tissue-engineered bone by pre-seeding endothelial progenitor cells-derived endothelial cells. J Orthop Res 2008;26:1147-52.

[74] van Kooten TG, Schakenraad JM, van der Mei HC, Dekker A, Kirkpatrick CJ, Busscher HJ. Fluid shear induced endothelial cell detachment from glass--influence of adhesion time and shear stress. Med Eng Phys 1994;16:506-512.

[75] Consigny PM, Vitali NJ. Resistance of freshly adherent endothelial cells to detachment by shear stress is matrix and time dependent. J Vasc Interv Radiol 1998;9:479-485.

[76] Spence PA, Montgomery WD, Santamore WP. High flow demand on small arterial coronary bypass conduits promotes graft spasm. J Thorac Cardiovasc Surg 1995;110:952-962.

# CHAPTER 6

# The Effect of Polycaprolactone (PCL) Surface-Modifications on Endothelial Cell Proliferation, Function and Spatial Distribution *In Vitro*

## 6.1 INTRODUCTION

Several studies have highlighted the biomechanical influence of three-dimensional extracellular matrices (and adhering components) and shear stress on the growth of tissue and vascularization [1-2]. As an *in vitro* pre-vascularizations strategy, perfusion bioreactors sustain endothelial cell (EC) proliferation and promote tubulation across an embedded natural or engineered matrix, thereby imposing fluid shear stress and eliciting mechanotransduction. Existing angiogenesis bioreactors incorporate hydrogels (i.e. collagen, alginate and fibrin) for guided three-dimensional EC growth and migration [3-6]. Numerous co-culture studies of endothelial with osteogenic cell lineages have shown accelerated vessel in-growth and enhanced osteogenic differentiation post-implantation, using this pre-vascularization strategy [7-9]. The next generation of angiogenesis bioreactors should support co-cultures with osteogenic or chondrogenic lineages for the development of *in vitro* and/or implantable *in vivo* bone regeneration models. However, promulgated investigations of angiogenesis bioreactors employ hydrogels, which lack the mechanical (stiffness and strength) properties characteristic of bone, particularly trabecular bone for load-bearing applications [10-11]. These hydrogels are typically less than 2 mm thick [12-15]. Larger scaffolds would allow for the generation of thick tissue for larger defect sites. Large constructs can be readily fabricated with polymers, such as polycaprolactone (PCL) using numerous rapid prototyping techniques, such as selective laser sintering (SLS) [16]. The biodegradable polymer, PCL has been well documented in its application to benchtop tissue engineering and translational clinical applications [17]. The computer-based designs achievable through this fabrication process allow for

scaffolds to be scaled up to larger dimensions. Although versatile, in terms of the diffusion, permeability and mechanical properties it offers, the hydrophobic surface properties of PCL diminish its cytocompatibility. The functionalized groups at the surface of PCL are critical to the interaction with cells, in terms of cell attachment and proliferation. As such, several surface modification methods have been investigated in recent years: protein adhesion, growth factor immobilization, hydrolyzation and the incorporation of natural extracellular matrix molecules [18]. Gel-based cell attachment methods introduce flow constraints to a bioreactor and can be washed away with continual perfusion. Typically, angiogenesis bioreactor studies perform a static pre-culture on the scaffolds for roughly 2 - 72 hours or until confluence is reached, prior to the introduction of the fluid shear stress. Therefore, the attachment and uniform proliferation of ECs onto the surface of a large scaffold during the first 3 days is important for incorporation into a bioreactor. In the following study, endothelial cell response with respect to cell proliferation, cell function and spatial distribution were quantitatively assessed for three PCL surface modifications: sodium hydroxide (NaOH) hydrolyzation, Arg-Gly-Asp (RGD) conjugation and vascular endothelial growth factor (VEGF) immobilization.

PCL constructs strongly hydrolyzed with NaOH have been shown to increase the surface hydrophilicity and surface roughness of the constructs (wettable polymers), thereby improving cell interaction[19-20]. In a co-culture study of human bone marrow cells and human bone marrow endothelial cells (HBMEC-60), Choong et al. [19] reported increased attachment and proliferation of HBMECs-60 for strongly hydrolyzed PCL films (5 M NaOH for 48 hours), compared to weakly hydrolyzed (0.1 M NaOH for 48 hours) or untreated PCL films. Similarly, Serrano et al. [20] demonstrated that the NaOH-treated PCL films (2N for 2 hours) resulted in cell proliferation rates comparable to cultures on tissue culture polystyrene (TCPS). The untreated films supported EC cell viability, but did not promote similar proliferation rates.

A more commonly adopted surface modification is the attachment of extracellular matrix (ECM) components or their derived synthetic peptides. Arg-Gly-Asp (RGD) has been cited as a highly effective peptide sequence for improving cell attachment onto polymer surfaces through its interaction with the integrin receptors at focal adhesion points to

160

activate signal transduction between the ECM and cell [21-22]. A previous study by Zhang et al. [23-24] immobilized RGDC on PCL two-dimensional film surfaces and on 3D PCL scaffold surfaces via sulfosuccinimidyl-4-(N-maleimidomethyl)cyclohexane-1-carboxylate (sulfo-SMCC) crosslinking. For both PCL constructs, the adhesion of rat bone marrow stromal cell (BMSC) to the polymer was significantly increased and initiated integrin-mediated signal transduction that regulates subsequent increases in cell survival and growth [23-24]. Wang et al. enhanced endothelial cell (EC) attachment and proliferation on PEGyLated polymers surfaces with the incorporation of N-hydroxysuccinimide (NHS) coupled RGD [25].

VEGF is another common modification, which is either adsorbed or conjugated onto the surface of a construct. It is a potent mitogen that stimulates the migration and proliferation of ECs [26] and has been cited as an important growth factor acting in the initiation of angiogenesis [27]. When immobilized onto a scaffold, VEGF has been shown to lengthen and localize cell stimulation, resulting in increased EC proliferation [28-37]. Several groups have used VEGF's affinity for heparin to immobilized the growth factor on to polymer surfaces [38-39]. Amino groups are introduced to the PCL surfaces by a reaction with 1,6-hexanediamine, wherein one amino group reacts with the polymer ester group to form a covalent amide bond [40]. Heparin then binds to the other unreacted, free $-NH_2$ groups. Heparin is a naturally occurring polysaccharide composed of alternating units of sulphated glucuronic acid and glucosamine derivatives. At sufficient low concentrations, heparin can potentiate VEGF binding, while at higher concentrations can inhibit VEGF binding [41]. As well, researchers have suggested that there is an optimum dose of VEGF to be loaded onto scaffolds, and have noted this window as a critical factor in promoting angiogenesis [34,36,38,42]. Based on the literature, a constant release concentration of approximately 70 - 100 ng/day produces favorable conditions for angiogenesis *in vitro* (see Appendix F, Table F.1).

Numerous polymer surface modifications have been investigated to improve EC attachment, viability and proliferation within *in vitro* studies. The goal of this study was to optimize the growth conditions for human umbilical vein endothelial cells (HUVECs) on polycaprolactone (PCL) two-dimensional discs and three-dimensional scaffolds. To

161

determine the most effective surface modification that elicits the best cell response in terms of cell proliferation and function.

## 6.2 MATERIALS AND METHODS

### 6.2.1 PCL Vascular Network and Scaffold Design and Fabrication

The two-dimensional discs (2.1 mm height and 15 mm diameter) and three-dimensional cylindrical scaffolds (11 mm height and 11 mm diameter) were fabricated using the same SLS protocol. Sections 2.3.1.1 and 2.3.2.2 detail the SLS fabrication and the scaffold design process, respectively. After fabrication, the discs and scaffolds were sonicated for 2 hours in ethanol to remove excess powder. (Henceforth, the collective of discs and scaffolds may be referred to as constructs.)
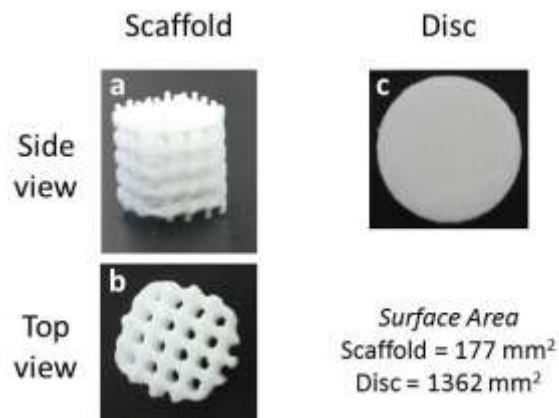


**Figure 6.1 (a) Side view of scaffold. (b) Top view of scaffold. (c) Top view of disc. Surface area for each construct is provided.**

### 6.2.2 Heparin Immobilization and VEGF Conjugation

Amine groups were introduced to the constructs based on a protocol established by Zhu et al. [40]. Each construct first underwent aminolysis. Constructs were submerged in a 10% (w/v) 1,6-hexanediamine solution (Fluka Chemie AG, Buchs, Switzerland) in isopropanol (Reagent ACS, Fisher Scientific) for 4-5 hours at 37˚C. The constructs were initially pulled under a vacuum for 1 hour to allow for solution penetration. The constructs had an $NH_2$ density of approximately 0.21 µmol/cm$^2$ [40]. Then, the constructs were washed in deionized water for 24 hours and dried at room temperature under

vacuum. The constructs were washed in phosphate buffered saline (Gibco, Inc., Grand Island, NY) and 2-morpholinoethane sulfonic acid (MES, pH 5.40, Thermo Scientific, Waltham, MA). Thereafter, the activated carboxylic acid groups of unfractionated sodium heparin (Sigma-Aldrich, St Louis, MO) were immobilized on the constructs (see Fig. 5.2) by a chemical crosslinking of amino end-functionalized PCL with 1-ethyl-3-(3-dimethylaminopropyl) carbodiimide/N-hydroxysulfosuccinimid (EDC/Sulfo-NHS) (Thermo Scientific, Waltham, MA) . 0.05 M MES buffer, 10 mg/ml heparin, 4 mg/ml EDC and 11 mg/ml Sulfo-NHS were allowed to react for 15 minutes. The reaction was quenched by 14 µl/ml 2-mercaptoethanol (Sigma-Aldrich, St Louis, MO). The pH of the heparin solution was adjusted to 7.2-7.5 using NaOH. The constructs were immersed in the heparin solution for 24 hours at 37˚C. Thereafter the constructs were washed twice in deionized water, for twenty minutes each time. The constructs were sterilized in ethanol for 24 hours at room temperature. Table 6.1 summarizes the respective heparin concentrations loaded onto the scaffolds and discs.
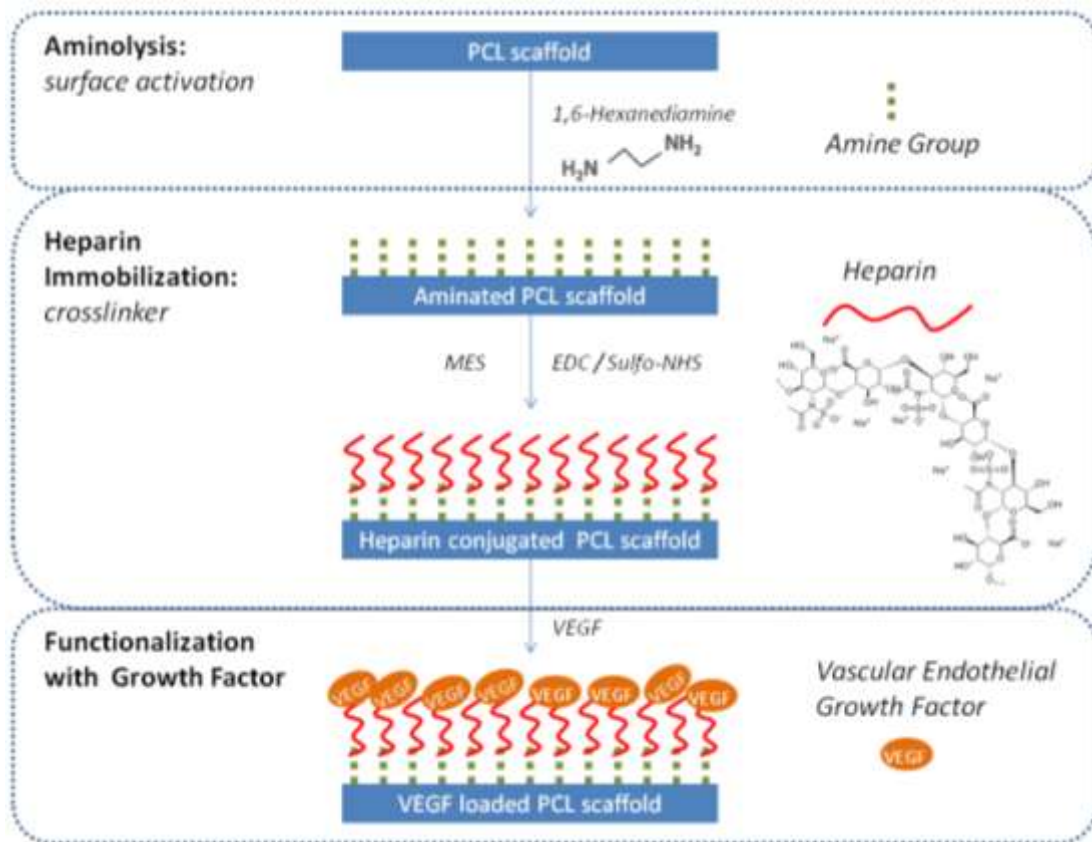


**Figure 6.2 Schematic diagram for immobilization of heparin on the surface of PCL construct.**

## 6.3  VEGF IMMOBILIZATION

Table 6.1 outlines the three experimental groups for which a conjugation efficiency and release study were completed. Groups 2 and 3 were used in cell culture studies. After each construct was aminated, then functionalized with heparin, VEGF (VEGF 165 Protein, Novus Biologicals, Littleton, CO) was conjugated onto the PCL surface. The constructs were washed in deionized distilled water for thirty minutes. 1 ml of VEGF (10µg/ml) was added to each scaffold and 0.5 ml of VEGF (20µg/ml) to each disc. The discs were reacted in low-attachment 24-well plates and the scaffolds in 5 ml centrifuge tubes coated with 1% bovine serum albumin (Sigma-Aldrich, St Louis, MO). The VEGF reacted for two hours at room temperature.

**Table 6.1 Experimental groups in VEGF conjugation and adsorption study.**

| Group | Construct Type | Heparin Immobilization | Loaded Heparin (mg) | Loaded 0.5VEGF (µg) |
|-------|----------------|------------------------|---------------------|---------------------|
| 1 | Discs | Adsorption | 0 | 10 |
| 2 | | Heparin | 0.1 | 10 |
| 3 | Scaffolds | Heparin | 0.5 | 10 |

### 6.3.1.1  VEGF Release

Following conjugation, *in vitro* VEGF release studies (n = 3) were performed in triplicate over five days for Group 2 and 3 outlined in Table 6.1. The discs were incubated in 1 ml of EC media, while the scaffolds were incubated in 2 ml of media. The discs and scaffolds were incubated in low attachment 24-well plates at 37ºC with gentle shake. On days 1, 3 and 5, the supernatant in each well was collected and replaced with fresh EC media of equal volume. The concentration of VEGF in the collected samples was measured using a VEGF ELISA.

### 6.3.1.2 VEGF Quantification

After conjugation or adsorption, the constructs were washed for ten minutes with sterile water to remove unconjugated VEGF. The washes were collected, along with the residual from the VEGF loading solution. The conjugation or adsorbed efficiency was calculated indirectly, as the amount initially in the conjugation solution minus the amount washed off following the conjugation, which remained in the assayed fluid. For the release study, the media was gently suspended in the wells to remove unconjugated VEGF. The released amount of VEGF was calculated as the direct measurement of VEGF collected in the fluid samples on day 1, 3, 5 and 7.

To quantify the amount of conjugated VEGF on the treated constructs, enzyme-linked immunosorbent assay (ELISA) was performed using an optimized version of a general double antibody sandwich ELISA protocol (Thermo Scientific and Invitrogen's Antibody Pairing Kit). VEGF standards (Invitrogen) were reconstituted and prepared: 1500 pg/ml, 750 pg/ml, 375 pg/ml, 188 pg/ml, 93.8 pg/ml, 46.9 pg/ml, 23.4 pg/ml and 0 pg/ml. The assay buffer (pH 7.4) consisted of sodium chloride, potassium chloride, disodium phosphate, monopotassium phosphate, Tween 20 and bovine serum albumin diluted in deionized distilled water. Aqueous Tween 20 was used as the wash buffer (pH 7.4). VEGF Purified, Mouse Monoclonal Antibody Unconjugated was diluted to 3 µg/ml in aqueous sodium bicarbonate to prepare a coating buffer (pH 9.4). The incubation buffer (pH 7.4) consisted of sodium chloride, potassium chloride, Disodium hydrogen phosphate, monopotassium phosphate, EDTA and bovine serum albumin diluted in deionized distilled water. VEGF Rabbit Anti-human-Biotin Conjugated (Invitrogen) was diluted to 0.3125 µg/ml in a detection antibody solution (pH 7.4) that consisted of sodium chloride, sodium dihydrogen phosphate, disodium phosphate, mouse serum and bovine serum albumin. A stock solution of Streptavidin HRP solution (ELISA Grade) (Invitrogen) was dissolved in assay buffer to prepare a 0.24 µg/ml solution. Tetramethylbenzidine stabilized chromagen (Invitrogen) was used as the substrate solution. 0.9 M (1.8N) sulfuric acid was used as the stop solution. The absorbance of the samples was measured in 96-well plates at 450 nm by microplate reader (Multiskan Spectrum, Thermo Electron Corporation). Based on a derived calibration curve, the amount of VEGF that remained in the loading solution was estimated. The average

amount of retained VEGF from each respective 0 µg sample group was subtracted from the average of each sample within that group to remove the baseline absorbance.

## 6.3.2  RGD Conjugation

The discs and scaffolds were modified with RGDC peptide following the protocol previously established by Zhang et al. [24] (based on published bioconjugation techniques [43]). Aminolysis was performed identical to the methods outlined in section 5.2.2. Then, the aminated constructs were thoroughly washed for 24 hours in deionized distilled water under a vacuum at 37˚C. Then the constructs were washed three times in activation buffer (0.1 M phosphate-buffered saline containing 0.15 M NaCl pH 7.2). RGDC peptides were conjugated onto the surface of the constructs using the heterobifunctional crosslinker sulfosuccinimidyl 4-(N-maleimidomethyl) cyclohexane-1-carboxylate (sulfo-SMCC) (Pierce Biotechnology, Rockford, IL).  Each construct was submerged in a 4 mg/ml solution of the sulfo-SMCC and incubated for one hour at room temperature. Thereafter, each construct was washed twice in activation buffer and once in the conjugation buffer (activation buffer containing 0.1 M EDTA, pH 7.0). The RGDC peptide (Bachem California, Inc., Torrance, CA) was dissolved in conjugation buffer at a concentration of 0.125 mg/ml. 0.5 ml of the peptide solution was added to the sulfo-SMCC-treated discs and 1 ml to the sulfo-SMCC-treated scaffolds. All constructs were incubated overnight at 4°C. The RGDC peptide immobilized density was approximately $6.35 \times 10^{-10}$ mol/cm$^2$ [24]. The peptide-conjugated scaffolds were washed conjugation buffer twice and in PBS three times, then dried under a vacuum at room temperature overnight.

## 6.3.3  Sodium Hydroxide Hydrolysis

The discs and scaffolds were submerged in 5 M NaOH (Certified A.C.S, Fisher Scientific) at room temperature on a shaker for 72 hours. Thereafter, the constructs were soaked in distilled water and 90% ethanol for 3 hours. The pH of the resultant supernatant stabilized at 7.4. For three scaffolds, before NaOH treatment, the dry weight of the

scaffolds was recorded. After treatment, the scaffolds were dried and their dry weights were recorded. The percent weight loss was calculated using Equation 6.1.

$$weight\ loss\ (\%) = \frac{M_{initial} - M_{final}}{M_{initial}} \times 100, \qquad\qquad \text{Equation 6.1}$$

where $M_{initial}$ and $M_{final}$ are the weights of the dried untreated and treated samples, respectively.

### 6.3.4  Surface Wettability

The wettability of the control and modified PCL surface was determined by measurements of the water contact angle made on the surface of the flat disc (see Fig 6.3) (n = 3) using a goniometer (Rame-Hart Instrument Co., Netcong, NJ). The discs were dried for 24 hours prior to measurement. The measurements were made at room temperature. A digital camera (Net GmbH 1394 Digital Camera) captured the series of advancing sessile water drops for 30-35 samples. The contact angles were extracted from the collected series using image processing software (Advanced DROP Image Software, Rame-Hart Instrument Co., Netcong, NJ). Surfaces with smaller contact angles were characterized as less hydrophobic.
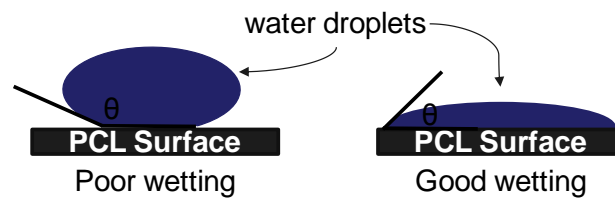


**Figure 6.3 Look how we measure the wettability of a surface.**

### 6.3.5  Static Cell Culture

Human Umbilical Vein ECs were isolated from harvested umbilical cords and acquired from the Stegmann Lab. The HUVECs were used at Passage 8 or 9. The initial seeding density was between 2,500 - 5,000 cells/cm$^2$. The cells were cultured until 70-80% confluence (4-6 days after plating). The HUVECs were cultured in EC media (EBM-2®, Lonza, Walkersville, MD) consisting of fetal bovine serum, ascorbic acid,

167

gentamicin/amphotericin-B, VEGF, hydrocortisone, human epidermal growth factor, human Fibroblast growth factor-basic, heparin, and human recombinant analog of insulin-like growth factor-I. Cell culture studies were performed in 24-well TCPS (discs) and 48-well TCPS (scaffolds) under static incubation (humidified atmosphere, 37°C, 5% $CO_2$) conditions. Prior to cell seeding, all constructs were sterilized under an ultraviolet (UV) lamp for one hour, equilibrated in PBS (Dulbecco) for 30 minutes, and then submerged in EC media once for 30 minutes. Heparinized constructs were sterilized by UV prior to the addition of VEGF.

The seeding densities were $1.2 \times 10^4$ cells/disc for discs with a surface area of 1362 mm$^2$ and $9.0 \times 10^4$ cells/scaffold for scaffolds with a surface area of 177 mm$^2$. A cell suspension of known cell density was added to the top of each disc. Similarly, the top of the scaffolds was seeded, then incubated for 30 minutes, before they were flipped to expose the bottom of the scaffold for seeding. Fig. 5.4 illustrates the drop-wise seeding technique used. The media was changed every other day. The ten experimental groups are shown in Table 6.2. The effect of sodium hydroxide treatment, bound VEGF and bound RGD on cellular behavior was investigated by seeding cells onto PCL discs and scaffolds modified with the respective treatments (to be referred to as PCL-N, PCL-HV and PCL-R, respectively). Untreated PCL served as the control. Heparinized constructs with no VEGF present (to be referred to as PCL-H) were compared to Group 2 and 3 from Table 6.1. The cells were cultured for up to four days.

**Table 6.2 Experimental groups for in vitro static HUVEC culture.**

| Group | Construct Type | Treatment | Attachment | Distribution | Proliferation | Cell Function |
|-------|----------------|-----------|------------|--------------|---------------|---------------|
| 1 | Discs | PCL | 1 | — | 3 | 3 |
| 2 | | PCL-NaOH | 1 | — | 3 | 3 |
| 3 | | PCL-RGD | 1 | — | 3 | 3 |
| 4 | | PCL-Heparin | 1 | — | 3 | 3 |
| 5 | | PCL-Heparin -VEGF | 1 | — | 3 | 3 |
| 6 | Scaffolds | PCL | 1 | 1,3 | 3 | 3 |
| 7 | | PCL-NaOH | 1 | 1,3 | 3 | 3 |
| 8 | | PCL-RGD | 1 | 1,3 | 3 | 3 |
| 9 | | PCL-Heparin | 1 | 1,3 | 3 | 3 |
| 10 | | PCL-Heparin -VEGF | 1 | 1,3 | 3 | 3 |
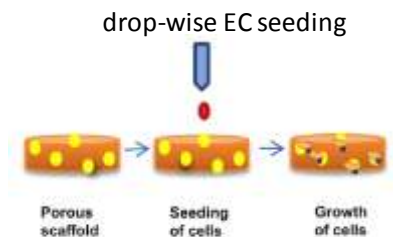
**Figure 6.4 Drop-wise seeding method used for discs and scaffolds.**

### 6.3.6 Cell Viability

Cell attachment, proliferation and spatial distribution across the disc and/or scaffold were determined by a MTT assay. Prior to the conducting the assay, the culture medium was aspirated and the discs and scaffolds were washed in PBS three times to remove unattached cells. The colorimetric MTT assay used a 3-(4,5-dimethylthiazol-2-yl)-5-(3-carboxymethoxyphenyl)-2-(4-sulfonphenyl)-2H-tetrazolium (MTS tetrazolium) compound (Cell-Titer 96 Aqueous One Solution Cell Proliferation Assay; Promega, Madison, WI). The seeded ECs were incubated for three hours with the 20% MTS solution in serum-free culture medium in 48-well paltes. The metabolically active ECs reacted with the of MTS reagent to produce soluble formazan product. From each scaffold-well, three aliquots of the reagent were pipetted into a 96-well plate then placed into a microplate reader (Multiskan Spectrum, Thermo Electron Corporation). The absorbance was measured at 490 nm.

Cell attachment was assessed within 24 hours (Day 1) of initial attachment. Cell proliferation was evaluated after 72 hours (Day 3) of static culture. The spatial distribution was evaluated on Day 1 and 3. The three-dimensional scaffolds were sectioned in three parts with a razor. The distribution of seeded cells on scaffolds was determined over the three sections: top (20% of surface area), center (60% of surface area) and bottom (20% of surface area). Comparisons between edge and center cell viability account for the difference in surface area.

### *6.3.7* **Von Willebrand Factor (vWF) Assay**

On day 3, the amount of vWF released into the medium was determined using the standard protocol from a commercially available vWF ELISA kit (AssayPro, St Charles, Missouri).

### *6.3.8* **Statistical Analysis**

Each assay was performed in triplicate for three independent samples. The results were expressed as means ± standard deviations. In Minitab (Minitab Inc., State College, PA), Pairwise comparisons between the treatment groups was performed with the ANOVA procedure, followed by Tukey's post hoc test at a significance level of P-value < 0.05 or P-value < 0.01. Two-tail Student's *t*-test assuming equal variance was used to determine whether there was significant difference between two groups. P-values below 0.05 were considered significant.

## 6.4 RESULTS

### 6.4.1 Effect of Surface Modifications on PCL Wettability

The surface charge of untreated PCL was largely neutral due to the prevalence of ester groups (-COO-) in PCL molecules, which made it weakly acidic. The negatively charged residue from the RGD peptide and the strong negative charge of heparin deposited a negative charge onto the PCL surface. Hydrolyzation broke down the ester groups present in PCL molecules and formed carboxylic and alcohol by-products, which created a negative surface charge. Figure 6.5 shows the range of contact angles measured for the four surface treatments. The untreated PCL exhibited the largest contact angle and was significantly different from all other groups (P-value < 0.01). All groups were signficantly different from one another (P-value < 0.01). The average degree of the contact angle increased as follows: PCL-N (14° ± 8°) < PCL-R (29° ± 19°) < PCL-H (59° ± 11°) < PCL (87° ± 12°). The chemical modification produced a significantly lower contact angle than the biological modifications and control group.

170
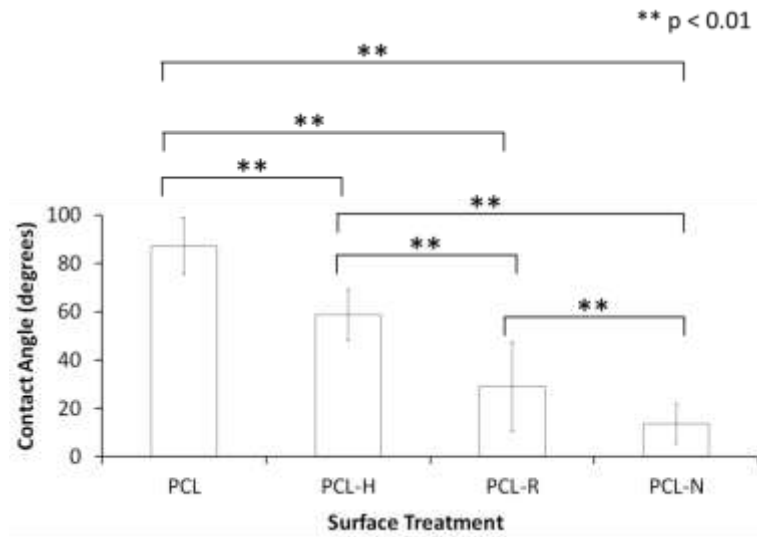
**Figure 6.5 Contact angles (ascending) for surface modified PCL surfaces (n = 3). Illustrates statistical significant difference between each group (p-value < 0.01). PCL – untreated; PCL-H – Heparinized; PCL-R – RGD immobilization; PCL-N – NaOH-treated.**

## 6.4.2 Effect of Surface Modifications on HUVEC proliferation

After day 1, HUVECs cultured on PCL-HV discs and scaffolds exhibited the greatest average number of cells than all other groups (Fig 6.6a). On PCL-HV discs, the average number of cells was 4 times higher, and on scaffolds, seven times greater than the control group. For both discs and scaffolds, PCL-HV groups were statistically different from the untreated control group. All scaffold surface modified groups exhibited greater proliferation than the control group (Fig 6.6a). On the scaffolds, the average number of cells on PCL, PCL-R, PCL-N, PCL-HV were $5,183 \pm 2,951$, $49,999 \pm 10,541$, $28,517 \pm 6,018$ and $37,421 \pm 6,786$, respectively. All groups were statistically different from the control group. For discs, the PCL-N proliferation was comparable to the PCL control group (Fig 6.6a). The mean percent degradation for NaOH-treated PCL scaffolds (at room temperature, 25°C) was $8.5 \pm 1.2\%$ and $0.43 \pm 0.38\%$ for PCL disks (n = 3). On day 3, the trends remained the same (Fig 6.6b). For the scaffolds, there was no statistical difference between PCL-R ($51,385 \pm 4,974$), PCL-N ($50,537 \pm 7,324$) and PCL-HV ($56,391 \pm 5,085$) scaffolds. On PCL-R, PCL-N and PCL-HV discs, the average number of cells was twice as high, and on scaffolds, three times greater than the control group.

171
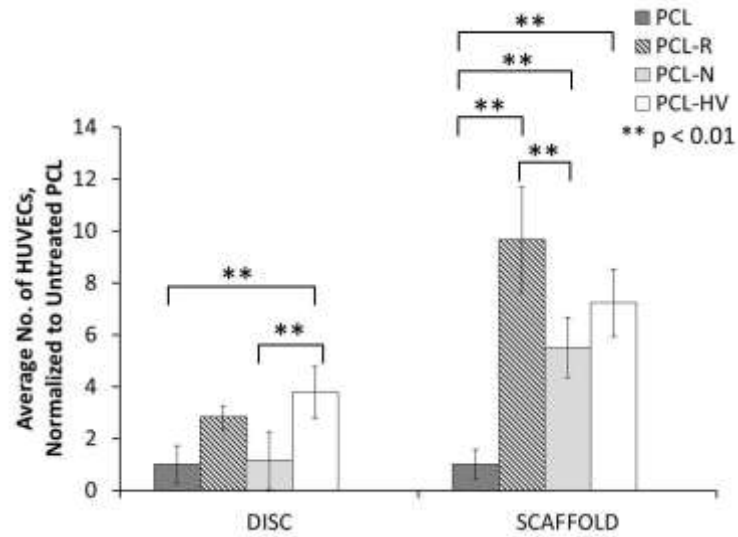
(a)
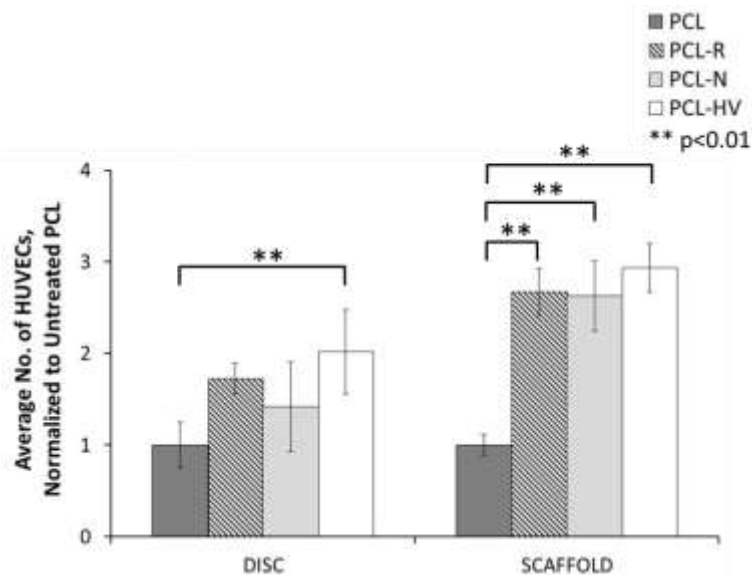


(b)

**Figure 6.6 The average amount of HUVECs proliferated at (a) day 1 and (b) day 3 for discs and scaffolds (n = 3). Statistically significance shown between groups with * (p < 0.01).**

### 6.4.3 Effect VEGF conjugation on HUVEC proliferation

Both PCL-HV discs and scaffolds demonstrated an increase in proliferation on day 1 and 3 of culture (Fig. 6.7). The presence of VEGF (10μg loaded) on heparinized scaffolds

promoted slightly higher cell proliferation. After day 1, on discs, the presence of VEGF results in an average cell amount of three times as much as the heparinized discs with no VEGF present. However the two groups, PCL-H and PCL-HV were not statistically different on day 1 or 3, the relationship between PCL-H to PCL-HV was roughly one to one. Based on the VEGF conjugation efficiency study, $8.7 \pm 0.01$ µg (87% of initial loaded amount) of VEGF was immobilized on to untreated scaffolds and $8.1 \pm 1.2$ µg (81 % of initial loaded amount) to heparinized scaffolds. $8.5 \pm 0.23$ µg (85% of initial loaded amount) of VEGF was immobilized on to untreated discs and $7.9 \pm 0.22$ µg (79% of initial loaded amount) to heparinized discs. Over seven days, there was less than 10 ng/day (0.1% of initial loaded amount) release of VEGF from either group (PCL or PCL-HV), for discs or scaffolds (Fig 6.8a-b). Table 6.3 summarizes the release of VEGF over 7 days. There is negligible release (less than 10 ng/day) for untreated and heparinized scaffolds over the entire duration of the study. After day 1, the untreated discs demonstrated negligible release. The heparinized discs demonstrated stimulating (greater than 10ng/day) release levels from day 1-3, with a slight drop on days 5 and 7.
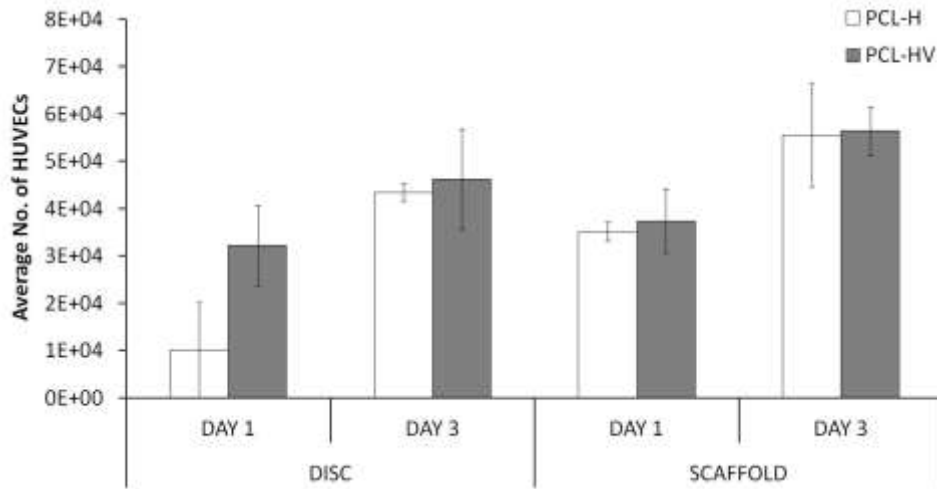


**Figure 6.7 Average amount of HUVECs at day 1 and 3 on heparin immobilized PCL discs and scaffolds without (PCL-H) and with 10µg of VEGF loaded (PCL-HV). No statistical significance between PCL constructs with and without VEGF loaded (p-value > 0.05). (n = 3)**
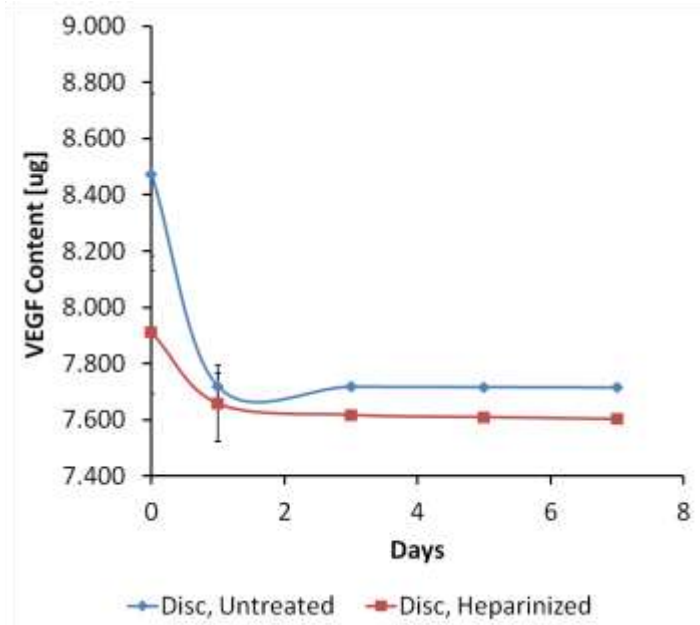
(a)
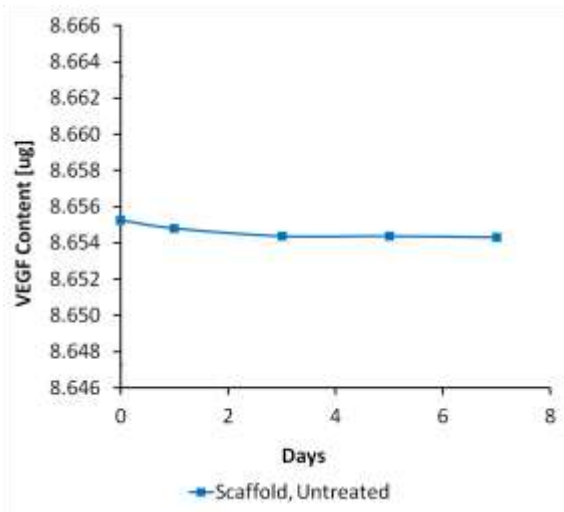


(b)
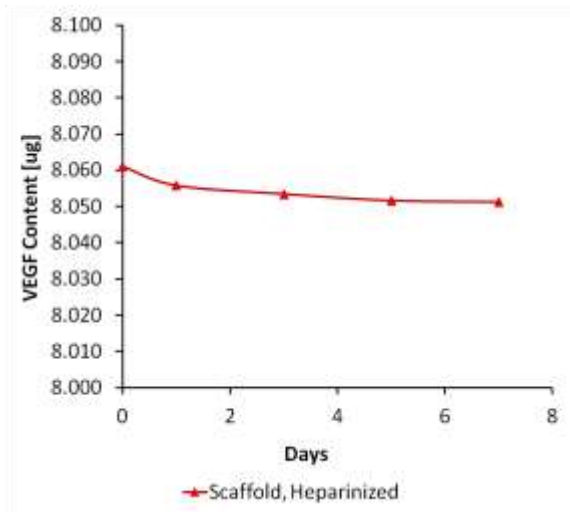
(c)

**Figure 6.8 VEGF retention over 7 days for (a) heparinized and untreated discs and (b) untreated scaffolds and (c) heparinized scaffolds (n=3). 10 μg of VEGF loaded and heparin (based on values in Table 6.1) onto discs and scaffolds.**

**Table 6.3 VEGF release over 7 days. Burst release on day 1 for all groups, except the untreated scaffolds.**

| | VEGF RELEASE (ng) | | | |
|---|---|---|---|---|
| | Discs | | Scaffolds | |
| | Heparinized | Untreated | Heparinized | Untreated |
| Day 1 | 254 | 754 | 5 | 0.4 |
| Day 3 | 40 | 1 | 2 | 0.4 |
| Day 5 | 8 | 1 | 2 | 0 |
| Day 7 | 7 | 1 | 0.4 | 0.1 |

### 6.4.4 Effect of Surface Modifications on the Localization of HUVECs

Sectioning and MTT analysis of the three-dimensional scaffolds revealed that the initial distribution of HUVECs on each treatment group had high variability at the edge and center of the scaffold (Fig. 6.9a). By day 3, the PCL-N (average number of HUVECs: 27,310 ± 9,880) and PCL-R (average number of HUVECs: 61,946 ± 22,390) group showed higher HUVEC densities at the edge of the scaffold, compared to the control group (average number of HUVECs: 14,675 ± 8,762). While PCL-HV (average number of HUVECs: 36,486 ± 13,913) demonstrated at a higher density at the center compared to the control group (average number of HUVECs: 29,549 ± 2,218) (Fig 6.9b). There was no statistical difference among the groups, in terms of the edge density. At day 3, the edge-to-center ratios for PCL, PCL-R, PCL-N and PCL-HV were 2.3 ± 1.5, 1.0 ± 2.0, 1.3 ± 1.6 and 0.2 ± 0.3 respectively. PCL and PCL-N showed more uniform distribution, with PCL-N promoting greater cell proliferation.
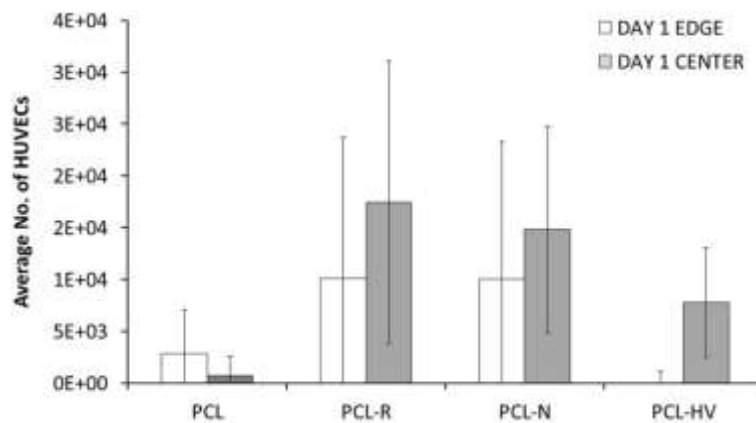
(a)
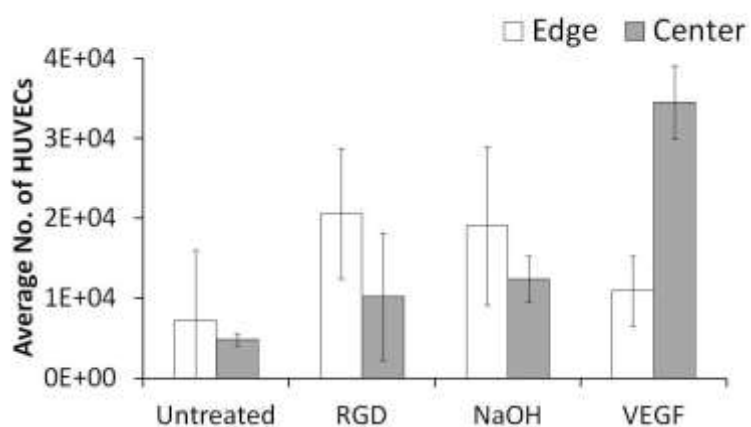


(b)

**Figure 6.9 Average number of HUVECs at (a) day 1 and (b) day 3 at the edge and center of a sectioned scaffold. There was no statistical significance between localization of HUVECs on day 1 across surface treatments or regions of the scaffold (p-value > 0.05) (n = 3). By day 3, there was no statistical signficance at the edges between the PCL surface treatments associated with **, but RGD-modified scaffold showed the largest edge attachment and the VEGF-loaded scaffold showed the greatest attachment at the center of the scaffold (p-value > 0.05). PCL – untreated; PCL-H – Heparinized; PCL-R – RGD immobilization; PCL-N – NaOH-treated.**

### 6.4.5 Effect of Surface Modifications on vWF release

The cell response to the treatment groups showed that PCL-N, PCL-R and PCL-HV released significantly lower levels of vWF than the control group (Fig. 6.10). For discs, the vWF release was twice as low, while for scaffolds the release was 3-4 times lower

than the respective control groups. However, there was no statistical difference among the release amounts among the surface modified groups. For discs, the vWF concentrations for PCL, PCL-R, PCL-N and PCL-HV were as follows $5.3 \pm 0.16$ IU/10,000 cells, $3.4 \pm 0.14$ IU/10,000 cells, $3.1 \pm 0.17$ IU/10,000 cells and $2.3 \pm 0.03$ IU/10,000 cells. For scaffolds the vWF concentrations were $6.0 \pm 0.11$ IU/10,000 cells, $2.1 \pm 0.18$ IU/10,000 cells, $1.6 \pm 0.07$ IU/10,000 cells and $1.4 \pm 0.05$ IU/10,000 cells, respectively.
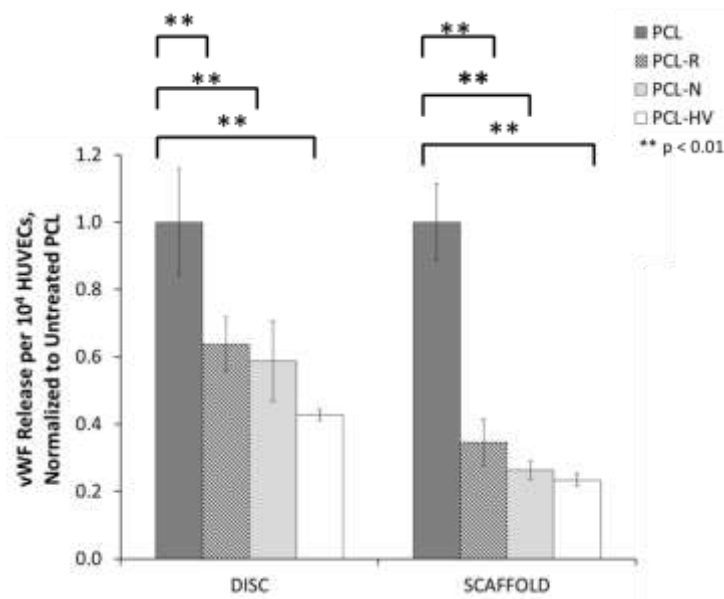


**Figure 6.10 Relative amount of vWF released by surface modified discs and scaffolds into media over 48 hours, at day 3 (n = 3). Normalized to the amount of HUVECs at day 3. PCL – untreated; PCL-H – Heparinized; PCL-R – RGD immobilization; PCL-N – NaOH-treated.**

## 6.5 DISCUSSION AND CONCLUSIONS

Within a three-dimensional *in vitro* bioreactor, each component of the system plays a critical role in recreating appropriate conditions for chemical and mechanical stimulation of cells. In particular, the following factors are critical: (i) scaffold composition and biocompatibility, (ii) scaffold architecture and associated properties, (iii) cell line and culture type, (iv) perfusion source and hydrodynamic conditions, (v) oxygen exchange / pH levels, (vi) presence of pro-angiogenic factors, (vii) initial static cell culture and (viii)

177

cell distribution. The work presented in this chapter is an initial step to a larger study that would systematically evaluate each of these parameters. Chapter 5 evaluated the influence of architecture on the adherent cells under constant, non-pulsatile flow conditions, within the designed bioreactor. In this chapter, the results have demonstrated the effect of surface modified PCL discs (two-dimensional) and scaffolds (three-dimensional) on the proliferation and activity of HUVECs in an initial static culture. These static cultures are a typical precursor step to dynamic bioreactor cultures.

Among the four groups (PCL, PCL-V, PCL-R, PCL-N), the hydrolyzed scaffolds exhibited the largest wettability (Fig. 6.5). Each of the surface modifications showed improved wettability compared to the control group. Each contact angle range (minimum/maximum) was statistically different from all other groups. Based on its low contact angles, PCL-N had the most hydrophilic surface, followed by PCL-R and lastly PCL-H.

For discs and scaffolds, PCL-HV demonstrated significantly higher proliferation levels than the control, at day 1 and 3 (Fig. 6.6a-b). Day 1 proliferation on PCL and PCL-N discs were similar contrary to what would be expected based on their respective wettabilities (Fig. 6.6 and Fig 6.6a). For all scaffolds, more cells proliferated on the treatment groups than on the control, with PCL-R demonstrating the largest average number of cells (Fig. 6.6a-b). The NaOH degradation to discs was lower than for scaffolds. This decrease in degradation may have affected the degree of surface roughness and surface area achieved on the discs. For both discs and scaffolds, PCL-R and PCL-HV demonstrated the highest levels of proliferation and were not statistically different from one another (Fig. 6.6a-b). For both constructs, the average number of cells peaks at day three indicating that cell quiescence may have occurred between 24-72 hours, once the ECs reach a high confluence on the constructs (Fig. 6.6b). By day 3, there is no statistical difference in viable ECs among the PCL-R, PCL-N and PCL-HV discs or scaffolds (Fig. 6.6b). All scaffold treatment groups had more viable cells than the control group. The uniform proliferation across treatment groups may indicate that although PCL-R and PCL-HV promoted greater attachment (or initial proliferation during the initial attachment period), for scaffolds and discs, the critical factor in proliferation may be the increased surface wettability, which was exhibited across all treatment groups.

The investigation on dose effect of 10μg of loaded VEGF revealed that PCL-HV demonstrated approximately the same average number of viable cells in comparison to PCL-H at day 1 and day 3 (Fig. 6.7). There was no significant difference in the number of proliferated cells between the two groups. There was no statistical difference in proliferation at day 1. The results indicate that a larger amount of VEGF must be loaded to produce a cell response. The VEGF release study showed that there was negligible release across all constructs, except for the heparinized disc group (Fig. 6.8 and Table 6.3). The VEGF content that remains on the scaffold may be bound too tightly for gradual release or adequate exposure of functional end groups. Further investigations should compare PCL-H to PCL-R proliferation over 72 hours. As well, the dose of effect of VEGF should be investigated to determine if larger doses can elicit a distinctive response compared to PCL-H, in less than 72 hours.

Heparin dosage can be increased in effort to improve VEGF binding and reduce opportunities for VEGF adsorption onto the scaffold. As such, in a second proliferation study (data not shown), designed to evaluate the heparin dose cell response to increased heparin, the PCL, PCL-R and PCL-N treatment groups were cultured over 72 hours, with the addition of a high dose heparin group (5 mg on discs and 10 mg on scaffolds) with 10 μg of VEGF loaded. PCL-HV (high heparin content) had less and statistically different average number viable cells than PCL-R, on both scaffolds and discs. However, the increase in dose invoked a negative cell response, which made cell proliferation comparable to the control group. The heparin dose effect should be further evaluated, to determine an optimal dosage of VEGF needed to counteract potential heparin inhibition.

The decrease in cumulative vWF released over 48 hours was roughly the same for all treatment groups on discs and scaffolds. They were all significantly lower than the control group. Starke et al. reported that a decrease in vWF was linked to increase *in vitro* angiogenesis [44]. Based on this finding, all surface modifications demonstrated greater angiogenic function: PCL-HV > PCL-N > PCL-R.

Simulations in chapter 5 showed that for *in vitro* perfusion bioreactor, apoptosis is greater at the edges of a scaffold, where the largest shear stresses are experienced. As such, a surface modification to a PCL scaffold that produces high EC density at the edges and

179

core would provide the ideal spatial distribution for both *in vitro* and long-term *in vivo* application. The edges of PCL-R supported the highest average number of ECs among all groups (Fig. 6.9b). The average cell viability at the edges of PCL-R was higher than all other groups, although not statistically different. There was also no statistical difference between the viability of cells at the core of the scaffold.

Overall, the implications to a bioreactor study were (i) each surface modification improved the hydrophilicity and as a result the cytocompatibility of PCL (Fig. 6.5), (ii) there was no significant difference in EC proliferation among modifications over three days (Fig. 6.6b), (iii) ECs should be cultured for less than 72 hours to avoid quiescence, but promote attachment/proliferation (Fig. 6.6b), (iv) there was no significant difference in EC function, in terms of vWF release, among the modified surfaces, making the cheaper modification (PCL-R compared to PCL-HV) advantageous (Fig. 6.10), and (v) the high edge density of RGD-modified scaffolds after 72 hours makes it ideal for bioreactor studies, without compromising EC density at the core of the scaffold (Fig. 6.9b). In a preliminary assembly and run of the bioreactor enclosing a PCL-R scaffold (after 72 hour static culture), after 1 hour of perfusion, at room temperature, there was approximately a 30% retention of ECs on the scaffolds (n = 3). Further studies are required to determine the viability and maturation of cells with time within an incubator. Most three-dimensional bioreactor studies employ translucent matrices, such as alginate, Matrigel or collagen, which can be readily imaged to assess EC migration and the formation of tubules during angiogenesis. However, given the proposed bioreactor design, further studies are needed to determine the ideal method of evaluating cell and vessel form and function within this PCL bioreactor. Cumulative and cyclic protein/factor production (i.e. vWF) may be used to assess changes, but typically vessel morphology is the standard metric for evaluation of angiogenesis. Chapter 7 discusses imaging opportunities for non-translucent biomaterials.

Tissue engineering often focuses on the treatment and restoration of damaged tissue sites to normal function and/or morphology. However, given its toolbox of biomaterials, computational models, bioengineering approaches and cell culture systems, the field of tissue engineering inherently lends itself to the development of disease systems [45]. As such, over the past few years, the challenge of moving in vitro tumor modeling from a

two-dimensional to three-dimensional in vitro platform has been the focus of interdisciplinary work between cancer researchers and tissue engineers [46-48]. Recent studies have highlighted the biomechanical influence of three-dimensional extracellular matrices (and adhering components) on the growth of normal tissue and solid tumors [49-50]. The practical implementation of a cell bioreactor (with the addition of other signaling factors) for the growth of cancerous tumor models remains to be further explored. A localization of HUVECs on the scaffold that provides a higher density at the edges versus the center, may favor necrosis typical of tumorigenesis, in a co-culture with tissue cell lines.

## 6.6 ACKNOWLEDGEMENTS

## 6.7 REFERENCES

[1] Peyton, S., Ghajar, C., Khatiwala, C., and Putnam, A. The emergence of ECM mechanics and cytoskeletal tension as important regulators of cell function. Cell Biochemistry and Biophysics **47**, 300, 2007.

[2] Teichmann J, Morgenstern A, Seebach J, Schnittler HJ, Werner C, Pompe T. The control of endothelial cell adhesion and migration by shear stress and matrix-substrate anchorage. Biomaterials **33,** 2012.

[3] Lee, E.J., and Niklason, L.E. A novel flow bioreactor for in vitro microvascularization. Tissue Eng Part C Methods **16**, 1191, 2010.

[4] Ng, C.P., Helm, C.L., and Swartz, M.A. Interstitial flow differentially stimulates blood and lymphatic endothelial cell morphogenesis in vitro. Microvasc Res **68**, 258, 2004.

[5] Frese, J., Motejlek, K., Schmitz-Rode, T., Neulen, J., and Jockenhoevel, S. Bioreactor Development for the Study of Angiogenesis within Tissue Engineered Constructs. **150**, 2010.

[6] Helm, C.L., Zisch, A., and Swartz, M.A. Engineered blood and lymphatic capillaries in 3-D VEGF-fibrin-collagen matrices with interstitial flow. Biotechnol Bioeng **96**, 167, 2007.

[7] Rouwkema J, de Boer J, Van Blitterswijk CA. Endothelial cells assemble into a 3-dimensional prevascular network in a bone tissue engineering construct. Tissue Engineering **12** ,2006.

[8] Santos MI, Unger RE, Sousa RA, Reis RL, Kirkpatrick CJ. Crosstalk between osteoblasts and endothelial cells co-cultured on a polycaprolactone-starch scaffold and the in vitro development of vascularization. Biomaterials **30**, 2009.

[9] Grellier M, Bordenave L, Amedee J. Cell-to-cell communication between osteogenic and endothelial lineages: implications for tissue engineering. Trends Biotechnol **27**, 2009.

[10] Drury, J.L., and Mooney, D.J. Hydrogels for tissue engineering: scaffold design variables and applications. Biomaterials **24**, 4337, 2003.

[11] Misch CE, Qu ZM, Bidez MW. Mechanical properties of trabecular bone in the human mandible: Implications for dental implant treatment planning and. surgical placement. *J* Oral Maxillofac Surg **57**, 1999.

[12] Lee, E.J., and Niklason, L.E. A novel flow bioreactor for in vitro microvascularization. Tissue Eng Part C Methods **16**, 1191, 2010.

[13] Ng, C.P., Helm, C.L., and Swartz, M.A. Interstitial flow differentially stimulates blood and lymphatic endothelial cell morphogenesis in vitro. Microvasc Res **68**, 258, 2004.

[14] Frese, J., Motejlek, K., Schmitz-Rode, T., Neulen, J., and Jockenhoevel, S. Bioreactor Development for the Study of Angiogenesis within Tissue Engineered Constructs. **150**, 2010.

[15] Helm, C.L., Zisch, A., and Swartz, M.A. Engineered blood and lymphatic capillaries in 3-D VEGF-fibrin-collagen matrices with interstitial flow. Biotechnol Bioeng **96**, 167, 2007.

[16] Williams, J.M., Adewunmi, A., Schek, R.M., Flanagan, C.L., Krebsbach, P.H., Feinberg, S.E., Hollister, S.J., and Das, S. Bone tissue engineering using polycaprolactone scaffolds fabricated via selective laser sintering. Biomaterials **26**, 4817, 2005.

[17] Dash, T.K., and Konkimalla, V.B. Poly-ϵ-caprolactone based formulations for drug delivery and tissue engineering: A review. J Control Release **158**, 15, 2012.

[18] Novosel, E.C., Kleinhans, C., and Kluger, P.J. Vascularization is the key challenge in tissue engineering. Advanced Drug Delivery Reviews **63**, 300, 2011.

[19] Choong, C.S., Hutmacher, D.W., and Triffitt, J.T. Co-culture of bone marrow fibroblasts and endothelial cells on modified polycaprolactone substrates for enhanced potentials in bone tissue engineering. Tissue Eng **12**, 2521, 2006.

[20] Serrano, M.C., Portoles, M.T., Vallet-Regi, M., Izquierdo, I., Galletti, L., Comas, J.V., and Pagani, R. Vascular endothelial and smooth muscle cell culture on NaOH-treated poly(epsilon-caprolactone) films: a preliminary study for vascular graft development. Macromol Biosci **5**, 415, 2005.

[21] Ruoslahti, E. RGD and other recognition sequences for integrins. Annu Rev Cell Dev Biol **12**, 697, 1996.

[22] Hersel, U., Dahmen, C., and Kessler, H. RGD modified polymers: biomaterials for stimulated cell adhesion and beyond. Biomaterials **24**, 4385, 2003.

[23] Zhang, H., Lin, C.Y., and Hollister, S.J. The interaction between bone marrow stromal cells and RGD-modified three-dimensional porous polycaprolactone scaffolds. Biomaterials **30**, 4063, 2009.

[24] Zhang, H., and Hollister, S. Comparison of bone marrow stromal cell behaviors on poly(caprolactone) with or without surface modification: studies on cell adhesion, survival and proliferation. J Biomater Sci Polym Ed **20**, 1975, 2009.

[25] Wang, X., Heath, D.E., and Cooper, S.L. Endothelial cell adhesion and proliferation to PEGylated polymers with covalently linked RGD peptides. J Biomed Mater Res A **100**, 794, 2012.

[26] Ferrara, N., Gerber, H.P., and LeCouter, J. The biology of VEGF and its receptors. Nat Med **9**, 669, 2003.

[27] Veikkola, T., Karkkainen, M., Claesson-Welsh, L., and Alitalo, K. Regulation of angiogenesis via vascular endothelial growth factor receptors. Cancer Res **60**, 203, 2000.

[28] Odedra, D., Chiu, L.L., Shoichet, M., and Radisic, M. Endothelial cells guided by immobilized gradients of vascular endothelial growth factor on porous collagen scaffolds. Acta Biomater **7**, 3027, 2011.

[29] Taguchi T, Kishida A, Akashi M, Maruyama I. Immobilization of human vascular endothelial growth factor (VEGF165) onto biomaterials: an evaluation of the biological activity of immobilized VEGF165. J Bioactive Compatible Polym **15**, 2000.

[30] Rahman N, Purpura KA, Wylie RG, Zandstra PW, Shoichet MS. The use of vascular endothelial growth factor functionalized agarose to guide pluripotent stem cell aggregates toward blood progenitor cells. Biomaterials **31**, 2010.

[31] Shen YH, Shoichet MS, Radisic M. Vascular endothelial growth factor immobilized in collagen scaffold promotes penetration and proliferation of endothelial cells. Acta Biomater **4**, 2008.

[32] Koch S, Yao C, Grieb G, Prevel P, Noah EM, Steffens GC. Enhancing angiogenesis in collagen matrices by covalent incorporation of VEGF. J Mater Sci Mater Med **17**, 2006.

[33] Chiu LL, Radisic M. Scaffolds with covalently immobilized VEGF and angiopoietin-1 for vascularization of engineered tissues. Biomaterials **31**, 2010.

184

[34] Davies, N., Dobner, S., Bezuidenhout, D., Schmidt, C., Beck, M., Zisch, A.H., and Zilla, P. The dosage dependence of VEGF stimulation on scaffold neovascularisation. Biomaterials **29**, 3531, 2008.

[35] Richardson, T.P., Peters, M.C., Ennett, A.B., and Mooney, D.J. Polymeric system for dual growth factor delivery. Nat Biotech **19**, 1029, 2001.

[36] Silva, E.A., and Mooney, D.J. Effects of VEGF temporal and spatial presentation on angiogenesis. Biomaterials **31**, 1235, 2010.

[37] Ozawa, C.R., Banfi, A., Glazer, N.L., Thurston, G., Springer, M.L., Kraft, P.E., McDonald, D.M., and Blau, H.M. Microenvironmental VEGF concentration, not total dose, determines a threshold between normal and aberrant angiogenesis. Journal of Clinical Investigation **113**, 516, 2004.

[38] Singh, S., Wu, B.M., and Dunn, J.C.Y. The enhancement of VEGF-mediated angiogenesis by polycaprolactone scaffolds with surface cross-linked heparin. Biomaterials **32**, 2059, 2011.

[39] Masters, K.S. Covalent growth factor immobilization strategies for tissue repair and regeneration. Macromol Biosci **11**, 1149, 2011.

[40] Zhu, C.S., Xu, J.B., Yu, M.H., Zhao, W., Zhang, Y., Yao, F.L., and Yang, J. The Immobilization of VEGF-Fc for Promoting Endothelial Cells Proliferation in Porous PCL Scaffolds. Advanced Materials Research **554**, 1721, 2012.

[41] Gitay-Goren, H., Soker, S., Vlodavsky, I., and Neufeld, G. The binding of vascular endothelial growth factor to its receptors is dependent on cell surface-associated heparin-like molecules. J Biol Chem **267**, 6093, 1992.

[42] Richardson, T.P., Peters, M.C., Ennett, A.B., and Mooney, D.J. Polymeric system for dual growth factor delivery. Nat Biotech **19**, 1029, 2001.

[43] G.T. Hermanson Bioconjugate techniques Academic Press, San Diego, CA (1996).

[44] Starke, R.D., Ferraro, F., Paschalaki, K.E., Dryden, N.H., McKinnon, T.A.J., Sutton, R.E., Payne, E.M., Haskard, D.O., Hughes, A.D., Cutler, D.F., Laffan, M.A., Randi, A.M. Endothelial von Willebrand factor regulates angiogenesis Blood **3**, 117, 2011.

[45] Hutmacher, D.W., Horch, R.E., Loessner, D., Rizzi, S., Sieh, S., Reichert, J.C., Clements, J.A., Beier, J.P., Arkudas, A., Bleiziffer, O., and Kneser, U. Translating tissue engineering technology platforms into cancer research. Journal of cellular and molecular medicine **13**, 1417, 2009.

[46] Fischbach, C., Chen, R., Matsumoto, T., Schmelzle, T., Brugge, J.S., Polverini, P.J., and Mooney, D.J. Engineering tumors with 3D scaffolds. Nature Methods **4**, 855, 2007.

[47] Verbridge, S.S., Chandler, E.M., and Fischbach, C. Tissue-engineered three-dimensional tumor models to study tumor angiogenesis. Tissue engineering. Part A **16**, 2147, 2010.

[48] Rabbany, S.Y., James, D., and Rafii, S. New dimensions in vascular engineering: opportunities for cancer biology. Tissue engineering. Part A **16**, 2157, 2010.

[49] Peyton, S., Ghajar, C., Khatiwala, C., and Putnam, A. The emergence of ECM mechanics and cytoskeletal tension as important regulators of cell function. Cell Biochemistry and Biophysics **47**, 300, 2007.

[50] Lunt, S., Chaudary, N., and Hill, R. The tumor microenvironment and metastatic disease. Clinical and Experimental Metastasis **26**, 19, 2009.

# CHAPTER 7

## A Review of Three-dimensional Imaging Methods for Assaying Tubule Formation in Three-Dimensional *In Vitro* Culture Models

**Abstract**

The structure and function of blood vessels is a key determinant of the viability and proliferation of cells in both healthy and diseased tissue. *In vivo* imaging of angiogenesis is a routine procedure to monitor treatment responses and disease progression, in both animal research studies and clinical practice. Two-dimensional microscopy is often implemented in biomedical research to visualize cell monolayers. Recently, investigations of physiologically-relevant *in vitro* three-dimensional culture models have heightened the need for three-dimensional, non-invasive methods to evaluate vessel formation and function within tissue. In order to garner real-time, structural and/or functional information from these models, various imaging techniques were modified to track angiogenesis within *in vitro* studies that employ synthetic or natural matrices. Advances in medical imaging systems and image processing make multi-scale imaging from the tissue-level down to molecular-level, a viable tool for the qualitative assessment or quantification of angiogenesis within *in vitro* three-dimensional culture studies. Static and dynamic image series acquired using imaging systems offer valuable temporal insight on the proliferation, migration and tubule anatomy of ECs involved in angiogenesis. Tissue properties, such as elasticity are also extracted from these images. In this article, we review the recent literature to demonstrate the utility and potential of imaging technologies when adapted to *in vitro* three-dimensional culture models. Magnetic resonance, optical, nuclear and ionizing radiation imaging systems are among the medical imaging systems discussed.

## 7.1 INTRODUCTION

Angiogenesis is a critical step to the sustainment of healthy regenerative tissue and to the growth of solid cancerous tumors. The determination of whether three-dimensional *in vitro* angiogenesis models can successfully re-create favorable environments for endothelial cell (EC) tubulation is key to their practical application to angiogenesis or tumor angiogenesis research. Recent studies explored the utility of physiologically-relevant angiogenesis and tumor angiogenesis culture models that provided biomechanical stimulus (via an extracellular matrix or flow): three-dimensional gel embedded matrices (collagen, fibrogen, alginate and Matrigel), three-dimensional biocompatible polymers and microfluidic models [1-10]. The success of these three-dimensional *in vitro* angiogenesis models in terms of their potential to sustain tissue viability (normal or pathological) is often qualitatively and quantitatively characterized by the structure and function of newly formed blood vessels [11-12]. The physical phenomenon of capillary sprouting, termed angiogenesis, is the process by which new capillary blood vessels are created, either as offshoots or as splits from existing vessels [13]. Tumor angiogenesis is the rate limiting stage of tumorigenesis, marked by initiation and sprouting of new vessels from existing neighboring vessels [14-15]. This stage encourages the survival and uncontrolled proliferation of cancerous cells by providing the cancerous site with access to nutrient and waste exchange [14]. Under healthy conditions, angiogenesis is marked by EC migration, initiation, formation, maturation, network remodeling, differentiation, and regression stages as cells grow into tubules and networks [14]. During tumor angiogenesis, the basement epithelial layer of the extracellular matrix (ECM) thins, the altered cells' mechanics allow for cell crowding and anchorage-independent growth, and the sensitivity to growth stimuli increases for neighboring cells [14-16]. The new vascular networks are markedly more tortuous and leaky, compared to a normal capillary network [17]. The vascular network created via tumor angiogenesis lacks the organization and maturation of vessels characteristic of normal vascular networks [17-18]. The formation of the vascular networks can be characterized in terms of EC biology (i.e. gene expression), EC proliferation, EC migration, EC differentiation and tubule formation [19]. Imaging techniques have increasingly been adapted to track the activity of ECs and changes in tissue properties indicative of the formation of

vascular networks (comprised of 4-10 micron vessels). These imaging techniques facilitate the evaluation of blood vessel development and/or regression within angiogenesis and tumor angiogenesis [20-22].

Commonly, static (well plates and natural/engineering constructs) and dynamic (microfluidics and *in vivo*) angiogenesis and tumor angiogenesis models are characterized based on results of histology and two-dimensional microscopy. These models are evaluated based on hypoxia distribution, epithelial proliferation, extracellular matrix composition, angiogenic factor secretions, the presence of transmembrane adhesion proteins, EC proliferation, blood vessel density, blood vessel diameter, tumor weight and tumor volume. Quantification of the tubule formation usually involves an estimation of the total or average number of tubules, lengths and area based on scaled measurements from a portion of the area of tubule growth. The presence and function of tubules is also quantitatively evaluated via enzyme-linked immunosorbent assays (ELISAs) that estimate the amount of EC surface glycoproteins that promote cell-cell adhesion, respectively, cluster of differentiation 31 (CD31) and von Willebrand factor (vWF).

Imaging-based tubule formation assays of two-dimensional *in vitro* systems evaluate properties visible from the top or bottom surface of a Petri dish or well plate. As such, quantification of cell behavior, specifically EC migration or formation into tubules during angiogenesis is easily discernible in static images captured from a camera, or light or electron microscope [23], as illustrated in Fig. 7.1a. Techniques such as histology (hematoxylin and eosin staining), and immunostaining for CD31 and vWF are used to visualize tubules [23-25], as shown in Fig. 7.1b. Microscopy techniques that yield two-dimensional topographic data, such as phase contrast and fluorescence imaging offers visualization and monitoring of *in vitro* vessel growth in translucent constructs, such as Matrigel. In a study of human umbilical vein endothelial cells (HUVECs) cultured on a Matrigel basement membrane matrix, Mezentsev et al. performed topological analysis on captured time-lapse microscopy data. The imaging data was qualitatively and quantitatively to evaluate the growth and regression of capillary-like networks over time in response to potential markers of EC dysfunction (endothelial microparticles) that were introduced during the observation period.
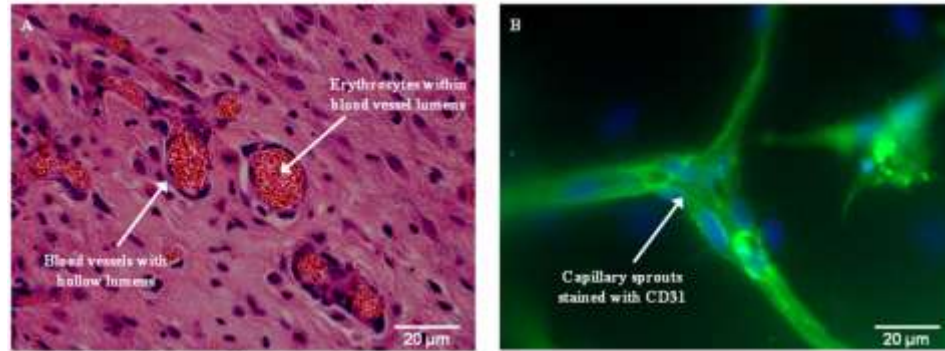
**Figure 7.1 Two-dimensional tubule formation assays.** Representative images of (A) *in vivo* immunohistochemical images of hematoxylin and eosin-stained fibrin implant sections showing the presence of red blood cells within anastamosed lumenal structures and (B) *in vitro* immunofluorescent images of capillaries formed within a fibrin tissue. Images courtesy of S. Grainger and A. Putnam, Cell Signaling in Engineered Tissues Lab, Department of Biomedical Engineering, University of Michigan.

However, the complexity in geometry of three-dimensional engineered constructs renders assessments based on two-dimensional, surface imaging uninformative. Three-dimensional constructs encompass pores, crevices, and other tortuous paths that are hidden from a top or bottom orthogonal view. Three-dimensional assays on tubule formation can be thwarted by light impenetrable synthetic polymer scaffolds and by the dissection of tubules in preparation for histology or microscopy. In addition, assessment in terms of structure (i.e. volume) and function (i.e. perfusion characteristics) of un-mineralized tissue/blood vessels, non-calcified tissue/blood vessels are useful parameters in the characterization of engineered three-dimensional constructs. Quantification via CD31 and vWF remains a feasible assessment of vessel presence and function, respectively. However, the localization of ECs requires the cryosectioning of scaffolds, which introduces error to the measurement from the inevitable displacement and damage to cells and tubules. Thus, in order to better capture the information available in three-dimensional angiogenesis models, three dimensional imaging methods are needed to qualitatively and quantitatively characterize tubule formation under *in vitro* conditions in three-dimensional constructs. At the sub-cellular level, microscopy studies of kinetochore microtubule cell division dynamics have demonstrated that trajectories observed in two-dimensional imaging may significantly differ from those visualized in three-dimensional imaging [26]. The use of three-dimensional imaging methods may provide a more

190

complete and accurate representation needed to characterize cellular processes and outcomes during *in vitro* angiogenesis and tumor angiogenesis studies [27].

Since the late 1890s, the challenge of non-invasive penetration of the human body has been achieved through medical imaging systems. These imaging systems generate datasets from which informative quantitative vascular metrics are extracted based on image voxel intensity values. In clinical radiology and oncology practice, static imaging (mainly, Magnetic Resonance Imaging and Computed Tomography) provides a qualitative and quantitative method to localize large vessel structures and assess their microvascular density. In addition, Radiation Oncology teams in therapeutic assessments of radiation treatment use dynamic perfusion imaging (via Magnetic Resonance Imaging, Computed Tomography, Positron Emission Tomography and Single-Photon Emission Computed Tomography) to capture image datasets over a given period of time (1-2 minutes) in order to quantify tumor perfusion and angiogenesis. In whole-body and animal studies, static and dynamic imaging techniques have been employed to study xenograft, allograft and tissue engineered graft post-implantation [28-33]. Increasingly, tissue engineers have adopted whole-body and small animal imaging systems, such as Magnetic Resonance (MR) imaging techniques, Computed Tomography (CT) and Nuclear Imaging to evaluate *in vitro* normal and tumor angiogenesis. Several groups have capitalized on the strengths of the different imaging modalities to evaluate angiogenesis, despite some of the system's limitations for practical cell-level biological application: low penetration depth (microscopy), low spatial resolution (MR), use of ionizing radiation (CT and x-ray) or lengthy imaging time (MR). Several molecular imaging modalities have also been investigated, particularly optical fluorescence imaging, targeted MR imaging and bioluminescence imaging.

Utilized at fixed endpoints, these static and dynamic imaging methods provide observations of single-cell responses and bulk property changes (i.e. microvessel density) that are directly and indirectly related to normal and/or pathological angiogenesis and the resultant altered microenvironment. Existing imaging modalities used in angiogenesis research examine the structure and/or function of tubules and their local environment in terms of cellular composition, local environment (i.e. presence of biomarkers), stiffness (associated with tumor angiogenesis), length, coverage area, density, diameter and/or

branching. Direct metrics evaluate the structural characteristics of tubule formation, while indirect metrics assess changes caused by angiogenesis, such as construct stiffness and vascular permeability.

In this paper, the methodologies available for noninvasive, *in vitro* imaging of tubules created during angiogenesis are explored. As well, their experimental requirements, potential benefits and inherent limitations are explored from the vantage point of applying these tools to the nascent explorations on *in vitro* three-dimensional angiogenesis models. This paper primarily focuses on the image-based characterization of tubule formation in terms of structural, mechanical and/or functional properties extracted from imaging methodologies, since angiogenesis studies commonly use the extent of vascularization as an end marker of tissue viability and tumor therapy. There is also brief mention of cell seeding and migration visualization.

## 7.2 MEDICAL IMAGING MODALITIES

### 7.2.1 Optical Imaging

#### 7.2.1.1 *Phase Contrast and Fluorescence* Microscopy

Microscopy provides an assay method to capture live-cell kinetics. Specifically, phase-contrast microscopy uses the fact that denser mediums transmit light at slower rates, than do less dense mediums. The change in this optical path of light allows for the visualization of living and otherwise transparent biological tissue and sub-cellular components, without the use of fixation or dyes [34]. Fluorescence microscopy offers enhanced contrast using near-monochromatic illumination to excite fluorescent-labeled biomolecules within a biological sample [35] to visualize structure and function of molecular or cellular components [35]. The stimulated fluorescent molecules emit a lower energy light (in the presence of light, biological parameters or gradients) that is used to produce an image that enhances the excited features [36], as shown in Fig. 7.2c. To visualize the distribution of a molecule within a sample, immunofluorescence employs antibody-antigen pairings tagged with fluorescent dyes to localized biomolecule targets [37]. Biological compounds, such as hemoglobin, nicotinamide adenosine diphosphate (NAD/NADH) and matrix metallo-proteases (MMPs), which are present

during metabolic processes can be indirectly measured [38-40]. McDonald and Choyke [41] summarized a list of available markers to labeling ECs. Each of these microscopy methods can be used to acquire a two-dimensional surface image of section sample (sub-millimeter field of view).
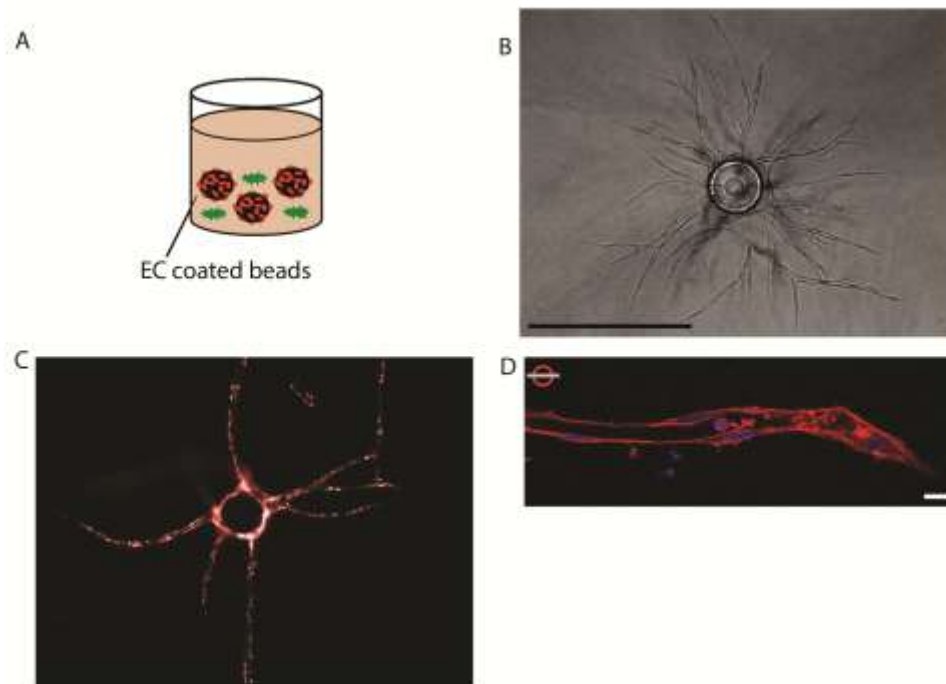


**Figure 7.2 Example of three-dimensional phase-contrast microscopy coupled with fluorescent optical imaging. (A) Schematic of the fibrin/bead assay. Endothelial cells (red) are coated onto Cytodex beads and embedded into fibrin gels. (B) Phase contrast image of branching vascular sprouts emerging from a bead. Scale bar is 500um. (C) Endothelial cells were transduced with retrovirus expressing mCherry and sprouts were visualized under epifluorescence. (D) Confocal image of a sprout stained with phalloidin (actin) and DAPI (nuclei), demonstrating the presence of a lumen in the trunk of the vessel and a non-lumenized tip cell at the head of the sprout. Scale bar 10um. Images courtesy of C. W. Hughes and M. N. Nakatsu, Department of Molecular Biology and Biochemistry, University of California Irvine, Irvine, California.**

In a study that evaluated the distribution and survival of fibroblasts seeded onto a poly(lactic-co-glycolic acid) (PLGA) salt-leached scaffold, Thevenot and Tang [42] imaged 20-micron sections of the scaffold from top to bottom, using phase-contrast, and red and green fluorescence imaging. A three-dimensional rendering in NIH Image J (U. S. National Institutes of Health, Bethesda, MD) allowed for the direct quantification of viability and distribution of cells using three distinct seeding methods.

In time-lapse microscopy, the dynamic and transient behavior of cells is captured within a given two-dimensional (x-y) field of view determined by the contrast mode (i.e. phase or fluorescence) adopted using an inverted microscope, at discrete intervals, for a given period of time [43]. Typically, time-lapse experiments comprise of hundreds of images that are analyzed by an automated post-processing method [43]. The visual output offers limited, quantitative information, since only a few vessels are visible in the small region imaged— a function of the required magnification (approximately 40-200 times). As well, the assay is subject to the selection of the field of view and the inherent variability within the network. Time-lapse microscopy is commonly used to track cell migration and growth, and can be combined with phase contrast microscopy [44-45].

### 7.2.1.2 Confocal Microscopy

In contrast to phase contrast and fluorescence microscopy, confocal microscopy generates three-dimensional volume reconstructions of scanned optical sections of a translucent three-dimensional sample. Three-dimensional confocal microscopy improves the quality of the image and offers a slighter higher resolution improvement (by roughly a factor of 1.4 [46]) over other microscopy techniques, making it useful for observations of three-dimensional structures thicker than 2-3 micrometers [47-48]. Image formation in a confocal microscope is achieved through point by point, serial reconstructions (i.e. 0.1-30 Hz frame rate for a 512 x 512 image) of three-dimensional (z-series) data collected from the illuminated volumes [49-50]. The volume reconstructions are assembled from the series of thin vertical slices collected. Within confocal microscopy, a laser emitting monochromatic, coherent light is focused at a motor-driven dichromatic mirror(s) that scans the sample and then selectively excites thin sections of the sample [47,51]. Fluorescence emitted from the excited volumes is transmitted back through the mirror(s); low frequencies are reflected by the mirror(s), while higher frequencies are transmitted through the mirror, and then focused through a pinhole aperture. Only light in confocal (along a conjugate plane) with the source and pinhole passes through the aperture and is detected by a single photodiode or photomultiplier tube. The confocal pinhole or single-mode fiber restricts the scanned volume confocal to the source and pinhole, thereby ignoring the scattered or unfocused light produced by the fluorescence background that

would otherwise contribute to the detected signal. A barrier filter is employed to ensure that none of the excitation light is detected in the final signal [51]. Confocal microscopy achieves roughly a 1 micron resolution, and submillimeter field of view and depth of penetration [52].

Similarly, two-photon confocal microscopy uses the simultaneous absorption of two infrared photons to excite section of a sample, in the same manner as previously described in confocal (one-photon) microscopy [53-54]. The two-photon method utilizes longer excitation wavelengths (higher frequency), which produce less scatter and out-of-focus fluorescent background (at depths of about 1 mm) [53-55]. The longer wavelengths improve depth penetration and provide greater spatial confinement of light-matter interactions to reduce the absorption of excitation light outside the focal plane. The resulting biological implications are decreased phototoxicity and photobleaching on scanned cells [52-54,56].

Dawood et al. used z-stack three-dimensional image reconstruction of images from immunofluorescent confocal microscopy to evaluate the number of HUVEC cells and tubule formation in multichanneled hydrogels (collagen VI and Matrigel) [57]. In the evaluation of translucent fibrogen gels, Nakatsu and Hughes stained the vessel walls within their construct with vimentin, and the EC nuclei with 4',6-diamidino-2-phenylindole (DAPI) to visualize the three-dimensional hollow lumens recently sprouted in their *in vitro* angiogenesis study. They coupled phase-contrast microscope images with fluorescent (optical) images to generate a z-sliced image dataset, in order to confirm the presence of intercellular lumens and the polarity of HUVEC cell orientation relative to the collagen IV basement membrane and fibrin gel. Nakatsu and Hughes captured fluorescent images using a two-photon Carl Zeiss MicroImaging LSM 510 Meta microscope, then generated three-dimensional renderings [58]. Fig. 7.2a illustrates the setup of their fibrin/bead assay and Fig. 7.2b shows results from their phase contrast. Fig. 7.2c-7.2d shows the results of three-dimensional renderings of fluorescent optical image stacks.

Within a microfluidic device, volume renderings of tubule formation within individual channels were realized in a study by Chau et al., using z-stack image reconstructions and confocal fluorescent imaging of a vWF staining [59]. Similarly, Vickerman et al. in an

evaluation of capillary morphogenesis within a microfluidic system, generated three-dimensional reconstructions of confocal images to visually confirm the patency of newly created fluorescent marked lumen structures [60]. Other investigations using microfluidic devices have combined fluorescent, confocal and/or time-lapse microscopy to optimize their set-up to monitor soluble chemicals such as oxygen tension [6,61].

In an evaluation of engineered capillary networks, Grainger and Putnam co-cultured human lung fibroblasts and micro-carrier beads coated with HUVECs in a fibrinogen gel for 14 days [62]. The seeded gels were immersed in a fluorescent dextran tracer to allow for tracer perfusion into the luminal space of newly formed vessels. The technique evaluated the permeability of the networks, as immature early sprouts are highly permeable, while mature networks possess mature cell-cell cadherin junction that are less permeable to the tracer. Confocal microscopy images were collected to quantify the total network length and to estimate a pixel intensity-based permeability measurement, which illustrated a decrease in tracer uptake over the 14 days. Although, the Grainger and Putnam, performed the study using Matrigel, the technique may be adapted to other three-dimensional *in vitro* models and the pixel intensity-based permeability algorithm could be expanded to a three-dimensional volume rendered from confocal images. As well, the technique provided a useful analytical tool to distinguish normal vascular networks from leaky, cancerous networks.

Song and Munn illustrated the effects of positive and negative localized vascular endothelial growth factor (VEGF) gradients and fluid forces (approximately 0 - 3 dynes/cm$^2$) on *in vitro* angiogenic sprouting in microchannels [63]. Vascular endothelial-cadherins were stained with a cyanine (Cy3) dye and HUVECs with 5'bromo-2'-deoxyuridine (BrdU) in a microfluidic device fabricated with poly(dimethylsiloxane) (PDMS) and containing a localized coating of collagen gel. Phase constrast and fluorescent images were collected with an epifluorescence microscope, then processed to quantify EC proliferation and to qualitatively and quantitatively evaluate EC invasion into the collagen gel. Z-stacks of confocal images were also acquired to count the number of filopodia formation in sprouting HUVECs in a given area. The combined use of phase contrast, fluorescent, and confocal microscopy demonstrated the benefit of strategically

combining microscopy techniques to further understand angiogenesis and to assess tubule formation within a dynamic *in vitro* model.

Meijering et al. [43] highlights that living cells are sensitive to photodamage due to excessive light exposure, such as that received during time-lapse microscopy. As such, before using these imaging protocols, validation studies should be performed to confirm that neither the light nor fluorescent probes alter cell physiology. Experimental set-ups should include controls and treatments that evaluate the sensitivity of cell-types under different culture conditions to light exposure and probes.


### 7.2.1.3 Bioluminescent imaging (BLI)

Bioluminescent imaging (BLI) provides a high sensitivity and specificity imaging technique to track cell viability/proliferation and localize neovascularization, using a cool charge-coupled device (CCCD) camera. *In vitro* BLI of cells is another noninvasive imaging technique that is useful in the evaluation of angiogenesis. It offers a colorimetric evaluation of the hypoxia levels of cells. Within BLI, energy in the form of light that is emitted from a chemical reaction within a biological sample is captured to form an image. Luciferins, light-emitting biological pigments, can be introduced to a sample to react with oxygen [64]. The light emission from these reactions is transient, and may be influenced by factors that are not controllable in the study. Liu demonstrated the viability of the assay for three-dimensional scaffolds by effectively visualizing oxygen gradients across cylindrical engineered agarose gels (4.8 mm x 4.8 mm), seeded with transfected Chinese hamster ovary A4-4 cells, and then subcutaneously implanted into nude mice [65]. Wang and El-Deiry [66], Wang et al. [67] and Jenkins et al. [68] performed *in vitro* BLI imaging on wells seeded with mesenchymal stem cells, ECs and/or tumor cells that were transfected with the firefly luciferase gene. In each study, image intensity was directly correlated with cell counts in order to quantify viability and proliferation. BLI has mainly been limited to *in vivo* whole body imaging and *ex vivo* imaging of excised tissue. Nadella et al. [69] and Xie et al. [70] tracked disease progression, in terms of tumor volume, through the delineation of tumor boundaries volumes using BLI. Preliminary work reported by S.J. Lapp [71], demonstrated the application of to a

dynamic bioreactor. In the study, chitosan scaffolds (13 mm × 13 mm × 25 mm) were embedded in a bone perfusion bioreactor and imaged over 11 days with BLI to monitor cell viability and bone morphogenetic protein 2 (BMP-2) expression of both MB-Luc and MC3T3-E1 cells.

For a three-dimensional engineered scaffold or dynamic construct, the sensitivity of the BLI technique may be diminished as the material properties of the 3-D construct can produce high scatter and attenuation causing a low transmission of the bioluminescence signal at increased depths. BLI does not resolve depth, instead produces a two-dimensional image representation of the visualized activity in the sample, whereby overlapped signals from the structure sum to form the final image. In a study by Logeart-Avramoglou et al. [72], the cell counts for tagged murine stem (C3H10T1/2) cells in a known cell suspension were correlated to the number of cells adherent to a hydrogel (6 mm diameter x 2 mm height) and ceramic (3 mm x 3 mm x 3 mm) scaffold. Logeart-Avramoglou et al. suggested that the degree of signal attenuation and corresponding linear decrease in cell count were a material constant dependent on the scaffold properties (i.e. size, shape and porosity).

As well, it should be noted that sources closest to the imaging source may appear brighter than those towards the bottom or at the core of the engineered scaffold. Initial studies should determine the percent loss of signal with increased depth for a given *in vitro* three-dimensional model. Multiple CCCD cameras could be configured to capture multiple views of the construct in order to provide depth information. The sensitivity of the CCCD camera (and filters), along with spectral analysis techniques used to acquire and evaluate data can greatly enhance the sensitivity and resolution of BLI images. Along with an evaluation of signal loss, the potential inherent physiological changes that may be induced by the introduction of the luciferins should be assessed in a control study. Similarly, the transduction efficiency of the retroviral vectors for EC lines should be optimized. As an imaging modality for examining network formation, BLI fails to visualize anatomical changes, but can indirectly monitor tubule formation through the assessment of bulk changes in vessel formation, and the correlation between cell proliferation and pro-angiogenic cell function.

*7.2.1.4 Additional Optical Imaging Techniques*

Investigations of optical imaging techniques, such as optical coherence tomography (OCT) and photoacoustic microscopy (PAM) have shown their utility in to monitor cell migration, spatial distribution, proliferation and morphology within three-dimensional culture models. OCT forms an image based on the indirect measurement of intensity from an interference pattern generated by reflected broad bandwidth, near-infrared that was focused light onto a given sample [73-74]. The echo time-of-flight produced from the scattered light is used to resolve the depth dimension. The axial and transversal resolutions of the system are governed by the spectral bandwidth and incident beam focusing, respectively [73-74]. OCT can image up to several millimeters deep, dependent on the optical properties of the sample, to form either two-or three-dimensional images. A variation of OCT, whole-field optical coherence microscopy (WFOCM, also referred to as full-field OCT) provides greater depth penetration than confocal microscopy [73-75]. OCM provides high sensitivity and contrast in scattering (non-transparent) and non-scattering (translucent) samples. Yang et al. [75] rendered three-dimensional cell distributions from volumetric WFOCM data for bone cells seeded on poly(l-lactic acid) (PLLA) scaffolds (9 mm diameter x 4 mm height) using WFOCM (resolution on order of 0.8 μm x 0.9 μm x 0.7 μm) for 250 micrometer field of view. Coupled with multiphoton microscopy, OCM can be used to simultaneously acquire structural and functional information at the cell level [76].

PAM is a modified photoacoustic tomography technique, which forms an image by ultrasonically detecting pressure waves induced by the absorption of photons by local molecules irradiated by a pulsed laser beam [77-78]. The axial and lateral resolutions are determined by the dual detection/excitation focusing and the acoustic travel time, respectively [77]. The final is speckle-free image can have a resolution of few hundred nanometers to about a millimeter and a depth of a few millimeters [77-78]. Zhang et al. [79] generated three-dimensional renderings of fibroblasts which were allowed to proliferate on poly($_{D,L}$-lactide-co-glycolide) (PLGA) scaffolds (approximately 5 mm diameter). A depth penetration of 1.2 mm was achieved. However, EC studies of vascularization have not been imaged by these methods. The thermal sensitivity of ECs to

increases in temperature, as well as their response to pressure changes during imaging should be considered.
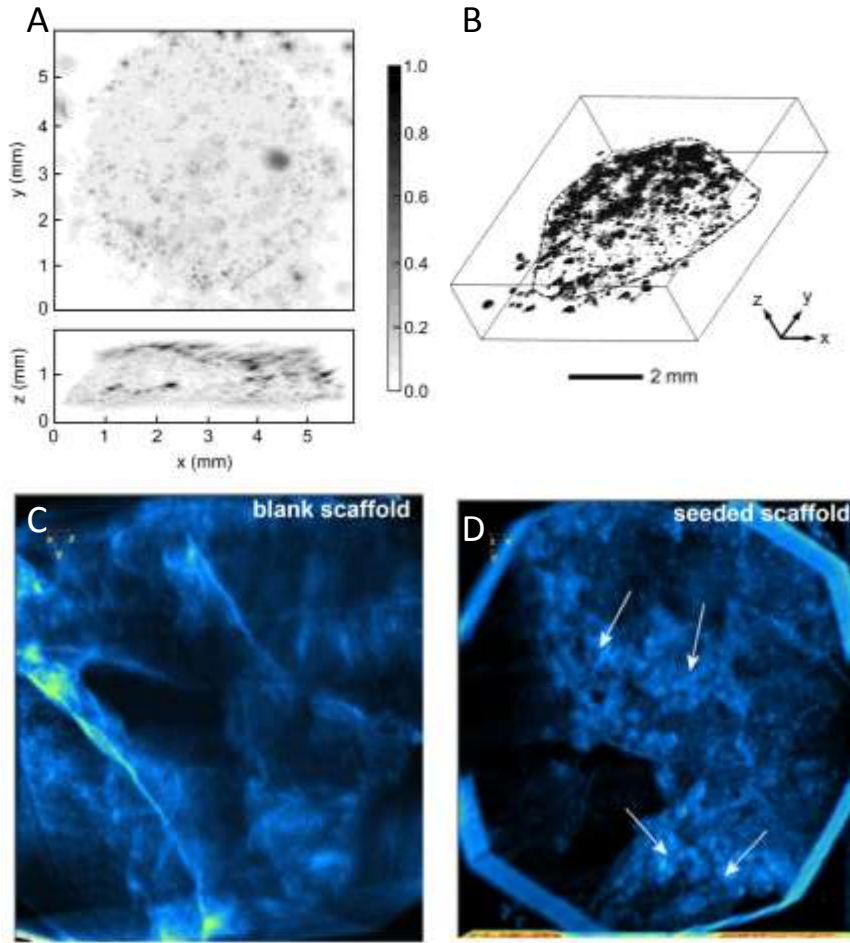


**Figure 7.3 (A) Photoacoustic microscopy (PAM) maximum amplitude projection (MAP) image and (B) the corresponding three-dimensional volume rendering of the MAP image illustrate the spatial distribution of fibroblast seeded on PLGA scaffold. (C) and (D) are three-dimensional renderings generated from optical coherence tomography (OCT) data. Reprinted from Cell Imaging, 50, Zhang, Y., et al., Noninvasive photoacoustic microscopy of living cells in two and three dimensions through enhancement by metabolite dye, 7359-7363, 2011, with permission from Wiley-VCH Verlag GmBH & Co. Reprinted from Physics in Medicine and Biology, 51, Yang, Y., et al., Investigation of optical coherence tomography as an imaging modality in tissue engineering, 1649-1658, 2006, with permission from IOP Science [75,79].**

In vivo small animal studies have illustrated the successful application of various optical imaging techniques, e.g. PAT [77-78] , OCT [80-81], multiphoton microscopy [82] and laser speckle imaging [83-84] to imaging functional vasculature (normal and diseased) in soft tissue (less than 1 mm depth penetration) imaging (Doppler, microscopy or

computed tomography), where the relative transient motion of fluorescence labeling, hemoglobin gradients, reporter genes, dyes or nanoparticles were detected. These dynamic imaging methods have not been applied to in vitro three-dimensional culture models, wherein the function of nascent vasculature is typically not assessed.

### 7.2.2 Magnetic Resonance Imaging

Magnetic Resonance Imaging (MRI) generates high contrast between different types of soft tissues (resolution of about 1 mm) [85]. The magnetization of hydrogen atoms present in the water within soft tissue causes the atoms to align their spin states, either with or against the applied magnetic field [85]. The image created by MRI is a function of how quickly the hydrogen atoms return to their original orientation (termed the relaxation time, $T_1$ and $T_2$), after the application of a radiofrequency pulse [85]. These variances in relaxation times are highly dependent on the water content of the tissue, and thus are used to distinguish tissues in the body. References to $T_1$ and $T_2$-weighted images indicate that most of the contrast between tissues is due to differences in the specified relaxation value [86]. In $T_1$-weight images fat appears brighter than water, while in $T_2$-weight images water appears brighter than fat (typically pathological tissue has a high water content) [86]. $T_2^*$-weighted images offer greater contrast in tissue or lesions with hemorrhaging, calcification, and *iron* deposition [87]. Before image acquisition, a contrast agent that is impenetrable to the cell membrane is often administered to enhance the appearance of blood vessels in a particular region of tissue. The contrast agents reduce the $T_1$ or $T_2$ relaxation times [88]. MR studies have primarily evaluated the material stiffness of tumors and three-dimensional spatial distribution of microvessels grown on engineered tissue constructs, using contrast techniques such as, T1-weighting, T2-weighting, paramagnetic particles, magnetization transfer, perfusion and elastography [89-94].

Clinically, the studies are limited in spatial resolution since regions of interest deeper than about 2 cm are poorly targeted by MRI, due to the rapid decrease of field strength with increased distance from the magnet. With respect to *in vitro* systems, three-

dimensional culture models are typically between 0.3 - 1 cm, with "thick tissue" constructs extending the range beyond 1 cm.

### 7.2.2.1 Magnetic Resonance Elastography (MRE)

Recent developments in MRE have taken advantage of the remodeled and stiffened ECM that is evident during tumorigenesis. Animal and human (breasts, aorta, brain and liver) studies have demonstrated that MR elastography is sensitive to these stromal (ECM, MMPs, ECM glycoproteins) changes and can offer an evaluation of stiffness, in terms of shear modulus and shear elasticity estimations [94-96]. MRE involves the propagation of mechanical waves, at a controlled frequency (100-1000 Hz [95]) and amplitude (less than 100 μm [95]), through a target sample via a wave driver, which is positioned as close as possible to the sample [96-97]. The MR image acquisition is synchronized with the periodic vibrations. The mechanical excitation induces a shear stress on the sample, which results in a displacement captured by the real (elasticity) and imaginary (viscosity) components of the shear modulus of the scanned sample [98]. From the visco-elastic MR data, quantitative elasticity maps are generated [96-97]. These changes are inherent to the multistep process of tumorigenesis (and tumor angiogenesis), which is characterized by a thinned basement epithelial layer of the ECM, and cell crowding and anchorage-independent growth [16-18]. Transmembrane protein function is diminished for integrins that regulate cellular shape and for adheren proteins that hold epithelial cells onto the basement membrane together [99]. The interstitial fluid pressure is amplified with the increased volume of inefficient, dense ECM within the tumor [100]. The increased cell tension and ECM-remodeling contribute to the stiffened ECM during tumorigenesis [100-102].

Although performed *in vivo*, the study conducted by Jugé et al. [89,103] compared immunostained histology (CD 31 and KI67) to acquired MRE data to draw conclusions about tumor behavior. Jugé et al. concluded that the blood vessel density (based on cellularity and number of vessels) ($mm^{-2}$) and elasticity (based on number of vessels and elasticity) (kilopascals) measurements from the respective techniques, both showed distinction in visual and mechanical properties of tissue prior to, and post-angiogenesis

phase of tumorigenesis. Fig. 7.4 illustrates the MRE data that was collected from a colorectal mouse cancer model using $T_2$-weighting on a 7 Telsa scanner over the course of 18 days. However, no comparable *in vitro* studies using engineered constructs have been published.
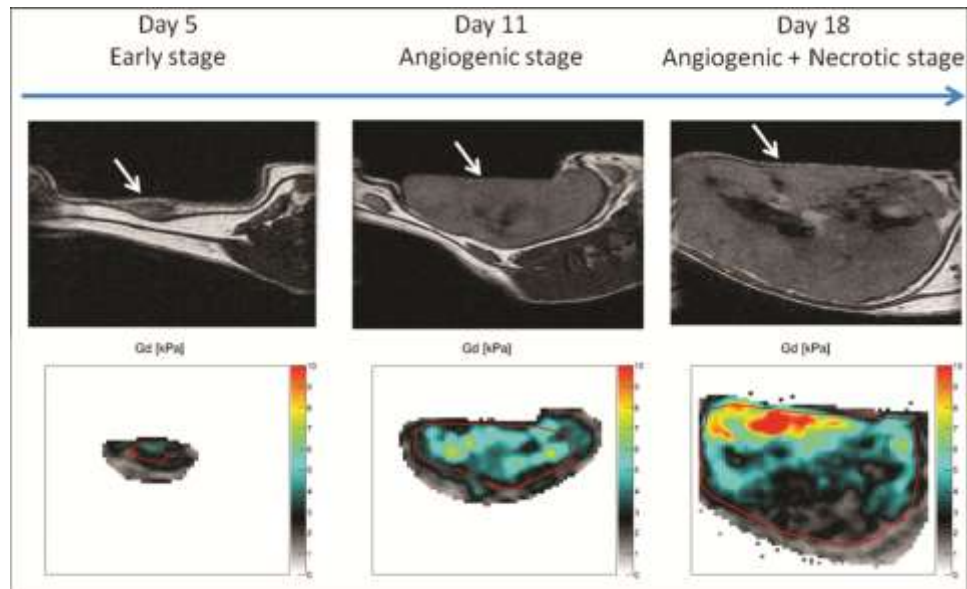


**Figure 7.4 *In vivo* MRE mapping. T2-weighted images (top row) and Gd maps (bottom row) of selected ectopic tumors (outlined in red) as a function of colorectal mouse tumor evolution. Gd measurements showed an increase of the mechanical properties when the tumor switched from its early stage (3.8 ± 0.6 kPa) to its angiogenic and late stage (6.5 ± 0.8 kPa to 5.8 ± 0.5 kPa). White arrow indicates region of interest. Images courtesy of L. Jugé and R. Sinkus, Centre de Recherche Biomédicale Bichat-Beaujon, INSERM U773, Clichy, France [104].**

MRE is an emerging area that can offer an indirect method to evaluate the progression or regression of tubule formation during tumor angiogenesis, particularly when vessels may be too leaky or nonfunctional for perfusion methods of evaluation (i.e. DCE-MRI). The shear modulus changes captured by MRE may be a biomarker indicative of changes induced by increased microvessel density. The model would be most applicable to a natural or engineered matrix with a low stiffness that may be altered during tumorigenesis, under the conditions of an *in vitro* tumor angiogenesis model. However, additional studies would be required to understand the role of the composition and structure extracellular matrix and cellularity in these viscoelastic changes [104].

*7.2.2.2 Dynamic Contrast Enhanced - MRI*

Dynamic Contrast Enhanced (DCE) - MRI, a method of perfusion imaging, involves the acquisition of a time series of images after the injection of a bolus of paramagnetic contrast agent (i.e. iodinated radiographic contrast material or radionuclides) into the bloodstream [105]. The presence of contrast agent allows for the temporal and spatial localization of blood in a region of interest. DCE-MRI receives these transient changes in the local magnetic field as temporal changes in the collected signal. Data is typically collected for 1-10 minutes, for each time point over some study period dependent on the time course of the transient activity being observed. DCE-MRI offers voxel resolution on the order of millimeters and a temporal resolution of less than five seconds when optimized MR imaging sequences are employed. DCE-MRI data can be performed on a standard 1.5 Tesla MR system [106]. Perfusion metrics (i.e. flow rate, microvessel density and volume) indicative of the extent and functionality of the vasculature are extracted from the collected image datasets [105]. These metrics are based on the conversion of the temporal signal data to tissue contrast concentration data.

In an *ex vivo* study by Buschmann et al. [90] on the endothelialization of DegraPol® foam scaffold, quantitative contrast enhanced MRI ($T_1$-weighted) perfusion analysis was performed. First, the scaffolds were seeded with ECs and cultured *in vitro* to allow for tubule formation. Subsequently, gadolinium (Gd)-DTPA dimeglumin salt (contrast agent) was used to outline the in-growth of new vascular networks into scaffolds assayed *ex vivo,* in a chorioallantoic membrane (CAM). MR image analysis of the scaffolds, saturated with contrast intravenously, demonstrated low contrast uptake by the scaffold. There was significant distinction between the vascular network and the background scaffold. The uptake of Gd was evaluated across the scaffold and used as a metric of microvessel density. As often seen across scaffolds, the greatest uptake was seen at the periphery and the least at the center of the scaffold. Buschmann et al. also evaluated three seeding methods to determine if the distribution of these capillaries was a function of whether ECs, osteoblasts or a co-culture were seeded on the scaffold. MRI showed insignificant differences in relative relaxation times based on the seeding method. The *ex vivo* model angiogenesis assay demonstrated the utility of DCE-MRI to evaluate microvessel density and distribution across scaffolds.

Although not yet extended to a completely *in vitro* study, the work by Buschmann et al. showed that saturation of a contrast agent on the surface (not intravenously) of a scaffold implanted in CAM still produced an increase in the relaxation rate, but with less sensitivity to changes in perfusion. These findings demonstrated the potential for DCE-MRI technique to provide a visualization and quantification method for observing gross changes in tubule formation (surface area covered and vasculature permeability). Future studies may employ the technique to evaluate the presence or the function of newly formed vessels in dynamic *in vitro* angiogenesis models (i.e. microfluidic device or bioreactor). The three-dimensional dynamic culture models offer a flow source thru which contrast agent can be injected for uptake by permeable sprouting capillary-like structures. The degree of contrast agent uptake by tubules can be an indicator of vasculature function. Key parameters that should be optimized to ensure the credibility of extracted perfusion metrics include the image's signal-to-noise ratio and contrast-to-noise ratio, and the length of contrast agent retention in new formed vessels.

### 7.2.2.3 Targeted MRI

The application of targeted MRI to cellular and molecular imaging was first introduced as an alternative to MRI contrast agents [107]. Highly negatively charged superparamagnetic iron oxide nanoparticles (SPIONs), such as ferumoxides, shorten MRI $T_2$ and $T_2$* relaxation times to produce contrast enhanced images from which useful metrics, such as tubule volume and area, can be extracted [108]. The ability to estimate tubule properties, in terms of length or number of tubules using enhanced or unenhanced MRI is otherwise limited by its low spatial resolution of 200 - 400 micrometers [109]. Cell uptake of the nanoparticles occurs via phagocytosis, but intake by nonphagocytic methods can also be facilitated by cationic compounds that interact with the negatively charged cell surface to promote endosomal uptake [110-111]. SPIONS tag biological molecules such as antibodies, peptides and hormones [112]. They can also be functionalized to localize cells or subcellular structures.

In an *in vitro* targeted MRI study, Terrovitis et al. [91] cultured iron-labelled mesenchymal stem cells (MSC) seeded onto a collagen scaffold for four weeks. Using a

1.5 Tesla MRI scanner, $T_2$-weighted scans were performed and resulting images demonstrated that iron-labelled MSCs on a collagen scaffold could be visualized using MRI. This study also illustrated that the biocompatibility of ferumoxide and its lack of adverse effects on the viability and proliferation of MSCs. The study methodology demonstrated by Terrovitis et al. could be applied to ECs in a three-dimensional tumor angiogenesis model.

In the design of an in vitro method to control endothelial progenitor cell (EPC) migration, Wilhelm et al. [93] tagged EPCs with iron oxide magnetic nanoparticles. The tagged EPCs were cultured in Matrigel for 18 hours, then imaged using a high resolution MRI (29 micron x 29 micron) and videomicroscopy (12,000 - 24,000 times real-time). Using videosmicroscopy, individual vessel structures were visible. The MRI images were acquired with a 9.4 Tesla horizontal MRI system, using gradient echo sequences (T2* sensitive). The magnetic nanoparticles induced changes in the MR contrast agent properties, which led to visible changes in local magnetic susceptibility within images. Tagged EPCs appeared as black voids on a brightened Matrigel structure. In this study however, no quantitative metrics were used. Nonetheless, the study by Wilhelm et al. has implications that can be extended to tumor angiogenesis tube formation assays, since EPC recruitment was linked to tumor angiogenesis in both patient studies [113-114] and preclinical models [115-116]. In mouse models, EPCs have been shown to control the angiogenic switch in lung mouse metastasis [117].

Gimi et al. [118] tagged HUVECs with superparamagnetic iron oxide $T_2$ contrast agent and cultured them *in vitro* for five days adjacent to MDA-MB-231 breast cancer cells seeded onto an ECM gel. After 24 hours of culture, a vascular network was present. The migration and subsequent tubule formation of the HUVECs within the gel was observable using an 11.74 Telsa MRI, fluorescence microscopy and phase-contrast microscopy. The light microscopy techniques were used to confirm that no observable physiological differences occurred between the tagged and untagged HUVECs. Three-dimensional reconstruction of the MRI data and post-processing produced an isolated volume rendering of the HUVEC vessel network. The volume renderings are shown in Fig. 7.5. The rendered volume was used to determine the fractional area of the gel occupied by HUVECs. In both studies, iron oxide tags did not harm cell viability or tubule formation.

Similarly, other macromolecular contrast media have been used in cellular imaging to tag biomarkers of tumor aggressiveness and to monitor normal angiogenesis [119-121]. Gimi et al. demonstrated how multiple imaging modalities can be simultaneously used to garner the additional information on tubule formation within an *in vitro* model.
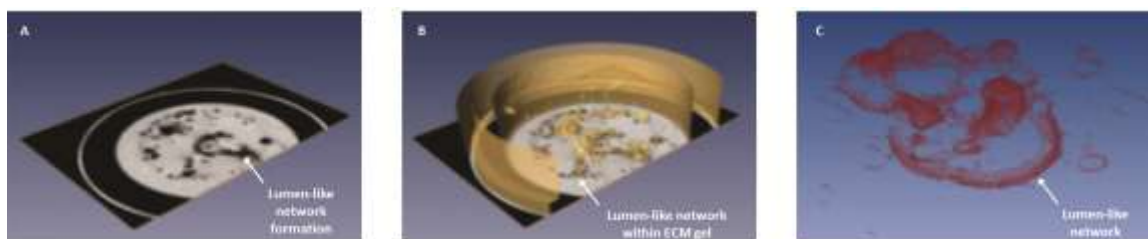


**Figure 7. 5 Representative image and volume renderings from targeted MR imaging of endothelial cells 24 hours post-seeding in ECM gel. (A) Axial image of 0.5-mm-thick slice, obtained using a T2-weighting, contains HUVECs labeled with 9 µg/ml Feridex. (B) Three-dimensional reconstruction of images from multi-slice MRI data, orthogonally sliced in the axial direction to visualize network structure. (C) Volume rendering produced from segmented three-dimensional reconstruction, which illustrates intricate HUVEC network (red). Reproduced from Gimi et al. with permission [118].**

In another study, although carried out in a subcutaneous xenograft mouse model, the potential use of paramagnetic $^{19}$F perfluorocarbon (PFC) nanoparticles was explored to quantify (in terms of the number of enhanced voxels) and visualize the extent of neovascularization at the periphery of tumors, using small animal MRI [122]. Bound PFC nanoparticles can be directly detected with high specificity once the threshold of detection is achieved, using MRI or MRS [123]. In addition to improvements in nanoparticles, advances in magnetic resonance microscopy may also provide nanometer resolution to visualize the mechanisms involved in tubule formation [124].

The application of target MRI to *in vitro* three-dimensional angiogenesis models provides tool for the assessment of temporal and spatial cell migration and gene expression (via green fluorescent protein marker) [125] over a three-dimensional spatial distribution. Many studies have demonstrated the biocompatibility of these particles in terms of cell apoptosis rates, differentiation and proliferation for specific cells types. However, cell exposure to SPIONs may induce DNA damage, mitochondrial disfunction, apoptotic bodies, membrane leakage of lactate hydrogenase, or generate reactive oxygen species [126-128]. As such, to apply nanoparticle targeting (less than 200 nm in diameter) to i*n*

*vitro* three-dimensional angiogenesis models, an investigation of the particle-EC uptake efficiency, retention, dose effect, detection threshold, and biocompatibility should be explored for the particular cell line. In addition, for surface-modified nanoparticles, the shelf-life, by-products of degradation, aggregation and precipitation of particles under *in vitro* conditions should be investigated prior to use in the model. Zhang et al. noted that the ability to track SPIONs over 5 days diminishes due to cell's release of the iron particle [129].

### 7.2.3 Ionizing Radiation Imaging Systems

*7.2.3.1 X-ray, Fluoroscopy and Computed Tomography (CT)*

In X-ray imaging system (wavelength of 10 to 0.010 and energy range of 120eV to 120keV), X-rays emitted from a source penetrate a tissue, then attenuate at different levels dependent on the density of the material. The X-rays which penetrate the tissue are received by scintillation detectors [130]. From these readings, a grayscale two-dimensional image is generated. Fluoroscopy provides a real-time continuous video of X-ray images. The technique is useful for viewing whole-body motions, and contrast agent or instrument motion in tissue or bloodstreams [131]. Computed Tomography (CT) imaging (sub-millimeter spatial resolution) involves the reconstruction of a three-dimensional volume from a collection of two-dimensional X-ray projections taken about a central axis of rotation [131].

Imaging techniques, such as X-ray, fluoroscopy and CT (including MicroCT), which emit ionizing radiation offer useful structural information regarding a construct's porosity, strut/throat size, mineralization and overall architecture of tissue-engineered constructs with high-attenuation. To visualize low-attenuation structures such as blood vessels, MicroCT (spatial resolution 1-50 microns [132]) has been used in experimental animal studies to characterize structural properties [133-134]. Rai et al. [135] used Micro-CT to quantify vascular in-growth into poly(ε-caprolactone)-tricalcium phosphate (PCL-TCP) composite scaffolds implanted in rats, in terms of a vascular volume fraction. The animals were anesthetized, then injected with the contrast medium, Microfil, to enhance vessel contrast in the MicroCT images. Similarly, Patel et al. [136] used the same method

for poly(propylene fumarate) (PPF) scaffolds coated with vascular endothelial growth factor (VEGF) to measure changes in blood vessel volumes in rats over a four week study. Fig. 7.6 provides an example MicroCT images produced in a similar study by Schmidt et al. [137]. In the study by Schmidt et al., Microfil was injected into a rat to quantify the ingrowth of vasculature into a porous polyurethane construct. Vessels between 6 - 144 micron were visualized using MicroCT. However, the well-documented anti-angiogenic effect of ionizing radiation, even at low doses, abrogates its use in an ongoing study of angiogenesis [138-140]. There is potential use for these methods in static imaging of non-living constructs with patent vessel structures large enough to have iodinated contrast agents injected, similar to DCE-MRI [135-137,141].
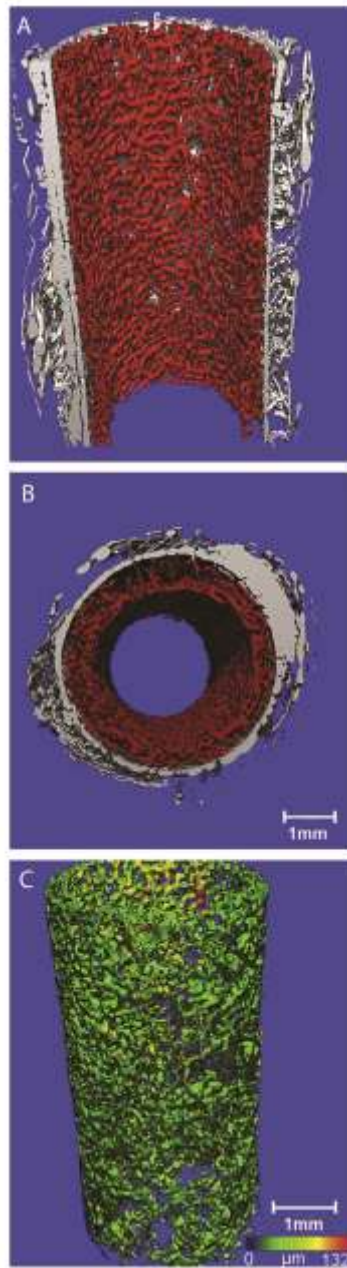
**Figure 7.6 MicroCT of Microfil-injected vessels. Representative volume renderings generated from MicroCT datasets of neovasculature within polyurethane construct, 10 days after delivery of vascular endothelial growth factor growth factor. (A) Longitudinal center slice through volume rendering. (B) Horizontal slice. Red color represents microvascular network and gray represents the construct. (C) Color-coded distribution of vessel diameter distribution across construct. Reprinted from publication Rapid three-dimensional quantification of VEGF-induced scaffold neovascularisation by microcomputed tomography, 30/5959, Schmidt, C., Bezuidenhout, D., Beck, M., Van der Merwe, E., Zilla, P., and Davies, N., 5959-68, Copyright (2009), with permission from Elsevier [137].**

Conversely, radiation exposure has been shown to induce tumorigenesis [142-143]. Accordingly, X-ray and CT could be used to introduce radiation to an experimental set-up to investigate or control the response or rate of tumor angiogenesis or cell death in the presence of drugs or other factors [144-145].

### 7.2.3.2 Nuclear Imaging

Positron Emission Tomography (PET) imaging introduces a low radiation dose to the body using short-lived radionuclide tracers. The system then detects gamma rays emitted indirectly by the positrons released from the injected radionuclides. Scintillation crystals in the gamma ray detectors covert the emitted gamma rays to photons, which are then amplified and converted to electrical signals by photomultiplier tubes to form PET images [146]. A second nuclear imaging system, Single-Photon Emission Computed Tomography (SPECT), detects these emitted gamma rays directly to generate images [147]. Both systems can create clinically relevant three-dimensional volume visualizations of functional and metabolic processes (i.e. glucose metabolism) [148]. In spite of the sensitivity of radionuclides to highlight physiological effects on the level of 100 picomolar, compared to other modalities, nuclear imaging techniques offer an inferior spatial resolution [148]. The clinical resolution of PET ranges between 3-5 mm and between 1-2 mm for small animal PET imaging [149]. Clinical SPECT resolutions are typically greater than 1 cm, with decreased sensitivity than PET systems [150]. Both systems' poor resolution outweighs its potential benefit in the evaluation of bulk properties characteristic of tubule formation in angiogenesis. MRI-compatible PET scanners are currently under investigation as a method for fusing complementary capabilities in small animal imaging: high sensitivity, good spatial resolution and high contrast [151]. There is currently no literature to support the use of nuclear imaging radioligands (molecules bound to radionuclides) or radiotracers to evaluate *in vitro* tubule formation or related properties, such as permeability or blood flow.

## 7.3 IMAGE PROCESSING

Five major steps are involved in the quantification of tubulation from three-dimensional images. Fig. 7.7 details these steps: image acquisition, image reconstruction, image segmentation, feature identification, and feature measurement. The appropriate imaging system to be used should be based on the experimental setup and constraints, and desired output measures. Post-processing of acquired images requires image processing and analysis software. The image analysis freeware, NIH Image J [152] (and derivative software, Scion Image) is often cited as the tool used to stack, reconstruct, render or post-process network formations.
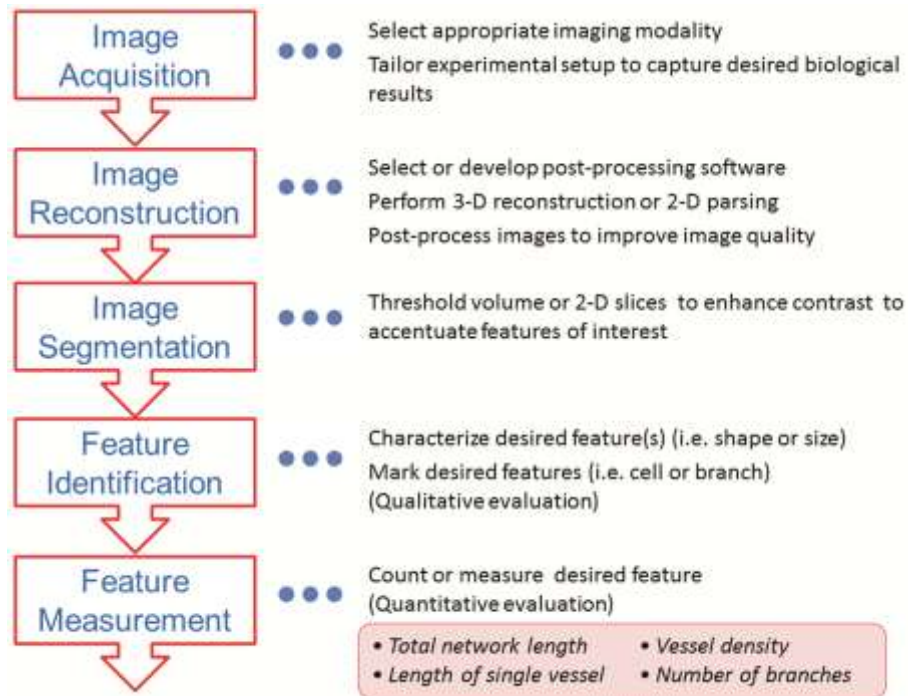


**Figure 7.7 Stages of image processing. Flowchart of image analysis process required to qualitatively and/or quantitatively evaluate angiogenesis.**

Rendered volumes are subjected to a threshold (automated image segmentation) to contrast the desired luminal features from the background larger tissue volume. In the evaluation of vessel diameter, length or area, threshold values can influence final estimates due to the error introduced by the threshold algorithm when the boundary of the

lumen is defined. Boundary detection between the tubule and background construct requires the optimization of a fixed or adaptive, local or global threshold algorithm. Semi-automatic methods of image segmentation implement snakes or splines for boundary delineation or edge detection. Manual and semi-automated methods of processing imaging data require visual inspection of image by a trained eye. The human reader performs 'feature identification' based on a set of pre-determined characteristics. Sarkanen et al. [153] employed a grading scale from 0 to 8 using visually inspection of microscopy images, to quantify the number of tubules and branching achieved for a co-culture of HUVEC and foreskin fibroblasts. Along with boundary detection, the number of tubules estimated is dependent on the shape and dimensional threshold parameters (feature identification and measurement) set either manually or by the software package. The cylindricality and contrast (produced by fluorophore, dye or contrast agent) of the tubule may be variable in given regions of the volume, and may potentially influence final measurements. Similarly, the length and diameter of a tubule may vary dependent on the level of bifurcation. Tubules may be faint, partially stained/tagged or clustered. Segmentation and the definition of its rubric are subjective and sensitive post-processing elements that are biased by the biomaterial (scaffold), cell type (and resultant vascular network properties) and imaging system adopted. Measurements are also subject to variance and user-based error incurred during manual or semi-automated segmentation methods. Several freeware and commercial software programs that perform automated and semi-automated image analysis produce output parameters such as, the number of tubules, branching point statistics, tube length statistics and tube size statistics [154-158].

Many automated and semi-automated quantification algorithms directly measure perfusion metrics (i.e. surface area) based on two-dimensional analysis of collected two-dimensional sectional data [159-161]. Rytlewski et al. [162] proposed a new algorithm to perform three-dimensional morphological analysis on two-dimensional sectional data, in order to increase the accuracy of output metrics. Initial evaluations of the algorithm were performed on an *in vitro* model, in which HUVECs were cultured within a PEGylated fibrin gel and allowed to sprout tubules. Rytlewski et al. performed confocal imaging on the in vitro model and then extracted morphological data, which included estimations of network volume, number of segments and total network length. Their study determined

that measurements based on three-dimensional models were significantly different than those based on two-dimensional planar data for multi-plane anisotropic tubule formation.

In the post-processing of DCE images acquired for indirect measures of perfusion, segmentation should be performed, and then followed by the application of perfusion algorithms adopted or specifically developed to evaluate flow characteristics of the newly formation vasculature. In the evaluation of stiffness, using MRE, the acquired three-dimensional images provide phase and amplitude maps that are modeled using an inversion algorithm that yields an elastogram. The generated elastogram indicates the spatial distribution of stiffness within the imaged construct. For each of the imaging methods used to acquire direct or indirect measures, the final angiogenesis metrics are compared across several time points within the duration of the study (minutes or days), in order to assess angiogenesis within the *in vitro* construct. For metrics that assess spatial deviations, image registration of the two-dimensional images across time points should be performed before feature isolation or other post-processing algorithm are applied. Image registration aligns the spatial overlay of the constructs coordinate systems for the given points, in order to facilitate the tracking of temporal changes.


## 7.4 CONCLUSION

The *in vitro* studies described above confirm the practical application of imaging to characterize blood vessel formation and function within natural or synthetic constructs. At the cellular level, the tracking of EC motility and alignment in the formation of tubules is best resolved using optical imaging, MRI or CT. The rendering of three-dimensional volumes provides a non-invasive method to observe the structure and distribution of blood vessels, which may otherwise be compromised or lost through histology sectioning. BLI, contrast enhanced MRI, MRE and microscopy coupled with fluorescent tracers can provide temporal and functional information (i.e. metabolic activity, permeability, proliferation and stiffness) on neo-vasculature and/or the surrounding extracellular matrix.

New techniques in molecular imaging (for MR, optical and nuclear imaging) that tag cellular structures with nano- and micro-contrast agents or particles are being developed

to further improve achievable resolution limits. As well, nascent imaging techniques such as magnetic particle imaging (MPI) may offer a more reliable or precise method of dynamic perfusion imaging through the quantitative detection SPIONs [163-164]. Although some of the techniques (i.e. MRE) have published findings only under *in vivo* conditions, the techniques still lend themselves to an *in vitro* environment.

Initial implementations of these techniques require validation studies to assess toxicity and to identify any adverse effects caused by the introduction of light, magnetic resonance, particles or ionizing radiation to the given cell and cell environment. As well, the incorporation of an imaging modality into an experimental set-up requires a careful consideration of the hardware and software choices made, in terms of processor needs, frame rates, threshold algorithms, among other parameters that may reduce the reliability of quantitative estimations. In the determination of an appropriate imaging modality, the scaffold architecture (shape and dimension), scaffold material characteristics (physical, optical, mechanic and acoustic properties), and the features of interests (subcellular or bulk property) should be considered. Dependent on the set-up conditions and scaffold architecture, multi-modality imaging can be leveraged to take advantage of the respective features of the systems to provide more spatial, depth, structural and/or functional information about the imaged features.

Future applications of imaging techniques to *in vitro* three-dimensional angiogenesis studies will provide more reliable, robust methods for comparison of the vascular properties exhibited within these *in vitro* models to animal models. Correlation of changes in between the two models has the potential to outline the advantages and/or limitations of three-dimensional angiogenesis and tumor angiogenesis culture models as practical tools for the investigation of mechanisms or pathophysiology acting at the cellular level in engineered tissue and tumors, respectively.

## 7.5 ACKNOWLEDGEMENTS

215

## 7.6 REFERENCES

[1] Szot, C.S., Buchanan, C.F., Freeman, J.W., and Rylander, M.N. 3D in vitro bioengineered tumors based on collagen I hydrogels. Biomaterials **32**, 7905, 2011.

[2] Kievit, F.M., Florczyk, S.J., Leung, M.C., Veiseh, O., Park, J.O., Disis, M.L., and Zhang, M.Q. Chitosan-alginate 3D scaffolds as a mimic of the glioma tumor microenvironment. Biomaterials **31**, 5903, 2010.

[3] Khoo, C.P., Micklem, K., and Watt, S.M. A Comparison of Methods for Quantifying Angiogenesis in the Matrigel Assay In Vitro. Tissue Engineering Part C-Methods **17**, 895, 2011.

[4] Yates, C., Shepard, C.R., Papworth, G., Dash, A., Stolz, D.B., Tannenbaum, S., Griffith, L., and Wells, A. Novel three-dimensional organotypic liver bioreactor to directly visualize early events in metastatic progression. Advances in Cancer Research **97**, 225, 2007.

[5] Wlodkowic, D., and Cooper, J.M. Tumors on chips: oncology meets microfluidics. Current Opinion in Chemical Biology **14**, 556, 2010.

[6] Stroock, A.D., and Fischbach, C. Microfluidic Culture Models of Tumor Angiogenesis. Tissue Engineering Part A **16**, 2143, 2010.

[7] Verbridge, S.S., Chandler, E.M., and Fischbach, C. Tissue-Engineered Three-Dimensional Tumor Models to Study Tumor Angiogenesis. Tissue Engineering Part A **16**, 2147, 2010.

[8] Peyton, S., Ghajar, C., Khatiwala, C., and Putnam, A. The emergence of ECM mechanics and cytoskeletal tension as important regulators of cell function. Cell Biochemistry and Biophysics **47**, 300, 2007.

[9] Fischbach, C., Chen, R., Matsumoto, T., Schmelzle, T., Brugge, J.S., Polverini, P.J., and Mooney, D.J. Engineering tumors with 3D scaffolds. Nature Methods **4**, 855, 2007.

[10] van Moorst, M., and Dass, C.R. Methods for co-culturing tumour and endothelial cells: systems and their applications. Journal of Pharmacy and Pharmacology **63**, 1513, 2011.

[11] Staton, C.A., Reed, M.W.R., and Brown, N.J. A critical analysis of current in vitro and in vivo angiogenesis assays. International Journal of Experimental Pathology **90**, 195, 2009.

[12] Khoo, C.P., Micklem, K., and Watt, S.M. A Comparison of Methods for Quantifying Angiogenesis in the Matrigel Assay In Vitro. Tissue Engineering Part C-Methods **17**, 895, 2011.

[13] Risau, W. Mechanisms of angiogenesis. Nature. **386**, 671, 1997.

[14] Nussenbaum, F., and Herman, I.M. Tumor angiogenesis: insights and innovations. J Oncol **2010**, 132641, 2010.

[15] Carmeliet, P., and Jain, R.K. Angiogenesis in cancer and other diseases. Nature **407**, 249, 2000.

[16] Mbeunkui, F., and J., J.D.,Jr. Cancer and the tumor microenvironment: a review of an essential relationship. Cancer chemotherapy and pharmacology 63, 571, 2009.

[17] Bergers, G., and Benjamin, L.E. Tumorigenesis and the angiogenic switch. Nature Reviews Cancer **3**, 401, 2003.

[18] Payne, S.J, and Jones, L. Influence of the tumor microenvironment on angiogenesis. Future Oncology **7**, 395, 2011.

[19] Auerbach, R., Lewis, R., Shinners, B., Kubai, L., and Akhtar, N. Angiogenesis assays: A critical overview. Clinical Chemistry **49**, 32, 2003.

[20] Folkman, J. Angiogenesis-dependent diseases. Seminars in Oncology **28**, 536, 2001.

[21] Hlatky, L., Hahnfeldt, P., and Folkman, J. Clinical application of antiangiogenic therapy: Microvessel density, what it does and doesn't tell us. Journal of the National Cancer Institute **94**, 883, 2002.

[22] Folkman, J. What Is the Evidence That Tumors Are Angiogenesis Dependent. Journal of the National Cancer Institute **82**, 4, 1990.

[23] Staton, C.A., Reed, M.W.R., and Brown, N.J. A critical analysis of current in vitro and in vivo angiogenesis assays. International Journal of Experimental Pathology **90**, 195, 2009.

[24] Sun, H.C., Qu, Z., Guo, Y., Zang, G.X., and Yang, B. In vitro and in vivo effects of rat kidney vascular endothelial cells on osteogenesis of rat bone marrow mesenchymal stem cells growing on polylactide-glycoli acid (PLGA) scaffolds. Biomedical Engineering Online **6**, 2007.

[25] Yan, S., Zhang, H.F., Xie, Y.F., Sheng, W.H., Xiang, J., Ye, Z.M., Chen, W.C., and Yang, J.C. Recombinant Human Interleukin-24 Suppresses Gastric Carcinoma Cell Growth In Vitro and In Vivo. Cancer Investigation **28**, 85, 2010.

[26] Dorn, J.F., Jaqaman, K., Rines, D.R., Jelson, G.S., Sorger, P.K., and Danuser, G. Yeast kinetochore microtubule dynamics analyzed by high-resolution three-dimensional microscopy. Biophysical journal **89**, 2835, 2005.

[27] Stephens, D.J., and Allan, V.J. Light microscopy techniques for live cell imaging. Science **300**, 82, 2003.

[28] Hathout, E., Chan, N.K., Tan, A., Sakata, N., Mace, J., Pearce, W., Peverini, R., Chinnock, R., Sowers, L., and Obenaus, A. In vivo imaging demonstrates a time-line for new vessel formation in islet transplantation. Pediatric transplantation **13**, 892, 2009.

[29] Cartwright, L., Farhat, W.A., Sherman, C., Chen, J., Babyn, P., Yeger, H., and Cheng, H.M. Dynamic contrast-enhanced MRI to quantify VEGF-enhanced tissue-engineered bladder graft neovascularization: Pilot study. Journal of Biomedical Materials Research Part A **77A**, 390, 2006.

[30] Cao, M., Liang, Y., Shen, C., Miller, K.D., and Stantz, K. M. Developing DCE-CT to Quantify Intra-Tumor Heterogeneity in Breast Tumors With Differing Angiogenic Phenotype. IEEE Trans Med Imaging **28,** 861, 2009.

[31] Ungersma, S.E., Pacheco, G., Ho, C., Yee, S.F., Ross, J., van Bruggen, N., V., P.F.,Jr, Ross, S., and Carano, R.A. Vessel imaging with viable tumor analysis for quantification of tumor angiogenesis. Magnetic resonance in medicine : official

journal of the Society of Magnetic Resonance in Medicine / Society of Magnetic Resonance in Medicine **63**, 1637, 2010.

[32] Ehrhart, N., Kraft, S., Conover, D., Rosier, R.N., and Schwarz, E.M. Quantification of Massive Allograft Healing with Dynamic Contrast Enhanced-MRI and Cone Beam-CT: A Pilot Study. Clinical Orthopaedics and Related Research **466**, 1897, 2008.

[33] Haubner, R., Wester, H.J., Weber, W.A., Mang, C., Ziegler, S.I., Goodman, S.L., Senekowitsch-Schmidtke, R., Kessler, H., and Schwaiger, M. Noninvasive imaging of alpha(v)beta(3) integrin expression using F-18-labeled RGD-containing glycopeptide and positron emission tomography. Cancer Research **61**, 1781, 2001.

[34] Davidson, M.W., and Abramowitz, M. Optical Microscopy. In: Anonymous Encyclopedia of Imaging Science and Technology. : John Wiley & Sons, Inc., 2002.

[35] Lang, P., Yeow, K., Nichols, A., and Scheer, A. Cellular imaging in drug discovery. Nature reviews. Drug discovery **5**, 343, 2006.

[36] Bradbury, S., and Evennett, P. Contrast Techniques in Light Microscopy. : Bios Scientific Publishers, 1996.

[37] Ntziachristos, V. Going deeper than microscopy: the optical imaging frontier in biology. Nature Methods 7, 603, 2010.

[38] Chance, B. Near-infrared images using continuous, phase-modulated, and pulsed light with quantitation of blood and blood oxygenation. Advances in Optical Biopsy and Optical Mammography **838**, 29, 1998.

[39] Sokolov, K., Aaron, J., Hsu, B., Nida, D., Gillenwater, A., Follen, M., MacAulay, C., Adler-Storthz, K., Korgel, B., Descour, M., Pasqualini, R., Arap, W., Lam, W., and Richards-Kortum, R. Optical systems for In vivo molecular imaging of cancer. Technology in Cancer Research & Treatment **2**, 491, 2003.

[40] Faber, D.J., Mik, E.G., Aalders, M.C.G., and van Leeuwen, T.G. Light absorption of (oxy-) hemoglobin assessed by spectroscopic optical coherence tomography. Optics Letters **28**, 1436, 2003.

[41] McDonald, D.M., and Choyke, P.L. Imaging of angiogenesis: from microscope to clinic. Nature medicine **9**, 713, 2003.

[42] Thevenot, P.T., and Liping Tang. Novel Method to Monitor Cell Survival and Distribution in PLGA Degradable Scaffolds. Engineering in Medicine and Biology Workshop, 39, 2007.

[43] Meijering, E. Time-lapse imaging. In: Anonymous Microscope Image Processing. , 2008, pp. 401.

[44] Errington, R.J., Marquez, N., Chappell, S.C., Wiltshire, M., and Smith, P.J. Time-lapse microscopy approaches to track cell cycle progression at the single-cell level. Curr Protoc Cytom **Chapter 12**, Unit 12 4, 2005.

[45] Celis, J.E. Cell Biology: A Laboratory Handbook. **: Elsevier Academic, 2006**.

[46] Cox, G. Biological confocal microscopy. Materials Today **5**, 34, 2002.

[47] Claxton, N.S., Fellers, T.J., and Davidson, M.W. Laser scanning confocal microscopy. Olympus. Available online at www.olympusconfocal.com/theory/LSCMIntro.pdf, 2006.

[48] Fujimoto, J.G., and Farkas, D. Biomedical Optical Imaging. : Oxford University Press, USA, 2009.

[49] Prasad, V., Semwogerere, D., and Weeks, E.R. Confocal microscopy of colloids. Journal of Physics-Condensed Matter **19**, 2007.

[50] Webb, R.H. Confocal optical microscopy. Reports on Progress in Physics **59**, 427, 1999.

[51] Wnek, G.E., and Bowlin, G.L. Encyclopedia of Biomaterials and Biomedical Engineering: L-Z. : Marcel Dekker, 2004.

[52] Niesner, R.A., and Hauser, A.E. Recent advances in dynamic intravital multi-photon microscopy. Cytometry A **79**, 789, 2011.

[53] Diaspro, A., Bianchini, P., Vicidomini, G., Faretta, M., Ramoino, P., and Usai, C. Multi-photon excitation microscopy. Biomed Eng Online **5**, 36, 2006.

[54] Diaspro, A., Chirico, G., and Collini, M. Two-photon fluorescence excitation and related techniques in biological microscopy. Quarterly reviews of biophysics **38**, 97, 2005.

[55] Huang, B., Bates, M., and Zhuang, X. Super-resolution fluorescence microscopy. Annual Review of Biochemistry **78**, 993, 2009.

[56] Isherwood, B., Timpson, P., McGhee, E.J., Anderson, K.I., Canel, M., Serrels, A., Brunton, V.G., and Carragher, N.O. Live Cell in Vitro and in Vivo Imaging Applications: Accelerating Drug Discovery. Pharmaceutics 3, 141, 2011.

[57] Dawood, A., Lotfi, P., Dash, S., Kona, S., Nguyen, K., and Romero-Ortega, M. VEGF Release in Multiluminal Hydrogels Directs Angiogenesis from Adult Vasculature *In Vitro*. Cardiovascular Engineering and Technology **2**, 173, 2011.

[58] Nakatsu, M.N., and Hughes, C.C. An optimized three-dimensional in vitro model for the analysis of angiogenesis. Methods in enzymology **443**, 65, 2008.

[59] Chau, L.T., Rolfe, B.E., and Cooper-White, J.J. A microdevice for the creation of patent, three-dimensional endothelial cell-based microcirculatory networks. Biomicrofluidics **5**, 2011.

[60] Vickerman, V., Blundo, J., Chung, S., and Kamm, R. Design, fabrication and implementation of a novel multi-parameter control microfluidic platform for three-dimensional cell culture and real-time imaging. Lab on a Chip **8**, 1468, 2008.

[61] Chung, S., Sudo, R., Vickerman, V., Zervantonakis, I.K., and Kamm, R.D. Microfluidic platforms for studies of angiogenesis, cell migration, and cell-cell interactions. Sixth International Bio-Fluid Mechanics Symposium and Workshop March 28-30, 2008 Pasadena, California. Annals of biomedical engineering **38**, 1164, 2010.

[62] Grainger, S.J., and Putnam, A.J. Assessing the Permeability of Engineered Capillary Networks in a 3D Culture. PLoS ONE **6**, e22086, 2011.

[63] Song, J.W., and Munn, L.L. Fluid forces control endothelial sprouting. Proc Natl Acad Sci U S A **108**, 15342, 2011.

[64] Hastings, J.W. Biological diversity, chemical mechanisms, and the evolutionary origins of bioluminescent systems. Journal of molecular evolution **19**, 309, 1983.

[65] Liu, J., Barradas, A., Fernandes, H., Janssen, F., Papenburg, B., Stamatialis, D., Martens, A., van Blitterswijk, C., and de Boer, J. In vitro and in vivo bioluminescent imaging of hypoxia in tissue-engineered grafts. Tissue engineering. Part C, Methods **16**, 479, 2010.

[66] Jenkins, D., Oei, Y., Hornig, Y., Yu, S., Dusich, J., Purchio, T., and Contag, P. Bioluminescent imaging (BLI) to improve and refine traditional murine models of tumor growth and metastasis. Clinical and Experimental Metastasis **20**, 733, 2003.

[67] Wang, W., and El-Deiry, W. Bioluminescent Molecular Imaging of Endogenous and Exogenous p53-Mediated Transcription In Vitro and In Vivo Using an HCT116 Human Colon Carcinoma Xenograft Model. Cancer Biol Ther **2**, 194, 2003.

[68] Wang, J., Najjar, A., Zhang, S., Rabinovich, B., Willerson, J.T., Gelovani, J.G., and Yeh, E.T.H. Molecular Imaging of Mesenchymal Stem Cell / Clinical Perspective. Circulation: Cardiovascular Imaging **5**, 94, 2012.

[69] Nadella, M.V., Kisseberth, W.C., Nadella, K.S., Thudi, N.K., Thamm, D.H., McNiel, E.A., Yilmaz, A., Boris-Lawrie, K., and Rosol, T.J. NOD/SCID mouse model of canine T-cell lymphoma with humoral hypercalcaemia of malignancy: cytokine gene expression profiling and in vivo bioluminescent imaging. Veterinary and comparative oncology **6**, 39, 2008.

[70] Xie, Y., Yin, T., Wiegraebe, W., He, X.C., Miller, D., Stark, D., Perko, K., Alexander, R., Schwartz, J., Grindley, J.C., Park, J., Haug, J.S., Wunderlich, J.P., Li, H., Zhang, S., Johnson, T., Feldman, R.A., and Li, L. Detection of functional haematopoietic stem cell niche using real-time imaging. Nature **457**, 97, 2009.

[71] Lapp, S.J. Bioluminescence Imaging Strategies for Tissue Engineering Applications [Master's Thesis]. Blacksburg: Virginia Polytechnic Institute and State University, 2010.

[72] Logeart-Avramoglou, D., Oudina, K., Bourguignon, M., Delpierre, L., Nicola, M.A., Bensidhoum, M., Arnaud, E., and Petite, H. In vitro and in vivo bioluminescent

quantification of viable stem cells in engineered constructs. Tissue engineering Part C, Methods **16**, 447, 2010.

[73] Liang, X., Graf, B.W., and Boppart, S.A. Imaging engineered tissues using structural and functional optical coherence tomography. J Biophotonics **2**, 643, 2009.

[74] Graf, B.W., and Boppart, S.A. Imaging and analysis of three-dimensional cell culture models. Methods Mol Biol **591**, 211, 2010.

[75] Yang, Y., Dubois, A., Qin, X.P., Li, J., El Haj, A., and Wang, R.K. Investigation of optical coherence tomography as an imaging modality in tissue engineering. Physics in medicine and biology **51**, 1649, 2006.

[76] Tan, W., Vinegoni, C., Norman, J.J., Desai, T.A., and Boppart, S.A. Imaging cellular responses to mechanical stimuli within three-dimensional tissue constructs. Microsc Res Tech **70**, 361, 2007.

[77] Wang, L.V., and Hu, S. Photoacoustic tomography: in vivo imaging from organelles to organs. Science **335**, 1458, 2012.

[78] Yao, J., and Wang, L.V. Photoacoustic tomography: fundamentals, advances and prospects. Contrast Media Mol Imaging **6**, 332, 2011.

[79] Zhang, Y., Cai, X., Wang, Y., Zhang, C., Li, L., Choi, S.W., Wang, L.V., and Xia, Y. Noninvasive photoacoustic microscopy of living cells in two and three dimensions through enhancement by a metabolite dye. Angew Chem Int Ed Engl **50**, 7359, 2011.

[80] Jia, Y., Bagnaninchi, P.O., Yang, Y., Haj, A.E., Hinds, M.T., Kirkpatrick, S.J., and Wang, R.K. Doppler optical coherence tomography imaging of local fluid flow and shear stress within microporous scaffolds. J Biomed Opt **14**, 034014, 2009.

[81] Vakoc, B.J., Lanning, R.M., Tyrrell, J.A., Padera, T.P., Bartlett, L.A., Stylianopoulos, T., Munn, L.L., Tearney, G.J., Fukumura, D., Jain, R.K., and Bouma, B.E. Three-dimensional microscopy of the tumor microenvironment in vivo using optical frequency domain imaging. Nat Med **15**, 1219, 2009.

[82] Kamoun, W.S., Chae, S.S., Lacorre, D.A., Tyrrell, J.A., Mitre, M., Gillissen, M.A., Fukumura, D., Jain, R.K., and Munn, L.L. Simultaneous measurement of RBC

velocity, flux, hematocrit and shear rate in vascular networks. Nat Methods **7**, 655, 2010.

[83] Rege, A., Murari, K., Seifert, A., Pathak, A.P., and Thakor, N.V. Multiexposure laser speckle contrast imaging of the angiogenic microenvironment. J Biomed Opt **16**, 056006, 2011.

[84] Rege, A., Thakor, N.V., Rhie, K., and Pathak, A.P. In vivo laser speckle imaging reveals microvascular remodeling and hemodynamic changes during wound healing angiogenesis. Angiogenesis **15**, 87, 2012.

[85] Webb, S. The Physics of Medical Imaging. : Hilger, 1988.

[86] Haacke, E.M. Magnetic Resonance Imaging: Physical Principles and Sequence Design. : J. Wiley & Sons, 1999.

[87] Chavhan, G.B., Babyn, P.S., Thomas, B., Shroff, M.M., and Haacke, E.M. Principles, Techniques, and Applications of T2*-based MR Imaging and Its Special Applications. Radiographics **29**, 1433, 2009.

[88] Rummeny, E.J., Reimer, P., and Heindel, W. MR Imaging of the Body. : Thieme, 2009.

[89] Jugé, L., Doan, B.T., Seguin, J., Albuquerque, M., Larrat, B., Scherman, D., Vilgrain, V., Paradis, V., Van-Beers, B. and Sinkus, R. MR-Elastography, a new biomarker of the tumor vascularization in a colon cancer mice model. International Society for Magnetic Resonance in Medicine **19**, 3485, 2011.

[90] Buschmann, J., Welti, M., Hemmi, S., Neuenschwander, P., Baltes, C., Giovanoli, P., Rudin, M., and Calcagni, M. Three-Dimensional Co-Cultures of Osteoblasts and Endothelial Cells in DegraPol Foam: Histological and High-Field Magnetic Resonance Imaging Analyses of Pre-Engineered Capillary Networks in Bone Grafts. Tissue Engineering Part A **17**, 291, 2011.

[91] Terrovitis, J.V., Bulte, J.W.M., Sarvananthan, S., Crowe, L.A., Sarathchandra, P., Batten, P., Sachlos, E., Chester, A.H., Czernuszka, J.T., Firmin, D.N., Taylor, P.M., and Yacoub, M.H. Magnetic Resonance Imaging of Ferumoxide-Labeled

Mesenchymal Stem Cells Seeded on Collagen Scaffolds Relevance to Tissue Engineering. Tissue engineering **12**, 2765, 2006.

[92] Ravindran, S., Gao, Q., Kotecha, M., Magin, R.L., Karol, S., Bedran-Russo, A., and George, A. Biomimetic extracellular matrix-incorporated scaffold induces osteogenic gene expression in human marrow stromal cells. Tissue engineering Part A **18**, 295, 2012.

[93] Wilhelm, C., Bal, L., Smirnov, P., Galy-Fauroux, I., Clement, O., Gazeau, F., and Emmerich, J. Magnetic control of vascular network formation with magnetically labeled endothelial progenitor cells. Biomaterials **28**, 3797, 2007.

[94] Li, W., Hong, L., Hu, L., and Magin, R.L. Magnetization transfer imaging provides a quantitative measure of chondrogenic differentiation and tissue development. Tissue engineering. Part C, Methods **16**, 1407, 2010.

[95] Xu, H.H., Othman, S.F., and Magin, R.L. Monitoring Tissue Engineering Using Magnetic Resonance Imaging. Journal of Bioscience and Bioengineering **106**, 515, 2008.

[96] Di Ieva, A., Grizzi, F., Rognone, E., Tse, Z.T.H., Parittotokkaporn, T., Baena, F.R.Y., Tschabitscher, M., Matula, C., Trattnig, S., and Baena, R.R.Y. Magnetic resonance elastography: a general overview of its current and future applications in brain imaging. Neurosurgical Review **33**, 137, 2010.

[97] Mariappan, Y.K., Glaser, K.J., and Ehman, R.L. Magnetic resonance elastography: a review. Clinical anatomy (New York, N Y) **23**, 497, 2010.

[98] Asbach, P., Klatt, D., Schlosser, B., Biermer, M., Muche, M., Rieger, A., Loddenkemper, C., Somasundaram, R., Berg, T., Hamm, B., Braun, J., and Sack, I. Viscoelasticity-based staging of hepatic fibrosis with multifrequency MR elastography. Radiology **257**, 80, 2010.

[99] Lunt, S.J., Chaudary, N., and Hill, R.P. The tumor microenvironment and metastatic disease. Clinical & Experimental Metastasis **26**, 19, 2009.

[100] Yu, H., Mouw, J.K., and Weaver, V.M. Forcing form and function: biomechanical regulation of tumor evolution. Trends in cell biology **21**, 47, 2011.

[101] Kumar, S., and Weaver, V.M. Mechanics, malignancy, and metastasis: the force journey of a tumor cell. Cancer Metastasis Reviews **28**, 113, 2009.

[102] Huang, S., and Ingber, D.E. Cell tension, matrix mechanics, and cancer development. Cancer Cell **8**, 175, 2005.

[103] Jugé, L., Doan, B.T., Seguin, J., Larrat, B., Herscovici, J., Scherman, D., and Sinkus, R. Characterization of tumor vascularization in mice using MRE. International Society for Magnetic Resonance in Medicine **18**, 1053, 2010.

[104] Juge, L., Doan, B.T., Seguin, J., Albuquerque, M., Larrat, B., Mignet, N., Chabot, G.G., Scherman, D., Paradis, V., Vilgrain, V., Van Beers, B.E., and Sinkus, R. Colon tumor growth and antivascular treatment in mice: complementary assessment with MR elastography and diffusion-weighted MR imaging. Radiology **264**, 436, 2012.

[105] Choyke, P.L., Dwyer, A.J., and Knopp, M.V. Functional tumor imaging with dynamic contrast-enhanced magnetic resonance imaging. Journal of Magnetic Resonance Imaging **17**, 509, 2003.

[106] O'Connor, J.P., Jackson, A., Parker, G.J., and Jayson, G.C. DCE-MRI biomarkers in the clinical evaluation of antiangiogenic and vascular disrupting agents. British journal of cancer **96**, 189, 2007.

[107] Bulte, J.W., and Kraitchman, D.L. Iron oxide MR contrast agents for molecular and cellular imaging. NMR in biomedicine **17**, 484, 2004.

[108] Matsuo, M., Kanematsu, M., Itoh, K., Ito, K., Maetani, Y., Kondo, H., Kako, N., Matsunaga, N., Hoshi, H., and Shiraishi, J. Detection of Malignant Hepatic Tumors. American Journal of Roentgenology **177**, 637, 2001.

[109] Shapiro, E.M., Skrtic, S., Sharer, K., Hill, J.M., Dunbar, C.E., and Koretsky, A.P. MRI detection of single particles for cellular imaging. Proceedings of the National Academy of Sciences of the United States of America **101**, 10901, 2004.

[110] Yu, M.K., Park, J., and Jon, S. Targeting strategies for multifunctional nanoparticles in cancer imaging and therapy. Theranostics **2**, 3, 2012.

[111] Babic, M., Horak, D., Trchova, M., Jendelova, P., Glogarova, K., Lesny, P., Herynek, V., Hajek, M., and Sykova, E. Poly(L-lysine)-modified iron oxide nanoparticles for stem cell labeling. Bioconjug Chem **19**, 740, 2008.

[112] Sadeghiani N, Barbosa LS, Silva LP, Azevedo RB, Morais PC, Lacava ZGM. Genotoxicity and inflammatory investigation in mice treated with magnetite nanoparticles surface coated with polyaspartic acid. J. Magnetism Magnetic Materials 2005; 289: 466–8.

[113] Shirakawa, K., Shibuya, M., Heike, Y., Takashima, S., Watanabe, I., Konishi, F., Kasumi, F., Goldman, C.K., Thomas, K.A., Bett, A., Terada, M., and Wakasugi, H. Tumor-infiltrating endothelial cells and endothelial precursor cells in inflammatory breast cancer. International Journal of Cancer **99**, 344, 2002.

[114] Dome, B., Timar, J., Dobos, J., Meszaros, L., Raso, E., Paku, S., Kenessey, I., Ostoros, G., Magyar, M., Ladanyi, A., Bogos, K., and Tovari, J. Identification and clinical significance of circulating endothelial progenitor cells in human non-small cell lung cancer. Cancer Research **66**, 7341, 2006.

[115] Lyden, D., Hattori, K., Dias, S., Costa, C., Blaikie, P., Butros, L., Chadburn, A., Heissig, B., Marks, W., Witte, L., Wu, Y., Hicklin, D., Zhu, Z.P., Hackett, N.R., Crystal, R.G., Moore, M.A.S., Hajjar, K.A., Manova, K., Benezra, R., and Rafii, S. Impaired recruitment of bone-marrow-derived endothelial and hematopoietic precursor cells blocks tumor angiogenesis and growth. Nature medicine **7**, 1194, 2001.

[116] Duda, D.G., Cohen, K.S., Kozin, S.V., Perentes, J.Y., Fukumura, D., Scadden, D.T., and Jain, R.K. Evidence for incorporation of bone marrow-derived endothelial cells into perfused blood vessels in tumors. Blood **107**, 2774, 2006.

[117] Gao, D., Nolan, D.J., Mellick, A.S., Bambino, K., McDonnell, K., and Mittal, V. Endothelial Progenitor Cells Control the Angiogenic Switch in Mouse Lung Metastasis. Science **319**, 195, 2008.

[118] Gimi, B., Mori, N., Ackerstaff, E., Frost, E.E., Bulte, J.W., and Bhujwalla, Z.M. Noninvasive MRI of endothelial cell response to human breast cancer cells. Neoplasia **8**, 207, 2006.

[119] Barrett, T., Kobayashi, H., Brechbiel, M., and Choyke, P.L. Macromolecular MRI contrast agents for imaging tumor angiogenesis. European journal of radiology **60**, 353, 2006.

[120] Kiessling, F. Noninvasive Cell Tracking; Molecular Imaging II. In: Semmler, W. and Schwaiger, M., eds.: Springer Berlin Heidelberg, 2008, pp. 305-321.

[121] Zhang, C., Jugold, M., Woenne, E.C., Lammers, T., Morgenstern, B., Mueller, M.M., Zentgraf, H., Bock, M., Eisenhut, M., Semmler, W., and Kiessling, F. Specific targeting of tumor angiogenesis by RGD-conjugated ultrasmall superparamagnetic iron oxide particles using a clinical 1.5-T magnetic resonance scanner. Cancer Research **67**, 1555, 2007.

[122] Schmieder, A.H., Caruthers, S.D., Zhang, H., Williams, T.A., Robertson, J.D., Wickline, S.A., and Lanza, G.M. Three-dimensional MR mapping of angiogenesis with alpha5beta1(alpha nu beta3)-targeted theranostic nanoparticles in the MDA-MB-435 xenograft mouse model. The FASEB journal: official publication of the Federation of American Societies for Experimental Biology **22**, 4179, 2008.

[123] Waters, E.A., Chen, J., Allen, J.S., Zhang, H., Lanza, G.M., and Wickline, S.A. Detection and quantification of angiogenesis in experimental valve disease with integrin-targeted nanoparticles and 19-fluorine MRI/MRS. J Cardiovasc Magn Reson **10**, 43, 2008.

[124] Pathak, A.P., Kim, E., Zhang, J., and Jones, M.V. Three-dimensional imaging of the mouse neurovasculature with magnetic resonance microscopy. PloS one **6**, e22643, 2011.

[125] Zhang, Z., Mascheri, N., Dharmakumar, R., Fan, Z., Paunesku, T., Woloschak, G., and Li, D. Superparamagnetic iron oxide nanoparticle-labeled cells as an effective vehicle for tracking the GFP gene marker using magnetic resonance imaging. Cytotherapy **11**, 43, 2009.

[126] Jeng, H.A., and Swanson, J. Toxicity of metal oxide nanoparticles in mammalian cells. Journal of environmental science and health Part A, Toxic/hazardous substances & environmental engineering **41**, 2699, 2006.

[127] Hussain, S.M., Hess, K.L., Gearhart, J.M., Geiss, K.T., and Schlager, J.J. In vitro toxicity of nanoparticles in BRL 3A rat liver cells. Toxicology in vitro : an international journal published in association with BIBRA **19**, 975, 2005.

[128] Stroh, A., Zimmer, C., Gutzeit, C., Jakstadt, M., Marschinke, F., Jung, T., Pilgrimm, H., and Grune, T. Iron oxide particles for molecular magnetic resonance imaging cause transient oxidative stress in rat macrophages. Free radical biology & medicine **36**, 976, 2004.

[129] Zhang, Z., van den Bos, E.J., Wielopolski, P.A., de Jong-Popijus, M., Bernsen, M.R., Duncker, D.J., and Krestin, G.P. In vitro imaging of single living human umbilical vein endothelial cells with a clinical 3.0-T MRI scanner. MAGMA **18**, 175, 2005.

[130] Drobny, J.G. Radiation Technology for Polymers. : CRC Press/Taylor & Francis, 2010.

[131] Webster, J.G. Minimally Invasive Medical Technology. : Institute of Physics Pub., 2001.

[132] Louis, L., Wong, T., Baud, P., and Tembe, S. Imaging strain localization by X-ray computed tomography: discrete compaction bands in Diemelstadt sandstone. Journal of Structural Geology **28**, 762, 2006.

[133] Wan, S.Y., Kiraly, A.P., Ritman, E.L., and Higgins, W.E. Extraction of the hepatic vasculature in rats using 3-D micro-CT images. Ieee Transactions on Medical Imaging **19**, 964, 2000.

[134] Garcia-Sanz, A., Rodriguez-Barbero, A., Bentley, M.D., Ritman, E.L., and Romero, J.C. Three-dimensional microcomputed tomography of renal vasculature in rats. Hypertension **31**, 440, 1998.

[135] Rai, B., Oest, M.E., Dupont, K.M., Ho, K.H., Teoh, S.H., and Guldberg, R.E. Combination of platelet-rich plasma with polycaprolactone-tricalcium phosphate

scaffolds for segmental bone defect repair. Journal of Biomedical Materials Research Part A **81A**, 888, 2007.

[136] Patel, Z.S., Young, S., Tabata, Y., Jansen, J.A., Wong, M.E.K., and Mikos, A.G. Dual delivery of an angiogenic and an osteogenic growth factor for bone regeneration in a critical size defect model. Bone **43**, 931, 2008.

[137] Schmidt, C., Bezuidenhout, D., Beck, M., Van der Merwe, E., Zilla, P., and Davies, N. Rapid three-dimensional quantification of VEGF-induced scaffold neovascularisation by microcomputed tomography. Biomaterials **30**, 5959, 2009.

[138] Kerbel, R.S. Tumor Angiogenesis. N Engl J Med **358**, 2039, 2008.

[139] Kargiotis, O., Geka, A., Rao, J.S., and Kyritsis, A.P. Effects of irradiation on tumor cell survival, invasion and angiogenesis. Journal of Neuro-Oncology **100**, 323, 2010.

[140] Takahashi, Y., Teshima, T., Kawaguchi, N., Hamada, Y., Mori, S., Madachi, A., Ikeda, S., Mizuno, H., Ogata, T., Nojima, K., Furusawa, Y., and Matsuura, N. Heavy ion irradiation inhibits in vitro angiogenesis even at sublethal dose. Cancer Research **63**, 4253, 2003.

[141] Young, S., Kretlow, J.D., Nguyen, C., Bashoura, A.G., Baggett, L.S., Jansen, J.A., Wong, M., and Mikos, A.G. Microcomputed tomography characterization of neovascularization in bone tissue engineering applications. Tissue Engineering Part B-Reviews **14**, 295, 2008.

[142] Kim, I.G. Radiation-induced tumorigenesis. Journal of biochemistry and molecular biology **36**, 144, 2003.

[143] Mullenders, L., Atkinson, M., Paretzke, H., Sabatier, L., and Bouffler, S. Assessing cancer risks of low-dose radiation. Nat Rev Cancer **9**, 596, 2009.

[144] Hlushchuk, R., Riesterer, O., Baum, O., Wood, J., Gruber, G., Pruschy, M., and Djonov, V. Tumor recovery by angiogenic switch from sprouting to intussusceptive angiogenesis after treatment with PTK787/ZK222584 or ionizing radiation. The American journal of pathology **173**, 1173, 2008.

[145] Sasaki, T., Yamamoto, M., Yamaguchi, T., and Sugiyama, S. Development of Multicellular Spheroids of Hela-Cells Cocultured with Fibroblasts and Their Response to X-Irradiation. Cancer Research **44**, 345, 1984.

[146] Saha, G.B. Basics of PET Imaging: Physics, Chemistry, and Regulations. : Springer, 2010.

[147] Knoll, G.F. Single-photon emission computed tomography. Proceedings of the IEEE **71**, 320, 1983.

[148] Niu, G., and Chen, X. PET Imaging of Angiogenesis. PET clinics **4**, 17, 2009.

[149] Cherry, S.R., Shao, Y., Siegel, S., Silverman, R.W., Meadors, K., Young, J., Jones, W.F., Newport, D., Moyers, C., Mumcuoglu, E.U., Chatziioannou, A., Farquhar, T., Andreaco, M., Paulus, M., Binkley, D., Nutt, R., and Phelps, M.E. MicroPET: A high resolution PET scanner for imaging small animals. 1996 IEEE Nuclear Science Symposium - Conference Record, **Vols 1-3** , 1120, 1997.

[150] Zeniya, T., Watabe, H., Aoi, T., Kim, K.M., Teramoto, N., Takeno, T., Ohta, Y., Hayashi, T., Mashino, H., Ota, T., Yamamoto, S., and Iida, H. Use of a compact pixellated gamma camera for small animal pinhole SPECT imaging. Annals of Nuclear Medicine **20**, 409, 2006.

[151] Zaidi, H., and Del Guerra, A. An outlook on future design of hybrid PET/MRI systems. Medical Physics **38**, 5667, 2011.

[152] Abramoff, M.D., Magalhaes, P.J.,Ram S.J. Image Processing with Image J. Biophotonics International **11**, 36, 2004.

[153] Sarkanen, J.R., Mannerstrom, M., Vuorenpaa, H., Uotila, J., Ylikomi, T., and Heinonen, T. Intra-Laboratory Pre-Validation of a Human Cell Based in vitro Angiogenesis Assay for Testing Angiogenesis Modulators. Frontiers in pharmacology **1**, 147, 2010.

[154] Beilmann, M., Birk, G., and Lenter, M.C. Human primary co-culture angiogenesis assay reveals additive stimulation and different angiogenic properties of VEGF and HGF. Cytokine **26**, 178, 2004.

[155] Sarabi, A., Kramp, B.K., Drechsler, M., Hackeng, T.M., Soehnlein, O., Weber, C., Koenen, R.R., and von Hundelshausen, P. CXCL4L1 inhibits angiogenesis and induces undirected endothelial cell migration without affecting endothelial cell proliferation and monocyte recruitment. Journal of Thrombosis and Haemostasis **9**, 209, 2011.

[156] Wang, C.K., Cao, J.G., Qu, J.Q., Li, Y.F., Peng, B., Gu, Y.X., and He, Z.M. Recombinant Vascular Basement Membrane Derived Multifunctional Peptide Blocks Endothelial Cell Angiogenesis and Neovascularization. Journal of Cellular Biochemistry **111**, 453, 2010.

[157] Wang, B.H., Pearson, T., Manning, G., and Donnelly, R. In Vitro Study of Thrombin on Tubule Formation and Regulators of Angiogenesis. Clinical and Applied Thrombosis-Hemostasis **16**, 674, 2010.

[158] Niemisto, A., Dunmire, V., Yli-Harja, O., Zhang, W., and Shmulevich, I. Robust quantification of in vitro angiogenesis through image analysis. Ieee Transactions on Medical Imaging **24**, 549, 2005.

[159] Doukas, C.N., Maglogiannis, I., Chatziioannou, A., and Papapetropoulos, A. Automated angiogenesis quantification through advanced image processing techniques. Conf Proc IEEE Eng Med Biol Soc **1,** 2345, 2006.

[160] Gould, D.J., Vadakkan, T.J., Poche, R.A., and Dickinson, M.E. Multifractal and lacunarity analysis of microvascular morphology and remodeling. Microcirculation **18**, 136, 2011.

[161] Abdul-Karim, M.A., Al-Kofahi, K., Brown, E.B., Jain, R.K., and Roysam, B. Automated tracing and change analysis of angiogenic vasculature from in vivo multiphoton confocal image time series. Microvasc Res **66**, 113, 2003.

[162] Rytlewski, J.A., Geuss, L.R., Anyaeji, C.I., Lewis, E.W., and Suggs, L.J. Three-dimensional image quantification as a new morphometry method for tissue engineering. Tissue engineering Part C, Methods **18**, 507, 2012.

[163] Borgert, J., Schmidt, J.D., Schmale, I., Rahmer, J., Bontus, C., Gleich, B., David, B., Eckart, R., Woywode, O., Weizenecker, J., Schnorr, J., Taupitz, M., Haegele,

J., Vogt, F.M., and Barkhausen, J. Fundamentals and applications of magnetic particle imaging. Journal of cardiovascular computed tomography **6**, 149, 2012.

[164] Markov, D.E., Boeve, H., Gleich, B., Borgert, J., Antonelli, A., Sfara, C., and Magnani, M. Human erythrocytes as nanoparticle carriers for magnetic particle imaging. Physics in medicine and biology **55**, 6461, 2010.

# CHAPTER 8

## Summary and Future Works

### 8.1 SUMMARY

The *in vitro* modeling of blood vessels from the artery down to capillary-level is a complex challenge, in terms of the anatomical and bio-fluid considerations. This dissertation addresses the problem through experimental and computational studies of a branching network that mimics artery/arteriole and vein/venuole structure and connects to a compartment with embedded porous scaffolds. Based on Murray's Law of branching networks and published anatomical studies, the computer-generated networks bifurcate along a single plane. The flexibility of the computer-generated vascular trees will allow for the design to be extended, such that the tree bifurcates in three dimensions. The idealized "arterial-like" vascular tree (in terms of inner diameter and cylindrical geometry) bifurcates over four generations to reach the minimum inner diameter resolution of most rapid prototyping methods. There are a myriad of rapid prototyping methods available to tissue engineers. For the fabrication of the presented dynamic imaging phantom, selective laser sintering (SLS) (along with fused deposition modeling) provided the best spatial resolution to reliably generate hollow, cylindrical, bifurcating networks. To achieve the luminal diameter and/tortuosity that could achieve bulk flow behavior characteristic of microcirculation, scaffolds (pore diameters 0.11 - 2.2 mm) were incorporated into the design of the distributed flow construct. For both the dynamic imaging phantom and dynamic bioreactor, the SLS technique was used to generate scaffolds that met the target flow ranges (in terms of differential flow and shear stress, respectively) of the system designed. The same construct was used for both applications; however, the fluid and boundary conditions were optimized for the respective systems.

In the development of the dynamic imaging phantom, the inlet flow rate of the system was chosen to mimic the velocity within arteries. A clinical dynamic contrast enhanced

(DCE)-Computed Tomography (CT) patient protocol and setup, which included contrast agent solution and contrast injector were used within their normal operating ranges. An inline mixer was incorporated into the streamline of the system prior to the phantom inlet, in order to achieve the mixing of contrast agent and blood-like fluid through the body, which normally occurs in the patient's bloodstream. Adequate mixing was visualized in simulations of the system. Simulations also confirmed theoretical estimates of uniform flow splitting across the bifurcations of the vascular tree and porous scaffold compartments. Experimental and computational differential flow (DF) measurements confirmed that high and low differential flows were generated within the phantom, using scaffolds with controlled architecture and perfusion characteristics. Using a porous jump computational fluid dynamics (CFD) model, based on the desired differential flow, the intrinsic permeability required of the scaffold was determined. This information can be used to design an appropriate SLS scaffold to incorporate into future generations of the dynamic imaging phantom, in order to fine-tune or expand the range of fluid flow rate changes realized by the dynamic imaging phantom. The phantom successfully demonstrated distinct differential flows, wherein imaged anatomical structures were below the resolution of a clinical scanner, as with actual patient data. The simplicity of the manufacturing method and the reusability of the system (due to acetic acid surface treatment) render the phantom a useful tool to be further studied for use in the quality assurance of DCE-CT. Initial DCE-CT post-processing analysis based on a single input, single output, capillary model demonstrated similar results to the experimental and computational differential flow measurements. Further studies can be performed to validate and/or understand the sensitivity of post-analysis tools and methods, using these comparison standards (computational and experimental).

The second application of the designed construct involved the development of thick engineered tissue. The vascular tree design distributed uniform flow to scaffolds, mimicking the bathing of tissue volumes by arterioles/small arteries. A perfusion bioreactor was adopted as a favorable i*n vitro* pre-vascularization strategy to enable future implantation studies, in which the construct would be anastomosed to a nearby artery and vein. The biocompatibility and operating conditions of the bioreactor were considered in order to enhance cell proliferation and ultimately the mechanism of

angiogenesis. Two large scaffold architectures were considered to determine which geometry stimulated endothelial cell growth over 1 - 10 dynes/cm$^2$ under laminar flow conditions, with the best tradeoff between cell stimulation and detachment. Based on simulations, the spherical scaffold was selected to perform biocompatibility studies, as the geometry provided more uniform flow across the scaffold and achieved the target shear stress range over a larger portion of the surface area. The biocompatibility properties of untreated PCL were compared to three surface modifications: RGD peptide conjugation, vascular endothelial growth factor conjugation and sodium hydroxide hydrolysis. The cell proliferation and cell spatial distribution of human umbilical vein endothelial cells cultured under static conditions for three days on surface-modified PCL matrices was assessed. Cells were seeded drop-wise onto the scaffold to avoid washout of seeding gels. Across treatment groups, the cell proliferation and vWF release were comparable, with RGD peptide-modified constructs exhibiting slightly higher cell proliferation across the edges of the scaffold. The successful implementation of the optimized *in vitro* perfusion bioreactor lends itself to future bone cell co-culture studies, as well as three-dimensional tumor model investigations where the localization of endothelial cells can create gradients needed for necrosis or be uniform for homogenous tissue growth.

### 8.1.1 Original Contributions

The original contributions of this research are as follows:

(1) Developed a computerized "arterial" vascular tree for fabrication using SLS. The vascular tree has an inlet and outlet inner diameter of 2.2 mm and 0.620 mm, respectively.

(2) Developed a construct that adjoined two vascular trees to modular scaffold compartments for distribution and then the collection of fluid. The construct allowed for the connection of a fluid source to perfuse the system, mimicking small artery-like inlet perfusion characteristics, in terms of either shear stress or differential flow, dependent on the boundary conditions and the particular scaffold incorporated.

(3) Developed a prototype dynamic imaging phantom manufactured using SLS. The phantom achieves the range of differential flow measurable by DCE-CT imaging post-processing analysis.

(4) Demonstrated the utility of CFD in the validation of a dynamic imaging phantom. Validated experimental differential flow measurements against computational simulations through the bioreactor, for low and high permeability scaffolds. The entire phantom system was simulated to ensure proper fluid mixing and the uniformity of flow through the system.

(5) Introduced a predictive model to determine the flow changes characteristics of a model scaffold (based on input architecture), in terms of the intrinsic permeability required to realize a range of differential flow useful for imaging within a dynamic phantom.

(6) Demonstrated the usefulness of using computational simulations to determine the fluid-induced shear stress distribution within tissue engineered scaffolds (structured lattice) in a cell bioreactor. Determined the inlet velocity for which large (11 mm height x 11 mm diameter) spherical pore scaffold imposed a shear stress between 1 - 10 dynes/cm$^2$ over a larger surface area than orthogonal pore scaffold.

(7) Confirmed that of the two bone scaffold architectures previously studied in the Hollister group, the spherical pore (2.22 mm pore diameter) geometry was more likely than the orthogonal geometry to produce shear stress within the range required for *in vitro* endothelial cell dynamic studies.

(8) Determined that RGD-functionalized PCL scaffolds supported greater endothelial cell proliferation and cell function, over the hydrolyzed and protein conjugated (particularly, vascular endothelial growth factor) PCL scaffolds. The RGD-functionalized PCL scaffolds also demonstrated greater attachment at the edges of the scaffold, which is ideal for use in an angiogenesis bioreactor, where the greatest detachment occurs at the edges.

(9) Determined that vascular endothelial growth factor conjugation onto heparin functionalized PCL scaffolds fabricated using SLS did not improve the temporal release of VEGF. Conjugation and adsorption showed similar VEGF retention and burst releases on day 1.

(10) Developed an *in vitro* dynamic endothelial cell bioreactor that supports the proliferation of endothelial cells anchored by RGD onto large bone scaffolds.

## 8.2 FUTURE RESEARCH

There are several directions for future projects that can extend from this dissertation. The following outlines a few of them:

### 8.2.1 Future Design Considerations for a Distributed Flow Polymer Construct

- It would beneficial for future re-designs to consider alternate fabrication methods that produce less permeable structures. During the course of a 5 - 30 minute DCE imaging study, the network leaked. Based on observations, the cause of leakage at the entry of the porous compartment was due to the continued fluid force imposed on the structure prior to entering the compartment. Thicker vessel walls were not feasible, since an increased wall thickness would result in a narrowing of luminal spaces and/or the loss of features (i.e. holder threading). A stronger polymer such as ABSplus (used in fused deposition modeling) may withstand greater pressure. Polymers available for SLS and other RP systems with comparable resolutions should also be explored.

- In Chapter 3, the DCE imaging studies were performed on vascular trees that bifurcated along a single plane. The vascular tree perfused four porous compartments (volume approximately 4 ml). Future iterations of the phantom design should develop a vascular tree that bifurcates along three-dimensions to perfuse a larger volume of porous compartments. Chapter 2 references previously promulgated algorithms for achieving larger, randomly generated structures. A three-dimensional vascular tree would increase the complexity and anatomical accuracy of the system, and provide a

volume comparable to a given tissue volume of interest e.g. a lobule of the liver ≈ 900 ml.

### 8.2.2 Next Generation of Dynamic Phantom

- The current phantom system does not circulate fluid, instead requires the continuous addition of simulated blood fluid. The implementation of a filter or cleansing method that removes or separates (i.e. by chelation) the iodinated contrast agent from the waste reservoir would allow for a circulating closed system that would only require periodic (over weeks or months) changes of fluid. The addition of 10% bleach to the fluid would reduce potential for molding. The 0.5 mm spaces, preceding and following the scaffold within the compartment, provide a space for air bubbles to aggregate in the system. Sealing of all the connection points within the system would reduce the opportunities for air to be introduced to the system. A gear or dispensing pump may also minimize air-bubbles in the closed system. These design changes would make the phantom re-useable and improve the reproducibility of results over time.

- Based on the relationship between the intrinsic permeability and differential flow discussed in Chapter 4, alternate scaffold fabrication techniques can be explored to expand the range of differential flows, lower than 20%. The pore diameter of SLS scaffolds can be tailored to generate differential flows between 20 - 80%. The sensitivity of image-extracted perfusion metrics can be evaluated to understand the influence of partial volume averaging and fluid behavior (constant versus pulsatile), in the context of the single-input, single-compartment model for a given system/protocol/post-processing algorithm. Similar studies would be needed to experimentally and computationally validate flow across a two-input compartment model. A longitudinal study should also be conducted to evaluate the repeatability of metrics over the course of weeks, in order to determine the lifetime of the phantom and the long-term contrast agent uptake activity of PCL.

- DCE-Magnetic Resonance Imaging (MRI) has practical benefits over DCE-CT and other functional imaging modalities. The technique offers evaluation of angiogenesis, in terms of blood flow, blood volume, vascular density and vascular permeability [1], without the introduction of ionizing radiation. DCE-MRI can also visualize structures compromised by bone artifacts under CT. The developed phantom system can be adapted to DCE-MRI with minor modifications to the system to ensure magnetic compatibility. The tissue equivalent liquid surrounding the vascular phantom can be modified by the addition of paramagnetic ions (water or gel-based) to achieve $T_1$ and $T_2$ relaxation times characteristic of human tissue, 270 - 860 ms and 50 – 80 ms respectively [2]. The peristaltic pump would also require magnetic field shielding. Gadolinium (similar viscosity and density properties to iodinate contrast agent) would be used as the contrast agent within the non-water-soluble PCL polymer that would otherwise be invisible under MRI. A recent study by Blanquer et al. investigated the development of a MRI-visible poly(epsilon-caprolactone) (PCL) graft coated with paramagnetic agents that improved $T_1$ contrast enhancement [3]. Advances in the field of materials/macromolecules would be needed to establish coatings that lengthen $T_2$ relaxation times characteristic of polymers and strengthen the MRI signal.

- The designed vascular network can also be scaled to meet the requirements of particular organ systems, such as the liver, which requires a dual-input single compartment model with separate input arterial and venous perfusion. With the addition of a second inlet into the phantom box, two boluses can be injected at two different rates, on delays, into the dynamic phantom to generate the three time-enhancement curves typically evaluated in liver perfusion analysis.

- Lastly, future experiments should investigate a new inlet flow rate for contrast agent and simulated blood fluid. The two fluids should have identical or closely matching input velocities, so as to avoid the fluctuations in speed that can influence the measured velocity that is computed in the post-analysis.

### 8.2.3 Modeling of an Endothelial Cell Bioreactor

- Chapter 5 discusses the initial flow rate conditions required to achieve an ideal range of shear stress rates within the developed endothelial cell bioreactor. However, the model does not account for the growth of endothelial cells and ultimately blood vessels on the surface of the PCL. The integration of a cell growth model, which takes into account this growth over time, would provide a guide for flow rate adjustments over a 7-14 day study. These changes would further create favorable conditions for cell growth and sprouting.

### 8.2.4 Enhancement of Endothelial Cell Activity on PCL

- Future work should include a larger scale investigation of the PCL surface modification study discussed in Chapter 6. The preliminary findings were adequate for an initial dynamic bioreactor study. To further support this work, the investigation should be repeated for 4 - 5 independent studies for Passage 5-10 endothelial cells to quantify the increased growth expected for HUVECs and human microvascular dermal endothelial (HMVEC-ds) cultured on VEGF immobilized by heparin on sodium hydroxide treated PCL scaffolds, dependent on the amount of loaded and retained heparin and VEGF.

- The effects of VEGF are dose dependent. Large doses have been shown to produce a greater fraction of immature vessels, compared to lower effective doses, which generate mature vessels. The generation of mature or immature vessels would be relevant to the investigation of tumor-like and/or normal vasculature. An increased dose of VEGF may increase the amount of VEGF release per day, after the initial burst effect. The release kinetics for PCL scaffolds loaded with varying amounts of VEGF should be explored to determine if higher amounts of loaded VEGF can increase the daily release to 100 ng/day, as recommended by the literature (summarized in Table 1 of Chapter 6) after the initial burst release. Currently, the literature does not provide a standard method to assess VEGF bioactivity under *in vitro* culture conditions. In order to indirectly assess bioactivity, variable doses of

VEGF may be added to the PCL using the conjugation method discussed in Chapter 6, then evaluated based on the rate of endothelial cell proliferation measured through MTT assays.

- Advancements in conjugation methods for the immobilization of VEGF onto PCL scaffolds may improve release kinetics. Alternate methods may eliminate the need for heparin, which competes with angiogenesis through the inhibition of endothelial cell proliferation and organization [4]. He et al. [5] demonstrated that the cross-linker reagents, Traut's reagent and sulfo-SMCC (4-(N-maleimidomethyl) cyclohexane-1-carboxylic acid 3-sulfo-N-hydroxysuccinimide ester sodium salt), can be used to immobilize VEGF onto collagen. These two reagents can be explored for PCL.


### 8.2.5 Endothelial Cell Bioreactor

- Chapter 6 discusses only the viability of HUVEC cells in the bioreactor. Continued studies should also examine the viability of HMVEC-ds in the bioreactor, under appropriate shear stress conditions. Under *in vivo* conditions, microvascular and macrovascular cells are exposed to different levels of shear stress. An HMVEC-d study would demonstrate the robustness of the design.

- In addition, the endothelial cell bioreactor study was performed under constant flow, which would be ideal for microvascular cells, but may not be for macrovascular cells, which under *in vivo* conditions experience oscillatory or pulsatile flow. Future studies should examine the influence of the flow behavior on the proliferation of HUVECs and HMVEC-ds within the endothelial cell bioreactor.

- Future angiogenesis bioreactor investigations can use the constructed system to study tumor angiogenesis and explore *in vitro* tumorigenesis. Wells et al. [6] demonstrated the feasibility of growing solid tumor masses *in vitro* in a microfluidic device. The developed perfusion bioreactor can be adapted to provide a platform for future basic cancer research related to bone or breast cancer. The bioreactor environment needs to be enhanced to provide the complex signaling (i.e. addition of stromal cells, Kupffer

242

cells and leukocytes) that promote cancer cell proliferation and ultimately the formation of a solid tumor mass.

- The developed bioreactor lends itself to *in vivo* studies, where the inlet and outlet would be anastomosed to an artery and vein, respectively. The design can be scaled down to fit a mouse model. As a pre-vascularization strategy, bone marrow stromal cells or chondrocytes can be seeded onto the scaffolds, cultured *in vitro* then implanted to study the degree of bone in-growth and the associated mechanical properties of the generated bone or cartilage, respectively.

### 8.2.6 Imaging Angiogenesis

- It has been hypothesized that Von Willebrand factor (vWF) regulates angiogenesis through the promotion of EC migration [7-8]. The work by [Zanetta] et al. suggested that vWF messenger ribonucleic acid levels correlated with the endothelium or angiogenesis activation [9]. An investigation of the relationship (cumulative and/or temporal) between vWF release and tubulation may support findings garnered using emergent *in vitro* angiogenesis imaging methods for opaque constructs.

- In this thesis, proliferation across the large scaffolds was assessed at the center and two outer sections of the porous scaffold. An MTT assay of the three sections quantified the proliferation across each section. This intrusive method can be substituted with a bioluminescence imaging (BLI) assay. Measurement of a BLI signal from the luciferase-transfected endothelial cells can provide a non-invasive method of evaluating cell attachment and proliferation under both static and dynamic culture conditions. Initial work should assess the cell toxicity and/or changes in proliferation due to the introduction of luciferase.

- Chapter 7 discusses recent investigations into the use of DCE-MRI and targeted MRI in the evaluation of angiogenesis through the localization of endothelial cells or related-signals. The use of either of these methods to evaluate tubulation under static and dynamic cell culture conditions may be used to evaluate the maturity of blood

vessels. The vascular permeability can be evaluated based on the uptake of these agents, as shown in the investigation reported by Grainger et al. [10]. Vasculature generated during tumor angiogenesis is characterized by the leakiness of the vessel network [11]. Thus, in the development of vascular networks characteristic of tumor growths, enhanced MRI techniques may be valuable. Initial work requires an initial cell toxicity and cell growth study to determine the effects of the contrast agent or nanoparticles on the endothelial cells.

## 8.3  MAJOR CONTRIBUTIONS

The major achievements of this dissertation to the field are as follows

(1) *Prototyping of a dynamic flow imaging phantom*: In this thesis, the <u>first</u> dynamic imaging phantom to incorporate a vascular tree and scaffolds was prototyped for end-to-end DCE-CT testing. Using SLS, A fourth-order vascular phantom with vessels between 2.2 mm and 790 µm (below typical CT scanner resolution). A minimum inner diameter size of 620 microns was achievable for hollow vessels, with a minimum resolution of $770 \pm 110$ microns being reliably achieved. The DCE-CT data collected demonstrated a bolus entrance and clearance form within a desired behavior range, and image-extract DFs of $-96 \pm 5\%$ and $-15 \pm 8\%$, for low and high permeability compartments, respectively. Measured experimental DF values were $-81\% \pm 6\%$ and $-22\% \pm 3\%$, for the low and high permeability compartments, respectively.

(2) *Effect of inline mixer on contrast agent (CA) and simulation blood fluid (SBF) mixing:* Simulations illustrated that under laminar flow inlet boundary conditions, the CA and SBF fluid layers were stratified prior to entry into the helical mixer. The addition of an inline six-unit helical mixer (1.45 inches long) offered adequate mixing of layers. The stream path after the mixer demonstrated increased mixing of the fluids, with a reduced layering effect. However, existing DCE phantoms have not incorporated mixers. This dissertation is the <u>first</u>

promulgated work to discuss the importance of an inline mixer. These results suggest that all future DCE phantoms should incorporate a mixer to reduce the variability across the system, from which time-contrast enhancement curves are generated.

(3) *Computational validation of a dynamic imaging phantom:* The prototyped dynamic imaging phantom was modeled within a CFD software program. Prior patient-specific or idealized CFD models have focused on large vessels involved in cardiac circulation or have not been physically realized. This work is the <u>first</u> to valid a dynamic imaging phantom using CFD. Simulation results showed that the velocities exhibited at the inlet ($1.5 \times 10^{-3}$ m/s) and outlet ($3 \times 10^{-4}$ m/s) of the vascular tree were characteristic of microcirculation [12]. The DF was measured across the porous geometry model and compared to measurements extracted from DCE-CT data performed on the dynamic imaging phantom. The computational estimations of the DF across the low and high permeability compartments from the porous geometry model were -77% and -21%, respectively. Both values were within ±4% of experimental results, which had a standard deviation of 6% and 3%, respectively. Although, air bubbles within the system remain a prevalent issue, the computational results along with experimental measurements, for the high and low permeability scaffolds, provide benchmark range for comparisons to image-derived metrics.

(4) *Porous jump model to predict realizable differential flow range:* This investigation is the <u>first</u> to provide a porous jump model that uses experimentally determined intrinsic permeability values to determine the differential flow achievable across a compartment. The measured DFs were -73% and -25%, for the low and high permeability scaffolds, respectively. Simulations results for the porous geometry and porous jump-geometry closely matched (± 4%). The DFs were significantly less than the experimentally measured DF for the high permeability compartment. For the low permeability compartment, the DF was significantly higher than the DCE-CT imaging measurements. The experimental results for the low permeability compartment were significantly less than the

porous jump DF measurement. Overall, the predictive model provides a DF range with some error. Based on the suggested intrinsic permeability value, an appropriate scaffold should be selected to create a porous geometry model for further simulations, as previously discussed.

(5) *Evaluation of shear stress across large spherical and orthogonal scaffold:* Orthogonal and spherical scaffold architectures are commonly adopted in bone tissue engineering to promote bone in-growth; while, recent bone growth investigations have demonstrated the utility of seeding endothelial and osteogenic cell lineages [13-15]. These simulations are the first for a scaffold embedded within an endothelial cell bioreactor system. These results were used to determine the appropriate inlet velocity for an *in vitro* perfusion bioreactor construct. For inlet velocities between 0.54 - 0.61 m/s, the spherical geometry provided the best balance between EC detachment and stimulation. More than 50% of SA experienced 1 - 10 dynes/cm$^2$ of shear stress for an inlet velocity equal to or greater than 0.54 m/s. The simulation showed that scaffolds with a well-organized spherical pore (2.22 mm diameter) lattice, provided more uniform shear stress across the scaffold, within the target shear stress range, under a laminar flow regime, compared to an orthogonal design (1.46 mm). The computational model can readily be extended to other pore geometries (i.e. hexagonal and cubical) to identify an optimal bone scaffold design for future EC co-culture studies.

(6) Determined that endothelial cells cultured on RGD-modified scaffolds over 7 days proliferated at a significantly higher rate and demonstrated more favorable cell function (in term of vWF productive) than sodium hydroxide treated and VEGF (10µg) conjugated and untreated PCL constructs. Identified RGD-modified PCL scaffolds as an optimal modification for future bioreactor investigations. Demonstrated that RGD-modified scaffolds supported cell viability across the scaffold, with higher densities at the edges of the scaffold. In computational simulations, the top edge of spherical scaffold was shown to experience the greatest shear stress; hence, cell detachment is more likely at this edge.

(7) Optimized the <u>first</u> PCL endothelial cell bioreactor in terms of imposed shear stress and cell-scaffold biocompatibility. A protocol for implementing the *in vitro* perfusion bioreactor system was outlined.

## 8.4 REFERENCES

[1] O'Connor, J.P., Jackson, A., Parker, G.J., and Jayson, G.C. DCE-MRI biomarkers in the clinical evaluation of antiangiogenic and vascular disrupting agents. British Journal of Cancer **96**, 189, 2007.

[2] Yoshimura, K., Kato, H., Kuroda, M., Yoshida, A., Hanamoto, K., Tanaka, A., Tsunoda, M., Kanazawa, S., Shibuya, K., Kawasaki, S., and Hiraki, Y. Development of a tissue-equivalent MRI phantom using carrageenan gel. Magn Reson Med **50**, 1011, 2003.

[3] Blanquer, S., Guillaume, O., Letouzey, V., Lemaire, L., Franconi, F., Paniagua, C., Coudane, J., and Garric, X. New magnetic-resonance-imaging-visible poly(epsilon-caprolactone)-based polyester for biomedical applications. Acta Biomater **8**, 1339, 2012.

[4] Khorana, A.A., Sahni, A., Altland, O.D., and Francis, C.W. Heparin inhibition of endothelial cell proliferation and organization is dependent on molecular weight. Arterioscler Thromb Vasc Biol **23**, 2110, 2003.

[5] He, Q., Zhao, Y., Chen, B., Xiao, Z., Zhang, J., Chen, L., Chen, W., Deng, F., and Dai, J. Improved cellularization and angiogenesis using collagen scaffolds chemically conjugated with vascular endothelial growth factor. Acta Biomater **7**, 1084, 2011.

[6] Wells, A., Griffith, L., Stolz, D., and Lauffenburger, D. An Organotypic Liver System for Tumor Progression, 2007.

[7] Starke, R.D., Ferraro, F., Paschalaki, K.E., Dryden, N.H., McKinnon, T.A., Sutton, R.E., Payne, E.M., Haskard, D.O., Hughes, A.D., Cutler, D.F., Laffan, M.A., and Randi, A.M. Endothelial von Willebrand factor regulates angiogenesis. Blood **117**,
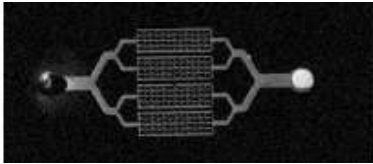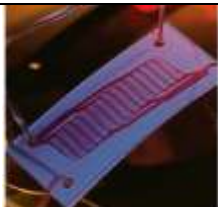
1071, 2011.
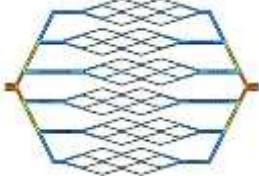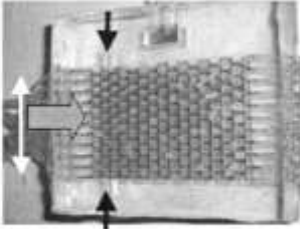
[8] Kastritis, E., and Dimopoulos, M.A. VWF, WM, and angiogenesis: is there a link? Blood **120**, 3163, 2012.

[9] Zanetta, L., Marcus, S.G., Vasile, J., Dobryansky, M., Cohen, H., Eng, K., Shamamian, P., and Mignatti, P. Expression of Von Willebrand factor, an endothelial cell marker, is up-regulated by angiogenesis factors: a potential method for objective assessment of tumor angiogenesis. Int J Cancer **85**, 281, 2000.

[10] Grainger, S.J., and Putnam, A.J. Assessing the permeability of engineered capillary networks in a 3D culture. PLoS One **6**, e22086, 2011.

[11] Dvorak, H.F., Nagy, J.A., Dvorak, J.T., and Dvorak, A.M. Identification and characterization of the blood vessels of solid tumors that are leaky to circulating macromolecules. Am J Pathol **133**, 95, 1988.

[12]  Boron, W.F. and Boulpaep, E.L., Medical Physiology : A Cellular and Molecular Approach (Philadelphia, PA: Saunders/Elsevier), 2009.

[13] Williams, J.M., Adewunmi, A., Schek, R.M., Flanagan, C.L., Krebsbach, P.H., Feinberg, S.E., Hollister, S.J., et al. Bone tissue engineering using polycaprolactone scaffolds fabricated via selective laser sintering. Biomaterials **26**, 4817-27, 2005.

[14] Mitsak, A.G., Kemppainen, J.M., Harris, M.T., Hollister, S.J. Effect of polycaprolactone scaffold permeability on bone regeneration in vivo. Tissue Engineering: Part A **17**, 1831-9, 2011.

[15] Yu, H., VandeVord, P.J., Mao, L., Matthew, H.W., Wooley, P.H., Yang, S.Y. Improved tissue-engineered bone regeneration by endothelial cell mediated vascularization. Biomaterials **30,** 508-17, 2009.

# APPENDIX A - CHAPTER 1

## A.1 SUMMARY OF RAPID PROTOTYED BRANCHING MODELS WITH MEDICAL APPLICATION

**Table A.1 Review of rapid prototyped air and fluid flow models.**

| Study Description | Model | Citation |
|---|---|---|
| Side view of the Sophia anatomical infant nose-throat (SAINT) model made using stereolithography, with the smallest opening approximately 30 - 40 mm. |  | [1] |
| Replica of vasculature of the human thoracic aorta (20 - 25 mm i.d.) from 3-D MRI data using PolyJet technology. |  | [2] |
| Tracheobronchial hollow airway model fabricated using selective laser sintering (1 - 2 mm i.d.). |  | [3] |
| Microfluidic phantom with four generations of channels (1 mm - 55 μm i.d.) produced via soft lithography, whereby a capillary network is patterned onto a silicon wafer using soft-lithography. |  | [4] |
| Microfluidic device produced using microfabrication (0.03 - 1 mm i.d.). Cells are seeded and cultured to spur endothelialization. |  | [5] |

| | | |
|---|---|---|
| Designed in FEMLAB, then fabricated using lithography from polymethylmethacrylate (PMMA) polymer. Root branch 120 μm i.d, with dimension halving at each bifurcation. |  | [6] |
| MRI microchannel phantom microfabricated using ion etching, then casted with PDMS. Each capillary network 2 mm deep and 0.8 mm wide, forming a 10 x 8 periodic array. |  | [7] **Error! ookmark not defined.** |
| Cross-sectional view (3 mm i.d.) of hepatic vascular system scaffold constructed using low-temperature deposition technology. | <br>Central channel | [8] **Error! ookmark not defined.** |

**REFERENCES**

[1] Janssens, H., de Jongste, J.C., Fokkens, W.J., Robben, S.G., Wouters, K., Tiddens, H.A.. The Sophia: Anatomical Infant Nose-Throat (Saint) Model: A Valuable Tool to Study Aerosol Deposition in Infants. Journal of Aerosol Medicine. **14**(4): 433-441, 2001.

[2] Markl, M., Schumacker, R., Küffer, J., Bley, T.A., Hennig, J.. Rapid Vessel Prototyping: Vascular Modeling Using 3T Magnetic Resonance Angiography and Rapid Prototyping Technology. MAGMA. **18**: 288-292, 2005.

[3] Clinkenbeard, R.E., Johnson, D.L., Parthasarathy, R., Altan, M.C., Tan, K.H., Park, S.M., Crawford, R.H.. Replication of Human Tracheobronchial Hollow Airway Models Using a Selective Laser Sintering Rapid Prototyping Technique. American Industrial Hygiene Association. **63**: 141-150, 2002.

[4] Ebrahimi, B., Swanson, S. D., Mosadegh, B., Chupp, T. E.. A Perfusion Phantom for Quantitative Medical Imaging. SPIE Medical Imaging 2008: Physics of Medical Imaging. **6913,** 2008.

[5] Borenstein, J., Weinberg, E., Orrick, B.K., Sundback, C., Kaazempur-Mofrad, M.R., Vacanti J.P.. Microfabrication of Three-Dimensional Engineered Scaffolds. Tissue Engineering. **13**(8) 1837-1844, 2007.

[6] Wang, G.J., Hsu, Y.. Structure Optimization of Microvascular Scaffolds. Biomed. Microdevices. **10**: 51-58, 2005.

[7] Raguin, L. G., Honecker, S. L., Georgiadis, J. G.. (2005). MRI Velocimetry in Microchannel Networks. Microtechnology in Medicine and Biology, 2005. 3rd IEEE/EMBS Special Topic: 319- 322.

[8] Wang, X., Yongnian, Y., Zhang, R.. (2007). Rapid Prototyping as a Tool for Manufacturing Bioartificial Livers. Trends in Biotechnology **25**(11): 505-513.

# APPENDIX B - CHAPTER 2

## B.1 INVERTED COLLOIDAL CRYSTAL SCAFFOLD FABRICATION

Name of Procedure: ICC Scaffold Fabrication
Prepared by: Auresa Thomas; based on Kotov Lab's published work.

Materials
Glass beads (Polysciences, 30-50 µm #18901; 3-10 µm #07666; 105-150 µm #15927)
Ethylene glycol (Fischer Scientific, BP230-1)
Ice
Sonicator
Oven
Furnace
Polycaprolactone (PCL) (Polysciences #19561, MW: 43,000-50,000)
Chloroform (Fischer Scientific, C298-1, Certified ACS)
5.75 inch glass pipettes w/ rubber tops
Glass vials (Fischer Scientific, 03-339-30F, shell type 1 glass, vial, 19x65mm 3 dram)

Procedure
Note:
•     The sonicator overheats, so monitor (by touch), adding ice or cold water to the bath every 45 minutes. Each time remove water to keep the water level consistent.
•     Ethylene glycol has a flashpoint of 111˚C.

*Before starting*
1.     Make space for the oven in the fume hood. Preheat oven to 90˚C.
2.     Mark the desired scaffold height on the glass vials with a black marker or tape. Allow for 2-3mm of additional height that will be removed later in the fabrication process.
3.     Setup glass vials with pipette tops in sonicator. Secure with zip ties.
4.     Prepare solution of beads. Add beads to ethylene glycol (1 g/ 5 mL).

*Step 1: Lattice*
5.     Fill vials with 5 ml of ethylene glycol.
6.     Add water to sonicator, to cover the glassware halfway (above level of black line).
7.     Fill pipette with bead solution. Add 6-7 drops every 20 minutes to the glass vial.
8.     Sonicate for 30 minutes after the desired height is achieved.

*Step 2: Drying*

9. Drain the sonicator.
10. Carefully cut the zip ties without disturbing the contents of the vial.
11. Carefully remove the vial from the sonicator.
12. Remove excess ethylene glycol from the top of the scaffold surface.
13. Place the vials in the oven in the fume hood. Remove the vials once the ethylene glycol has dried out.

*Step 3: Annealing*
14. Anneal the beads in the oven at X°C for Y hours.
15. Allow glass surface to cool down. Then, carefully break the glass vial around the scaffold (a wrench can be used).
16. Scrape off 1 mm of the top and bottom surface of the scaffold (and sides if needed).
17. Pour water at top of surface to assess the latency of porous structure.
18. Allow water to completely evaporate (overnight).

*Step 4: PCL infusing*
19. Prepare Z% PCL (g of PCL / mL of chloroform = X/100).
20. Infuse PCL into scaffold. Add Z% PCL to centrifuge tube with scaffold.
21. Centrifuge contents at 5800 rpm for 60 minutes (may need to break into 3 intervals).
22. All the contents of the tube to dry in the fume hood at room temperature.
23. Place under vacuum for 24 hours.
24. Remove top, bottom and side layers of the scaffold.

*Step 5: Glass dissolving*
25. Place scaffold in centrifuge tube and add 5% HF for 1 day to dissolve glass beads.
26. Change the 5% HF and saturate scaffolds for a second day.
27. Rinse scaffold with distilled water for 2 hours on shaker.
28. Saturate scaffold in 1 N HCl for 1 day. Change the solution every 6-8 hours for 24 hours.
29. Repeat steps 27 and 18 a second time.
30. Wash scaffolds in PBS until pH is 7.4.


**REFERENCES**

Cuddihy, Meghan J.: Utilizing Inverted Colloidal Crystal Scaffolds to Engineer in Vitro Bone and Bone Marrow. University of Michigan, Department of Biomedical Engineering; 2010.

## APPENDIX C - CHAPTER 3

## C.1 REDUCTION OF CONTRAST AGENT UPTAKE BY SURFACE-MODIFIED PCL

As such, a secondary objective of this chapter is to evaluate the hydrophobicity and uptake of contrast agent by surface-modified constructs. Initial DCE imaging experiments showed significant uptake of contrast agent in early designs of the phantom, which was made of polycaprolactone (PCL), a polyester with hydroxyl end groups (OH-) (Fig. C.1). Although, the aqueous iodine contrast agent, iopamidol is documented as stable and nonreactive agent, its interaction with PCL may lead to the replacement of hydroxyl groups on the surface of PCL. Another method of adherence of iopamidol onto PCL may be due to adsorption, as the rough surface of the polymer contains macro- and micro-pores, which may trap the contrast agent during perfusion. To resolve the issue of contrast agent retention after each experiment, the surface of the PCL constructs were chemically treated. Degradation of PCL occurs by hydrolysis of its ester linkages (R-CO2-R′, where R and R′ are alkyl groups) at the surface-level. The hydroxyl group on PCL was capped by acylation with acetic acid, converting them into acetoxy groups ($CH_3$-C(=O)-O-R). The relatively low reactivity of the acetoxy groups and iodine was hypothesized to reduce PCL uptake of the contrast agent. As a result of the hydrolysis, the PCL was hypothesized to become more hydrophobic.
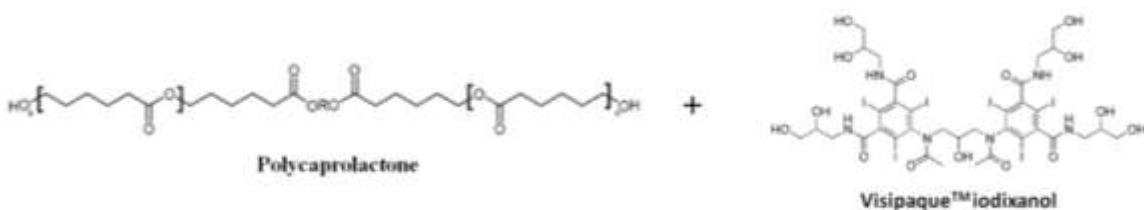


**Figure C.1 Chemical structure of reactants in DCE imaging: PCL  and iopamidol .**

PCL scaffolds and flat discs were treated with 17.4 M acetic acid (≥99.7 w/w %, Certified ACS, Fisher Scientific) (Fig. C.2). The wettability of discs treated for 15, 5 and 0 seconds was measured using a goniometer (Rame-Hart Instrument, Co., Netcong, NJ) and drop-shape analysis program (DROPImage, Rame-Hart Instrument, Co., Netcong, NJ). Three repeat tests were performed for three treated and untreated circular discs. For each disc, the water contact angle between the droplet and the surface of the disc was measured as water was added and removed from the surface. The goniometer measured the contact angle (receding an ascending) formed due to the surface tension between the discs and water droplets add to its surface. The average receding and ascending contact angle was calculated for each group. A two-tail Student's *t*-test assuming unequal variance was used to compare the measured contact angles. P-values less than 0.05 were considered to show significant difference between the two groups.
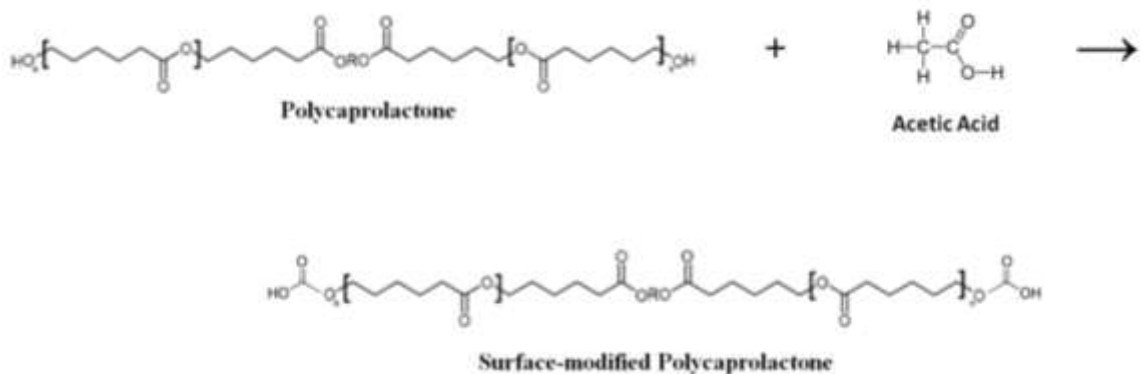


**Figure C.2 Hydrolysis of PCL surface.**

Changes in the perfusion characteristics of the treatment group that showed the greatest increase in hydrophobicity were assessed. The differential flow was experimentally measured using equations 3 and 4, then compared to the respective values for untreated PCL scaffolds. A two-tail Student's *t*-test assuming unequal variance was used to compare the measured differential flow. Significance was set at P -values< 0.05. Fig. C.3 illustrates acetic acid treatment increases the hydrophobicity of the PCL. A greater contact angle was measured for longer exposure times. Fig. C.4 shows that the differential flow was not significantly different for untreated high permeability scaffolds compared to acetic acid treated scaffolds.
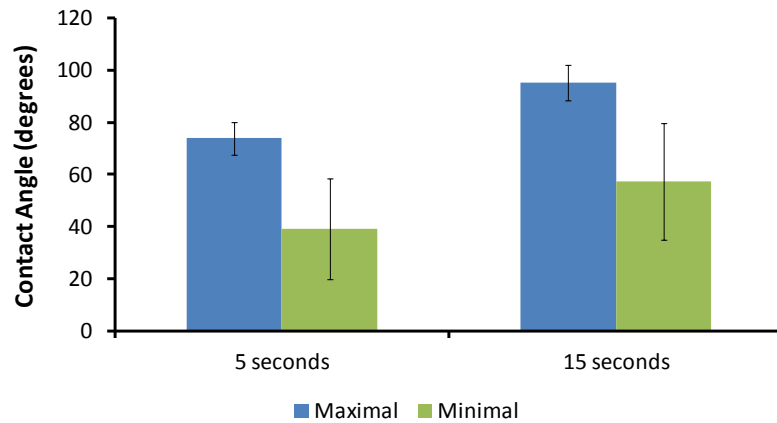
**Figure C.3 Average maximal (ascending) and minimal (receding) contact angle measurements for PCL disc treated with acetic acid for 5 seconds and 15 seconds. Increased wettability was observed for the longer treatment. The increased surface tension makes the acetic acid treated construct more hydrophobic.**
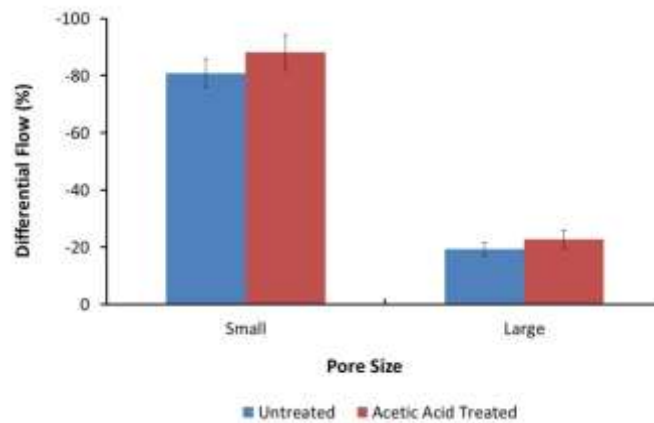


**Figure C.4 Average differential flow measurements for untreated scaffolds and scaffolds treated for 15 seconds with acetic acid. Treated scaffolds showed an increase in resistance to flow across the scaffold. Small = 2.02 mm spherical pore diameter (low permeability). (Sample size was 5 for large pore scaffolds and 6 for small pore scaffolds.)**

Lastly, the difference in intensity between the start (baseline: 1 - 5 seconds before bolus) and end (5 - 10 seconds during SBF flush after bolus injection) of a DCE analysis was computed for a treated and untreated vascular phantom to determine whether there was a difference in contrast agent uptake between the groups. Both experiments were performed with high permeability scaffolds in the vascular phantom. Section 3.4.2 details

256

the imaging protocol and system parameters used to collect the DCE data. Contrast agent uptake (HU) was defined as the final intensity after a 15 second flush with SBF, minus the baseline intensity during the first 5 seconds prior to injection. Figure C.5 shows that the acetic acid treatment to the PCL construct reduced the uptake of contrast agent. Thus, with acetic acid treatment for 15 seconds, the same vascular phantom can be used for repeated DCE imaging studies.
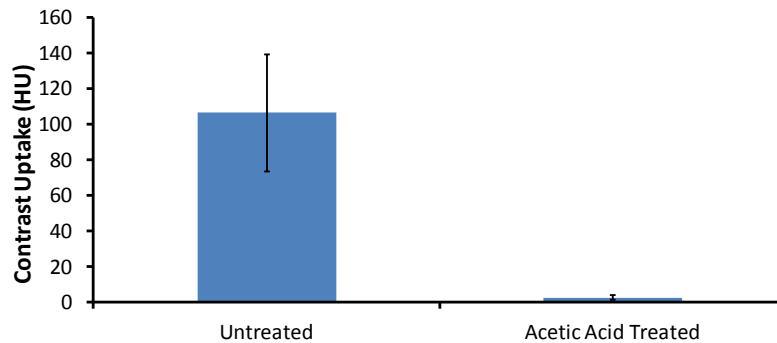


**Figure C.5 The average contrast agent uptake by a PCL construct treated with acetic acid was negligible compared to that of an untreated construct, for a single pass of bolus through the vascular construct. The reported average enhancement values represent the difference between the final plateau (after peak of bolus) and the initial baseline, for four regions of interests that encompassed each compartment.**

There was only a significant difference in differential flow for the larger pore diameter, which showed an increased differential flow for acetic acid treated scaffolds. As such, future experiments should evaluate the sensitivity of DCE-extracted flow rates to these small changes in experimentally measured differential flow ($\pm 10\%$).

257

# APPENDIX D - CHAPTER 4

## D.1 MESH INDEPENDENT TESTS

The following data confirms that the models evaluated in Chapter 4 were within acceptable mesh resolution limits that minimized the error associated with mesh settings.

**Table D.1 Mesh data over four levels of mesh refinement for the modeled T-junction/mixer model.**

| Mesh Refinement | Number of Elements | Number of Nodes |
|:---:|:---:|:---:|
| Baseline | 59,424 | 208,332 |
| 1 | 96,486 | 375,651 |
| 2 | 124,693 | 473,350 |
| 3 | 132,211 | 509,611 |
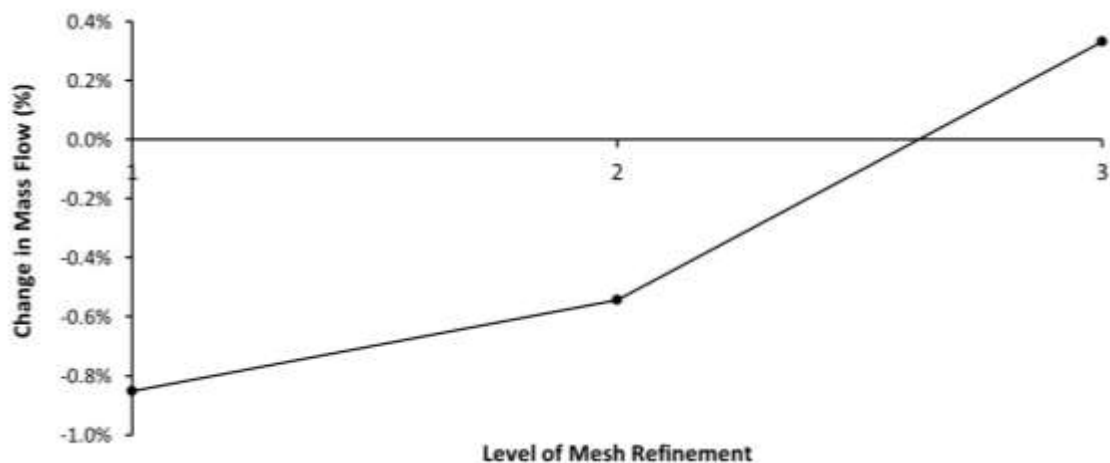


**Figure D.1 Spatial mesh independence for T-junction with an inline static mixer. Illustrates the variation in 'Mass Flow Average' at the mid-plane of the tube distal to the scaffold, with increased mesh resolution. Sensitivity falls within ±5%.**

**Table D.2 Mesh data over four levels of mesh refinement for the permeability chamber simulation for a high permeability scaffold.**

| Mesh Refinement | Number of Elements | Number of Nodes |
|:---:|:---:|:---:|
| Baseline | 293,870 | 110,606 |
| 1 | 383,550 | 144,232 |
| 2 | 463,056 | 169,577 |
| 3 | 506,473 | 182,441 |
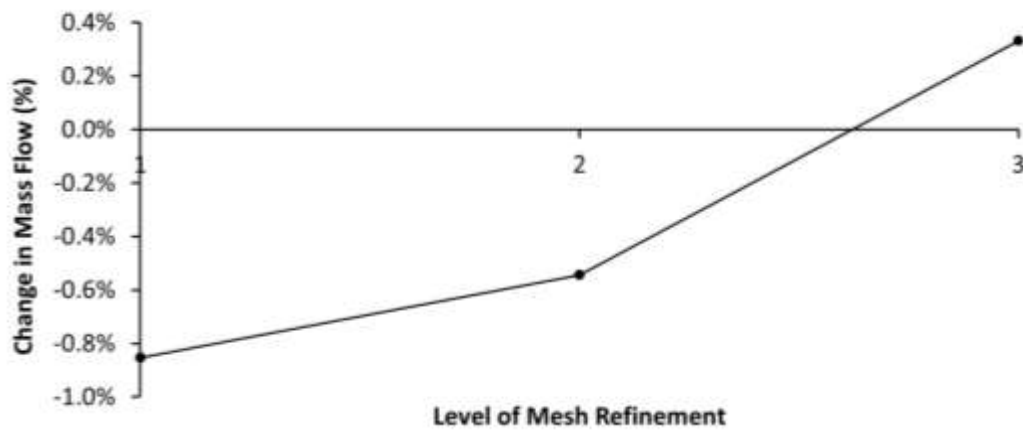


**Figure D.2 Mesh Independence. Illustrates the variation in 'Mass Flow Average' at the mid-plane of the tube distal to the scaffold, with increased mesh resolution. Sensitivity falls within ±5%.**

**Table D.3 Mesh data over four levels of mesh refinement for the modeled vascular tree.**

| Mesh Refinement | Number of Elements | Number of Nodes |
|:---:|:---:|:---:|
| Baseline | 217,299 | 45,427 |
| 1 | 311,195 | 60,091 |
| 2 | 404,505 | 74,731 |
| 3 | 491,181 | 88,397 |
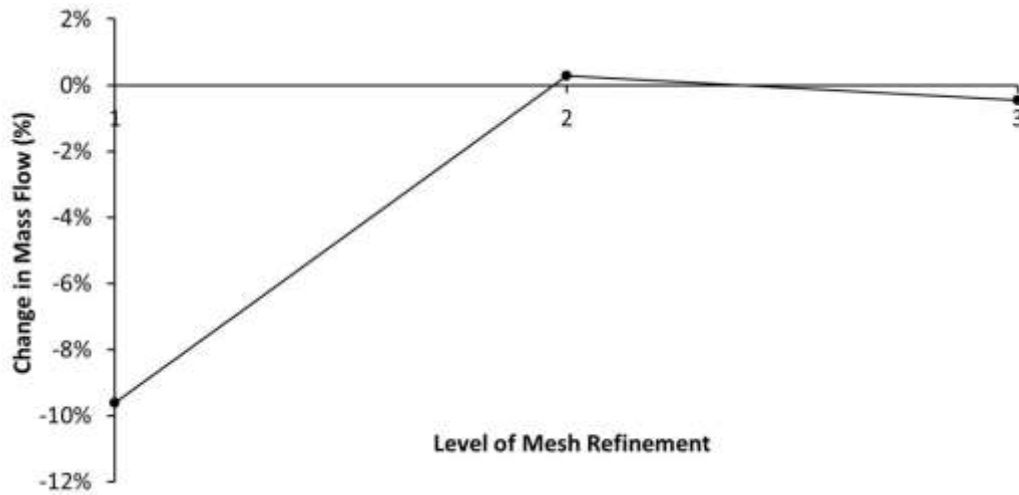


**Figure D.3 Vascular tree mesh independence. Illustrates the variation in 'Mass Flow Average' at the topmost outlet of the vascular tree, with increased mesh resolution. Sensitivity falls within ±5% over the last two level of mesh refinement.**

**Table D.4 Mesh data over five levels of mesh refinement for the low permeability compartment.**

| Mesh Refinement | Number of Elements | Number of Nodes |
|:---:|:---:|:---:|
| Baseline | 158, 540 | 36,892 |
| 1 | 241,426 | 54,096 |
| 2 | 322,369 | 70,405 |
| 3 | 455,239 | 96,994 |
| 4 | 506,663 | 107,040 |
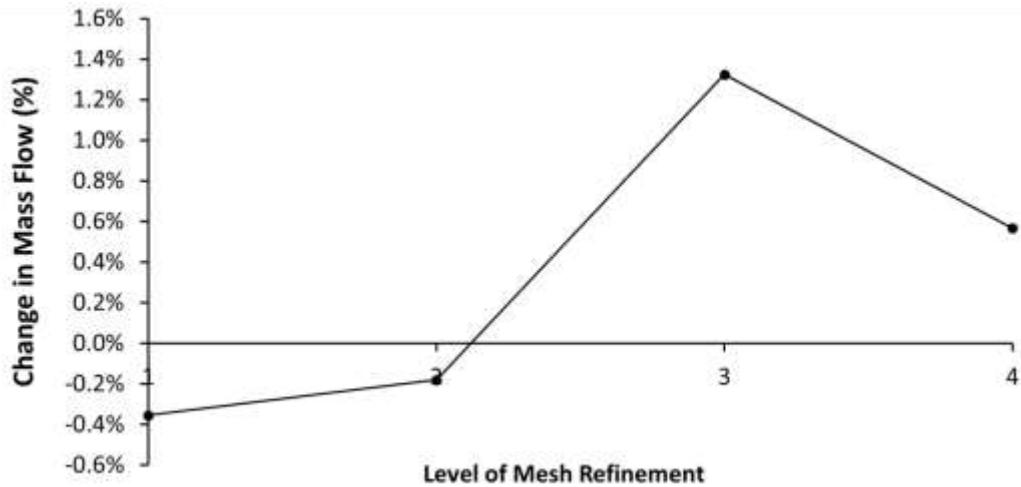


**Figure D.4 Low permeability compartment mesh independence. Illustrates the variation in 'Mass Flow Average' along plane downstream of scaffold and prior to the compartment outlets. Sensitivity falls within ±5% across all levels of refinement.**

**Table D.5 Mesh data over four levels of mesh refinement for the high permeability compartment.**

| Mesh Refinement | Number of Elements | Number of Nodes |
|:---:|:---:|:---:|
| Baseline | 204,389 | 45,220 |
| 1 | 305,798 | 70,947 |
| 2 | 461,123 | 102,716 |
| 3 | 509,073 | 112,531 |
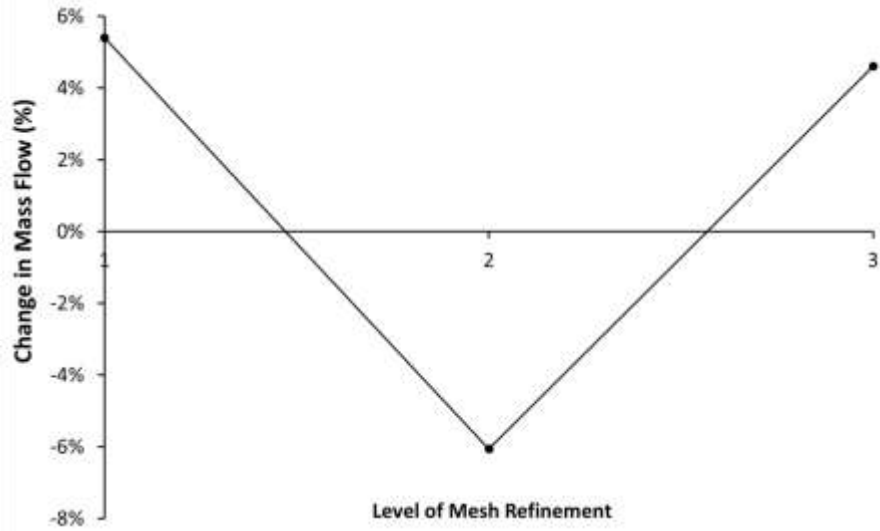
**Figure D.5 High permeability compartment mesh independence. Illustrates the variation in 'Mass Flow Average' along plane downstream of scaffold and prior to the compartment outlets. Sensitivity falls within ±5% for the third level of refinement.**

**Table D.6 Mesh data over five levels of mesh refinement for a single scaffold compartment with four 0.79 mm inlets and a porous jump (intrinsic permeability of $1 \times 10^{-9}$ m$^2$) positioned at the mid-plane.**

| Mesh Refinement | Number of Elements | Number of Nodes |
| --- | --- | --- |
| Baseline | 142,204 | 63,934 |
| 1 | 249,202 | 107,310 |
| 2 | 356,411 | 146,802 |
| 3 | 448,598 | 180,593 |
| 4 | 511,322 | 202,261 |
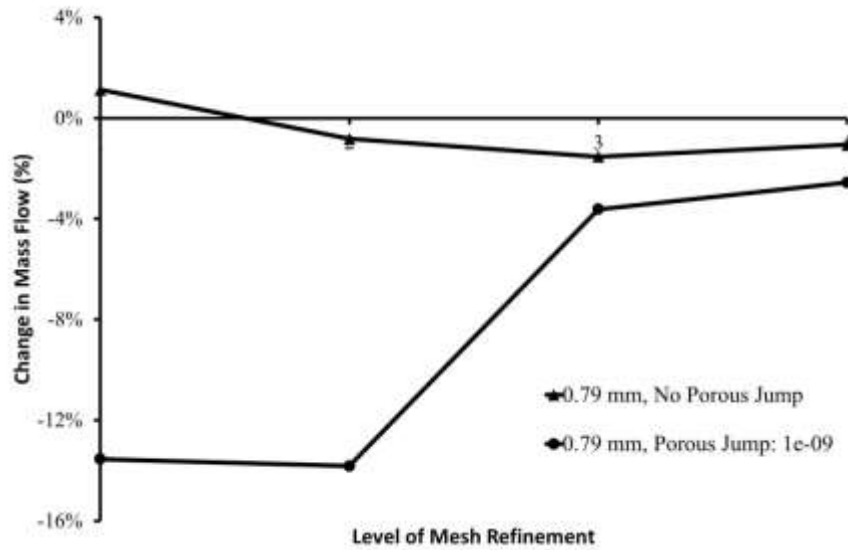
**Figure D.6 Mesh Independence. Variation in 'Mass Flow Average' with increasing mesh resolution. Sensitivity falls within ±5%.**

## D.2 EFFECT OF REYNOLDS NUMBER ON PERMEABILITY

In the discussion of the reliability of results acquired using the in-house mass flow/permeability system, it was shown that the system underestimated the permeability of the Sponceram® when compared to the results published by Sanz-Herrera et al. [1]. Further studies were conducted to determine the influence of the Reynolds number on the measured perfusion metric of permeability. Fig. D.7 shows that the measured intrinsic permeability using water (highest Reynolds number of approximately 100) generated lower permeability measurements. Using a glycerin/water mixture (60-80% v/v), the Reynolds number was reduced to less than or equal to 10, to be within assumptions limits of Darcy's Law. The data presented in Fig. D.7 indicates that true permeability may be 5 to 100 times larger than that estimated by water. There were similar trends in the permeability for both the high permeability and low permeability scaffolds. These findings support the data presented in Table 4.3, which indicated that compared to the results published by Sanz-Herrera et al. [1], our system when used with water, underestimates the permeability by an order of one or two. Based on these observations, a true value of permeability may not be attainable; instead, a range within the Reynolds of

263

1 to 10 may be used to provide a relative value. In chapter 4, a correct factor of 2.7 is applied to the experimentally measured hydraulic permeabilities to closely match the differential flow values acquired using the porous geometry CFD model for the low and high permeability scaffolds.
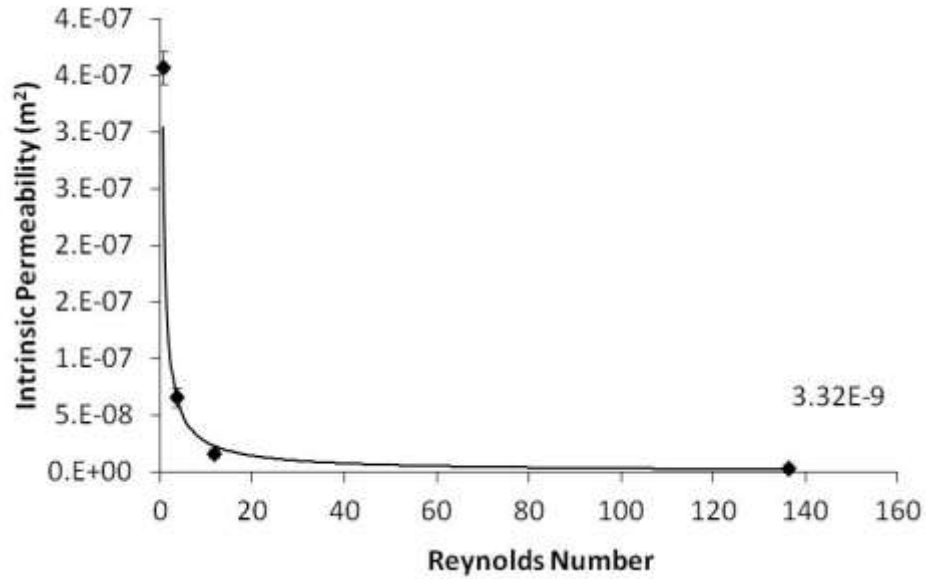


(a)
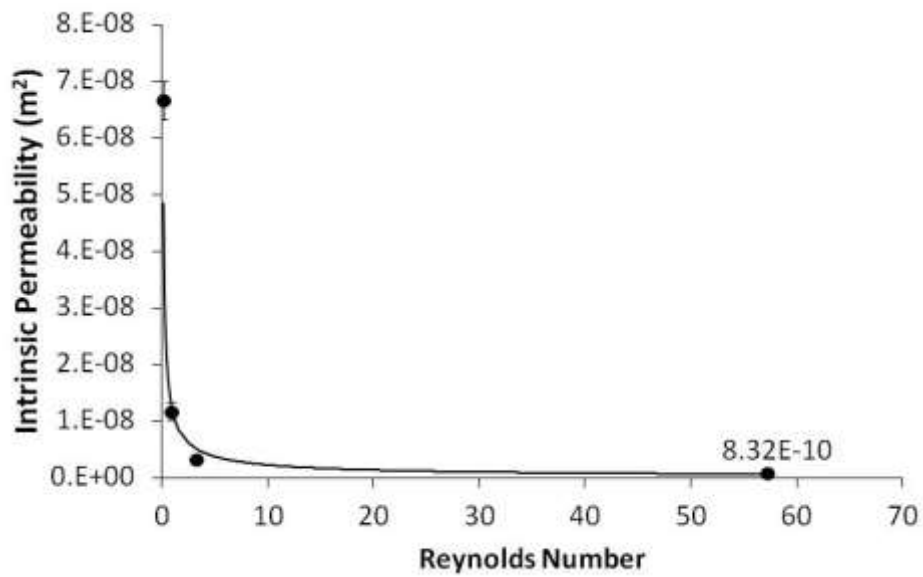


(b)

**Figure D.7 Illustrates exponential relationship between the Reynolds number and intrinsic permeability within the in-house flow meter system for (a) high permeability and (b) low permeability scaffolds. (Note: The scaffolds used were designed at a lower voxel higher resolution.) (All standard deviations of the intrinsic permeability values are an order smaller.)**

## D.3 TRANSIENT FLOW USER-DEFINED FUNCTIONS

Macros implemented to set material and boundary conditions for transient flow simulation of T-junction/mixer model.

```
/*****************************************************************
   UDF that simulates change in density of fluid type over time (kg/m^3)
*****************************************************************/
#include "udf.h"

DEFINE_PROPERTY(cell_density, c, t)
{
  real my_rho_baf = 1080;
  real my_rho_ca = 1369;

      if (CURRENT_TIME<=5)
              return my_rho_baf;
      else if (CURRENT_TIME == 6 || CURRENT_TIME == 7)
              return my_rho_ca;
      else if (CURRENT_TIME >=8)
              return my_rho_baf;
}



/*****************************************************************
   UDF that simulates change in viscosity of fluid type over time  (kg/m*s)
   UDF that simulates viscosity of non-Newtonian blood analog fluid based on Carreau
model
*****************************************************************/
#include "udf.h"

DEFINE_PROPERTY(cell_viscosity, c, t)
{
  real my_mu_baf, mu_z, mu_inf, n,lambda,gamma, a, temp;
  real my_mu_ca = 0.0047;

      if (CURRENT_TIME<=5)
    {
                mu_inf = 0.00364;
                mu_z = 0.076;
            n = 0.23;
              lambda = 22.06;
```

```
            a = 2;
            gamma = C_STRAIN_RATE_MAG(c,t);
        temp = n-1/a;
            my_mu_baf= mu_inf + (mu_z - mu_inf) * pow((1+pow(lambda,a) *
pow(gamma,a)), temp);
            return my_mu_baf;
    }

    else if (CURRENT_TIME == 6 || CURRENT_TIME == 7)
            return my_mu_ca;

    else if (CURRENT_TIME>=8)
    {
            mu_inf = 0.00364;
            mu_z = 0.076;
        n = 0.23;
          lambda = 22.06;
            a = 2;
            gamma = C_STRAIN_RATE_MAG(c,t);
        temp = n-1/a;
            my_mu_baf= mu_inf + (mu_z - mu_inf) * pow((1+pow(lambda,a) *
pow(gamma,a)), temp);
            return my_mu_baf;
    }
}


/***********************************************************************/
/* umyinlet.c                                  */
/* UDF for specifying a transient mass flow rate profile boundary condition */
/***********************************************************************/
/* at t<=2 sec the target mass flow rate set to 0.002748 kg/s for contrast agent   */
/* when t>2 sec the target mass flow rate will change to 0.0014 kg/s for blood analog
fluid */
/* ca_inlet_diameter = 3mm  and sbf_inlet_diameter= 3.2mm   */

#include "udf.h"

DEFINE_PROFILE(trans_mf, thread, position)
{
 real my_mf;
 face_t f;
 real mf_baf = 0.00108 ;
 real mf_ca = 0 .002738;

 begin_f_loop(f, thread)
```

```
    {
            if (CURRENT_TIME<=5)
            F_PROFILE(f, thread, position) = mf_baf;
            else if (CURRENT_TIME == 6 || CURRENT_TIME == 7)
                F_PROFILE(f, thread, position) = mf_ca;
            else if (CURRENT_TIME>=8)
            F_PROFILE(f, thread, position) = mf_baf;
    }
  end_f_loop(f, thread)
}
```

**REFERENCES**

[1] Sanz-Herrera, J A, Kasper, C, van Griensven, M, Garcia-Aznar, J M, Ochoa, I and Doblare, M 2008 Mechanical and flow characterization of Sponceram carriers: Evaluation by homogenization theory and experimental validation *J Biomed Mater Res B Appl Biomater* **87** 1 42-8

# APPENDIX E - CHAPTER 5

## E.1 SURVEY OF DYNAMIC ENDOTHELIAL CELL CULTURES

**Table E.1**Comparative summary of published in vitro dynamic angiogenesis bioreactor studies (3-10 days).

| Reference | Cell Line(s) | Scaffold Type | Flow | Dimensions | Angiogenesis Assays |
|---|---|---|---|---|---|
| [1] | RAEC and Rat MSC | collagen gel on PET membrane | constant: 300 ml/h ($\approx$ 6 dynes/cm$^2$) | undisclosed; manually perforated | Histology, cell proliferation assay, western blot, cell morphology (microscopy), VEGF/TGFβ1/ PDGF-BB ELISA |
| [2] | HUVEC | fibrin gel | constant: 7 ml/h | undisclosed | Quantification of VEGF receptor 1, cell morphology (microscopy) |
| [3-4] | BEC and LEC | fibrin/ collagen gel | Radial (2-20 dynes/cm$^2$) | 1.6 mm diameter; thickness undisclosed | Vessel morphology (confocal microscopy), human MMP ELISA |

**Table E.2   Summary of EC behavior and protein/gene expression from selected FSS studies performed on macrovascular cells (SS compared to 0 dynes/cm2 static environment, unless alternate SS value provided).**

| Reference | Cell Type | Study Environment | Shear stress (dynes/cm²) | Findings |
|---|---|---|---|---|
| [5] | HUVEC | modified 100-mm culture dish | 10 (orbital) | ECs elongated and aligned, ↓ apoptosis, ↑ VEGF receptor 2 expression |
| [6] | HUVEC | cone and plate rheological system | 0.5 and 12 | All conditions: ↔ cell density<br><br>Isolated cells at 0.5 dynes/cm$^2$: ↓ directionality of migration, ↓ migration speed;<br><br>Isolated cells at 12 dynes/cm$^2$: ↑ directionality of migration, ↓ migration speed (compared to static and 0.5 dynes/cm$^2$);<br><br>Monolayer at 12 dynes/cm$^2$: ↑ EC elongation, ↑ homogenous orientation in the direction of flow |
| [7] | HUVEC | channels in microfluidic device infused with 50 ng/ml of VEGF | 3 | attenuated sprout formation through NO signaling, ↑ area of sprout formation |
| [8] | HUVEC | collagen-coated parallel plate flow chamber | 0.12, 3, 5.3 and 12 | At 5 dyn/cm$^2$: maximum Atk activation<br><br>At 12 dyn/cm$^2$: ↑ sprouting density, ↑ sprouting extension, ↑ narrowing of sprouts, ↓ Atk activation |
| [9] | Dog EC | scaffold tube (layers of fibroblasts and collagen) in dynamic bioreactor | 1.5 - 5.3 (pulsatile, stepwise ramping) | elongated shape, alignment in the direction of flow, ↑cells retention rate |
| [10] | HUVEC | vascular construct in dynamic bioreactor | 5 (orbital) | time-dependent ↑ cell elongation and alignment, endothelial F-actin microfilament organization, ↑ E-selectin expression, ↓ ICAM-1 levels |

| Reference | Cell Type | Study Environment | Shear stress (dynes/cm²) | Findings |
|---|---|---|---|---|
| [11] | HUVEC | orbital shaker, parallel plate chamber (laminar) | $\approx 5 / \approx 11.5$ (orbital) and 14 (laminar) | At 5 dynes/cm$^2$: ↑ proliferation, ↑ apoptosis, ↓ Akt phosphorylation, ↑ ICAM expression, ↓ E-selectin down-regulation (greater than laminar and static) |
| [12] | BPMEC | collagen gel positioned within dynamic flow chamber | 3 (laminar) | ↑network formation, ↑ total network length, ↑ EC migration velocity, ↔ network density |
| [13] | HUVEC | culture dish within cone-and-plate viscometer | 1, 15, 30 (laminar) | ↓ evidence of apoptosis, ↑ expression of the anti-apoptotic FasExo6Del and Bcl-xL, ↑ pro-apoptotic Bak, ↓ apoptosis inducing Fas receptor |
| [14] | HUVEC | cone-and-plate apparatus | 2, 8, 12 dyn/cm$^2$ (laminar) | ↑ cumulative vWF release |
| [15] | BAEC | tissue culture plate within cone-plate viscometer | 15 (pulsatile, turbulent, laminar) and 36 (laminar) | All conditions: ↑ PDGF-B, ↑ bFGF mRNA, ↓ PDGF-B mRNA; At 36 dynes/cm$^2$: alignment in the direction of flow |
| [16] | BAEC | glass coverslips within cone-plate viscometer | 8-15 (laminar) and 1.5 (turbulent) | Laminar: alignment in the direction of flow, ↑ ellipsoidal shape, ↔ cell density; Turbulent: random orientation of cells in the monolayer, ↑ roundness, ↑ EC turnover, ↑ DNA synthesis, ↓ cell density, ↑ gaps in monolayer (cell retraction) |
| [17] | RPAEC and Rat SMC | semipermeable polypropylene capillary bundle within dynamic chamber | 0.07 - 3 (stepwise ramping) | adherent monolayer formed, typical subcellular and gross morphology, lack of alignment with flow direction |

## E.1 MESH INDEPENDENCE TESTS

The following data confirms that the models evaluated in Chapter 5 were within acceptable mesh resolution limits that minimized the error associated with mesh settings. Mesh refinement was performed until the number of meshing elements reduced the sensitivity in the maximum and average shear stress to less than 5%. Refinement was performed over approximately 100,000 to 600,000 elements.

**Table E.3 Mesh data over four levels of mesh refinement for the spherical compartment.**

| Mesh Refinement | Number of Elements | Number of Nodes |
| --- | --- | --- |
| Baseline | 186,884 | 41,168 |
| 1 | 270,112 | 60,173 |
| 2 | 329,068 | 71,884 |
| 3 | 418,579 | 89,850 |
| 4 | 511,814 | 108,766 |
| 5 | 1,535,792 | 339,922 |
| 6 | 2,504,894 | 519,208 |
| 7 | 3,185,524 | 639,985 |
| 8 | 5,735,078 | 1,112,063 |

**Figure E.1 Spatial mesh independence for the spherical compartment. Illustrates the variation in 'Average Shear Stress,' across the porous compartment shown in Fig. 5.2a, with increased mesh resolution. Sensitivity falls within ±5% for refinements 7 and 8.**


**Table E.4 Mesh data over six levels of mesh refinement for the orthogonal compartment.**

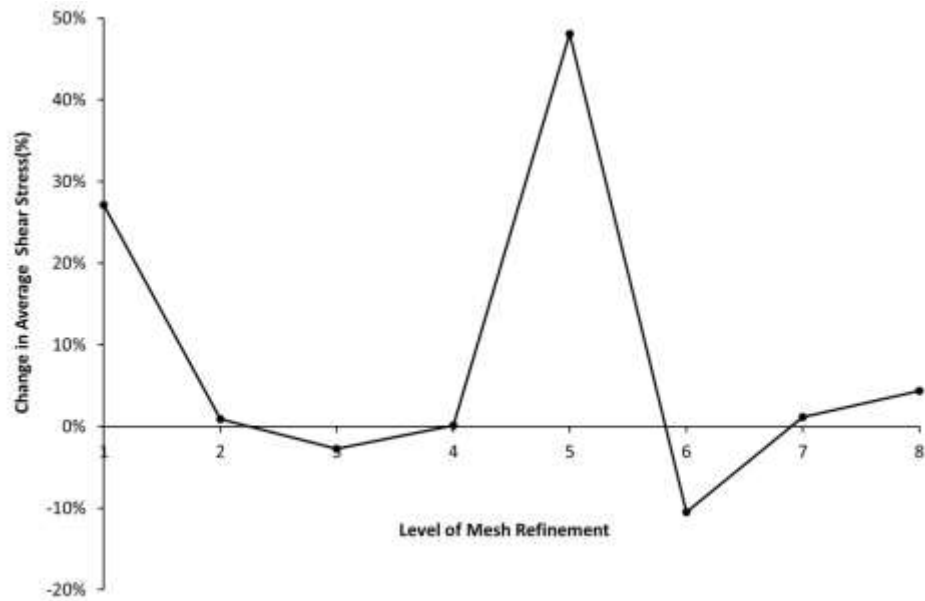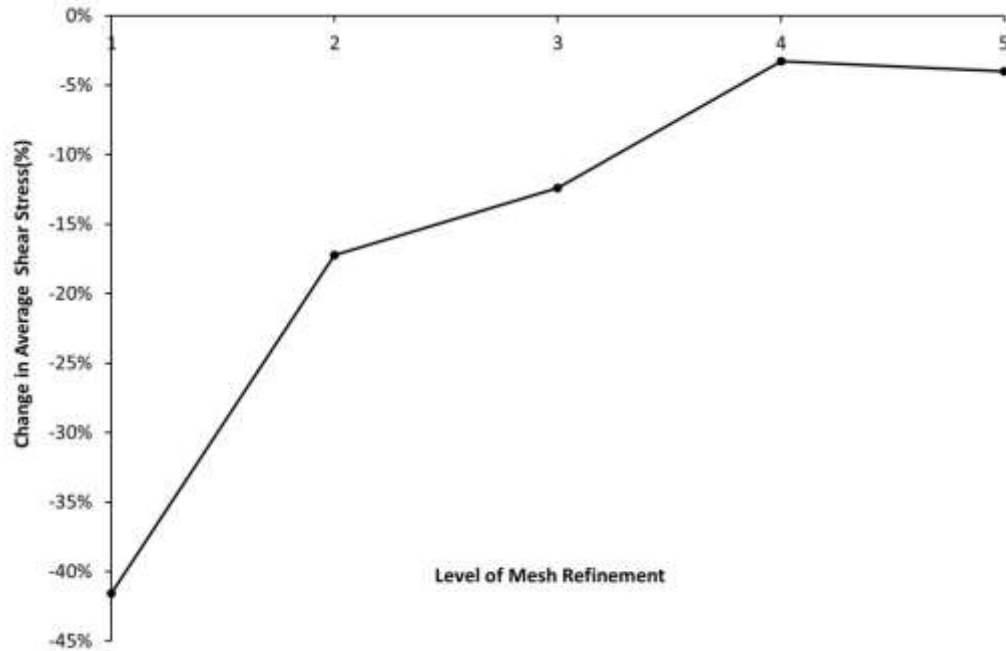| Mesh Refinement | Number of Elements | Number of Nodes |
| --- | --- | --- |
| Baseline | 299,885 | 74,501 |
| 1 | 680,255 | 147,956 |
| 2 | 1,357,644 | 273,586 |
| 3 | 2,308,528 | 476,849 |
| 4 | 3,284,090 | 668,384 |
| 5 | 6,198,1771 | 1,245,986 |

**Figure E.2 Spatial mesh independence for the orthogonal compartment. Illustrates the variation in 'Average Shear Stress,' across the porous compartment shown in Fig. 2b, with increased mesh resolution. Sensitivity falls within ±5% for refinements 4-5.**

## REFERENCES

[1] Lee, E.J., and Niklason, L.E. A novel flow bioreactor for in vitro microvascularization. Tissue Eng Part C Methods **16**, 1191, 2010.

[2] Frese, J., Motejlek, K., Schmitz-Rode, T., Neulen, J., and Jockenhoevel, S. Bioreactor Development for the Study of Angiogenesis within Tissue Engineered Constructs. , 150, 2010.

[3] Ng, C.P., Helm, C.L., and Swartz, M.A. Interstitial flow differentially stimulates blood and lymphatic endothelial cell morphogenesis in vitro. Microvasc Res **68**, 258, 2004.

[4] Helm, C.L., Zisch, A., and Swartz, M.A. Engineered blood and lymphatic capillaries in 3-D VEGF-fibrin-collagen matrices with interstitial flow. Biotechnol Bioeng **96**, 167, 2007.

[5] dela Paz, N.G., Walshe, T.E., Leach, L.L., Saint-Geniez, M., and D'Amore, P.A. Role of shear-stress-induced VEGF expression in endothelial cell survival. J Cell Sci **125**, 831, 2012.

[6] Teichmann, J., Morgenstern, A., Seebach, J., Schnittler, H.J., Werner, C., and Pompe, T. The control of endothelial cell adhesion and migration by shear stress and matrix-substrate anchorage. Biomaterials **33**, 1959, 2012.

[7] Song, J.W., and Munn, L.L. Fluid forces control endothelial sprouting. Proc Natl Acad Sci U S A **108**, 15342, 2011.

[8] Galbusera, M., Zoja, C., Donadelli, R., Paris, S., Morigi, M., Benigni, A., Figliuzzi, M., Remuzzi, G., and Remuzzi, A. Fluid shear stress modulates von Willebrand factor release from human vascular endothelium. Blood **90**, 1558, 1997.

[9] Zhang, Z., Xi, T., Wang, Y., Chen, X., Zhang, J., Wang, C., Gu, Y., Chen, L., Li, J., and Chen, B. Design of a novel bioreactor and application in vascular tissue engineering. Applied Surface Science **255**, 541, 2008.

[10] Punchard, M.A., Stenson-Cox, C., O'Cearbhaill E, D., Lyons, E., Gundy, S., Murphy, L., Pandit, A., McHugh, P.E., and Barron, V. Endothelial cell response to biomechanical forces under simulated vascular loading conditions. J Biomech **40**, 3146, 2007.

[11] Dardik, A., Chen, L., Frattini, J., Asada, H., Aziz, F., Kudo, F.A., and Sumpio, B.E. Differential effects of orbital and laminar shear stress on endothelial cells. J Vasc Surg **41**, 869, 2005.

[12] Ueda, A., Koga, M., Ikeda, M., Kudo, S., and Tanishita, K. Effect of shear stress on microvessel network formation of endothelial cells with in vitro three-dimensional model. Am J Physiol Heart Circ Physiol **287**, H994, 2004.

[13] Bartling, B., Tostlebe, H., Darmer, D., Holtz, J., Silber, R.E., and Morawietz, H. Shear stress-dependent expression of apoptosis-regulating genes in endothelial cells. Biochem Biophys Res Commun **278**, 740, 2000.

[14] Galbusera, M., Zoja, C., Donadelli, R., Paris, S., Morigi, M., Benigni, A., Figliuzzi, M., Remuzzi, G., and Remuzzi, A. Fluid shear stress modulates von Willebrand factor release from human vascular endothelium. Blood **90**, 1558, 1997.

[15] Malek, A.M., Gibbons, G.H., Dzau, V.J., and Izumo, S. Fluid shear stress differentially modulates expression of genes encoding basic fibroblast growth

factor and platelet-derived growth factor B chain in vascular endothelium. J Clin Invest **92**, 2013, 1993.

[16]   Davies, P.F., Remuzzi, A., Gordon, E.J., F., D.C.,Jr, and A., G.M.,Jr. Turbulent fluid shear stress induces vascular endothelial cell turnover in vitro. Proc Natl Acad Sci U S A **83**, 2114, 1986.

[17]   Redmond, E.M., Cahill, P.A., and Sitzmann, J.V. Perfused transcapillary smooth muscle and endothelial cell co-culture--a novel in vitro model. In Vitro Cell Dev Biol Anim **31**, 601, 1995.

# APPENDIX F - CHAPTER 6

## F.1   REVIEW OF OPTIMAL VEGF CONCENTRATIONS SHOWN TO PROMOTE ENDOTHELIAL CELL GROWTH *IN VIVO* AND *IN VITRO*.

**Table F.1 Summary of VEGF concentrations shown to support angiogenesis.**

| Optimal VEGF Concentration | VEGF Source | Study Environment | Reference |
|---|---|---|---|
| Released: < 70 ng/$10^6$ cells/day | neighboring cells | *in vivo* | [1] |
| Released: 50-150 ng/day | solubilized | *in vivo* | [2] |
| Loaded: 2 µg/scaffold Released: 79 ng/day | pre-encapsulated | poly(lactide-co-glycolide) (PLG) microspheres | [3] |
| Loaded: 95-145 ng/scaffold | solubilized | *in vitro* human microvascular dermal endothelial cells (HMVEC) | [4] |
| Loaded: 10µg Released: 100 ng/day | immobilized heparin crosslinked | *in vitro* and *in vivo* | [5] |
| Loaded: 4.8µg/day | solubilized | *in vitro* DegraPol® scaffolds dynamic bioreactor | [6] |
| Loaded: 5µg /$10^6$ cells/scaffold | immobilized EDC/Sulfo-NHS | *in vitro* Ultrafoam collagen sponge D4T cells dynamic bioreactor | [7] |

**F.2 HEPARIN CONJUGATION EFFICIENCY ASSAY**

The quantification of immobilized heparin was performed using a Toluidine blue assay described by Smith et al. [8]. A 0.0005% toluidine blue solution was prepared from toluidine blue (Sigma-Aldrich, St Louis, MO), 0.01 N HCl (Acros Organics) and 0.2% (w/v) NaCl (Certified ACS, Fisher Scientific). Heparin standards were prepared from stock solution of sterilized aqueous heparin solution: 100 µg, 50 µg, 25 µg, 12.5 µg, 6.25 µg, and 3.1 µg. Untreated and sodium hydroxide treated discs and scaffolds were prepared. Aminated and heparin-immobilized 2-D discs and 3-D scaffolds were submerged in 3 ml of toluidine blue solution in a glass vial. 400 µl of 0.2% NaCl solution was added to all samples. The scaffolds and standards were vortexed for 30 seconds, then placed on a shaker for 3-24 hours at room temperature. The PCL disks and scaffolds were stained purple in the presence of heparin. 3ml of n-hexane (Sigma-Aldrich, St Louis, MO), was added to each vial to extract the formed toluidine blue-heparin complexes. The toluidine blue-heparin complexes formed on the surface of the scaffolds were the scaffolds, but the hexane was still added to the samples to ensure uniform treatment. The vials were vortexed for 30 seconds, then placed on a shaker for 3 hours at room temperature. Thereafter, the aqueous layer containing unextracted toluidine blue was extracted from the vial and the absorbance of 500 µl samples of the solution were measured at 630 nm by microplate reader (Multiskan Spectrum, Thermo Electron Corporation). Based on a derived calibration curve, the amount of immobilized heparin on the PCL scaffold was estimated. The average amount of retained heparin from each respective 0 µg sample group was subtracted from the average of each sample within that group to remove the baseline absorbance. Fig. E.1 plots the retention of heparin onto aminated discs and scaffolds. There is a plateau effect seen for the scaffold.
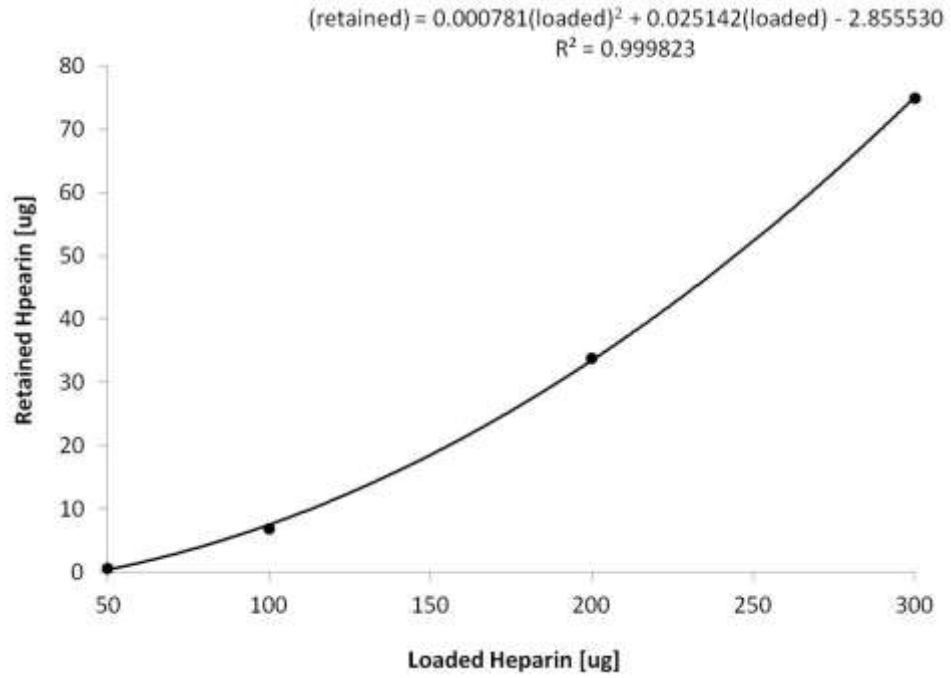
(a)
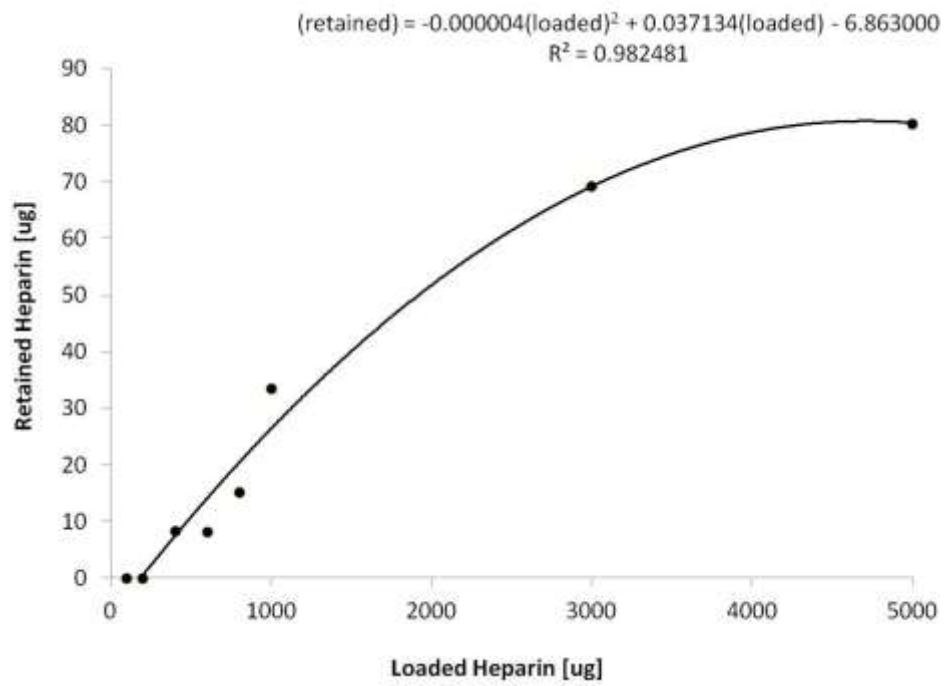


(b)

**Figure F.1 Amount of heparin immobilized onto the untreated PCL (a) discs and (b) scaffolds (n = 3).**

## F.3  CHARACTERIZATION OF DEGRADATION EFFECTS ON MECHANICAL AND PERFUSION PROPERTIES OF SODIUM HYDROXIDE-TREATED PCL SCAFFOLDS

Eight specimens were used to estimate the compressive modulus. The moduli were calculated through unconfined compression testing using an MTS Alliance RT30 electromechanical test frame (MTS Systems Corp., MN). TestWorks4 software (MTS Systems Corp., MN) was used to collect and analyze data during compression testing. Compressive modulus was calculated using area measurements derived from caliper height and diameter measurements of pre-tested samples. Compressive modulus was defined as the slope of the linear portion of the stress–strain curve. The permeability of the scaffolds was also estimated using our flow meter system described in Section 3.3.3. A two-tail Student's *t*-test assuming unequal variance was used to determine whether there significance was significant difference in the measured compressive moduli and hydraulic permeability.

The mean elastic moduli of the untreated and NaOH-treated PCL scaffolds were $23 \pm 1$ MPa and $20 \pm 2$ MPa, respectively. The stiffness of the two scaffolds was not significantly different (P-value $< 0.05$). The hydraulic permeability of the untreated and NaOH-treated PCL scaffolds was $4.3 \times 10^{-7} \pm 8.7 \times 10^{-8}$ $m^4/N \cdot s$ and $2.4 \times 10^{-6} \pm 5.8 \times 10^{-7}$ $m^4/N \cdot s$, respectively. NaOH-treated scaffolds were more permeable to water perfusion.
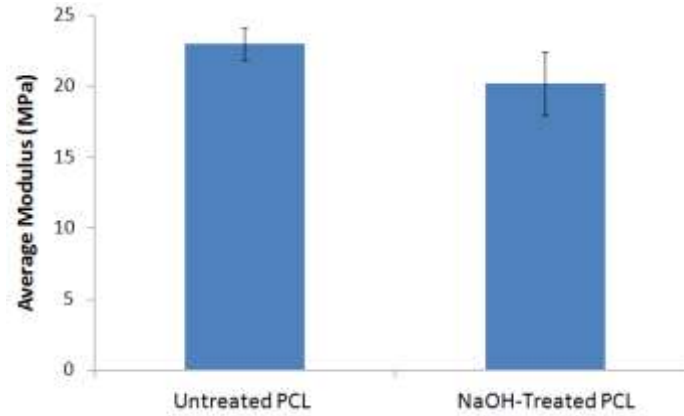
(a)
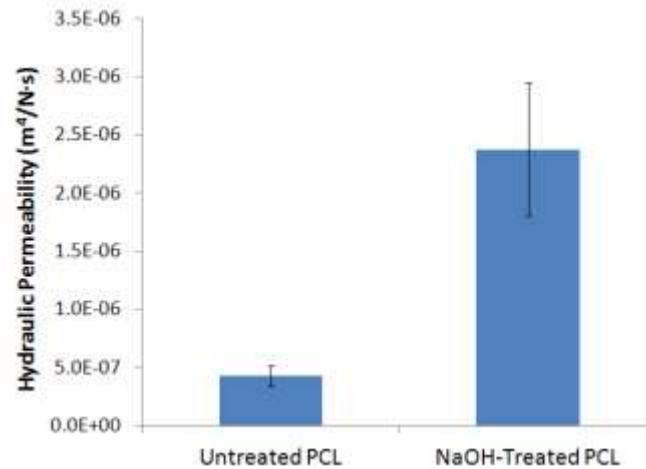


(b)

**Figure F.2 (a) Average elastic modulus and (b) average hydraulic permeability for the untreated and NaOH-treated PCL scaffolds.**

**REFERENCES**

[1]    Ozawa, C.R., Banfi, A., Glazer, N.L., Thurston, G., Springer, M.L., Kraft, P.E., McDonald, D.M., and Blau, H.M. Microenvironmental VEGF concentration, not total dose, determines a threshold between normal and aberrant angiogenesis. Journal of Clinical Investigation **113**, 516, 2004.

[2]    Davies, N., Dobner, S., Bezuidenhout, D., Schmidt, C., Beck, M., Zisch, A.H., and Zilla, P. The dosage dependence of VEGF stimulation on scaffold neovascularisation. Biomaterials **29**, 3531, 2008.

[3]     Richardson, T.P., Peters, M.C., Ennett, A.B., and Mooney, D.J. Polymeric system for dual growth factor delivery. Nat Biotech **19**, 1029, 2001.

[4]     Silva, E.A., and Mooney, D.J. Effects of VEGF temporal and spatial presentation on angiogenesis. Biomaterials **31**, 1235, 2010.

[5]     Singh, S., Wu, B.M., and Dunn, J.C.Y. The enhancement of VEGF-mediated angiogenesis by polycaprolactone scaffolds with surface cross-linked heparin. Biomaterials **32**, 2059, 2011.

[6]     Tan, Q., Steiner, R., Yang, L., Welti, M., Neuenschwander, P., Hillinger, S., and Weder, W. Accelerated angiogenesis by continuous medium flow with vascular endothelial growth factor inside tissue-engineered trachea. European journal of cardio-thoracic surgery **31**, 806, 2007.

[7]     Odedra, D., Chiu, L.L.Y., Shoichet, M., and Radisic, M. Endothelial cells guided by immobilized gradients of vascular endothelial growth factor on porous collagen scaffolds. Acta Biomaterialia **7**, 3027, 2011.

**[8]**     Smith, P., Mallia, A., and Hermanson, G. Colorimetric method for the assay of heparin content in immobilized heparin preparations. Analytical Biochemistry **109**, 466, 1980.

# APPENDIX G- CHAPTER 7

## G.1 OPERATING THE VASCULAR-LIKE ENDOTHELIAL CELL BIOREACTOR

**Name of Procedure:** Setting up and operating angiogenesis bioreactor.
**Prepared by:** Auresa Thomas and Leonie Genesteir
**Hazards:** none
**Protective equipment:** Use latex gloves, sterilizing with 70% ethanol, ethylene gas or autoclave; lab coat
**Waste disposal:** Items that interact with cells should be placed in the biohazard trash bin. All other items can go into normal trash.

### Materials

MasterFlex® Silicone Tubing (Platinum) L/S® 25 (25 ft)
Three-way stopcock Leurlock, PVDF
Rubber stopper
Clamp, punch valve,large
Clamp, punch valve,small
Male LuerLock coupling (for 3/16'' tube), polypropylene
Female LuerLock coupling (for 3/16'' tube), polypropylene
Male LuerLock caps
Female LuerLock caps
*˜Pulse dampener, for all Masterflex® L/S® and I/P® tubing
*Pump
*Flowmeter
(Modified) Petri dish
Flow splitter (manifold), polypropylene
Media storage bottle, 1 L
*Sterile 0.22 µm syringe filter
*Sterile 5 ml Syringe
Sterile Liquid Filters (larger than syringe filters)
*pH test strips
magnetic stirrer (1.5 in and 0.5 in - Length)
*Endothelial cell media
*70% ethanol

PBS
gauze
Autoclave tape
Cautery system (only tips autoclaved)
Sterile gloves

*Should not be autoclaved.
˜Ethylene oxide sterilization
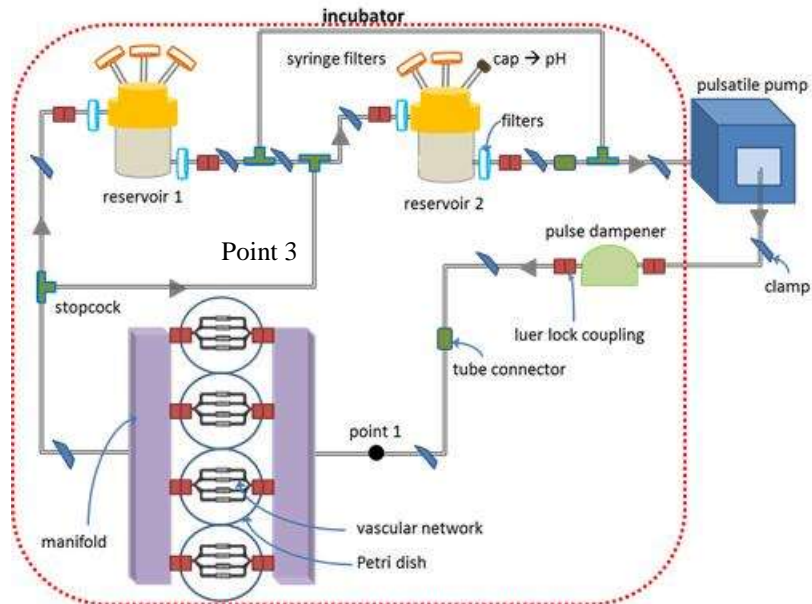


**Figure G.1 Bioreactor setup (for up to 4 connected network).**

## Connection Properties

| Connections | Connection Size |
|---|---|
| Pump Tubing (everywhere except reservoir II to pump to pulse dampener) | L/S® 25 (3/16'' ;  4.8 mm) |
| Pulse dampener inlet/out | 3/16'' tube end to  1/8" NPT |
| Pulse dampener out | 1/8" NPT to 3/16'' tube |
| Flow splitter inlet | 3/16'' tube end to 1/4" NPT |
| Flow splitter outlet | 3/16'' tube end  to 1/8" NPT |
| Flow meter | 1/8" NPT |
| Petri dish inlet/interior Luer Lock | 3/16'' tube end standard Luer Lock |

| | |
|---|---|
| Petri dish inlet/outlet/interior tube | 3/16'' |
| Vascular network inlet/outlet | 2.2 mm into standard Luer Lock |
| Stopcock (all) | standard Luer Lock |
| Reservoir I inlet | 5 mm |
| Reservoir II inlet | Glass rod fitting 3/16'' tube |
| Reservoir I outlet | Glass rod fitting 3/16'' tube |
| Reservoir II outlet | Glass rod fitting 3/16'' tube |

## A. **Getting Started: Testing the System**
1. No sterilization is needed.
2. Assemble the components in the incubator based on Figure 1. The follow meter should be connected to the system.
3. The Modified Petri Dishes should have a tube connecting the luer lock ends (as a place holder for the vascular networks).
4. Load 500-900 ml of water into reservoir 1.
5. Turn on pump at arbitrary setting (ml/min).
6. Monitor the flow meter readings. Determine the pump speed needed to have a 4 g/s reading at the flow meter.
7. Once the pump speed is determined, place the flow meter at each manifold tube outlet to ensure speed is the same at each outlet (that will be connected to a Petri dish).
8. Record how long it takes for the water to reach the flow meter.
9. Alternatively, the permeability chamber set-up can be used to measure flowrate.

## B. **Getting Started: Sterilization**

Ethylene Oxide Sterilization (1 week before study)
1. Ethylene oxide the pulse dampener. Allow to air out in the hood for 2-3 days before using with cells.

Sterilize Supplies (2 days before study)
2. Autoclave or ethylene oxide all supplies.
3. Decontaminate the incubator.
4. Sterile the stir plates with 70% ethanol. Place stir plates in the incubator. The stir plate cords should be run through the hole in the back of the incubator and plugged into a power source.
5. Cut up plenty of parafilm strips and soak them in a 70% ethanol bath in a large Petri dish. Allow to dry for 24 hours in hood.

Vascular Network and Scaffold Sterilization (2 days before study)
6. Soak scaffolds and vascular network/holders in 70% ethanol for 24 hours.
7. Wash with sterile water for 1 hour.

8.  Allow to dry for 24 hours in hood.

## C. <u>Getting Started: Bioreactor Study Day 0</u>
1.  Seed cells onto the scaffold at an appropriate density. (See 'Seeding Protocol')
2.  Incubate the scaffolds in EC media (2ml) in a 'Low Attachment' well plate for 24-48 hours (or longer, as desired).

## D. <u>Getting Started: Bioreactor Study Day 1</u>

<u>Caution:</u>
1.  Wash your hands with soap before begin the assembly.
2.  Next, change gloves every 30 minutes.
3.  Every time the hands are out of the hood, clean your gloves with ethanol before placing your hands in the hood.
4.  If you touch an unsterile item with your gloves outside of the hood, CHANGE your gloves
5.  Manipulate sterile elements in the center of the hood; always avoid manipulating close to the aeration grid.
6.  Do not handle above other sterile elements.

<u>In the hood</u>
1.  Disinfect the hood before using it with 70% ethanol.
2.  Bring incubator shelf into the hood.  Do all assembly of parts on the shelf (for easy transfer of shelf to incubator). Tape components to the shelf as needed based on the Figure 1.
3.  Define a place for waste in the hood.
4.  Insert the clamps around silicone tubing (see the figure 1).
5.  Place the filters and the luer lock couplings at the end of the tubes and connect it to the media storage bottles and to the pulse dampener.
6.  Place small magnetic stirrer in pulse dampener.
7.  Place the connectors and the three-way luer lock stopcocks and install the tubes.
8.  Place 2 male luer lock couplings at the ends of silicone tubings to connect them with the female luer lock couplings of the Petri Dish.
9.  Attach 3 filters with tubing to the rubber stoppers.
10. Check that all the system components are closed and well-fixed.
11. The Modified Petri Dishes should have a tube connecting the luer lock ends (as a place holder for the vascular networks).
12. Put 900 ml of 70% ethanol into the media storage bottles.
13. Connect the silicone tubing to the pump and cycle the ethanol through the system for 30 minutes. (Some of the tube will have to hang outside the hood. Place pump on table/chair.)
14. Turn off the pump. Empty the ethanol from the storage bottles by pipetting or aspirating .
15. Wipe cord that was outside the incubator with 70% ethanol.
16. Place 900 ml of media in the water bath to warm.

17. Pre-soak scaffolds in media in closed well plate.
18. Put 900 ml of sterilized water into the media storage bottles.
19. Connect the silicone tubing to the pump and cycle the water through the system for 30 minutes. (Some of the tube will have to hang outside the hood. Place pump on table/chair.)
20. Turn off the pump. Empty the water from the storage bottles by pipetting or aspirating.
21. Wipe cord that was outside the incubator with 70% ethanol.
22. Put 900 ml of PBS into the media storage bottles.
23. Connect the silicone tubing to the pump and cycle the PBS through the system for 30 minutes. (Some of the tube will have to hang outside the hood. Place pump on table/chair.)
24. Turn off the pump. Empty the PBS from the storage bottles by pipetting or aspirating.
25. Wipe cord that was outside the incubator with 70% ethanol.
26. Put 900 ml of media into the media storage bottles. Place magnetic stir bar in each media bottle.
27. Close the bottles with the rubber stoppers.
28. Connect the silicone tubing to the pump and run the media through the system until it reaches Point I. (Some of the tube will have to hang outside the hood. Place pump on table/chair.)
29. Turn the pump off. Clamp the tubing at Point 1.
30. Pre-fill networks as much as possible with media using a syringe and closing off an end of the network with a luer lock cap.
31. Carefully (so as to not disturb cells), place the scaffolds (retrieve from the incubator) in the network.
32. Use the cautery to seal the circumference of the holder at the two connection points.
33. Position the vascular network in the Modified Petri Dish using the male luer lock couplings at the extremities of the dish.
34. Aspirate any media that falls onto the dish.
35. Transfer the system to the incubator (May require 2-3 people).
36. Place the pulse dampener, and reservoir 1 and 2 on top of stir plates.
37. Connect the silicone tubing to the pump through the hole in the back of the incubator. Chose the value of the flow and turn on the pump.
38. Close the incubator hole with the rubber stopper or autoclaved gauze.
39. Open the clamp to the petri dish (Point 1 on the Figure 1).
40. Turn on pump a low speed and slowly ramp up to the pre-determined speed (ramp over 5 minutes, with 5 intervals).

**Figure F.4 (A) Sealed vascular network. (B) Operating bioreactor positioned within incubator.**

## Daily Operation During Study
1. Run bioreactor for 10 days.
2. Each day, spray 70% ethanol on tubing and connections in the incubator (and inside surfaces of the incubator)

3. Monitor bioreactor twice a day (early morning and late afternoon)

Monitoring Media pH
1) Attach a 5ml syringe to the capped tubing at the top of the rubber stopper on the media bottle.
2) Close the tubing with cap once the task is completed.
3) Measure the pH with a pH strip. Record the value. The value of the pH in the medium bottle should be $7.5 \pm 0.5$.

Changing the Media and Dampener
There will be no need to change the media for a culture study less than 10 days, if 500+ ml of media used at the start.

**REFERENCES**

Huang, Angela H., and Laura E. Niklason. Engineering biological-based vascular grafts using a pulsatile bioreactor. Journal of Visualized Experiments **52**, 2011.